Lithium Containing Complex Metal Oxides and Metal Phosphates: Investigations on their Synthesis and Various Characterizations for Rechargeable Lithium Battery Applications

Thesis submitted to

COCHIN UNIVERSITY OF SCIENCE AND TECHNOLOGY

In partial fulfillment of the requirements for the award of

DOCTOR OF PHILOSOPHY

By

K.Raveendranath

Department of Physics
Cochin University of Science and Technology
Cochin-682022, India

July2008

Lithium Containing Complex Metal Oxides and Metal phosphates: Investigations on their synthesis and various characterizations for rechargeable lithium battery applications

Ph.D thesis in the field of material science

Author:

Raveendranath.K
Division for Research in Advanced Materials
Department of Physics
Cochin University of Science and Technology
Cochin-682022, Kerala, India
Email: ravi_knath@yahoo.co.in

Supervisor:

Dr.S.Jayalekshmi
Reader
Division for Research in Advanced Materials
Department of Physics
Cochin University of Science and Technology
Cochin-682022, Kerala, India
Email: sjr@cusat.ac.in

July 2008

Department of Physics
Cochin University of Science and Technology
Cochin-682022, India

Date:06-08-2008

Dr.S.Jayalekshmi
Reader.

Certificate

Certified that the work presented in this thesis entitled **"Lithium Containing Complex metal oxides and metal phosphates: Investigations on their synthesis and various characterizations for rechargeable lithium battery applications"** is an authentic record of the bonafide research work done by Mr. Raveendranath.K, under my guidance and supervision in the Department of Physics, Cochin University of Science and Technology, Cochin-682022, and it has not been included in any other thesis submitted previously for award of any degree.

S Jayalekshmi

Dr.S.Jayalekshmi
Supervising Guide

Declaration

I hereby declare that the work presented in this thesis entitled "Lithium Containing Complex metal oxides and metal phosphates: Investigations on their synthesis and various characterizations for rechargeable lithium battery applications" is based on the original research work done by me under the guidance and supervision of Dr.S.Jayalekshmi, Reader, Department of Physics, Cochin University of science and Technology, Cochin-22 and it has not been included in any other thesis submitted previously for the award of any degree.

Cochin-22

K.Raveendranath

"You are successful and creative only when you see an opportunity in every difficulty"

Swami Chinmayanada

Dedicated to my parents and well wishers....

Words of Gratitude

It is with immense pleasure that I place on record my deep sense of gratitude to Dr. S. Jayalekshmi, Reader, Department of Physics, Cochin University of Science and Technology, for being my supervising guide and also for giving me proper encouragement throughout the work. Her meticulous dynamic guidance, scholastic suggestions, constant encouragement and comprehensive discussions at every stage have helped me to bring the work to a satisfactory completion.

I am extremely thankful to Prof. Godfrey Louis, Head of the department of Physics, CUSAT and Prof.V.C.Kuriakose, former HOD for providing the necessary library and laboratory facilities.

I have been privileged throughout the period of my research work to have the advice and help of Dr. M. K. Jayaraj, Reader, Department of Physics CUSAT. I also had the opportunity to interact with Dr. M.R Anantharaman, and Dr.B.Pradeep, Reader, Department of Physics CUSAT during the years of research work. I take this opportunity to thank them for the co-operation and timely assistance extended to me.

I am grateful to Prof. K. P. RajappanNair, former HOD for the co-operation and encouragement given to me. I take this opportunity to thank all the faculty members of the Department of Physics, CUSAT for the encouragement and timely help.

I express my deep sense of gratitude to Dr. Thomas Lee and Dr.Jyotsna Ravi (Departamento de Fisica Universidad de Concepcion, Casilla -160C Concepcion, Chile). They put me on the right track of research from my M.Phil course onwards. Their authentic approaches towards the subject, genuine scholarship and commitment to the high ideals of research have always been a source of inspiration to me. I am much indebted to them for allowing me to make use of their laboratory facilities without which it would have been almost impossible to complete this work.

I have enjoyed the friendship of Mr.Rajive Tomy, Research scholar, DREAM, CUSAT, whose skills in handling and maintaining equipments have been quite useful in various stages of my experimental work.

At this moment I express my sincere gratitude to my colleagues at the research lab, Mr.ArunKJoseph, Mr.Amrithesh, Mr.SreekanthVarma, Mr.Aravind, Mrs.Sreevalsa,Mrs.Jeeju,Mrs.Dhanya, Mrs.Sajimol, Miss Chandini and Mr.Febin Kurian for their help ,love and support. They have provided a harmonious research atmosphere, which is absolutely necessary for being creative.

I have had the opportunity to interact with many other research scholars, including Mr.U.S.Sajeev, Mrs.Vanaja.K.A, Mr.Joshy, Mr.Saji,Mr. Ajimshah, Mr.Manoj, Mrs.Rashmi, Mr.Anoop, Mrs.Anila, Mr.Sreekumar, Mrs.Asha, Mr.Aneesh, Mrs.MiniKrishna, Mr.E.M.A.Jamal, Mr.Narayanan, Mr.Jayakrishnan, Mr.Lyjo(ISP), Mr.Vimal, Mr.Sanoj, Mr.Arun, Mr.Krishnaprasad, Mr.Sinoy and Mr. Francis Xavier during the research work. I take this opportunity to express sincere gratitude for the affection and support given to me.

I extend my sincere thanks to the administrative, library and laboratory staff of the Department of Physics for their timely help and assistance. I would like to thank the Mr.Murali (USIC) for making my designs a practical reality.

I want to record thanks to Rev Dr.Francis MJ Fernandez, Manager Aquinas College for the support extended to me. I also express my deep gratitude to Mrs.D`Cruz Novella the former principal of Aquinas College for her help and support.

I would like to thank, the founder Principal of Aquinas College and my teacher Dr.P.M Joseph whose constant encouragement helped me to finish this work.

The encouragement and co-operation extended by my colleagues at Aquinas College Mr.Jerson K.J, Mr. Philip Neri K.I, Mr. Joseph John and other friends are gratefully acknowledged. With gratitude I cherish the interest shown by the superintendent Mr. Joseph John .C and Head

accountant Mr. Joseph T.X of Aquinas College in the progress of my research work. Special thanks are due to Mr.Rinku Jacob, guest lecturer, Department of Physics Aquinas College, for his assistance in the computer based designs and maintenance during the research work.

The motivation and affection shown by Shri.B.Raveendranathan Nair and Mrs.Chandrika the parents of Dr.Jyotsna Ravi have helped me quite a lot during various stages of my research work. I would like to remember with gratitude the advices and moral boosting extended to me by them.

I have enjoyed many wonderful moments with the family members of my guide, which include Dr.K.P.R.Kartha, Vinayak (Anku), Mr.JayaKrishnan, Smt.Ramadevi and Mr.Jayaraj.I would like to thank them all for their love and friendship.

I take this opportunity to cherish the memories of my eminent professors, Prof.Joseph Franklin Field, Prof.Antony Isaac of St.Paul's College, Prof.G.Ramnathan, Prof.Chakkunny (S.H.College Thevara), Prof.Govindankutty Menon and Prof.A.N.M Shenoy (U.C College), who have created in me the aptitude for pursuing Physics from my Pre-Degree days onwards.

I am also thankful to Prof.M.Rajendran, Prof.V.J Antony former HOD's of Physics Department, Cochin College, for their advice and help, especially at times when it really mattered. I acknowledge with thanks the constant encouragement extended by Dr.N.Hemalatha (BVM, Elamakkara), which has played a vital role in the completion of the research work.

My parents Shri.T.K.PankajakshanPillai and Smt.Lakshmi Amma, my brothers Mr.AravindakshaMenon, Mr. Rajendranth, Mr. Raghunath, Mr. Suresh, and sisters Mrs.Usha and Mrs. Jaya Sree have been the constant source of affection, support and encouragement for me. I do not have words to express my indebtedness to them for their prayers and moral boosting during the hectic years of my research work.

My wife Sudha and my beloved daughter Sree Rekha have shown indefinable patience love and support during the long and demanding years of hectic research activity. Their committed affection and encouragement

have worked as raindrops in the desert in many difficult situations of my research journey. Words cannot express my gratitude to them.

I am thankful to my father in law Mr.Puzhankara Aravindaksha Menon and mother in law Smt.Komalavally for their love and helps extended towards me.

Special thanks are due to Mrs.VisalamVijayan, Senior Teacher Good Shepard Convent Chennai (Rtd), sister of late Prof.V.Karunakara Menon for her invaluable encouragements, which is important in retaining my enthusiasm and attitude towards research.

It is my pleasure to mention here the names of the new generation members of my family Pournima, Pranav, Amit, Sree Lakshmi, Aswathy, Ayswarya for their everlasting love and support.

I thank my brothers in law Mr.M.Balakrishnan, Mr. Raghu Menon and Mr.Haridas for their affection and moral support.

With pleasure I express my sincere thanks to Mr.V.V Nair and family for their hospitality during my presentation at IIT Bombay.

Financial support in the form of Minor Research Project by UGC is gratefully acknowledged.

I feel highly blessed by Almighty the Supreme who controls all of us.

Raveendranath. K

Preface

For many years, nickel-cadmium had been the only suitable battery for portable equipments, from wireless communications to mobile computing. Nickel-metal-hydride and lithium-ion batteries emerged in the early 1990s, fighting nose-to-nose to gain customer's acceptance. Today, lithium-ion battery is the fastest growing and most promising battery technology. Rechargeable Li-ion cell is the key component in portable, entertainment, computing and telecommunication equipments offering high energy density, flexibility and lightweight design. The motivation for using this technology is the fact that Li is the most electropositive as well as the lightest metal that facilitates the design of storage systems with high energy density, good energy-to-weight ratio, no memory effect, long-term cycling stability and high charge/discharge rate capabilities. The most advanced batteries available in the market today are Li-ion and Li-ion polymer batteries. Another important factor affecting the demand for new battery systems is the shift towards the exploitation of alternating energy sources to replace the fossil fuel, which is progressively getting exhausted from the earth. To meet the constantly increasing energy needs of the developed countries of the world, the utilization of discontinuous energy sources such as solar power, wind power etc requires batteries as a storage facility. For this application, batteries should have the ability to under go large number of deep charge discharge cycles with high efficiency.

The advantage of using Li metal was demonstrated in the year 1970 with the assembly of primary Lithium cells. Originally, lithium metal foil was used as anode and an inorganic intercalation compound as cathode in secondary Li-batteries, thus exploiting the low weight and high reactivity of lithium. Safety concerns have led, however, to the replacement of metallic lithium by a Li-insertion compound. The discovery of such materials was crucial in the development of rechargeable Li systems. Thus the concept of Li-ion transfer cells was proposed to solve the problem of corrosion and thermal run away and possible explosion. The key to the successful development of a new generation of lithium batteries depends critically on the creation of new electrodes and electrolyte materials with composition and configuration, that offer high power density, long shelf and cycle life, low cost, and minimal capacity fade and disposal problems.

The current predominant cathode material is $LiCoO_2$, which is expensive, toxic, possesses limited practical capacity (<140 mAh g−1) and rates, and suffers from stability problems at elevated temperatures in the common electrolyte solutions. Consequently, intense research work on identifying new cathode materials for Li-ion batteries is being carried out today by hundreds of research groups throughout the world. The major cathode materials currently being explored are $LiMn_2O_4$, $LiFePO_4$, $LiMn_{1-x-y}Ni_xCo_yO_2$, $LiMn_{0.5}Ni_{0.5}O_2$, $LiMn_{1.5}Ni_{0.5}O_4$, $LiNi_{1-x}MO_2$ (M = a third metal, Co, Al) Li_xVO_y etc. . $LiMn_2O_4$ is inexpensive and 'green' (eco-friendly) in nature. Unlike layered structured cobalt oxide materials, all atoms in spinel shaped manganese

oxides are connected via genuine chemical bonds with large channels in the lattice for Li insertion and hence they have low discharge capacity and structural stability at moderately high temperature. However, batteries made of $LiMn_2O_4$ electrodes show drastic capacity fading after each charge-discharge cycle which may be due to the instability of the organic based electrolyte in the high voltage region, dissolution of $Li_xMn_2O_4$ electrode in the electrolyte as Mn^{2+} ions and onset of Jahn-Teller effect in deeply discharged $LiMn_2O_4$ electrodes.

Recently, it has been recognized that NaSICON (a family of Na super-ionic conductors) or olivine (magnesium iron silicate) oxyanion scaffolded structures, built from corner-sharing MO_6 octahedral (where M is Fe, Ti, V or Nb) and XO_4 tetrahedral anions (where X is S, P, As, Mo or W), offer interesting possibilities. Among them, Lithium metal phosphates, $LiMPO_4$ (M=Fe, Mn, Co, Ni) have attracted particular attention due to their high energy density, low cost and good environmental compatibility of their basic constituents. Moreover, these compounds display high redox potentials, fast Li^+ ion transport, excellent thermal stability, high lithium intercalation potential (not too high to decompose the electrolyte), and energy density comparable to that of conventional lithium metal oxides.

Lithium metal phosphates (LMPs) adopt an olivine-related structure, which consists of a hexagonal closed-packing (hcp) of oxygen atoms with Li^+ and M^{2+} cations located in half of the octahedral sites and P^{5+} cations in 1/8 of the tetrahedral sites. The major problem facing the commercial use of these Lithium Metal Phosphates (LMPs)

is their poor rate capability, which is attributed to their low electronic conductivity and slow kinetics of Li diffusion through the interfaces. Two approaches have been attempted to overcome this problem. One is to enhance electronic conductivity by coating an electron-conducting layer around the particles, such as carbon, copper, and silver, or by doping with guest cations. The other is to minimize particle size by modifying the synthesis conditions, such as using solution method or lowering the sintering temperature. In the present work we suggest another way to improve the electrical conductivity of LMPs (typically $10^{-7} - 10^{-3}$ Sm^{-1}) by doping them with carbon nanotubes (CNTs) which have high electrical conductivity (as high as 10^{5} Sm^{-1}). We expect these CNTs to serve as microconductors within and between the grains of LMPs, thereby increasing the electrical conductivity of LMPs.

Since their discovery in 1991 by S. Iijima, carbon nanotubes have been of great interest, both from a fundamental view point and from that for various device oriented applications .An ideal CNT can be thought of as a one dimensional, hexagonal network of carbon atoms (graphene) that has been rolled up to make a flawless structure . It is nearly a one-dimensional form of fullerenes forming a quantum wire with a large length (up to several microns) and small diameter (a few nanometers) resulting in a large aspect ratio. The most important types of CNT structures are single walled nanotubes (SWNTs) and multiwalled nanotubes (MWNTs). A SWNT is considered as a cylinder with only one wrapped graphite sheet and an MWNT as a collection of concentric SWNTs. The length and diameter, and hence properties of

these MWNTs differ a lot from those of SWNTs. Specifically, MWNTs can carry current densities up to 10^9 - 10^{10} A/cm^2 and have good thermal conductivity of 3000 W/mK. These properties could be beneficial in situations where heat dissipation and thermal stability are important factors. In addition, MWNTs can be used as mechanical supports because of their high axial strength.

In the present work attempts have been made to study in detail the thermal, optical, structural and electrical properties of the spinel structured $Li_xMn_2O_4$(x=0.8,0.9,1,1.1 and 1.2) and its delithiated form λ-MnO_2 and the olivine structured $LiMPO_4$ (M=Fe, Ni). The Jahn-Teller distortion effect on the thermal and optical properties of $Li_xMn_2O_4$ has been investigated in depth. The effect of MWNTs on the electrical, optical, structural and thermal properties of $LiMPO_4$ (M=Fe, Ni) has also been subjected to detailed investigations.

The thesis is entitled ***"Lithium Containing Complex metal oxides and metal phosphates: Investigations on their synthesis and various characterizations for rechargeable lithium battery applications"*** and consists of **six chapters**.

Chapter -1 gives a general introduction to the subject matter contained in this thesis. It includes a chronological description of the development of batteries, commonly used battery terminology, lithium battery concept, the significance of the materials selected for the present investigations, and a brief description of the various synthesis and characterization techniques used. The highlights of the present

investigations and their future scope are also briefly explained in this chapter.

Chapter-2 *gives an account of the relevant theoretical aspects used in the present investigations. This includes a detailed description of the Photo Acoustic Spectroscopy (PAS), Density Functional Theory (DFT) to analyse the photo acoustic spectra, theoretical aspects of ac and dc carrier transport properties, the salient features of X -ray Diffraction (XRD), Transmission Electron Microscopy (TEM) and Scanning Electron Microscopy (SEM)*

Chapter-3 describes the synthesis of spinel $Li_xMn_2O_4$ and λ-MnO_2, their structural characterization using XRD, SEM and TEM and a detailed account of the investigations on the influence of lithium content on the thermal and optical properties of $LiMn_2O_4$. . The thermal properties of the samples are evaluated from photoacoustic signal amplitude and phase as a function of modulation frequency in reflection configuration while information of their electronic band structure is obtained from the wavelength dependence of the photoacoustic signal. The role of lithium concentration and temperature for the occurrence of Jahn-Teller (J-T) distortion in $Li_xMn_2O_4$is investigated in detail using photo acoustic technique.

The synthesis of olivine $LiFePO_4$ and a detailed account of the investigations on its structural, thermal, electrical and optical properties are included in ***Chapter-4***. Structural characterization is done using XRD, SEM and TEM. The thermal properties of the samples are

evaluated from photoacoustic signal amplitude and phase as a function of modulation frequency in reflection configuration while information of their electronic band structure is obtained from the wavelength dependence of the photoacoustic signal. In this study, the band gap of $LiFePO_4$ is also estimated from the reflectance spectrum recorded in the range 300-2000 nm with a view to clear the ambiguity surrounding the band gap value of this material. The influence of the addition of MWNTs on the structural, thermal, optical and electrical properties of $LiFePO_4$ is also discussed in detail in this chapter.

Chapter-5 includes the synthesis of olivine LiNiPO4 and a detailed account of its structural, electrical, thermal and optical properties. As in the case of $LiFePO_4$ structural characterization is done using X-ray diffraction SEM and TEM studies and the thermal properties of the samples are evaluated from photoacoustic studies. The band gap of $LiNiPO_4$ is determined using reflectance spectrum recorded in the range 300-2000 nm. In this material also the influence of the addition of MWNTs on the structural, electrical, thermal and optical properties is investigated in a detailed way.

The conclusions drawn from the present investigations are summarized in ***Chapter -6***.The major achievements of the present investigations and the scope for further studies are also highlighted.

In International Journals

1. **K. Raveendranath,** Rajive M. Tomy, S. Jayalekshmi, R. V. Mangalaraja, J. Ravi and S. Thomas Lee "Evidence of Jahn-Teller Distortion in $Li_xMn_2O_4$ by Thermal Diffusivity Measurements" **Appl.Phy.A (2007) DOI: 10.1007/s00339-007-4294-0**

2. **K.Raveendranath**, Jyotsna Ravi, S.Jayalekshmi, T.M.A. Rasheed, and K.P.R.Nair "Thermal diffusivity measurement on $LiMn_2O_4$and its de-lithiated form λ–MnO_2 using Photo acoustic technique. **Material Science and Engineering B 131(2006) 210-215**

3. S.Thomas Lee, **K. Raveendranath**, M. Rajive Tomy. Paulraj, S. Jayalekshmi & J. Ravi, Evidence of band structure modification of $LiMn_2O_4$ upon lithium deintercalation by photoacoustic spectroscopy. **Applied Physics Letters 90, 1 (2007)**

4. S.Thomas Lee, **K Raveendranath**, Rajive M Tomy, Nibu. A George, S Jayalekshmi and Jyotsna Ravi Evidence of band structure modification due to Jahn–Teller distortion in LixMn2O4 by photo acoustic spectroscopy".**J. Phys. D: Appl. Phys. 40 (2007) 1–4**

5. S.Thomas Lee, **K. Raveendranath,** M. Rajive Tomy, Paulraj, S. Jayalekshmi & J. Ravi Effect of Lithium Concentration on the Thermal and Optical Properties of $Li_xMn_2O_4$ Investigated Using Photoacoustic Technique", **Physical Rev. B 76, 115112 _2007**

6. **K.Raveendranath,** S. Thomas Lee, Rajive M. Tomy, Jyotsna Ravi and S. Jayalekshmi "Experimental verification of electronic band structure of $LiFePO_4$ and its modification upon carbon nanotube doping by photo acoustic spectroscopy"(Communicated)

7. Jyotsna Ravi, **K. Raveendranath,** Rajive M Tomy, M Paulraj, S.Jayalekshmi, S.Thomas Lee."Band gap confirmation of Olivine $LiFePO_4$ and Effect of carbon nanotube doping on its electronic band structure.(Communicated)

8. S.Thomas Lee, **K. Raveendranath**, Rajive M. Tomy, S. Jayalekshmi and Jyotsna Ravi "Carbon Nanotube Doped $LiFePO_4$with Better Electrical Properties"(Communicated)

9. **K. Raveendranath,** Jyotsna Ravi, S.Thomas Lee Rajive M Tomy, S.Jayalekshmi."Band gap confirmation of Olivine $LiNiPO_4$ and Effect of carbon nanotube doping on its electronic band structure. (Communicated)

10. Jyotsna Ravi, **K.Raveendranath**, Rajive M Tomy S.Jayalekshmi, R.V.Mangalaraja, S.ThomasLee "Thermal properties of $LiMPO_4$ (M=Fe, Ni) by photoacoustic measurement and their modification upon adding multiwalled carbon nanotubes". (Communicated)

11. Jyotsna Ravi, **K.Raveendranath**, Rajive M Tomy S.Jayalekshmi, R.V.Mangalaraja, S.ThomasLee "Band Structure of Olivine Lithium Nickel Phosphate from Reflectance Spectrum and its modification upon multiwalled carbon nanotubes addition" (Communicated)

Papers presented in International Conferences

1. Photo acoustic investigation on thermal diffusivity of $LiMn_2O_4$ and its delithiated form, **Raveendranath.K,** Jyostna Ravi, S.Jayalekshmi, T.M.A Rasheed and K.P.R. Nair Proceedings of the Indo-Dutch workshop on "Current trends in photonic materials and devices" conducted during the **14th and 15th January 2003 at ISP, CUSAT**

2. **Raveendranath.K**, Jyostna Ravi, S.Jayalekshmi, T.M.A Rasheed, K.P.R.Nair "Synthesis,Characterisation and photo acoustic studies on $Li_xMn_2O_4$ spinel".International Conference on Optoelectronic Materials and Thin films for Advanced Technology(OMTAT-2005) **October 24-27 ,2005 CUSAT, India**

3. M.Rajive Tomy, R. Reshmi, **K. Raveendranath**, S. Jayalekshmi, M.K. Jayaraj, Optical absorption studies on $LiMn_2O_4$ films prepared by Pulsed Laser Deposition, presented at the 9th international conference on laser ablation, **'COLA-07', September 24-28, 2007, Spain**

4. **K.Raveendranath**, S. Thomas Lee, Jyotsna Ravi, M Rajive Tomy, and S. Jayalekshmi, "Evidence of Jahn-Teller Distortion in $Li_xMn_2O_4$ by Thermal Diffusivity Measurements", to be presented at International conference on advances in energy research (ICAER), **December 12-14, 2007 Indian Institute of Technology, Bombay.**

5. S.Thomas Lee **K. Raveendranath**, Rajive M. Tomy, R. V. Mangalaraja, S. Jayalekshmi & Jyotsna Ravi "Spectroscopic Evidence of Band Structure Modification in $Li_xMn_2O_4$ due to Jahn-Teller Distortion" International conference on advances in energy research **(ICAER), December 12-14, 2007 Indian Institute of Technology, Bombay**

6. M.Rajive Tomy, K.C. Haridas, **K. Raveendranath,** S. Jayalekshmi, "Effect of Ag^+ ion concentration on the optical absorption and photoluminescence observed in the silver–glass nanocomposites", presented at the International Symposium for Research Scholars on Metallurgy, Materials Science & Engineering, **December 18-20, 2006, IIT Madras.**

7. S.Thomas Lee, **K. Raveendranath**, Rajive M. Tomy, S. Jayalekshmi and Jyotsna Ravi "Optical absorption spectrum of $Li_xMn_2O_4$ by Photo

Acoustic spectroscopy" International Conference on Condensed Matter Physics **(ICCMP-2007) 25-28 November 2007 Jaipur Rajasthan**

8. **K.Raveendranath**, Rajive M. Tomy S. Thomas Lee, Jyotsna Ravi, , and S. Jayalekshmi "A comparison of Electrical transport Properties of the important battery material $LiMn_2O_4$ and $LiFePO_4$"International Conference on Solar cells **IC-SOLACE 2008, 21-23 January 2008 CUSAT,Kochi Papers presented in National Conferences/Seminars**

Papers presented in National Seminars

1. **K.Raveendranath**, M. Rajive Tomy, S.Jayalekshmi, "Synthesis, Characterization and Electrical properties of a Novel High Energy Density $LiNiPO_4$ Nanocomposite", presented at the national conference on smart electro ceramics **(NCSE-2007), March 8-9 2007, C-MET, Thrissur, Kerala**

2. **K.Raveendranath**, M. Rajive Tomy, S.Jayalekshmi, Investigations on the Electrical properties of $Li_x Mn_2O_4$ Nanocomposite, presented at the National conference on current trends in material science (CTMS-07), **March 25-27, 2007 Christian college Chengannur, Kottayam, India.**

3. M.Rajive Tomy, **K.Raveendranath**, Rini Thomas, S. Jayalekshmi "A comparative study of electrical properties of $LiMn_2O_4$ and its de-lithiated form" presented at the 17th Annual General Meeting, Materials Research Society of India **(MRSI) Conference, February 13-15, 2006, Lucknow University.**

4. **K.Raveendranath**, S. Thomas Lee, Jyotsna Ravi, Rajive M. Tomy, and S. Jayalekshmi "Determination of Band Gap of Pure and Carbon Nanotubes Doped $LiFePO_4$ by Diffuse Reflectance Measurements" National Conference on New Horizons in Theoretical and Experimental Physics" **(NHTEP) October8-10, 2007, CUSAT, Kochi**

5. **K.Raveendranath**, Rajive M. Tomy, S. Thomas Lee, Jyotsna Ravi, and S. Jayalekshmi" Electronic Band structure Determination of $LiFePO_4$ using Photoacoustic Spectroscopy" National Conference on Nano materials &Nanotechnology **MRSI 8-10 December 2007 University of Lucknow**

Contents

Chapter 1

Chapter 2

Chapter 3

Chapter 1

Introduction

The present chapter gives a general introduction to the subject matter contained in this thesis. It includes a chronological description of the development of batteries, commonly used battery terminology, description of the lithium battery concept, the significance of the materials selected for the present investigations and a brief description of the various synthesis and characterization techniques employed.

1.1 A Brief History of Development of Batteries

Among all the power sources that man has invented, batteries find a commendable position owing to their versatile applications ranging from medical implants to space applications. Aiming at better power and life for batteries, researchers all over the globe are searching for newer and newer materials for battery developments. The invention of the battery in 1800 paved the way for major advances in the theories of electric current and electrochemistry. This invention resulted in the rapid development of both science and technology, making the 19^{th}

century, the age of electricity. Italian physicist Alessandro Volta gave the first authenticated description of an electrochemical cell. It was the introduction of telegraphy that increased the demand of reliable commercial batteries, capable of sustaining a substantial flow of electric current, with out much loss in cell voltage.

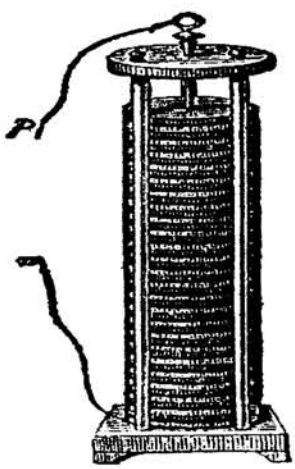

Fig.1.1 The Voltaic pile

Following the earlier work of his compatriot Luigi Galvani, Volta performed a series of experiments on electrochemical phenomena during the 1790s. By about 1800 he had built his simple battery, which later came to be known as the "Voltaic Pile"(Figure-1.1) This device consisted of alternating zinc and silver disks separated by layers of paper or cloth soaked in a solution of either sodium hydroxide or brine.

Experiments performed with the voltaic pile eventually led Faraday to derive the quantitative laws of electrochemistry (about 1834). These laws, which established the exact relationship between the quantity of

electrode material and the amount of electric power desired, formed the basis of modern battery technology. Various commercially significant primary cells were produced on the heels of Faraday's theoretical contribution. In 1836 John Frederic Daniel, a British chemist, introduced an improved form of electric cell consisting of copper and zinc in sulfuric acid. The Daniel cell was able to deliver sustained currents during continuous operation far more efficiently than Volta's device. Further advances were effected in 1839 by William Robert Grove with his two-fluid primary cell consisting of amalgamated zinc immersed in dilute sulphuric acid, with a porous pot separating the sulphuric acid from a strong nitric acid solution containing a platinum cathode. The nitric acid served as an oxidizing agent, which prevented voltage loss resulting from an accumulation of hydrogen at the cathode. The German chemist Robert Wilhelm Bunsen substituted inexpensive carbon for platinum in Grove's cell and thereby helped to promote its wide acceptance.

In 1859 Gaston Planté (1) of France invented a lead-acid cell, the first practical storage battery and the forerunner of the modern automobile battery. Planté's device was able to produce a remarkably large current, but it remained a laboratory curiosity for nearly two decades. Georges Leclanché's prototype of the zinc–manganese dioxide system paved the way for the development of the modern primary cell. The original version of the Leclanché cell was "wet," as it had an electrolyte consisting of a solution of ammonium chloride. The idea of employing an immobilized electrolyte was finally introduced in the late

1880s leading to the launching of dry-cell industry, which continues to flourish, even today. The invention of alkaline electrolyte batteries (specifically storage batteries of the nickel–cadmium and nickel–iron type) between 1895 and 1905 provided systems that could furnish much-improved cycle life for commercial application. The 1930s and '40s saw the development of the silver oxide–zinc and mercuric oxide–zinc alkaline cells, systems that provided the highest energy yet known per unit weight and volume.

Shortly before the Second World War mercury primary cell invented by Samuel Ruben was introduced in the market. At first, mercury cells were expensive, and due to their small size, they weren't used in many applications. With the invention of the transistor in the 1950s, mercury cells found their way into hearing aids and transistor radios. In the 1950s, the alkaline manganese cell was further refined. At the same time, small cameras with built in flash units were developed that required high power in a small package. Alkaline cells worked in this and other new consumer applications so well that, they gained tremendous popularity. They remain one of the largest portions of revenue for portable battery sales to this day. Development of the nickel metal hydride rechargeable cell began in the 1970s, but it was a long time before hydride alloys could perform well enough to begin production. Since the late 1980s, the performance of nickel metal hydride cells has steadily improved, and there may still be room for further performance enhancement.

Since mid-century, advances in construction technology and the availability of new materials have given rise to smaller, yet more powerful batteries suitable for use in a wide array of portable equipments. The latest developments in batteries, both primary and rechargeable, have centered on the use of lithium. Lithium is the lightest of all metals, has the greatest electrochemical potential, and provides the maximum energy. Lithium primary batteries were popularized in the 1970s and 80s. They have replaced the alkaline cell in most photovoltaic applications and are better suited to military and scientific applications than any other type. Attempts to make lithium rechargeable batteries go back to the 1980s. Problems with safety prevented the commercial use of the technology at that time. Finally rechargeable cells that use lithium metal were abandoned. Investigations were shifted to the use of lithium ions containing oxides and phosphates such as $LiMn_2O_4$, $LiCoO_2$, $LiFePO_4$, $LiNiPO_4$ etc. Since then lithium-ion batteries have become the most popular choice for use in high tech applications such as cellular phones and laptop computers.

What's next? Lithium polymer batteries are already being produced in a small scale, and offer the high performance of lithium combined with unparalleled packaging flexibility. Growing demands for development and introduction of battery-powered electric vehicle to keep cleaner environments have greatly stimulate the research on lithium insertion materials for high-volume, high –energy density, lithium ion batteries.

1.2 Battery

A battery is a device that converts the chemical energy contained in its active materials directly into electric energy by means of an oxidation–reduction reaction. In the case of rechargeable system, the battery is recharged by a reversal of the process. This involves the transfer of electrons from one material to another through an electric circuit. While the term "battery" is often used, the basic electrochemical unit being referred to as the "cell" (A cell is the basic electrochemical unit providing a source of electrical energy by direct conversion of chemical energy. The cell consists of an assembly of electrodes, separators, electrolyte, container and terminals) A battery consists of one or more of these cells, connected in series, parallel or the combinations of these, depending on the desired output voltage and capacity. Batteries, therefore, are capable of having higher energy conversion efficiencies.

1.3 Basic Components of an Electrochemical Cell.

Each cell consists of a positive and a negative electrode separated by an electrolyte solution containing dissociated salts (Figure1.2), which enable ion transfer between the two electrodes [2]. Once these electrodes are connected externally, the chemical reactions proceed in tandem at both the electrodes, thereby liberating electrons and enabling the current to be trapped by the user. The electrode materials and electrolyte are chosen and arranged so that sufficient electromotive force (voltage) and electric current (amperes) can be developed between the terminals of a battery to operate electrical gadgets. Since

an electrode contains only a limited number of units of chemical energy convertible to electrical energy, it follows that a battery of a given size has a certain capacity to operate devices and will eventually become exhausted. The active parts of a battery are usually encased in a box (or jacket).

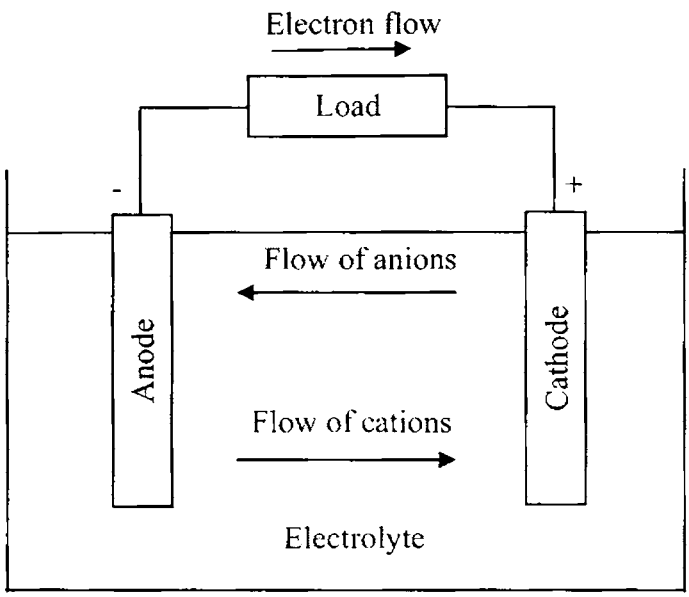

Fig.1.2. Electrochemical operation of a cell

Battery usefulness is limited not only by capacity but also by how fast current can be drawn from it. The salt ions chosen for the electrolyte solution must be able to move fast enough through the solvent to carry chemical matter between the electrodes in accordance with the rate of electrical demand. Battery performance is thus limited by the diffusion rates of internal chemicals as well as by capacity. The voltage of an individual cell and the diffusion rates inside it are both reduced if the temperature is lowered from a reference point. If the

temperature falls below the freezing point of the electrolyte, the cell will usually produce very little useful current and may actually change internal dimensions, resulting in internal damage and diminished performance even after it has warmed up again. On the other hand, if the temperature is raised deliberately, faster discharge can be sustained, but this is not generally advisable because the battery chemicals may evaporate or react spontaneously with one another, leading to early failure. Beyond the technical factors so far discussed, it must be recognized that commercially available batteries are designed and built with market factors in mind. The quality of materials and the complexity of electrode and container design are reflected in the market price sought for any specific product. As new materials are discovered or the properties of traditional ones improved, however, the typical performance of even older battery systems sometimes improves by large percentages.

Batteries are divided into two general groups: (1) primary batteries and (2) secondary, or storage, batteries. Primary batteries are designed to use until the voltage is too low to operate a given device and then discarded. Secondary batteries have many special design features, as well as particular materials for the electrodes, that permit them to be reconstituted (recycled). After partial or complete discharge, they can be recharged to their original state by dc voltage and current. While this original state is usually not restored completely, the loss per cycle in commercial batteries is only a small fraction of 1 percent even under varied conditions.

1.4 Principles of Operation of an Electrochemical Cell.

The anode of an electrochemical cell (Figure 1.2) is usually a metal that is oxidized (gives up electrons) at a potential between 0.5 volt and about four volts above that of the cathode. The cathode generally consists of a metal oxide or sulfide that is converted to a less-oxidized state by accepting electrons, along with ions, into its structure. A conductive link via an external circuit (e.g., a lamp or other device) must be provided to carry electrons from the anode to the cathode. Sufficient electrolyte must be present as well. The electrolyte consists of a solvent (water, an organic liquid, or even a solid) and one or more chemicals that dissociate into ions in the solvent. These ions serve to deliver electrons and chemical matter through the cell interior to balance the flow of electric current outside the cell during cell operation. The fundamental relationship of electrochemical cell operation put forth by Faraday in 1834 is that for every ampere that flows for a period of time, a matching chemical reaction or other change must take place. The extent of these changes is dependent on the molecular and electronic structure of the elements comprising the battery electrodes and electrolyte. Secondary changes may also occur, but a primary pair of theoretically reversible reactions must take place at the electrodes for electricity to be produced. For a cell with electrodes of zinc and manganese dioxide (e.g., the common flashlight dry cell), one finds that a chemical equivalent of zinc weighs 32.5 grams and that of manganese dioxide about 87 grams. The discharge of one equivalent weight of each of these electrodes will cause 32.5 grams of zinc to dissolve in the electrolyte to produce Zn ions and 87 grams of manganese

dioxide to change into a different oxide containing more hydrogen and zinc ions. Some of the electrolyte also will be consumed in the reaction. One chemical equivalent of each electrode produces one faraday, or 96,500 coulombs of current equal to 26.8 amperes per hour. There are a large number of elements and compounds from which one can select potentially useful combinations for batteries.

1.5 Battery terminology

The following are the commonly used terms used while dealing with batteries [2,3].

1.5.1 Active material

Active materials are the chemically reactive materials at the positive or negative electrodes that engage in the charge and discharge reactions.

1.5.2 Ampere-hours

It is a measure of cell capacity. It is the product of current in amperes and by the discharge time.

1.5.3 The anode

The electrode at which oxidation reaction occurs is the anode. In secondary cells, either electrode may become the anode, depending upon direction of current flow.

1.5.4 The cathode

An electrode at which reduction reaction occurs is the cathode. The positive electrode is the cathode on discharging and the negative electrode is the cathode on charging.

1.5.5 Electrolyte

The medium for movement of ions within the cell is the electrolyte.

1.5.6 Electrodes

Parts of the cell where the electrochemical reaction occurs are called electrodes. They normally consist of the active material and the current collector

1.5.7 Theoretical capacity

The ability of the battery or cell to supply current to an external circuit is termed as the theoretical capacity. It is determined by the amount of active materials in the cell. It is expressed as the total quantity of electricity involved in the electrochemical reaction and is defined in terms of coulombs or ampere-hours.

1.5.8 Cycle

In a rechargeable battery a cycle consists of a charge followed by a discharge.

1.5.9 Duty cycle

The pattern for using a battery including charge, overcharge, rest and discharge is commonly known as duty cycle.

1.5.10 Theoretical energy density

The energy stored in a cell or battery as a function of the weight or volume is termed as energy density [2,4]. It is often expressed as the ratio of its power to weight or size .The preferred terminology for this

ratio on weight basis is Watt-hour/kilogram (Wh/kg) or on volume basis is Watt-hour/litre (Wh/L)

Energy density = $\frac{1000E}{W} Wh/kg$, where W is the equivalent weight of anode and cathode and E the cell emf which is related to free energy, ΔG, of the cell reaction by

$$\Delta G = -nEF$$

where n is the number of electrons passed per mole of reactant and F is Faraday constant.

1.5.11 Shelf life

The length of acceptable performance received from a battery, measured in years or in charge/discharge cycles.

1.5.12 Open circuit voltage

The voltage of a battery with no load applied to it is referred to as Open circuited voltage.

1.5.13 Operating voltage

Voltage of a battery under load is its operating voltage.

1.5.14 Primary cell

A cell designed to be used only once, and then discarded.

1.5.15 Secondary cell

A cell capable of repeated use as it uses chemical reactions that are reversible-, i.e., supplying electrical current to recharge the cell may restore the discharge energy.

1.6 Different Nomenclature Representing Voltage of a Battery

a. The *theoretical voltage* is a function of the anode and cathode material parameter, the composition of the electrolyte and the temperature (usually stated at 25°C).

b. The *open-circuit voltage* is the voltage under a no-load condition and is usually a close approximation of the theoretical voltage.

c. The *closed-circuit voltage* is the voltage under a load condition.

d. The *nominal voltage* is one that is generally accepted as typical of the operating voltage of the battery as, for example, 1.5 V for a zinc-manganese dioxide battery.

e. The *working voltage* is more representative of the actual operating voltage of the battery under load and will be lower than the open-circuit voltage.

f. The *average voltage* is the voltage averaged during the discharge.

g. The *midpoint voltage* is the central voltage during the discharge of the cell or battery.

h. The *end* or *cut-off voltage* is designated as the end of the discharge. Usually it is the voltage above which most of the capacity of the cell or battery has been delivered. The end voltage may also be dependent on the application requirements.

1.7 Thermal Runaway

The loss of the gas barrier in one or more cells of a vented nickel-cadmium battery can lead to thermal runaway [1]. Loss of this function allows oxygen, generated in overcharge, to reach the negative plate and recombine on it. This generates heat. The temperature increase, which follows, causes the internal cell voltage to decrease. Charge current then increases exponentially to increase cell voltage to match the charger voltage. Thermal runaway occurs with the use of a voltage-regulated charge source on a battery containing cells with a failed gas barrier. Thermal runaway begins when the failed cells approach overcharge following recharge. The over- charge current may reach a minimum and then gradually increases. Voltage inequities may exist at this point unless all cells are experiencing similar recombination (gas barrier damage). Oxygen recombination heats up, and begins to increase the temperature of the failed cell or cells and thus their neighboring cells also unless the battery is effectively air-cooled. The resulting temperature increase, however, proceeds slowly due to the large thermal mass involved. It may take 2 to 4 hours of (nearly) consecutive overcharging for a cell to reach boiling temperature. If the boiling phase continues long enough, or is repeated, and the failed cell becomes dry, large inequities in cell voltage will appear. The voltage across the cell that has boiled dry will increase, thereby decreasing the charge current and the voltage across the cells that are still wet with electrolyte. The next event probably will be internal short-circuiting of the dried-out cell due to very high temperatures and voltage at the last remaining damp spots with consequent burning of the

electrical separator insulation. The over-charge current then increases sharply due to cell loss, and the process repeats itself with the next cell to go dry. Because of extensive heating and boil away times, thermal runaway may go un detected for many hours following the onset of gas barrier failure if the use of the system is not consecutive or continuous. This can confuse the perceived connection between the cause of the gas barrier damage and the resultant thermal runaway.

1.8 Memory Effect in Batteries

The gradual reduction of both power and capacity of a battery with cycling in a battery especially in Ni-Cd cell is an added disadvantage. This effect, sometimes referred to as 'memory effect,' 'fading,' or 'voltage depression,' results from charging following repetitive shallow discharges where some portion of the active materials in the cell is not used or discharged, such as in a typical engine-start use [1]. This effect is noticed when the previously undischarged material is eventually discharged. The terminal voltage during the latter part of that full discharge may be lowered a little (i.e. a depression of voltage). The total capacity is not reduced, however, if the discharge is continued to the lower voltages. This effect is completely reversible by a maintenance cycle consisting of a thorough discharge followed by a full and complete charge-overcharge.

1.9 Classification of Batteries

Electrochemical cells and batteries are identified as primary or secondary depending on their capability of being electrically recharged. Primary batteries are not capable of being easily or effectively recharged electrically and, hence, are used once and discarded. Many primary cells in

which there are no liquid electrolytes are termed "dry cells.' The primary battery is a convenient, usually inexpensive, lightweight source of packaged power for portable electronic and electric devices, lighting, photographic equipments, toys, memory backup, and a host of other applications, giving freedom from utility power. The general advantages of primary batteries are good shelf life, high energy density at low to moderate discharge rates, little, if any, maintenance, and ease of use. Although large high capacity primary batteries are used in military applications, signaling, standby power, and so on, the vast majority of primary batteries are the familiar single cell cylindrical and flat button batteries or multicell batteries using these component cells.

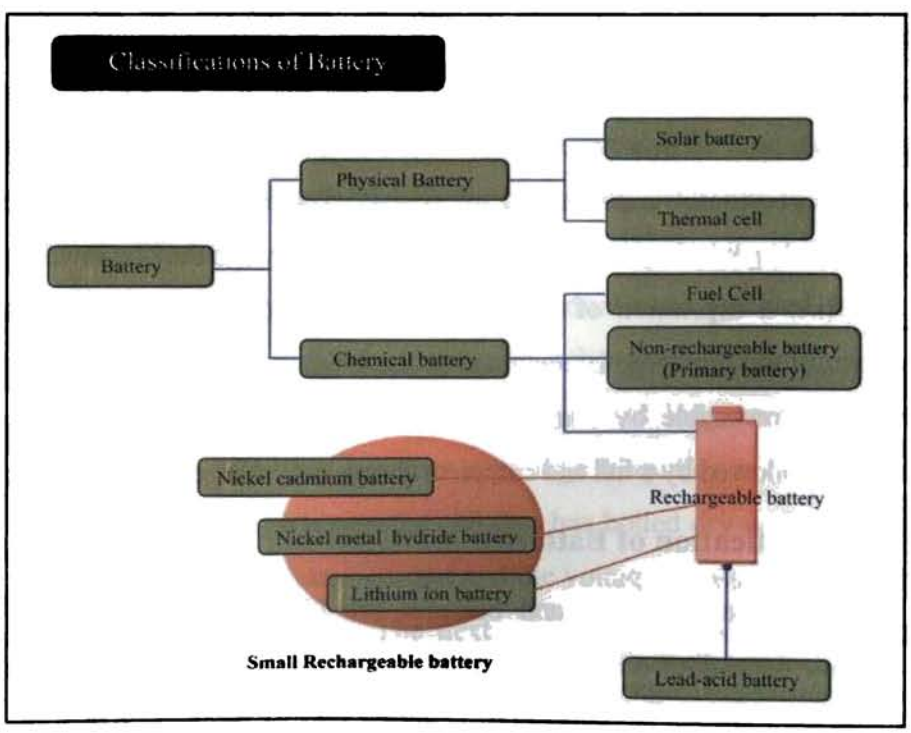

Fig. 1.3 Classifications of Battery

1.9.1 Comparison Data among Various Lithium based Batteries

Battery	$LiFePO_4$	$LiCoO_2$	$LiMn_2O_4$	$LiNiPO_4$	$Li(NiCo)O_2$
Safety	Safest	Not stable	Acceptable	Safe	Not stable
Environmental Concern	Most Enviro-friendly	Very dangerous	Green	Enviro-friendly	Very dangerous
Cycle life	Excellent	Acceptable	Acceptable	Better	Acceptable
Power/weight density	Acceptable	Good	Acceptable	Acceptable	Best
Long term cost	Most Economic	High	Acceptable High	High	High
Temperature Range	Excellent (-20°C to 70°C)	Decay beyond (-20°C to 50°C)	Decay extremely fast over 50°C	Excellent (-20°C to 70°C)	-20°C to 55°C

1.10 Ion Conductors and their Classifications

According to the ability of carrying electric current at room temperature solid materials can be classified in to (1) metals (conductivity $\sigma = 10^4 - 10^6$ S/cm) (2) insulators ($\sigma < 10^{-10}$ S/cm) and (3) semiconductors ($10^4 > \sigma > 10^{-10}$ S/cm). Solids having mainly electronic conductivity are the first type; where as solids having ionic conductivity predominance is the second type. The solid conductors, having electrons and ions contributing equally to conductivity, are mixed conductors. The high ion conductivity in certain solids approach similar values ($\sigma = 1\text{-}10^{-3}$S/cm) as in liquid salt solutions or melted salts. Therefore, such materials are called

solid electrolytes. Their conductivity is caused by a delocalization of metal ions over an excessive number of free interstitials in an immobile sublattice. Most of the solids show certain ion localization. However, in some compound at a certain temperature, a phase transition is possible, where the localized cation sublattice gets disordered over numerous interstitials. The conductivity spontaneously increases by several orders upon the melting of cation sublattice. Therefore, the term "solid electrolyte" can rather be used for the identification of a particular state of solid material. However, many other materials being ion conductors with a lower conductivity are also often referred to as solid electrolytes. According to Ratner et.al a solid electrolyte exhibits a characteristic ionic conductivity in the range 10^{-6} S/cm to 10^{-1} S/cm near ambient temperature. A more general approach is to use the term of "ion conductor" instead of using "solid electrolyte". A schematic representation of the classification of ion conductors according to chemical composition, polarity of mobile ions and morphology of solids are shown in Figure-1.4. The scheme comprises of a wide spectrum of solids starting from crystalline and ending with amorphous ones.

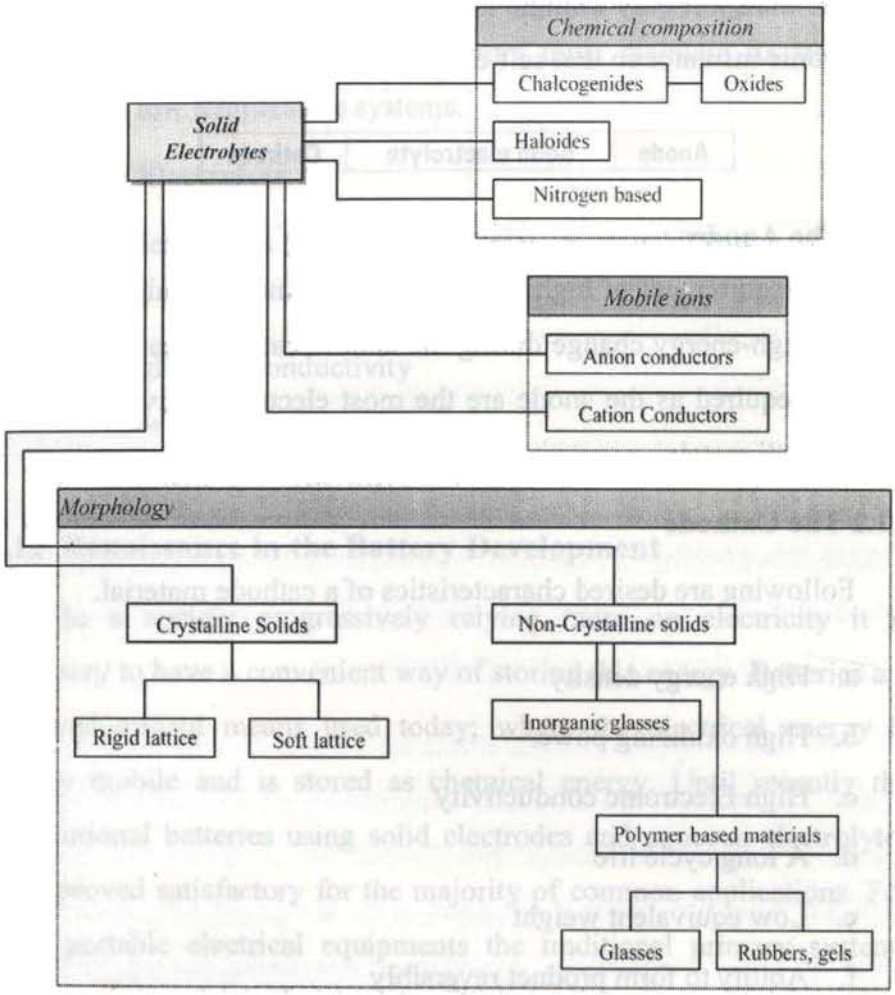

Fig .1.4 Types of solid ion conductors

1.11 Properties of the Components of a Battery

A solid-state battery consists of three active components as shown below. The anode is the electropositive half of the cell, typically a metal, and the cathode the electronegative half. The electrolyte must

be able to transport only a single ionic species, and at the same time be an electronic insulator so that self-discharge is minimized.

1.11.1 The Anode

The requirement of high energy density demands a high voltage, that is, a high-energy change during the anode- cathode reaction. Thus materials required as the anode are the most electro positive elements such as alkali metals.

1.11.2 The Cathode

Following are desired characteristics of a cathode material.

a. High energy density
b. High oxidizing power
c. High Electronic conductivity
d. A long cycle life
e. Low equivalent weight
f. Ability to form product reversibly
g. No reactivity with electrolyte
h. No solubility in electrolyte
i. Low corrosive properties.

More over it is desired that the material be easy to handle chemically stable, non-toxic and cost effective. The cathode must be capable of cycling daily with high efficiency for several years. This

dictates that the cathodic reaction must be readily reversible. This in turn demands that the cathode structure must maintain its structural integrity in low temperature systems.

1.11.3 The Electrolyte

The electrolytes for use in batteries must exhibit the following properties.

a. High ionic conductivity
b. Low electronic conductivity
c. Extreme chemical inertness

1.12 Renaissance in the Battery Development

In a society progressively relying more on electricity it is necessary to have a convenient way of storing this energy. Batteries are the predominant means used today; where the electrical energy is readily mobile and is stored as chemical energy. Until recently the conventional batteries using solid electrodes and aqueous electrolytes have proved satisfactory for the majority of common applications. For most portable electrical equipments the traditional primary systems such as Leclanché and mercury cells have been successful as power sources. In rural areas, in railways and in telephone systems the well-established rechargeable batteries such as those based on the lead-acid or nickel–cadmium batteries have long been employed as sources or auxiliary power sources. Research and developments in his direction has been taking place for improvements in efficiency, energy density and cyclability.

In the last two decades, however, the situation has changed considerably. Many advances have been made in the battery technology in recent years both through continued improvement of a specific electro chemical system and through the development and introduction of new battery chemistry. However batteries are not keeping pace with developments in electronic technology, where performance doubles every 18 months, phenomenon known as Moore's law. Micro electronic components are inexpensive and are widely used in the production of pocket calculators, electric watches, computers, mobile phones etc. Development of such miniature electronic instruments demands the evolution of miniature power supplies, which can offer a much higher energy density and superior discharge characteristics as compared with those of traditional batteries.

The most important factor affecting the demand for new battery systems is the shift towards the exploitation of alternating energy sources to replace the fossil fuel, which is progressively getting exhausted from the earth. To meet with the constantly increasing energy needs of the developed countries of the world, the utilization of discontinuous energy sources such as solar power, wind power etc requires batteries as a storage facility. For this application, batteries should have the ability to under go large number of deep charge /discharge cycles with high efficiency.

Batteries, unlike electronic devices, consume materials when delivering electrical energy and there are theoretical limits to the amount of electrical energy that can be delivered electrochemically by

the available materials. Recognizing the limitations of the battery materials researchers are focusing on reducing the ratio of inactive to active components to improve energy density, increasing conversion efficiency and rechargeability, maximizing performance under stringent operating conditions and enhancing safety.

1.13 Thin Film Batteries - A Trendsetter in Miniature Power Sources

The trend of power sources, in accordance with the shrinkage in the size of electronic devices have shifted from city line to regular batteries, and the final goal may be miniature power sources. By preparing electrochemical cells with thin-film architecture, extensive opportunities arise for their utilization in extremely diverse fields of technology, where small dimensions, high specific-energy ratings, reliable performance and long shelf life are required. The main advantages of thin film battery technology can be listed as follows.

a. Thin films are well accepted for device design,

b. The thinning of layers gives a lower resistance in the transverse direction in the case of poorly semi conducting materials,

c. The formation of a thin layer of electrolyte allows us to use glassy materials with a low ionic conductivity,

d. Some of the main difficulties in the behaviour of the electrolyte-electrode interface can be avoided,

e. Thin film batteries are manufactured by the same technique as currently used in microelectronics industry,

f. The micro battery is manufactured in almost any two-dimensional shape.

Thin film rechargeable lithium batteries have potentially many uses as low–current active or standby power supplies. A micro battery is a system, which can deliver energy in the range of few hundreds of μAh and can be used as a micro-power source applied to various devices. The most interesting application of solid-state micro batteries is in the field of electronic systems.

1.14 Major Events in Secondary Battery Development

Figure-1.5 shows a comparison of the different battery technologies in terms of volumetric and gravimetric energy density. The share of worldwide sales for Ni-Cd, Ni-MeH and Li –ion portable batteries is 23%, 14% and 63% respectively. The use of Lead-acid batteries is restricted mainly to SLI (starting, lighting and ignition) in automobiles of standby applications, while Ni-Cd batteries remain the most suitable technology for high-power applications (for example, power tools).

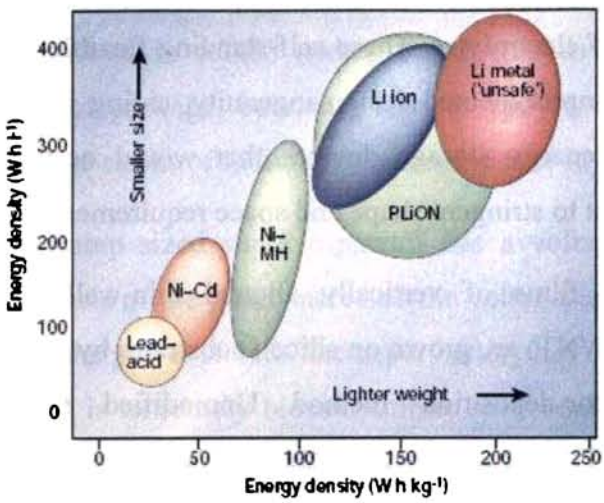

Fig. 1.5 Comparison of the different battery technologies in terms of volumetric and gravimetric energy density

1.15 The Concept of Flexible Paper Battery

Victor L. Pushparaj (Rensselaer Nanotechnology Center, NY, USA), Pulickel M. Ajayan (Rensselaer Polytechnic Institute Troy, NY, USA) et.al have recently demonstrated the design, fabrication, and packaging of flexible carbon nano tube (CNT)–cellulose–RTIL (room temperature ionic liquid) nanocomposite sheets, which can be used in configuring energy-storage devices such as super capacitors, Li-ion batteries, and hybrids [9,10]. The intimate configuration of CNT, cellulose, and RTIL in cellulose helps in the efficient packaging, operation, and handling of these devices. The discharge capacity and performance observed here compare well with other flexible energy-storage devices reported The robust integrated thin-film structure allows not only good electrochemical performance but also the ability to function over large

ranges of mechanical deformation and record temperatures and with a wide variety of electrolytes. These self-standing flexible paper devices can result in unprecedented design ingenuity, aiding in new forms of cost-effective energy storage devices that would occupy minimum space and adapt to stringent shape and space requirements.

Uniform films of vertically aligned thin-walled multiwalled nanotubes (MWNT) are grown on silicon substrates by using a thermal-chemical vapor-deposition method Unmodified plant cellulose dissolved in RTIL is infiltrated into the MWNT to form a uniform film of cellulose and 1-butyl, 3-methylimidazolium chloride ([bmIm][Cl]) embedding the MWNT. After solidification on dry ice, this nanocomposite is immersed in ethanol to partially or completely extract excess RTIL and dried in vacuum to remove residual ethanol. The resulting nanocomposite paper that forms the basic building unit is peeled from the substrate for use as the super capacitor. The nanocomposite paper (CNT cellulose–RTIL) shows excellent mechanical flexibility. The paper can be rolled up, twisted, or bent to any curvature and is completely recoverable. The nanocomposite paper, which can be typically a few tens of microns thick, contains MWNTs as the working electrode and the cellulose surrounding individual MWNTs, as well as the extra layer as the spacer and the RTIL in cellulose as the self-sustaining electrolyte. Two of the nanocomposite units bonded back-to-back make a single super capacitor [11,12] device. The thin lightweight (15mg/cm^2) design of the device results from avoiding the use of a separate electrolyte and spacer, generally

used in conventional super capacitors. The use of RTIL electrolyte (3 wt/wt % of cellulose in RTIL) makes the device environmentally friendly. In a final package, operating devices can be fabricated by laminating multiple stacks of individual nanocomposite layers.

Postage –stamp sized super capacitor has a voltage of almost 2.5V.Stacking sheets of the paper increases the voltage, and increasing its size increases the power stored. The paper battery has enough power to light LED and is extremely biocompatible, so it could be used as power supplies for devices implanted in the human body.

The fabrication of the flexible Li-ion battery based on the nanocomposite paper consists of RTIL-free nanocomposite as cathode and a thin evaporated Li-metal layer as anode with Al foil on both sides as current collectors. Aqueous 1 MLiPF6 (lithium hexaflouro phosphate) in ethylene carbonate and dimethyl carbonate (1:1 vol/vol) is used as the electrolyte. As with the super capacitor, this battery also uses the excess cellulose layer in the nanocomposite cathode as the spacer, without the use of any stand-alone spacer. The charge–discharge cycle voltages of the battery are measured between 3.6 and 0.1 V, at a constant current of 10 mA/g. A large irreversible-capacity (~ 430 mAh/g) is observed during the first charge–discharge cycle and further charge–discharge cycles resulted in a reversible capacity of 110-mAh/g .The battery devices operates under full mechanical flexibility.

In recent years, super capacitors coupled with batteries have been considered as promising hybrid devices (82,83) to combine with the

best features of a battery and a super capacitor. This battery and super capacitor devices could be integrated in parallel to build hybrids, as reported for conventional hybrids. In this case, the battery segment of the hybrid is used to charge the adjoining super capacitor.

1.16 Rechargeable Lithium- ion Battery Concept

For today's information rich, mobile society rechargeable Li-ion cells are indispensable as they are the key component in the portable, entertainment, computing telecommunication equipments. In most of the modern electronic equipments Li-ion batteries are the systems of choice, offering high energy density, flexibility and lightweight design. The motivation for using this technology is the fact that Li is the most electropositive as well as the lightest metal that facilitates the design of storage systems with high energy density. The most advanced batteries available in the market today are Li-ion and Li-ion polymer batteries [1,13,14]. The advantage of using Li metal was demonstrated in the year 1970 with assembly of primary Li cells. Owing to their high capacity and variable discharge rates, they could rapidly find applications as power sources for portable electronic devices such as watches, calculators and even in implantable medical equipments. Originally, lithium metal foil was used as anode in the secondary Li-batteries, and an inorganic intercalation compound as cathode, thus exploiting the low weight and high reactivity of lithium. (Metallic lithium is highly reactive with oxygen, making it a difficult material to handle). Safety concerns have led, however, to the replacement of metallic lithium by a Li-insertion compound. The discovery of such

materials was crucial in the development of rechargeable Li systems. By 1972 the concept of intercalation compounds and its potential use were clearly defined [2,3,4]. Thus the concept of Li-ion transfer cells was proposed to solve the problem of corrosion and thermal run away and possible explosion.

The invention of a new type of electrolyte based on lithium compounds dissolved in an ion conducting polymer cast as thin film made it possible to make all-solid state electrochemical batteries. This was the trigger for the lithium –polymer concept [13]. Today, these batteries generally incorporate a carbon based Li-compound or polymer-gel electrolyte. In this way active lithium is always present as an ion rather than as a metal.

1.17 Material Strategy for the Rocking Chair Battery

A lithium ion battery is comprised of three main components, a cathode, an anode and the electrolyte. The cathode material is a lithium metal oxide, while the anode is usually carbon. The electrolyte material can be an organic liquid containing dissolved electrolyte salts or a polymer electrolyte. Research is being carried out globally on developing all these three components. The present work however is focused on cathode materials and their innovations.

A lithium ion rechargeable battery is known as a rocking chair battery due to the two-way motion of lithium ions. The lithium ions are transported between the anode and the cathode through the electrolyte. During charging the lithium ions undergo deintercalation from the

cathode in to the electrolyte, simultaneously lithium ions intercalate from the electrolyte in to the anode. Intercalation is the process of inserting lithium ions into the structure of the electrodes. (Electrochemical reactions consisting of electron and lithium ion insertion into/extraction from a solid matrix with out much destruction of the core structure are called topotactic reactions and the materials for which such reversible reactions proceed are called insertion compound). During discharge the intercalation and deintercalation, reverse. The shift in charge, due to Li^+ movement during charging and discharging is compensated by electron flow through the external circuit. The topotactic Li-intercalation mechanism is the basis for the material's application as an electrode in a rechargeable battery. It is believed that Li is fully ionized in most lithium-metal oxides and donates its electron to the host without much affecting them. This substantial charge transfer to the anion is responsible for the voltage difference between oxides and sulphides. This makes it possible to control the band filling of the host material by varying the Li content electrochemically. In electrochromic applications, band filling is used to adjust the electronic and optical properties. Ionic relaxation, as a result of Li interaction, causes non rigid-band effects in density of states (DOS) of these materials [1-3,74]

Figure (1.6) shows schematically an electrochemical lithium cell. Two electrodes, the anode and cathode, are separated by an electrolyte. The electrolyte allows transfer of Li ions between the anode and cathode but does not allow for any electron transport. In most

applications the electrolyte is liquid, although glasses and solid polymers are being investigated as more versatile alternatives. The equilibrium voltage difference between the two electrodes, also referred to as the open circuit voltage (OCV), depends on the difference of the Li chemical potential between the anode (here Li metal) and cathode

$$V(x) = -\frac{\mu_{Li}^{cathode}(x) - \mu_{Li}^{anode}}{zF}$$

F is the Faraday constant and z is the charge transported by lithium in the electrolyte. In most nonelectronically conducting electrolytes z=1 for Li intercalation. For a battery, a large chemical-potential difference between cathode and anode is desirable as this leads to a high OCV.

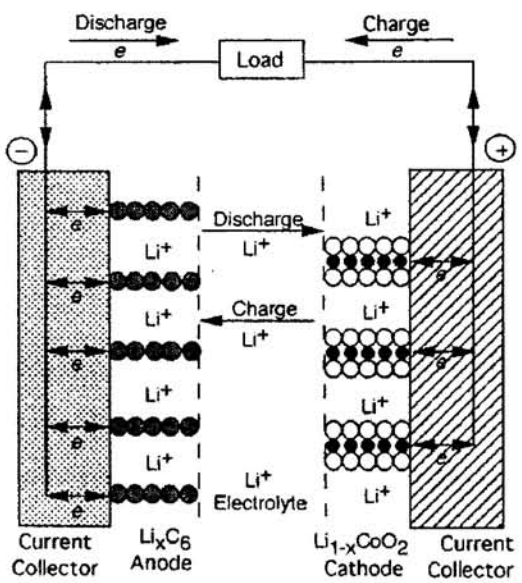

Fig.1.6 Dynamics of the Li-ion rocking chair battery

1.17.1 Reaction Mechanism

In lithium ion cells metallic lithium is substituted by insertion materials so that the safety and cycle life of the cells are remarkably improved. The reactions at both positive and negative electrodes consist of electron and lithium ion insertion in to/extraction from solid matrices with out the destruction of the core structure. The cathode materials are air stable 3d-transition metal compounds (say $LiMn_2O_4$) and anodes are usually carbon materials. The cells are fabricated in discharged state, so that the freshly prepared cells cannot deliver electricity. On charging, electrons and Li- ions move from positive to negative electrode storing electricity in the solid matrix. After charging the cells can deliver electricity while moving back the lithium ions. In other words, the cells are operated with lithium-ion shuttling between positive and negative electrodes. Hence the insertion materials are extremely important in developing the Li-ion batteries.

Lithium has got low density (0.53 g cm^{-3}), lightweight, low electro negativity, good conductivity, high electrochemical equivalence and high electron /atom mass ratio. Because of these features, lithium has become the preferred choice for the active element of anode, which, on discharge functions as an electron donor.

Anode:

$$x\,Li \Rightarrow x\,Li^{+} + x\,e^{-} \qquad \text{(Discharge)}$$

where Li^+ enters the electrolyte, and the electron exits the anode to the external circuit to power the load.

Ideally, an electrolyte would have electrical properties of a liquid and mechanical property of a solid. Such a material would serve both as electrolyte and separator and endow the battery with mechanical flexibility, a property unattainable in cells with conventional liquid electrolytes. So in this case, electrolyte must be an ionic conductor capable of solvating Li^+ ions. Because lithium is more electropositive than hydrogen, electrolyte must be non- aqueous and aprotic. A representative formulation is a solution (1:1 by volume) of ethylene carbonate and propylene carbonate containing a suitable lithium salt (at a concentration of about 1M) such as lithium hexaflourophosphate ($LiPF_6$) i.e. electrolyte must be a lithium salt dissolved in liquid/polymer gel. Non-aqueous phosphate electrolytes have to be employed since Li decomposes water. For safety, a separator made of a polyolefin such as micro-porous polypropylene is placed between the electrodes. If the electrolyte temperature exceeds a certain value, separator melts closing the pores, and current ceases to flow.

Cathode:

At the cathode, Li^+ engages in an electron transfer reaction that decreases the chemical potential of lithium relative to its value in the anode: on discharge, the cathode functions as an electron acceptor. In commercial cells, cathode active material is a lithiated transition metal oxide (TMO) such as lithium manganese oxide, which reacts according to

$$x\,Li + x\,e^- + LiMn_2O_4 \Rightarrow Li_{1+x}Mn_2O_4 \qquad \text{(Discharge)}$$

If the battery is to be rechargeable, the reactions must be reversible; ie if the load in the external circuit is replaced with a power supply, it should be possible to run the reaction at the cathode and anode in reverse.

1.18 General Characteristics of Lithium Rechargeable Batteries

Rechargeable lithium batteries operating at room temperature offer several advantages compared to conventional aqueous technologies, including

a. Higher energy density (up to 150 Wh/ kg, 400 Wh/L)
b. Higher cell voltage (up to about 4 V per cell)
c. Longer charge retention or shelf life (up to 5 to 10 years)

These advantageous characteristics result in part from the high standard potential and low electrochemical equivalent weight of lithium metal [1]. Ambient-temperature lithium rechargeable batteries, on the other hand, do not have the high-rate capability (because of the lower conductivity of the aprotic organic or inorganic electrolytes that must be used because of the reactivity of lithium in aqueous electrolytes) and in some instances, the cycle life of conventional rechargeable batteries. In addition, rechargeable lithium batteries that use lithium metal as the negative electrode present potential safety problems, which are more challenging than those with primary lithium batteries. This is due to a three- to five fold excess of lithium, which is required for these types of cells in order to obtain a reasonable cycle life, and to the reactivity of the high-surface-area lithium that is formed during cycling.

There is another type of rechargeable "lithium" battery, however, which uses a lithiated carbon or other intercalation material for the negative electrode in place of lithium. The absence of metallic lithium in these lithium-ion batteries minimizes these safety concerns.

1.19 Advantages and Disadvantages of Rechargeable Lithium Batteries Operating at Ambient Temperature

The advantages and disadvantages of rechargeable lithium batteries operating at ambient temperature are summarized as follows.

1.19.1 Advantages

a. High energy density and specific energy
b. High voltage
c. Good charge retention, low self-discharge rate

1.19.2 Disadvantages

a. Low cycle life with metallic lithium systems
b. Relatively poor high-rate performance (compared to conventional aqueous rechargeable batteries)
c. Relatively poor low-temperature performance (compared to conventional aqueous rechargeable batteries)
d. Capacity fading (with some systems)
e. Potential safety problems with metallic lithium systems

A number of different battery systems have been investigated by various teams all over the world for the development of lithium rechargeable batteries in order to achieve the high specific energy and

charge retention that lithium batteries can offer without sacrificing other important characteristics, such as specific power and cycle life, while maintaining safe and reliable operation [1]. The rechargeable lithium batteries are generally characterized by a high cell voltage, good charge retention, higher specific energy but poorer high-rate performance, and poorer cycle life than conventional aqueous rechargeable batteries. Rechargeable lithium metal batteries, because of their many potential advantages, have been considered for use in a wide variety of applications. Because of the reactivity of lithium and the possibility of safety problems, emphasis also has been placed on achieving safe operation under normal and abusive conditions .For these reasons, too, commercialization of rechargeable lithium batteries has been limited. They have been introduced into the market only on a limited scale and in small cell sizes. Coin-type batteries have been commercially available for use in low power portable applications and as memory backup. Small cylindrical cells, using a lithium metal anode, have been marketed briefly for consumer electronic applications but were withdrawn when safety problems arose. Rechargeable lithium metal batteries (including ambient-temperature as well as high-temperature types), because of their high energy density, have been investigated for applications requiring larger size cells and batteries as, for example, electric vehicles. More recently, the lithium-ion type battery has been introduced into the consumer market, again in small cylindrical and prismatic sizes for camcorders, cell phones and other portable electronic devices. The lithium ion battery became the dominant rechargeable lithium system during the 1990s.

1.20 Lithium Insertion Compounds

An insertion compound is a host structure that can accommodate mobile guest ions together with their charge compensating electrons. These guest species can be added or removed (i.e. the concentration of the guest in the insertion material can vary) in conjunction with redox processes normally involving a change in oxidation-state of transition metal ions [4]. Under alkali metal insertion, the alkali metal ions donate their outer s-electron to the electronic energy levels of the host. Here two factors are to be considered. (1) The availability of sites in the host and (2) the positions of the energy levels in the host. Several structure types can serve as host materials, typically 2-D hosts like $LiCoO_2$ and 3-D hosts like $LiMn_2O_4$, $LiFePO_4$, and $LiNiPO_4$. In a topotactic reaction, the structure of the host is changed only by atomic displacement; the reaction does not involve a diffusive rearrangement of the host atoms. Moreover, the guest species in such a reaction may be neutral, an electron donor, or an electron accepter. In other words, an insertion compound is an ionic and electronic conductor, and the intake or release of electrons compensates for a change in guest-ion concentration.

In a Li-ion battery Li^+ is the guest ion and a transition –metal-Oxide (TMO) is the most attractive candidate as the host. Phosphates, sulphates and arsenates of transition metals are also suitable as host material in the intercalation process. The alkali metal ions donate their s-electrons to the electronic energy level of the host. Here the

availability of the sites in the host and the position of the energy levels in the host must be taken into account.

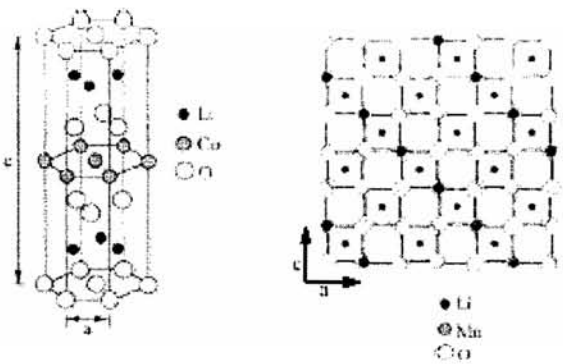

Fig. 1.7 (a). Two-dimensional layered host with -$NaFeO_2$ -type structure.

(b). Three-dimensional framework host with cubic spinel AB_2O_4 –type structure.

For transition –metal oxides the positive guest Li^+ occupy sites surrounded by negative oxygen ions. The guest ions strive to stay as far as possible from the transition metal ions. The sites available to the Li-ion are determined by the host structure. Due to the higher potential vs. Li/ Li^+ ratio giving a high specific energy and excellent reversibility, TMO`s are found to be the most attractive candidate for insertion electrode (15).

1.21 Classification of Insertion Compounds

Insertion compounds can be classified according to their crystal structure, chemical composition and morphology. The composition of the host lattice consists of transition metal Chalcogenides; spinel related, layered and 3D. There are numerous transition metal oxides that exist as separate group of Chalcogenides; layered and tunnel type,

three dimensional, spinel type $Li_xM_2O_4$ (M=Ti, V, Mn), layered Li_xMO_2 (M=Co, Ni, Mn) and so on. Several conjugated organic polymers have been found to have good electronic conductivity. They can exhibit host properties. Examples of such conducting type polymers are thin electro-polymerized electrode films of polyaniline and ploypyrrole [16]. Lithium forms alloys with carbon (graphite, coke), Al, Sn etc., which can also be treated as intercalation compounds. Since 1990, such alloys have found application as anode materials in lithium ion (rocking chair) rechargeable batteries. Use of insertion material for negative electrode solves the problems connected with the appearance of lithium dendrites (due to reactivity with electrolyte) and subsequent degradation of lithium electrode during cycling. However, due to the application of carbon morphology, a fraction of 20-40% of lithium, located at the cathode (e.g. $LiMn_2O_4$) irreversibly reacts in the passivation layer formed on the carbon anode surface. A scheme of classification of insertion compounds is shown in Figure-1.8.

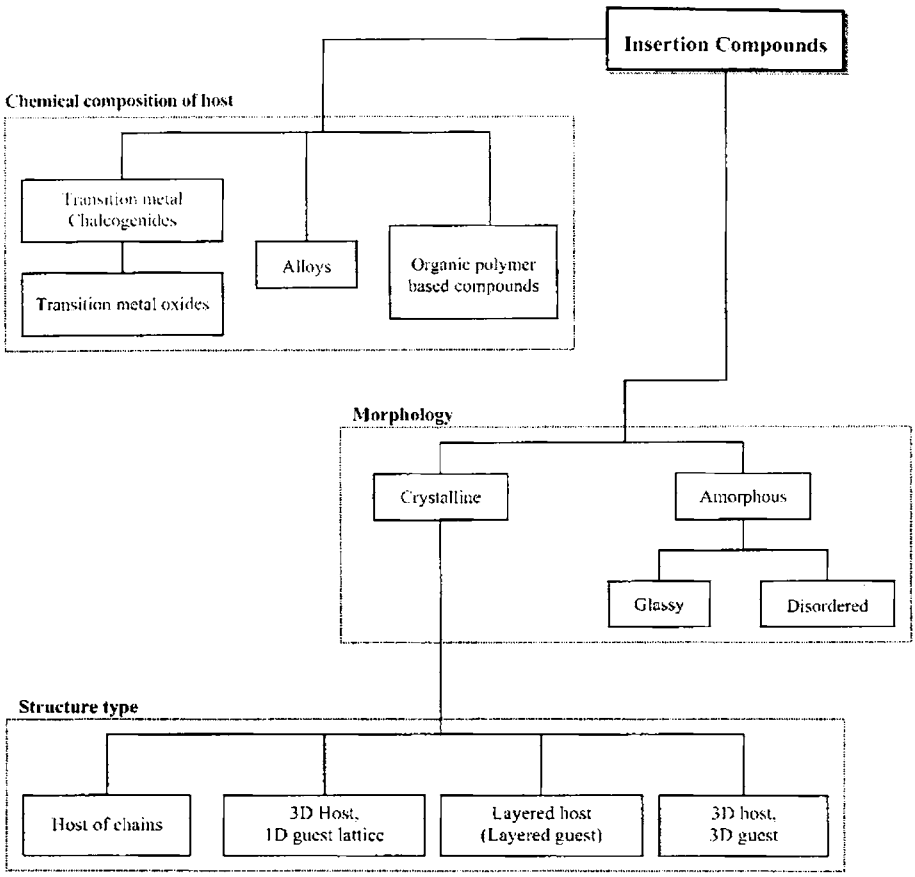

Fig. 1.8 Scheme of classification of insertion compounds

1.22 Properties Expected for Insertion Electrodes in a Li-Ion Cell

The following are the criteria required for intercalation compounds to be chosen as electrodes for a Li-ion battery [16].

a. Must be an intercalation host for lithium

b. Large value of Gibbs free energy (ΔG) for the total cell reaction to provide a high voltage.

c. Limited change in ΔG over the useful range of inserted Li-ions to ensure a stable operating voltage.

d. Low Fermi level and Li+ site energy which enable high open-circuit voltage

e. Low molar volume to get high volumetric energy density

f. Electrode potential should not vary significantly with lithium content (i.e. cell voltage varies little with state of charge)

g. Minimal changes in the host network to ensure good reversibility (i.e.to sustain high rates of lithium intercalation and deintercalation)

h. Light host structure, which is able to accommodate a significant amount of Li-ions to provide a high capacity

i. Good electronic and ionic conductivity to provide high rate capability.

j. Chemically and structurally stable over the whole voltage range and insoluble in the electrolyte (i.e. to avoid co-intercalation of solvent)

k. Non-toxic and inexpensive

l. Easily fabricated into electrode

m. Intrinsic safety and environmental acceptability (green nature).

1.23 Distinguishing Features of Li-ion Batteries

The overwhelming need for lightweight and compact sources of portable electricity has resulted in a massive international effort for the

development of radically new rechargeable batteries. The considerable technological impetus in this area comes from three main sources; consumer electronics (*e.g.* mobile telephones), electric vehicles and implantable medical devices (*e.g.* the artificial heart). The introduction of the world's first commercially successful rechargeable lithium battery represented (by Sony in 1990) a revolution in the power source industry. Following are the essential features of Li-ion cell [17].

a. High operating voltage.

b. Compact, light weight and high energy density.

c. Fast charging potential.

d. High discharge rate.

e. Wide range of operating temperature.

f. Superior cycle life.

g. Excellent safety.

h. Low self discharge.

i. Long shelf life.

j. No memory effect.

k. Non-polluting.

1.24 Phospho Olivines-A Breakthrough in Lithium ion Battery Technology

The standard Li-ion battery has been the leading energy storage material since the mid 1990`s but a new breed of lithium ion batteries is

being investigated, with a view to producing batteries that are cheaper, less toxic and electrochemically superior. The conventional nickel cadmium/cobalt batteries are toxic and they experience a detrimental memory effect. Cobalt is one of the primary constituents of standard cathodes for lithium batteries. Cobalt has a low abundance leading to high cost. Metals such as Mn could provide a cheaper alternative. Cobalt is also a heavy metal that can cause cumulative poisoning. Lithium cobalt batteries have an extra cost associated with a necessary protection circuit to ensure safety. Thus there is a significant drive in industry and research, to develop batteries with materials that are non-toxic and less expensive.

Possible alternative to lithium cobaltate include $LiNiO_2$, $LiMn_2O_4$, $LiFePO_4$ and other oxides. $LiNiO_2$ is a layered compound that has been investigated as a possible cathode material. This compound has the same structure as the lithium cobaltate compound, but due to its poor thermal stability it undergoes a structural change on heating, which causes an undesired reduction in its conductivity. Therefore, $LiNiO_2$ is not currently practical as battery material.

$LiMn_2O_4$ system undergoes structural change upon cycling [18]. The capacity fading of the lithium manganese oxide system is prominent. It is reported that this compound has an initial capacity of 120mAh/kg, but by the 100^{th} cycle the capacity falls to about 60%. The resulting capacity fade can be improved by partial substitution with cobalt. A lithium manganese cobalt oxide [Li_x ($Mn_{1-x}Co_x$) O_2] has been practiced but is difficult to prepare and also have a poor cycle life. Thus

these compounds are not at the forefront of the new generation of lithium battery cathode materials.

The recent developments in the Li-ion battery technology include the introduction of newer cathode materials such as the conductive lithium Phospho-olivines $LiFePO_4$, $LiNiPO_4$ etc by Padhi, Nanjudaswamy and Goodenough [19]. The lithium transition metal phosphates are emerging as materials of interest due to their low material cost, high energy density, safety and non-toxicity. But these materials have low electron conductivity. A dramatic increase in conductivity can be achieved through structure control [20]. This new breakthrough in identifying electrically conductive and "environmentally green" Phospho-olivines has evoked great interest in the research world.

The electrically conductive Phospho-olivines can be used for applications in safer and high power rechargeable Li-ion batteries [21]. The applications include power sources for hybrid and electric vehicles and implantable medical devices as well as back-up power.

1.25 Multi Walled Carbon Nano Tube (MWNT) as Additives

One of the drawbacks in Li -ion battery hindering the widespread applications is the insufficient electric capacity. Carbon materials such as carbon micro beads (MCMB) and graphite have been used for the anode instead of lithium metal foil mainly due to safety considerations although the theoretical capacity (372mAh/g) of carbon-based secondary Li ion battery is much lower than lithium metal. A host of

experiments have been conducted to enhance the capacity by adopting hard carbon, modified graphite carbon and metal oxide compounds as the anode electrode. Although the electric capacity increased to a certain extent, some obstacles such as irreversibility and constant discharge voltage still need to be overcome.

The very good electronic conductivity, mechanical and thermal stability of carbon nano tube can be exploited for enhancing the performance of lithium ion batteries. The unique properties of carbon nano tubes include, one dimensional, and well-graphetized structure with a central hollow core. Thus, it is expected that the discovery of MWNTs provide an opportunity to improve the electrochemical properties of the secondary Li ion battery. Since their discovery in 1991 by Iijima carbon nanotubes have been of great interest, both from a fundamental point of view and for future applications [22]. The most eye-catching features of these structures are their electronic, mechanical, optical and chemical characteristics, which open a way to future applications. These properties can even be measured on single nanotubes. For commercial application, large quantities of purified nanotubes are needed.

1.25.1 Fullerenes

Fullerenes are large, closed-cage, carbon clusters and have several special properties that were not found in any other compound before. As is the case with numerous, important scientific discoveries, fullerenes were accidentally discovered. In 1985, Kroto and Smalley found strange results in mass spectra of

evaporated carbon samples [23,24]. Herewith, fullerenes were discovered and their stability in the gas phase was proven. The search for other fullerenes had started. Since their discovery by Iijima and coworkers, many researchers all over the world have investigated carbon nanotubes. Their large length (up to several microns) and small diameter (a few nanometers) result in a large aspect ratio. They can be seen as the nearly one-dimensional form of fullerenes. Therefore, these materials are expected to possess additional interesting electronic, mechanic and molecular properties. Especially in the beginning, all theoretical studies on carbon nanotubes focused on the influence of the nearly one-dimensional structure on molecular and electronic properties.

Many exotic structures of fullerenes exist: regular spheres, cones, tubes and also more complicated and strange shapes. Single Walled Nanotubes (SWNT) can be considered as long wrapped graphene sheets (Figure-1.9). As stated before, nanotubes generally have a length to diameter ratio of about 1000 so they can be considered as nearly one-dimensional structures. Multi Walled Nanotubes (MWNT) can be considered as a collection of concentric SWNTs with different diameters. The length and diameter of these structures differ a lot from those of SWNTs and, of course, their properties are also very different.

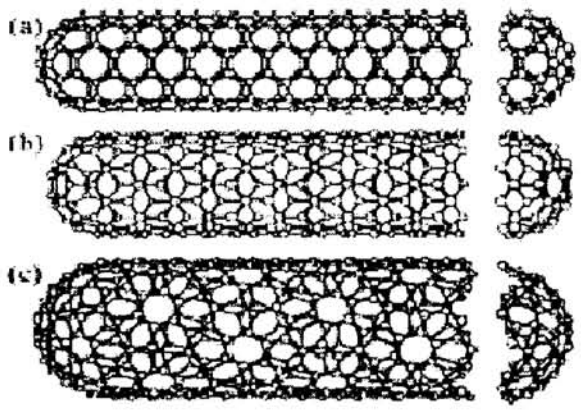

Fig.1.9: Some SWNTs with different chiralities. The difference in structure is easily shown at the open end of the tubes. a) armchair structure b) zigzag structure c) chiral structure

1.25.2 Special Properties of Carbon Nanotubes

Electronic, molecular and structural properties of carbon nanotubes are determined to a large extent by their nearly one dimensional structure. The most important properties of CNTs and their molecular background are stated below.

a. **Chemical reactivity.** The chemical reactivity of a CNT is, compared with a graphene sheet, enhanced as a direct result of the curvature of the CNT surface [25]. Carbon nanotubes reactivity is directly related to the pi-orbital mismatch caused by an increased curvature. Therefore, a distinction must be made between the sidewall and the end caps of a nano tube. For the same reason, a smaller nanotubes diameter results in increased reactivity. Covalent chemical modification of either sidewalls or end caps has shown to be possible. For example,

the solubility of CNTs in different solvents can be controlled this way. Though, direct investigation of chemical modifications on nanotubes behaviour is difficult as the crude nanotubes samples are still not pure enough.

b. **Electrical conductivity.** Depending on their chiral vector, carbon nanotubes with a small diameter are either semi-conducting or metallic. The differences in conducting properties are caused by the molecular structure that results in a different band structure and thus a different band gap. The differences in conductivity can easily be derived from the graphene sheet properties [26]. The resistance to conduction is determined by quantum mechanical aspects and was proved to be independent of the nanotubes length [27,28].

c. **Optical activity.** Theoretical studies have revealed that the optical activity of chiral nanotubes disappears if the nanotubes become larger [29]. Therefore, it is expected that other physical properties be influenced by these parameters too. Use of the optical activity might result in optical devices in which CNTs play an important role.

d. **Mechanical strength.** Carbon nanotubes have a very large Young's modulus in their axial direction. The nanotubes as a whole is very flexible because of the great length. Therefore, these compounds are potentially suitable for applications in composite materials that need anisotropic properties.

1.25.3 Potential Applications of CNTs

a. **Energy storage.** Graphite carbonaceous materials and carbon fiber electrodes are commonly used in fuel cells, batteries and other electrochemical applications. Advantages of considering nanotubes for energy storage are their small dimensions, smooth surface topology and perfect surface specificity. The efficiency of fuel cells is determined by the electron transfer rate at the carbon electrodes, which is the fastest on nanotubes following ideal Nernstian behaviour [28] Electrochemical energy storage and gas phase intercalation will be described more thoroughly in the following chapters of the report.

b. **Hydrogen storage.** The advantage of hydrogen as energy source is that its combustion product is water. In addition, hydrogen can be easily regenerated. For this reason, a suitable hydrogen storage system is necessary, satisfying a combination of both volume and weight limitations. The two commonly used means to store hydrogen are gas phase and electrochemical adsorption. Because of their cylindrical and hollow geometry, and nanometer-scale diameters, it has been predicted that carbon nanotubes can store a liquid or a gas in the inner cores through a capillary effect. It is reported that SWNTs were able to meet and sometimes exceed this level by using gas phase adsorption (physisorption). Another possibility for hydrogen storage is electrochemical storage. In

this case not a hydrogen molecule but an H atom is adsorbed. This is called chemisorptions.

c. **Lithium intercalation.** The basic principle of rechargeable lithium batteries is electrochemical intercalation and deintercalation lithium in both electrodes. An ideal battery has a high-energy capacity, fast charging time and a long cycle time. The capacity is determined by the lithium saturation concentration of the electrode materials. For Li, this is the highest in nanotubes if all the interstitial sites (inter-shell van-der Waals spaces, inter-tube channels and inner cores) are accessible for Li intercalation. SWNTs have shown to possess both highly reversible and irreversible capacities. Because of the large observed voltage hysteresis, Li-intercalation in nanotubes is still unsuitable for battery application. This feature can potentially be reduced or eliminated by processing, i.e. cutting, the nanotubes to short segments.

d. **Electrochemical super capacitors.** Super capacitors have a high capacitance and potentially applicable in electronic devices. Typically, they are comprised two electrodes separated by an insulating material that is ionically conducting in electrochemical devices. The capacity of an electrochemical super cap inversely depends on the separation between the charge on the electrode and the counter charge in the electrolyte. Because this separation is about a nanometer for nanotubes in electrodes, very large capacities result from

the high nanotube surface area accessible to the electrolyte. In this way, a large amount of charge injection occurs if only a small voltage is applied. This charge injection is used for energy storage in nanotubes super capacitors [30].

e. **Conductivity in CNTs.** Electron transport in metallic CNTs is ballistic of nature, which means that electrons move with a much higher speed than expected on the ground of thermal equilibrium. Ballistic transport can only occur in strictly confined semi-conductor regions and is totally determined by material properties. Electron transport in semi-conducting CNTs is far more complicated due countermand scattering, influences of charges at the electrode interface and adsorbed gasses. Therefore, conductivity in semi-conducting CNTs is usually described in classic physical laws of diffusivity [26]. Diffusive charge transport means that electron motion can be described with an effective mobility μ .In case of ballistic transport, the average free path l of an electron is relatively short (~ 2 nm.) compared with the ballistic transport situation ($l \sim 10$ μm).

1.26 Methods of Synthesis of Experimental Samples

1.26.1 Hand mortaring

The most commonly used approach to reduce particle size is to grind the substance using mortar and pestle, but mechanical mills also do a fine job. Mortar and pestles are usually made from agate or ceramics. Agate is suitable for grinding hard materials. When

aggregation effects are severe, adding a chemically inert liquid such as acetone, which does not dissolve the material may help to prevent excessive conglomeration.

In the present work grinding of material by hand with an agate mortar and pestle has been used for mixing and particle size reduction of small amounts of materials (less than 20 g). For getting homogeneity in mixing acetone is used as a mixing medium. For many a small- scale studies, hand- mortaring is perfectly adequate for reducing the particle sizes of powder samples. The successive grinding and mixing are done for a maximum of two hours for each batch of samples. Usually two stages of hand mortaring are adequate for the synthesis of the material. A facemask should be worn to prevent fine dust inhalation.

1.26.2 Solid-state reaction

Solid-state reaction is done by mixing the pre-dried precursors in the exact (stoichiometric) ratio to get a desired target product. To get the starting materials close to each other for mixing a homogeneous phase of final product, it is common to grind the and mix using mechanical milling techniques first. Alternatively, the precursors may be dissolved to give a homogeneous solution, which is stirred continuously and evaporated to dryness. Then the solid remaining is mechanically milled to yield a very homogeneous powder ready for conversion in to a final product.

Once the homogeneous precursor is obtained, it is placed into a furnace and heated to a suitable temperature for hours. Waste gases will

be generated and released. Chemicals will interact to form final product. Commonly, this material may be ground finely again and then put into the furnace a second time .the second sintering allows the crystals to form and grow in size. Some times powder materials are hydraulically pressed in to pellets to increase the inter activity between the powder grains and form a higher quality final product.

The spinel $LiMn_2O_4$ is prepared and sintered in a muffle furnace in air. While the phospho olivines $LiMPO_4$ (M=Fe,Ni) are prepared in a specially designed tubular furnace as shown in Figure1.10 for thermal decomposition under inert atmosphere.

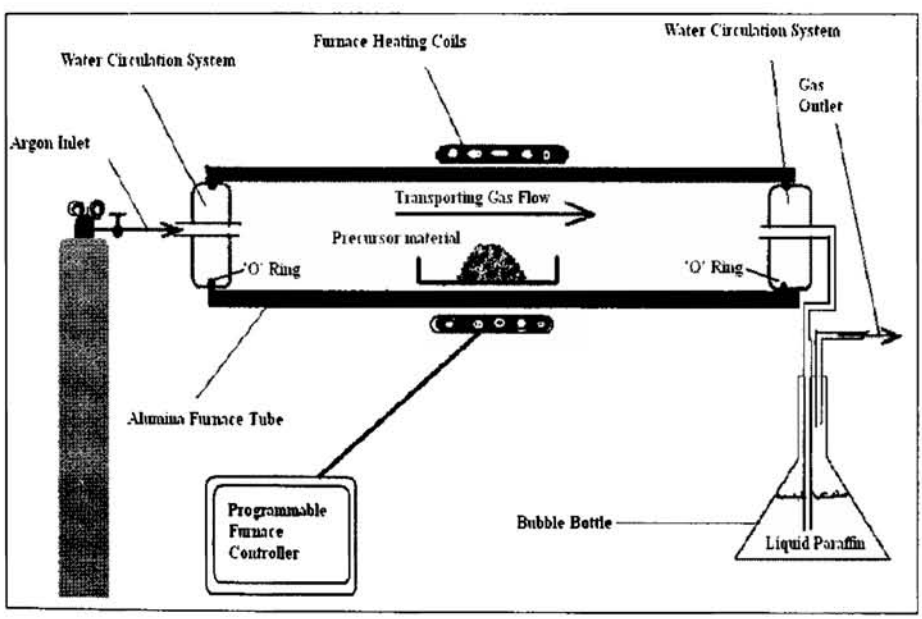

Fig.1.10. Arrangement for the synthesis of $LiMPO_4$(M=Fe,Ni) in an inert atmosphere

1.26.3 Sintering

Sintering commonly refers to processes involved in the heat treatment of powder compacts at elevated temperature, in the temperature range where diffusion mass transport is appreciable. Successful sintering usually results in a dense polycrystalline solid. However sintering can proceed only locally, (i.e. at contact points of grains), without any appreciable change in the average overall density of a powder compact .The principal goal of sintering is the reduction of compact porosity. The sintering process is usually accompanied by other changes within the material, some desirable and some undesirable.

On sintering the largest changes occur in

a. Strength, elastic modulus
b. Hardness, fracture toughness
c. Electrical and thermal conductivity
d. Permeability of gases and liquids
e. Average grain number and size
f. Average pore size and shape
g. Chemical composition and crystal structure

Sintering is a very widely used, but complex phenomenon.

1.27 Characterization Techniques

127.1 X-Ray Diffraction analysis

X-ray diffraction is an extremely important technique in the field of material characterization to obtain information on atomic scale from

crystalline and amorphous materials. The discovery of X-ray diffraction by crystals in 1912 by Max von Laue and its immediate application to structure determination in 1913 by W.L Bragg and his father W.H Bragg paved the way to determine crystal structures of metal and alloys, minerals, inorganic compounds, polymers and organic materials. When materials are irradiated with X-rays they get diffracted and the manner of diffraction reveals the structure of the crystal [75,76]. At first this tool was used only for the determination of crystal structure. To day the method is applied not only to crystal structure determination, but also to such diverse problems as chemical analysis and stress measurement, to the study of phase equilibrium and measurement of particle size, to the determination of orientation of one crystal or the ensemble of orientations in a polycrystalline aggregate.

Many factors affect the quality of powder diffraction data and the quality of the specimen used in a powder diffraction experiment is one of them. Poorly prepared samples will inevitably lead to additional efforts to repeat from the beginning .On the other hand, a high quality sample for powder diffraction may take longer to prepare, but this will be time well spent. The true powder diffraction pattern can only be obtained from specimen containing an infinite number of individual particles realizing an infinite number of orientations in the irradiate volume. In other words, the particles in the specimen should have a completely random distribution of crystallographic orientations of grains with respect to one another. This is usually achieved by reducing the average particle size. Another very effective approach to increase both the number of particles in the irradiated

volume and the randomness of their orientations is to spin the specimen continuously during data collection.

1.27.2 Electron beam techniques for characterizations

When a sample is irradiated with electrons the incident electrons are absorbed, emitted, reflected or transmitted and can, in turn cause light or X-ray emission. An electron of energy Ei incident on a sample (figure1.11) surface causes emission of electrons from surface over a wide range of energies. Usually three groups of electrons are distinguished. First group shows a maximum electron yield. The interaction of an electron beam with a solid can lead to the ejection of loosely bound electrons from conduction band. These are the secondary electrons with a lower range of energies. Auger electrons are emitted in an intermediate energy range. Back-scattered electrons that have undergone large angle elastic collisions leave the sample with essentially the same energy as the incident electrons. These electrons can be focused, deflected, and accelerated by appropriate potentials. They can be efficiently detected and counted. Their energy and angular distributions can be measured, and they do not contaminate the sample or the system.An electron microscope utilizes an electron beam to produce a magnified image of the sample [77-81]. There are three principal types of electron microscopes

a. Scanning
b. Transmission and
c. Emission.

All analytical techniques are based on similar principles. A primary electron, ion, or photon beam causes backscattering or transmission of the

incident particles or the emission of secondary particles. The mass, energy, or wavelength of the emitted entities is characteristic of the target element or compound from which it originated. The distribution of the unknown parameter can be mapped in the x-y plane and frequently also in depth. Each of the techniques has particular strengths and weaknesses, and frequently more than one method must be used for unambiguous identification. Differences between the various techniques include sensitivity, elemental or molecular information.

In the scanning and transmission electron microscope, an electron beam incident on the sample produces an image, while in the field - emission microscope the specimen itself is the source of electrons. Scanning electron microscopy (SEM) is similar to light microscopy with the exception that electrons are used instead of photons and the image is formed in a different manner. A detailed description of this method is given in Chapter-2

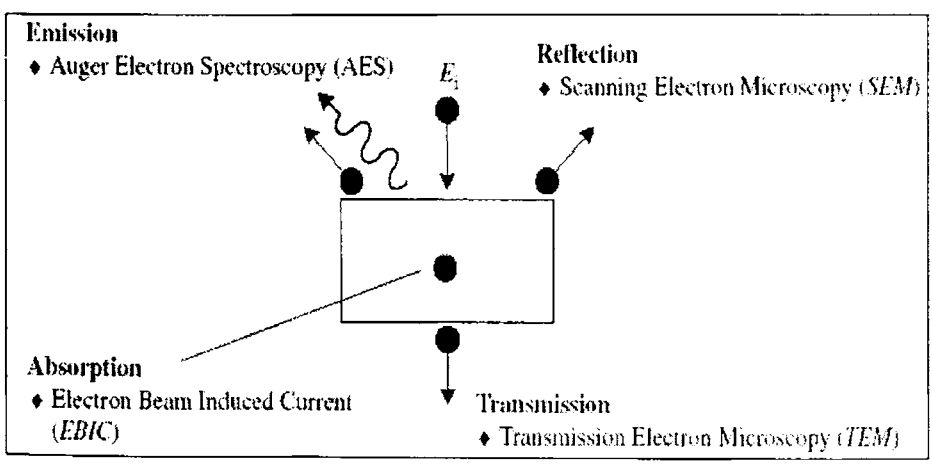

Fig. 1.11 Electron beam characterization techniques

In the present work SEM images are obtained using JEOL JSM – 6380 LV (JEOL Inc., Tokyo, Japan), operating at a voltage of 30 KV. TEM images are acquired using JEOL JEM 1200 EX 11 (JEOL Inc., Tokyo, Japan), maintained at a voltage of 120 KV.

1.27.3 Photoacoustic technique as a characterization tool

1.27.3.a *Photothermal science*

Photothermal (PT) science encompasses a wide range of techniques and phenomena based upon the conversion of absorbed optical energy into heat. Although the initial absorption processes in many materials are very selective, it is common for atoms or molecules in excited electronics states to lose their excitation energy by a series of non-radiative transitions that result in a general heating of the material. The main components of a photothermal system are an excitation source, a modulator, a detector and a signal processor with a display system. The modulated light beam absorbed by the sample generates modulated heating in and around the sample, giving rise to the various PT effects such as temperature rise, pressure change, refractive index gradient etc. Depending on the specific PT effect being probed [31], PT techniques are classified into Photopyroelectric (PPE) technique or Calorimetric technique (temperature rise) [32-45], Photoacoustic technique (pressure change) [46-48], Probe beam deflection or Mirage technique (Refractive index gradient) [49-51], Photothermal Radiometric technique (infrared emissions) [50-51] etc. The PPE signal (PT signal in general) not only carries information regarding the absorbed light energy which is the basis of their application in

absorption spectroscopy, but also contains details regarding the thermal properties of the sample

1.27.3 b. *Thermal, Electronic and Optical Characterization using PA Technique.*

For the past few decades, photoacoustic technique has been emerging as a powerful tool in the thermal, electronic and optical characterization of materials whether solids, liquids or they are gases [52-66]. Photoacoustic technique is based on an effect originally discovered by Bell in 1880, where a chopped light impinging on a solid surface enclosed in a cell produces an acoustic signal within the cell. The reason for this acoustic signal generation is the fact that after the absorption of light by the sample, non-radiative de-excitation processes convert a part or all of the light absorbed by the sample into heat. Hence, a periodic or chopped excitation results in a periodic heat generation in the sample, which diffuses into the surrounding gas. This periodic flow of heat into the gas produces pressure fluctuations in it resulting in periodic sound or acoustic signal. This periodic acoustic signal can be detected by a microphone and the signal output from the microphone can be recorded as a function of the wavelength of light used or as a function of the chopping frequency depending on the application [52-66].

It is being extensively used as a spectroscopic tool because of its relative advantage over other conventional spectroscopic techniques, in that it can be applied to any type of sample in general. This is due to the fact that scattering poses less difficulties in Photoacoustic Spectroscopy

(PAS) unlike other conventional spectroscopic techniques since the amount of signal generation is directly dependent on the amount of light absorbed. Due to the same reason, absorption spectra of opaque samples can also be accurately obtained. The PA signal recorded, as a function of wavelength will be the optical absorption spectra of the sample under investigation because the magnitude of the acoustic signal produced in the photoacoustic cell is proportional to the amount of heat emanating from the solid absorber, provided that non-radiative processes dominate in the dissipation of the absorbed light energy. Suitable normalization procedures remove the spectral characteristics of the excitation light source [52-65].

On the other hand, the PA signal obtained as a function of the chopping frequency is used in obtaining the thermal and electronic parameters like carrier diffusion coefficient, surface recombination velocity etc of the materials since the chopping frequency is related to the heat generation and propagation. In the case of semiconductors, heat generation under the irradiation with an intensity modulated light beam arises due to three processes namely thermalisation due to intra band transitions of photo-generated carriers, nonradiative bulk recombination and surface recombination due to inter band transitions of photo-generated carriers. All these different mechanisms finally result in the creation of heat energy, which is then transferred to the lattice through the creation of phonons, and which of these generation mechanisms is dominant in a PA signal depends on the frequency of excitation and de-excitation i.e. the chopping frequency [61,62]. The

heat propagation is described in terms of the thermal wave propagation having a wavelength $2\pi\mu$ where μ is the thermal diffusion length given by $\sqrt{\frac{\alpha}{\pi f}}$, α being the thermal diffusivity and f the chopping frequency.

1.28 Portable Radiometer for Band Gap Measurement

Portable spectroradiometers or radiometers, as they are generally known, are extensively and commonly used instruments in studying Earth Science, especially vegetation, soil, minerals, etc [67] Due to these applications, the radiometers are made compact with accessories for in situ measurements, such as different fields of view lenses from 1 degree to 10 degrees and/or a fiber-optic bundle with a 25 degree field of view. Besides these lenses, there are also other fore-optic accessories such as reduction tubes and remote cosine receptors in order to increase the freedom of collecting the light reflected from the object under investigation. This gives the added advantage of choosing the area of light collection, helping to perform in situ measurements, and making the measurement precise. These measurements are often done with the sun/halogen lamp as the excitation source, and the reflected light from the object under investigation is collected. This collected light from the object is projected on to a holographic diffraction grating where the wavelength components are separated and measured by detector(s). The detectors commonly used to detect the visible and near-infrared (Vis-NIR) portion of the collected light are512-channel silicon photodiode arrays with an order separation filter or 1024 ×128 (or 64) charge-coupled device (CCD) arrays, and the short-wave infrared (SWIR)

portion of the spectrum is acquired using two scanning spectrometers in the ranges 900–1850 nm and 1700–2500 nm, with the controlling software accounting for this wave length overlap. Unlike the Vis-NIR, each SWIR spectrometer has only one detector, which is exposed to the different wavelengths of light as the grating oscillates (at a period of 200 ms, i.e., 100 ms/scan). Data is recorded and saved very quickly (in less than one second).

The radiometer gives flexibility in the size of the samples to be studied since there is no restriction on the upper limit and the lower limit can be down to as little as 1 mm ×1 mm in size. Temperature dependence of the band edges in semiconductors is of great interest in electronic and opto electronic applications. [68-70] However, the shift is small and can be observed only with high resolution techniques; for example, the shift in band gap of silicon when the temperature changes from 300 K (room temperature) to 370 K is about 0.01 eV and so the shift occurring in the band edges will be very small for small temperature changes. Although the spectrophotometers available have a spectral resolution of 1 nm, the use of a radiometer that has the same spectral resolution will give the added advantage of in situ measurements. Hence, another way of rating the performance of a radiometer is by looking at the accuracy and resolution of the spectra while looking for shifts in band edges of semiconductors with change in temperature. In this regard, the advantage of varying the temperature during measurements is that the temperature of the sample can be varied easily (for example, coarse measurements can be done by

placing the sample in an ice bath or on a hot plate) as the size of the sample holding apparatus or heating/cooling apparatus does not matter since the sample is placed outside the instrument, contrary to the other techniques in which the sample is mounted inside a sample holder in the instrument. Band gap measurement of semiconductor nano particles is of immense interest due to their structural and electronic information carrying capability. This technique can act as a powerful tool for this application [71-73].

1.29 Motivation for the present investigation

The work presented in the thesis is centered around two important types of cathode materials, the spinel structured $Li_xMn_2O_4$ (x =0.8to1.2) and the phospho –olivine structured $LiMPO_4$ (M=Fe and Ni). The spinel system $Li_xMn_2O_4$, especially $LiMn_2O_4$ corresponding to x=1 has been extensively investigated to understand its structural electrical and electrochemical properties and to analyse its suitability as a cathode material in rechargeable lithium batteries. However there is no reported work on the thermal and optical properties of this important cathode material. Thermal diffusivity is an important parameter as far as the operation of a rechargeable battery is concerned. In $Li_xMn_2O_4$, the electronic structure and phenomenon of Jahn-Teller (J.T) distortion have already been established theoretically and experimentally. Part of the present work is an attempt to use the non-destructive technique (NDT) of photoacoustic spectroscopy to investigate the nature of the various electronic transitions and to unravel the mechanisms leading to the phenomenon of J.T distortion in $Li_xMn_2O_4$.

The phospho-olivines $LiMPO_4$ (M=Fe, Ni, Mn, Co etc) are the newly identified, prospective cathode materials offering extremely high stability, quite high theoretical specific capacity, very good cyclability and long life. Inspite of all these advantages, most of the phospho – olivines especially $LiFePO_4$ and $LiNiPO_4$ show poor electronic conductivity compared to $Li_xMn_2O_4$, leading to low rate capacity and energy density. In the present work attempts have been made to improve the electronic conductivity of $LiFePO_4$ and $LiNiPO_4$ by adding different weight percentage MWNT .It is expected that the addition of MWNT will enhance the electronic conductivity of $LiFePO_4$ and $LiNiPO_4$ with out causing any significant structural distortions, which is important in the working of the lithium ion battery.

References

[1] Handbook of Batteries, 2nd edition, D. Linden, Ed., McGraw-Hill, Inc., NewYork (1995)

[2] Modern Batteries: An introduction to Power sources Colin A. et.al Edward Arnold (1984)

[3] "Advanced Secondary Batteries" A review. R.M Dell U.K. Atomic Energy Authority (1979)

[4] P.G. Bruce, in Solid State Electrochemistry, P.G. Bruce, Ed., Cambridge University Press, Cambridge, (1995).

[5] R. Selim and P. Bro, "Performance Domain Analysis of Primary Batteries," Electrochemical Technology, J. Electrochem. Soc. 118(5) 829 (1971).

[6] D. I. Pomerantz, "The Characterization of High Rate Batteries," IEEE Transactions Electronics"36(4) 954 (1990).

[7] H. Bode, Lead-Acid Batteries, Wiley, New York, (1977)

[8] M. M. Thackeray et al., J. Electrochem. Soc. 139:363 (1992).

[9] Victor L. Pushparaj et.al, 13574–13577 PNAS August 21, Vol. 104 No. 34 (2007).

[10] Welton T Chem Rev 99:2071–2083(1999)

[11] Hammami A, Raymond N, Armand M Nature 424:635–636 (2003).

[12] Kim YJ, Matsuzawa Y, Ozaki S, Park KC, Kim C, Endo M, Yoshida H, Masuda G,Sato T, Dresselhaus MS J Electrochem Soc 152:A710–A715(2005).

[13] B. Scrosati, Nature, 373 ,557(1995)

[14] S. Megahed and B. Scrosati, Interface, 4 ,34(1995).

[15] T. Ohzuku and A. Ueda, Solid State Ionics, 69 ,201(1994).

[16] M.M. Thackeray, Prog. Solid. St. Chem., 25 ,1 (1997)

[17] D. Abraham, presentation at CMM-MRL-UIUC, 28 Feb. (2001).

[18] G.Vitins and K.West J.Ellectrochem.Soc, 144,2587(1997).

[19] A.K.Padhi, K.S.Nanjundaswamy, and Goodenough J.Electrochem.Soc, Vol.144, No.4 (1997)

[20] Devaraj Shanmukharaj and Ramaswamy Murugan. Ionics 10(2004)

[21] Chung, S.Y.Bloking, J.T and Chiang, Y.M Nature materials, 1,123-128(2002)

[22] Iijima, Sumio, Nature (London, United Kingdom), 354, (6348), (1991)

[23] D.A.Bochvar and E.G.Gal'pern, Dokl.Akad.Nauk.USSR, 209, 610, (1973)

[24] I.V.Stankevich, M.V.Nikerov, and D.A.Bochvar, Russ.Chem.Rev., 53, 640, (1984)

[25] Niyogi, S., Hamon, M. A., Hu, H., Zhao, B., Bhowmik, P., Sen, R., Itkis, M. E., and Haddon, R. C.,Accounts of Chemical Research, 35, (12),(2002)

[26] Avouris, P., Chemical Physics, 281, (2-3), 429-445,(2002)

[27] Tans, Sander J., Devoret, Michel H., Dal, Hongjie, Thess, Andreas, Smalley, Richard E., Geerligs, L. J., and Dekker, Cees, Nature (London), 386, (6624), (1997)

[28] Ajayan, P. M. and Zhou, O. Z., Carbon Nanotubes, 80, (391-425, (2001)

[29] Damnjanovic, M., Milosevic, I., Vukovic, T., and Sredanovic, R., Physical Review B, 60, (4), 2728-2739, (1999)

[30] Baughman, R. H., Zakhidov, A. A., and de Heer, W. A., Science, 297, (5582), 787-792, (2002)

[31] Sell J A, Photothermal investigations of solids and fluids, Academic Press, Boston (1989)

[32] A.Mandelis and Martin M. Zverm J.Appl.Phys 57, 4421 (1985)

[33] M.Chirtoc and G.Michailescu, Phy.Rev.B 40, 9606 (1989)

[34] C. P. Menon, J. Philip, Meas. Sci. Tech. 11, 1744 (2000)

[35] Salazar and A. Oleaga Journal De Physique Iv 125, 289 (2005)

[36] G. Aguirre, G. Arriola, J. Gomez-Hernandez, T. Lopez, M. Picquart, D. H. Aguilar, P. Quintana, J. J. Alvarado-Gil Thermochimica Acta 421, 211 (2004)

[37] S. Pittois, B. Van Roie, C. Glorieux, J. Thoen, J. Chem. Phys. 121, 1866 (2004)

[38] D. Bicanic, C. Neamtu, M. Manojlovic, D. Van Der Linden, D. Dadarlat, K. Posaveck, A. Gijsbertsen And Z. Kurtanjek, Acta Chimica Slovenica 51, 39 (2004)

[39] J. A. Balderas-Lopez, Revista Mexicana De Fisica, 49, 353 (2003)

[40] Cruz-Orea, E. H. Bentefour, P. Jamee, M. Chirtoc, C. Glorieux, G. Pitsi, J. Thoen, Rev. Scie. Instrum. 74, 818 (2003)

[41] S. Longuemart, A. G. Quiroz, D. Dadarlat, A. H. Sahraoui, C. Kolinsky, J. M. Buisine, E. C. da Silva, A. M. Mansanares, X. Philip and C. Neamtu Instrum. Scie. Tech. 30, 157 (2002)

[42] J. Philip, R. Rajesh, C. P. Menon Anal. Scie. 17, S99 (2001)

[43] P. K. John, L. C. M. Miranda *, And A. C. Rastogi Phys. Rev. B 34, 4342 - 4345 (1986)

[44] C. A. S. Lima, L. C. M. Miranda and H. Vargas Instrum. Scie. Tech. 34, 191 (2006)

[45] M. Angelmahr, A. Miklos and P. Hess, Appl. Phys. B. 85, 285 (2006)

[46] Allan Rosenwaig And Allen Gersho, J.Appl.Phys 47, 64 (1976)

[47] Nibu A. George, B. Aneeshkumar, P. Radhakrishnan and C. P. G. Vallabhan, J. Phys D: Appl. Phys 32, 1745 (1999)

[48] Jyotsna Ravi, S. Lekshmi, K. P. R. Nair and T. M. A. Rasheed, J. Quant. Spectro. & Rad. Transfer 83, 193 (2004)

[49] L. C Aamodt and J. C. Murphy, J. Appl. Phys. 52, 4903 (1981).

[50] D Jonathan. Spear and Richard E. RussoJ. Appl. Phys;70, 586 (1991)

[51] H.G.Walther, U.Seidel, W.Karpen, G.Busse Rev. Sci. Instr. 63, 5479 (1992)J. Ravi, Y. Lu, S. Longuemart, S. Paoloni, H. Pfeiffer, J. Thoen, C

[52] A.Rosencwaig, Phys. Today, September, 23,(1975)

[53] A.Rosencwaig and A.Gersho, Science, 190, 556,(1975)

[54] A.Rosencwaig and A.Gersho,J. Appl. Phys, 64, 64, (1976).

[55] C. Glorieux, J. Fivez and J. Thoen, J. Appl. Phys, 73, 684 (1993)

[56] A. Calderón, J. J. Alvarado-Gil, Yu. G. Gurevich, A. Cruz-Orea I. Delgadillo H. Vargas L. C. M. Miranda Phys. Rev. Lett. 79, 5022 (1997)

[57] J. A. Balderas-López and A. Mandelis Journal of Applied Physics, 90, 2273 (2001)

[58] Nibu A George, C P G Vallabhan, V P N Nampoori, A K George and P Radhakrishnan J. Phys.: Condens. Matter 13 365 (2001).

[59] Sajan D George, P Radhakrishnan, V P N Nampoori and C P G Vallabhan J. Phys. D: Appl. Phys. 36 990 ((2003)

[60] J. Ravi, M. K. Jayaraj, K. A. Vanaja, K. P. R. Nair and T. M. A. Rasheed Semiconductor Sci. Tech. 18, 693 (2003)

[61] A. Pinto Neto , H. Vargas, N. F. Leite and L. C. M. Miranda, Phys.Rev.B, 40, 3924 (1989)

[62] M. D. Dramićanin , P. M. Nikolić, Z. D. Ristovski, D. G. Vasiljević and D. M. Todorović, Phys. Rev B, 51, 14226 (1995).

[63] A M. Mansanares, M. L. Baesso, E. C. da Silva, F. C. G. Gandra, and H. Vargas L. C. M. Miranda, Phys. Rev. B, 40, 7912 (1989)

[64] A M. Mansanares, A. C. Bento, and H. Vargas N. F. Leite and L. C. M. Miranda Phys. Rev. B, 42, 4477 (1990)

[65] Sheenu Thomas, Johney Isaac, and J. Philip Rev. Sci. Instr. 66, 3907 (1995)

[66] Jacob Philip and K. N. Madhusoodanan Phys. Rev. B, 38, 4127 (1988)

[67] Jyotsna Ravi, S.Thomas Lee, M.Paulraj and Rolando Hernandez. Applied Spectroscopy, Volume 61.Number 4 (2007)

[68] N. Sarkar and S. Ghosh, J. Phys: Condens. Matter 18, 1687 (2006).

[69] M. Bednarz, V. A. Malyshev, and J. Knoester, Phys. Rev. Lett. 91, 217401(2003)

[70] T. H. Gfroerer, L. P. Priestley, M. F. Fairley, and M. W. Wanlass, J. Appl.Phys. 94, 1738 (2003).

[71] M. Marandi, N. Taghavinia, A. Irajizad, and S. M. Mahdavi, Nanotechnology 16, 334 (2005).

[72] M. Behboudnia and P. Sen, Phys. Rev. B 63, 035316 (2001).

[73] T. Clement, S. Ingole, S. Ketharanathan, J. Drucker, and S. T. Picraux, Appl. Phys. Lett. 89, 163125 (2006).

[74] M. K. Aydinol, A. F. Kohan, and G. Ceder .Phy.Rev.B Vol.56 No.3 .July (1997).

[75] B.D Cullity.Elements of X-Ray Diffraction.2nd Edn.Addison-Wesley.INC (1978).

[76] Vitalij K.Pecharsky,Peter y.Zavalij .Fundamentals of powder diffraction and structural characterization of Materials. Springer (2005)

[77] Dieter K.Schroder. Semiconductor material and device characterization. John Wiley 2nd Ed.

[78] J.I. Goldstein, D.E. Newbury, P. Echlin, D.C. Joy, C. Fiori and E. Lifshin, Scanning ElectronMicroscopy and X-Ray Microanalysis, Plenum Press, New York, (1984).

[79] R.A. Young and R.V. Kalin, "Scanning Electron Microscopic Techniques for Characterizationof Semiconductor Materials," in *Microelectronic Processing: Inorganic Material Characterization* (L.A. Casper, ed.), American Chemical Soc., Symp. Series 295, Washington, DC, 1986,49–74.

[80] P.E. Batson, "Scanning Transmission Electron Microscopy," in Analytical Techniques for ThinFilm Analysis (K.N. Tu and R. Rosenberg, eds.), Academic Press, Boston, pp. 337–387 (1988).

[81] R.J. Graham, "Characterization of Semiconductor Materials and Structures by TransmissionElectron Microscopy," in Diagnostic Techniques for Semiconductor Materials and Devices(T.J. Shaffner and D.K. Schroder, eds.), Electrochem. Soc., Pennington, NJ, 150–167(1988)

[82] Nelson PA, Owen JR J Electrochem Soc 150:A1313–A1317 (2003).

[83] Amatucci GG, et al Electrochem Soc148: A930–A939 (2001).

Chapter 2

Theoretical Aspects

This chapter gives an account of the fundamental theories of the experimental tools and their implementation, for the characterization of the materials under investigation in the present work. This includes a detailed description of the photo induced changes that occur during the photon –matter interaction which forms the basis of the Photoacoustic (PA) Technique, Density Functional Theory (DFT) to analyse the photo acoustic spectra, determination of electrical properties from ac and dc conductivity measurements and the fundamentals of X - ray Diffraction (XRD), Transmission Electron Microscopic (TEM) and Scanning Electron Microscopic (SEM) investigations.

2.1 Introduction

In the present work, photoacoustic technique has been used as a tool for spectroscopic measurements on the samples, which gives insight into the electronic band structure and its modifications with varying sample compositions and also the thermal transport properties. Spectroscopy is the measurement and interpretation of electromagnetic

(EM) radiation absorbed or emitted when the molecules, atoms or ions of a sample move from one state to another. The laser based spectroscopic techniques can be divided into

a. Absorption measurement method
b. Radiative transition technique
c. Non radiative transition technique

The absorption method is the basic and the simplest approach and by using this technique, information regarding the optical properties and composition of the sample can be obtained by varying different parameters such as intensity, wave length, etc. of the light beam that passes through or gets reflected from the sample [1-4]. There are, however several instances where these techniques are inadequate even for clear, transparent materials, where one has to measure a very weak absorption. This problem occurs for all forms of matter. Over the years various techniques have been developed to overcome this difficulty, such as derivative spectroscopy, which also seems to be generally inadequate. In addition, there are substances, both organic and inorganic, that are not readily amenable to the conventional transmission or reflection modes of optical spectroscopy. These are usually highly light-scattering materials, such as powders, amorphous solids, gels etc. There are a number of materials that are optically opaque and have dimensions that far exceed the penetration depth of the photons. External parameters such as surface quality, influence of stray light etc have a pronounced effect on the accuracy of the conventional absorption measurements. The situation will be much more worse in the case of solids, powders etc, especially if the sample is highly

scattering or reflecting. In such situations emission measurements are more appropriate and will give more information about the sample. The non-radiative relaxation of photo - excited state usually results in heating of the sample. The liberated heat energy not only carries the information regarding the absorbed energy but contains details regarding the thermal properties of the sample as well. The group of methods based on the measurement of photo induced heating of the sample is called photo thermal (PT) methods [5-7]. The thermalisation of a sample as a result of non-radiative relaxation brings about changes in many parameters such as density, pressure, refractive index, infrared emissions etc. The various effects produced by light induced heating (photo thermal effects) and their detection techniques are given in table-2.1.

Table 2.1 Common detection techniques used in photothermal spectroscopy

Thermodynamic Parameter	Measured Property	Detection Technique
Temperature	Temperature	Calorimetry Pyroelectric technique
	Infrared Emission	Photothermal Radiometry
Pressure	Acoustic Wave	Photoacoustic Spectroscopy
Density	Refractive Index	P T Lens P T Interferometry
	Surface Deformation	P T Deflection P T Refraction P T Diffraction Surface Deflection

The branch of photothermal spectroscopy based on the pressure wave measurement is known as Photoacoustic (PA) technique [8-21].

During the past four decades, Photoacoustic spectroscopy (PAS) has been developed to study those materials that are unsuitable for the conventional transmission or reflection methodologies. PAS is different from the conventional techniques chiefly in that the interaction of the incident optical photons with the material under investigation is studied through a direct measure of the energy absorbed by the material since the photoacoustic signal generation directly depends on the amount of energy absorbed. The various photothermal methods are depicted in figure 2.1

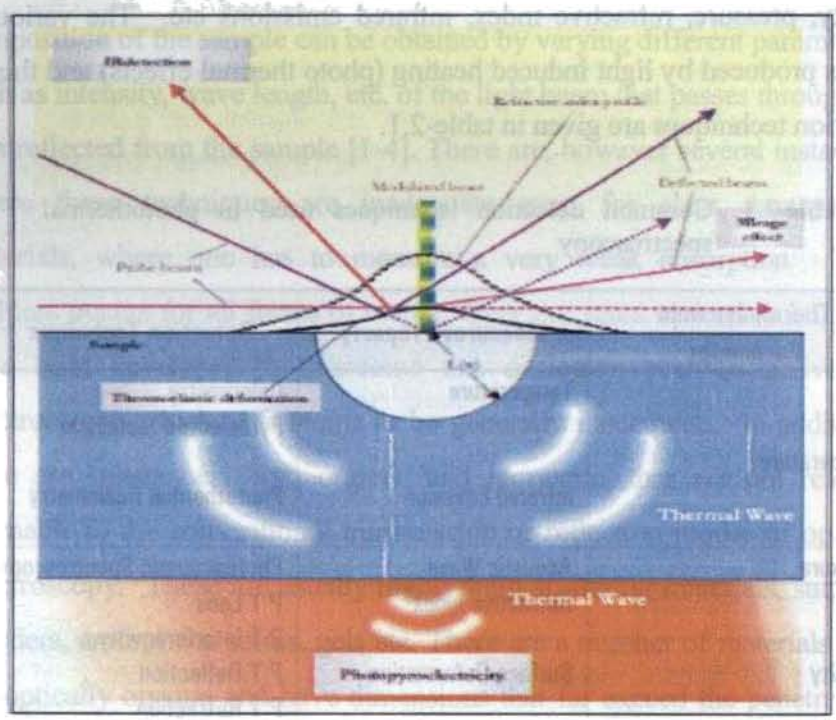

Fig. 2.1 Different types of photothermal signal generation

In Photoacoustic Technique, the sample is illuminated by an intensity modulated light source. The modulation can be achieved using

mechanical chopper, acoustoptic modulator, electroptic modulator etc. for continuous wave sources. When the incident photons are absorbed by the sample, internal energy levels within the sample are excited and upon subsequent de-excitation, all or part of the absorbed photon energy is transformed into heat energy through non-radiative de-excitation processes. This periodic heat flow (owing to the periodic excitation by intensity modulation), produces pressure fluctuations resulting in sound or acoustic signal. In gas samples, the detection can be done using a sensitive microphone, whereas in the case of liquid samples the resulting stress signals are detected using piezoelectric detectors. In the case of solid samples, two kinds of detection schemes are possible, viz. indirect detection and direct detection. In the indirect detection, the heat released by the solid sample causes pressure fluctuations in the surrounding air which can be detected by a sensitive microphone. In the direct detection scheme, a piezoelectric detector attached to the sample will measure the stress signal generated as a result of the modulated heating. The signal output from the microphone or the piezoelectric detector can be recorded as a function of the wavelength of light used or as a function of the chopping frequency.

Photoacoustic technique is, much more than just spectroscopy. It can be used to measure the absorption or excitation spectrum, the lifetime of excited states and the energy yield of radiative processes. These are all spectroscopic measurements. On the other hand, it can also be used to measure the thermal properties, thickness of layers and thin films and perform a variety of other non-spectroscopic

investigations. Thus photoacoustic studies can be performed on all types of materials – inorganic, organic and biological and on all states of matter.

2.2 History of Photo Acoustic Effect

The photoacoustic effect in both nongaseous and gaseous matter was discovered by Alexander Graham Bell in the year 1880. He showed that the solar radiation, dispersed with a prism and chopped at an audio frequency is absorbed by different materials to varying amounts depending upon the wavelength, and produced varying audio signals [22,23]. One of the transmitters developed by Bell called photophone consisted of a voice-activated mirror (which was activated by sound waves), a selenium cell and an electrical telephone receiver. The intensity-modulated sunlight was then focused onto a selenium cell. Since electrical resistance of selenium varies with the intensity of light falling on it, the voice-modulated beam of sunlight resulted in electrically reproduced telephonic speech.

Bell demonstrated that the photo acoustic effect in solids was dependent on the absorption of light and that the strength of the acoustic signal was in turn dependent on how strongly the incident light was absorbed by the material. He concluded that "The nature of the rays that produces sonorous effects in different substances depends upon the nature of the substances that are exposed to the beam, and that the sounds in every case are due to those rays of the spectrum that are absorbed by the body". Bell thus correctly deduced the intrinsic optical absorptive dependence of the photo acoustic effect.

Though Bell had prophesized the scope of his novel observation, after the initial flurry of interest generated by his original work, experiments with the photoacoustic effect remained almost in a dormant state for nearly 50 years. This was mainly because the experiments were difficult to perform since the investigator's ear had to serve as the signal detector. After the advent of microphones, Veingerov of Leningrad was able to observe this effect in gaseous samples. Between 1950 and 1970 the photoacoustic gas analyzer employing a conventional light source gave way to the more sensitive gas chromatographs and the spectrograph was overtaken by the more versatile infrared spectrophotometer. During this period, the photoacoustic effect was primarily employed to study vibrational life times and other aspects of radiation less de-excitation in gases. The advent of lasers in the early 1970's paved a new way in the photo acoustic spectroscopy of gaseous samples. The application of this technique was effectively and efficiently extended to liquids and solids only after the successful formulation of a general theoretical model by Rosencwaig and Gersho (R-G) in the mid seventies [8-10].

Subsequent developments in the theoretical aspects of photothermal phenomena are mere extensions of modifications of R-G model. A modification to the R-G theory by McDonald and Wetsel in 1978 by taking into account the contribution from thermally induced vibrations in the sample is somewhat intriguing. The most widely used model for describing photo acoustic effect in condensed sample in a gas–microphone cell was originally developed by Rosencwaig and

Gersho in 1976[10]. It is valid for acoustic wavelengths much greater than the dimensions of the sample and gas column.

2.3 Photo Induced Processes

The absorption of photons by atoms or molecules will result in a series of processes or effects in a material [5,6]. The excited level may loose its energy by radiative processes, such as spontaneous or stimulated emission, and by non-radiative processes, which mainly results in heat generation. If the photon energy is high enough, direct photochemical changes may take place. Destructive changes may take place at very high power densities of the incident light. A schematic representation of various photo-induced processes and main channels of photo-induced changes that occur in condensed matter is given in the following figure 2.2.

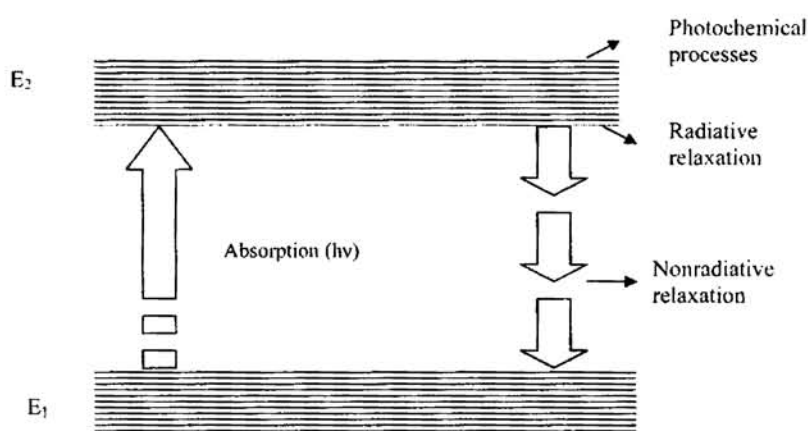

Fig 2.2 A Schematic representation of photo-induced processes

In the figure E_1 and E_2 represent the energies of the lower and upper levels and

E_2-E_1 = hν is the energy of the absorbed photon. The absorbed power in the sample I_{abs} is in accordance with

$$I_{abs} = I_0 [1-\exp(-\propto L)] \cong \propto I_0 L \quad \ldots\ldots\ldots\ldots\ldots\ldots (1)$$

with $\propto L << 1$. Here I_o and L are the incident light intensity and the sample length respectively and $\propto$ is the absorption coefficient.

Now, the absorbed energy will be liberated through radiative, nonradiative or chemical processes and each of these processes has specific quantum yield [24]

If n_r, n_{nr} and n_{pc} are the quantum yields of radiative, nonradiative and photochemical processes respectively, the total quantum yield of all the channels of de-excitation is given by

$$n_r + n_{nr} + n_{pc} = 1 \quad \ldots\ldots\ldots\ldots\ldots\ldots (2)$$

Accordingly, the intensity I_{abs} of the laser radiation, absorbed over all these channels is

$$I_{abs} = I_r + I_{nr} + I_{pc} \quad \ldots\ldots\ldots\ldots\ldots\ldots (3)$$

where $I_r = n_r I_{abs}$, $I_{nr} = n_{nr} I_{abs}$ and $I_{pc} = n_{pc} I_{abs}$ are the amounts of energy liberated through the radiative ,nonradiative and photochemical processes respectively.

Measurement of the energy absorbed or that released through any of these relaxation channels facilitates the study of various properties and related parameters of the sample.

2.4 Theory of Photoacoustic Effect by Rosencwaig &Gersho

The Rosencwaig-Gersho theory is a one dimensional heat flow model for the analysis of the production of a photoacoustic signal in a cell [8]. According to R-G theory with gas–microphone detection, the signal depends on the generation of an acoustic pressure disturbance at the solid–gas interface. The generation of the surface pressure disturbance, in turn depends on periodic temperature at the sample-gas interface. The formulation of R-G model is based on the light absorption and thermal wave propagation in an experimental configuration as in figure 2.3. Here a cylindrical cell of length L and diameter D is considered. Assume that the length L is small compared to the wavelength of the acoustic signal. The sample is considered to be in the form of a disk having diameter D and thickness l. The sample is mounted so that its front surface is exposed to the gas (air) within the cell and its back surface is a poor thermal conductor of thickness l_b. The length l_g of the gas column in the cell is then given by l_g= L-l- l_b. Further assumption is that the gas and backing materials are not light absorbing. Let k_i, ρ_i, C_i, and α_i represent the thermal conductivity, density, specific heat and thermal diffusivity respectively of the material i. Then $a_i = (\omega/2\alpha_i)^{1/2}$ is the thermal diffusion co-efficient and $\mu_i=1/a_i$, is the thermal diffusion length of the material. i can take subscripts s, g and b for solid, gas and backing material respectively,ω denotes the chopping frequency of the incident light beam in radians per second.

Assume that the sinusoidally chopped monochromatic light with wavelength λ is incident on the solid with intensity

$$I = (1/2)\, I_0 (1 + \cos \omega t) \qquad \text{.....(4)}$$

The main source of acoustic signal arises from the periodic heat flow from the solid to the surrounding gas. The periodic heating causes the boundary layer of gas to expand and contract periodically. This can be thought of as the action of an acoustic piston on the rest of the gas column, producing an acoustic pressure signal that travels through the entire gas column. The displacement of the gas piston due to the periodic heating can be estimated using the ideal gas law,

$$\delta x(t) = 2\pi\mu_g \frac{\bar{\phi}(t)}{T_0} = \frac{\theta\mu_g}{\sqrt{2}T_o} \exp\left[j\left(\omega t - \frac{\pi}{4}\right)\right] \qquad \text{.....(5)}$$

where the average dc temperature of the gas boundary layer is set as the dc temperature at the solid surface, $T_0 = \phi + \theta_0$, ϕ being the ambient temperature at the cell walls. Assuming that the rest of the gas responds to the action of the piston adiabatically, the acoustic pressure in the cell due to the displacement of the gas piston can be obtained from the adiabatic gas law PV^{γ} = constant, where P is the pressure, V is the gas volume in the cell, and γ the ratio of the specific heats. Thus the incremental pressure is

$$\delta P(t) = \frac{\gamma P_0}{V_0} \delta V = \frac{\gamma P_0}{l_g} \delta x(t) \qquad \text{.....(6)}$$

where P_0 and V_0 are the ambient pressure and volume respectively and $-\delta V$ is the incremental volume. Then from equations (5) & (6)

$$\delta P(t) = Q \exp\left[j\left(\omega t - \frac{\pi}{4} \right) \right] \quad \text{..... (7)}$$

where $Q = \dfrac{\gamma P_0 \theta}{\sqrt{2} l_g a_g T_0}$

The actual physical pressure variation is given by the real part of $\delta P(t)$ and Q specifies the complex envelope of the sinusoidal pressure variation. The ac temperature distribution θ is calculated by solving the heat diffusion equations. Rosencwaig and Gersho solved the one dimensional heat diffusion equations assuming no lateral heat flow.

The one dimensional heat diffusion equations in the three regions can be written as

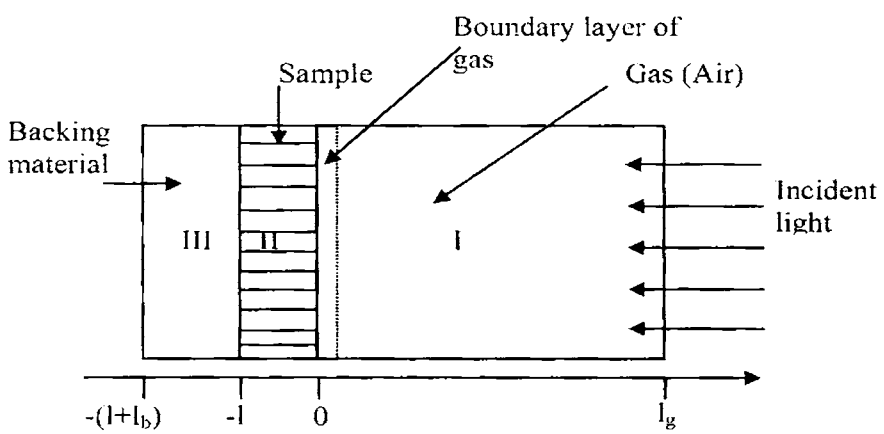

Fig.2.3 Schematic representation of photoacoustic experimental configuration

$$\frac{\partial^2 \varphi_b}{\partial t^2} = \frac{1}{\alpha_b} \frac{\partial \varphi_b}{\partial t} \quad , -l-l_b \leq x \leq -l \quad \text{Region III} \text{ ..... (i)}$$

$$\frac{\partial^2 \varphi_g}{\partial t^2} = \frac{1}{\alpha_g}\frac{\partial \varphi_g}{\partial t}, 0 \leq x \leq -l_g \qquad \text{Region I} \quad \ldots\ldots\ldots\ldots \text{(ii)}$$

$$\frac{\partial^2 \varphi_s}{\partial t^2} = \frac{1}{\alpha_s}\frac{\partial \varphi_s}{\partial t} - A\exp(\beta x)\left[1+\exp(j\omega t\right], -l \leq x \leq 0 \quad \text{Region II} \ldots \text{(iii)}$$

where $A = \dfrac{\beta I_0 \eta}{2k_s}$

Here φ is the temperature and η is the light conversion efficiency. The real part of the complex-valued solution φ(x, t) of the above equations is the solution of physical interest and represents the temperature in the cell relative to the ambient temperature as a function of position and time. Thus, the actual temperature field in the cell is given by

$$T(x,t) = \mathrm{Re}[\varphi(x, t)] + \phi$$

where Re denotes "the real part of " and ϕ is the ambient (room) temperature.

The complex amplitude of the periodic temperature distribution, θ at the solid-gas boundary (x=0) is given by

$$\theta = \frac{\beta I_0}{2k_s\left(\beta^2 - \sigma_s^2\right)}\left(\frac{(r-1)(b+1)\exp(\sigma_s l) - (r+1)(b-1)\exp(-\sigma_s l) + 2(b-r)\exp(-\beta l)}{(g+1)(b+1)\exp(\sigma_s l) - (g-1)(b-1)\exp(-\sigma_s l)}\right) \ldots\ldots \text{(iv)}$$

where $b = \dfrac{k_b a_b}{k_s a_s}$, $g = \dfrac{k_g a_g}{k_s a_s}$, $r = (1-j)\dfrac{\beta}{2a_s}$ and $\sigma_s = (1+j)a_s$.

Substituting for θ

$$Q = \frac{\beta I_0 \gamma P_0}{2\sqrt{2} k_s l_g a_g T_0 \left(\beta^2 - \sigma_s^2\right)} \; X$$

$$\left(\frac{(r-1)(b+1)\exp(\sigma_s l) - (r+1)(b-1)\exp(-\sigma_s l) + 2(b-r)\exp(-\beta l)}{(g+1)(b+1)\exp(\sigma_s l) - (g-1)(b-1)\exp(-\sigma_s l)} \right) \quad \text{..... (8)}$$

Thus, equation (8) can be used to evaluate the amplitude and phase of the acoustic pressure wave produced in the cell by photoacoustic effect. It can be observed that interpretation of the full expression for δP(t) is difficult because of the complex expression of Q. Some physical insight can be gained if certain special cases according to the optical opaqueness of solids are examined. For each category of optical opaqueness, three cases according to the relative magnitude of the thermal diffusion length μ_s, as compared to the physical length l and the optical absorption length μ_β can be considered.

Defining, $Y = \frac{\gamma P_0 I_0}{2\sqrt{2} l_g T_0}$, ... (9)

CASE I: Optically Transparent Solids ($\mu_\beta > 1$)

1. *Case Ia : Thermally Thin Solids ($\mu_s >> l$; $\mu_s >> \mu_\beta$)*

We can set $e^{-\beta l} \cong 1-\beta l$, $e^{\pm\sigma l} \cong 1$ and $|r| > 1$ in equation (8) and hence we obtain

$$Q = \frac{(1-i)\beta l}{2a_g} \left(\frac{\mu_b}{k_b} \right) Y \quad \text{..... (10)}$$

Thus the acoustic signal is proportional to βl and varies as f^{-1}. In addition, the thermal properties of the backing material come into play in the expression for Q.

2. *Case Ib: Thermally Thin Solids ($\mu_s > l$; $\mu_s < \mu_\beta$)*

Here we can set $\exp(-\beta l) \cong 1-\beta l$, $e^{\pm\sigma l} \cong 1 \pm \sigma_s l$ and $|r| < 1$ in equation (8).

Then $$Q = \frac{(1-j)\beta l}{2a_g}\left(\frac{\mu_b}{k_b}\right)Y \qquad \text{.....(11)}$$

This equation is identical with equation (10) and hence the acoustic signal behaves in the same fashion.

3. *Case Ic: Thermally Thick Solids($\mu_s > l$; $\mu_s << \mu_\beta$)*

In this case we set $\exp(-\beta l) \cong 1-\beta l$, $e^{\pm\sigma l} \cong 0$ and $|r| << 1$ in equation (8)

Now $$Q = -j\frac{\beta l}{2a_g}\left(\frac{\mu_s}{k_s}\right)Y \qquad \text{.....(12)}$$

The acoustic signal is now proportional to $\beta\mu_s$ rather than βl. This means that light absorbed within the first thermal diffusion length contributes to the signal, although light is being absorbed throughout the length of the solid. Moreover, μ_s being less than the thickness l, thermal properties of the backing material will not influence the signal. Here the signal varies as $f^{3/2}$ with the modulation frequency.

CASE II: Optically Opaque Solids

Case II a: Thermally Thin Solids ($\mu_s >> l$; $\mu_s >> \mu_\beta$)

In equation (8), we set $\exp(-\beta l) \cong 0$, $e^{\pm\sigma l} \cong 1$ and $|r| >> 1$

Then we obtain $Q = \frac{(1-j)}{2a_g}\left(\frac{\mu_b}{k_b}\right)Y$ ..... (13)

Here the photoacoustic signal is independent of β, which is valid for a perfect black absorber. The signal depends on the thermal properties of the backing material and varies as 1/f.

Case II b: Thermally Thick Solids ($\mu_s < l$; $\mu_s > \mu_\beta$)

We set $\exp(-\beta l) \cong 0$, $e^{-\sigma l} \cong 0$ and $|r| > 1$ in equation (8)

We obtain $Q = \frac{(1-j)}{2a_g}\left(\frac{\mu_s}{k_s}\right)Y$ . ..... (14)

Though equations (13) & (14) are similar, in the present case there is no contribution from the thermal properties of the backing material.

Case II c: Thermally Thick Solids ($\mu_s << l$; $\mu_s < \mu_\beta$)

We set $\exp(-\beta l) \cong 0$, $e^{-\sigma l} \cong 0$ and $|r| < 1$ in equation (8). Then we obtain

$$Q = \frac{-j\beta\mu_s}{2a_g}\left(\frac{\mu_s}{k_s}\right)Y \qquad \text{..... (15)}$$

The photo acoustic signal will be proportional to $\beta\mu_s$. The signal is independent of the thermal properties of the backing material and varies as $f^{3/2}$.A theoretical analysis of the photoacoustic effect applied to different cases has been discussed and can be applied to the study of any kind of sample.

The photo acoustic measurements can be done in two different configurations (1) by heat reflection configuration and (2) by heat transmission. The photo acoustic cell can be designed for the two configurations. In the reflection configuration, the microphone is situated above the sample surface. Hence the temperature distribution at x = 0 is to be determined. In the case of heat transmission configuration, the temperature distribution at x = -l has to be determined as the microphone is situated below the sample. In the above theoretical description, x = 0 case is solved and the different expressions for special cases are obtained for this particular case. For the heat transmission case, the expressions for the special cases will be different as the temperature distribution corresponding to x = *-l* will be used in the calculations.

The above analysis is based on the assumption of no lateral heat flow. However, if there exists a lateral heat flow, then three dimensional heat diffusion equations have to be solved for obtaining the temperature distribution.

The heat diffusion equations in the three layers can be written as

$$\frac{\partial^2 T_g}{\partial r^2}+\frac{1}{r}\frac{\partial T_g}{\partial r}+\frac{\partial^2 T_g}{\partial z^2}=\frac{1}{\alpha_g}\frac{\partial T_g}{\partial t} \qquad \text{.....(1a)}$$

for the gas in front of the sample with α_g being the thermal diffusivity of air (gas).

$$\frac{\partial^2 T_s}{\partial r^2}+\frac{1}{r}\frac{\partial T_s}{\partial r}+\frac{\partial^2 T_s}{\partial z^2}=\frac{1}{\alpha_s}\frac{\partial T_s}{\partial t}-\frac{Q}{k_s} \qquad \text{.....(1b)}$$

where the second term on the right hand side represents the source term as the sample absorbs light and acts as the source of heat with $Q=\frac{I_0\eta}{2}\beta\exp(-\beta x)(1+\exp(j\omega t))$. η is the light to heat conversion efficiency, β the absorption coefficient at the excitation wavelength, k_s is the thermal conductivity of the sample and α_s is the thermal diffusivity of the sample.

$$\frac{\partial^2 T_g}{\partial r^2}+\frac{1}{r}\frac{\partial T_g}{\partial r}+\frac{\partial^2 T_g}{\partial z^2}=\frac{1}{\alpha_g}\frac{\partial T_g}{\partial t} \qquad \text{.....(1c)}$$

for the backing (air).

The boundary conditions are

$$T_g(z=0,t)=T_s(z=0,t) \quad ,$$

$$k_s\frac{\partial T_s(z=0,t)}{\partial z}=k_g\frac{\partial T_g(z=0,t)}{\partial z}$$

$$T_g(z=-l,t)=T_s(z=-l,t),$$

$$k_s\frac{\partial T_s(z=-l,t)}{\partial z}=k_g\frac{\partial T_g(z=-l,t)}{\partial z}$$

$$T_g(z=\infty,t)=T_g(-\infty,t)=0$$

If the heating beam is Gaussian of power P and $1/e^2$ radius is 'a' then the source term Q can be written

$$Q(r,z,t)=\frac{\beta P\eta}{\pi a^2}\exp\left(-\frac{2r^2}{a^2}\right)\exp(\beta z)(1+\exp(j\omega t))$$

2.5 Thermal Diffusivity Measurement using Photoacoustic Technique

2.5.1 Heat Conduction in Solids

Heat conduction is a process in which heat is transferred from one part of the sample to another as a result of a temperature gradient. Mainly there are two mechanisms by which thermal transport is taking place in a solid [24-27].

a. The heat conduction due to charge carrier motion which is termed as electron or hole heat conductivity (k_e) and

b. The heat conduction due to lattice vibrations or phonons (k_l)

When a temperature gradient is built up in a substance the energy gradient is transmitted in such a manner that energy is transmitted from an atom, which oscillates with more intensity to an atom which oscillates with less intensity.

The total heat conductivity $k = k_e + k_l$

In this k_l is related to the elastic properties of the solid and k_e to the charge carrier concentration. In metals $k_e >> k_l$ and in dielectrics $k_l >> k_e$. In semiconductors k_e strongly depends on the composition and on the temperature.

When a semiconductor is irradiated with an optical radiation of suitable energy, in addition, photo generated carrier recombination will also contribute to the heat transport. Free carrier generation resulting from the light absorption occurs when the incident photon energy is greater than the band gap energy. The photon is absorbed in this process and excess energy $E_{ph} - E_g$ is added to the electron and hole in the form of kinetic energy. Now the non-radiative recombination of these carriers will result in the form of heat to the lattice [12,13]. Another form of non-radiative recombination process is the surface recombination. Surfaces and interfaces of semiconductors usually contain a large number of recombination centers because of the abrupt termination of the crystal, which leaves a large number of electrically active dangling bonds. In addition, surfaces and interfaces are likely to contain more impurities. The surface recombination is also an interband recombination process and excess energy is ultimately transferred to the lattice as heat. Trap assisted recombination is also one among the recombination mechanisms. Apart from this there exists an instantaneous thermalisation component, which arises from intra band interaction of excited electrons with the lattice. This process is an after effect of excitation of electrons to the higher levels in the conduction

band. Such hot electrons will come back to the minimum of the conduction band by imparting the excess energy to the lattice. This thermalisation takes place in pico seconds and hence is known as instantaneous thermalisation.

2.6 Thermal Conduction by Phonons

The transmission of heat can be conveniently explained by considering phonon gas transport. In every region of space there are phonons traveling in all directions, much like the molecules in a gas. The advantage of using this gas model is that many of the concepts of the kinetic theory of gases can also be applied here. The thermal conductivity is given by

$$k = cvl_m/3$$

where c is the specific heat per unit volume v is the speed of the particle and l_m its mean free path [26]. The only difference in solids is that phonons replace the molecules so that the velocity and mean free path now refer to phonons instead of gas molecules. The thermal conductivity k will be determined by the nature of the mean free path, since c is constant at high temperatures and varies as T^3 at low temperatures and v is almost a constant. Here l_m is the average distance the phonon travels between two successive collisions. This in turn is determined by the scattering mechanisms. The important scattering mechanisms are (1) scattering due to phonon-phonon interaction (2) scattering by imperfections such as impurities and dislocations and (3) boundary scattering caused by collision of phonons with the external boundaries of the sample.

The phonon-phonon collision becomes more pronounced at high temperatures, at which the atomic displacements are large and this gives rise to harmonic coupling between phonons, causing their mutual scattering. In this region the mean free path is inversely proportional to the temperature ($l_m \propto 1/T$). This is reasonable, since the larger the value of T, the greater is the number of phonons participating in the collision process.

Crystal imperfections such as impurities and defects also can scatter phonons because they partially destroy the perfect periodicity, which is the very basis of the concept of a freely propagating lattice wave. This scattering may be due to (1) point defects and/or due to (2) dislocations. Thus the random distribution of different isotopes leads to a decrease in thermal conductivity. For instance a substitution point impurity having a mass different from that of the host atom causes scattering of the wave at the impurity. The greater the difference in mass and the density of impurities, the greater is the scattering and the shorter the mean free path. This gives rise to a decrease in the value of thermal conductivity there by reducing the thermal diffusivity of the sample.

Though various techniques are available for the measurement, the photo acoustic technique has proved to be the most efficient and convenient tool for the measurement of thermal diffusivity. The detected signal is strongly dependent upon the interplay of the sample's optical absorption coefficient for the incident radiation, the light into heat conversion efficiency, as well as how heat

diffuses through the sample. The dependence of the photo acoustic signal on the absorption coefficient allows one to perform spectroscopic studies, where as the fact that the signal is proportional to the light into heat conversion efficiency means that it is complementary to other photo induced energy conversion processes. Thus the photo acoustic signal can be used for obtaining the information concerning the non-radiative de-excitation processes.

2.7 Significance of Thermal Diffusivity Measurement

The photoacoustic process depends not only on the optical properties of the sample but on its thermal and geometric parameters and in some cases on its elastic properties as well. The thermal diffusivity $\propto$ is of direct importance in heat flow studies as it determines the rate of periodic or transient heat propagation through a medium.

Jean Fourier has derived the basic law defining the propagation of heat in a one-dimensional homogeneous solid as [26-30].

$\partial Q/\partial t = -kA\partial T/\partial x$ this is known as Fourier equation.

This equation implies that the quantity of heat ∂Q conducted in the X–direction of a uniform solid in time ∂t is equal to the product of the conducting area A normal to the flow path, the temperature gradient $\partial T/\partial x$ along the path and thermal conductivity k of the material.

Formal definition of thermal diffusivity arises when deriving an expression for a transient temperature field in a conducting solid from Fourier equation. The equation describing the temperature field in a homogeneous, linear conducting solid with no internal heat source is

$$\nabla^2 T = 1/\alpha \, \partial T/\partial t$$

Here α is the thermal diffusivity, which is related to the thermal conductivity (k), density (ρ) and specific heat capacity c of the material as

$$\alpha = k/\rho c$$

The thermal diffusivity α is expressed in m^2/s. Because of its controlling effect and common occurrence in heat flow problems, its determination is often necessary and knowledge of the thermal diffusivity can in turn be used to calculate the thermal conductivity. Changes in the thermal parameters such as thermal conductivity can be used to monitor changes within a material. The significance of α is evident from the above relationship. The reciprocal $1/\alpha$ expressed in sm^{-2} is a measure of the time required to heat up a material to some temperature level. Therefore, the ratio of heating times for two materials of the same thickness will be inversely proportional to the thermal diffusivity values. Thus α is a significant thermodynamic parameter that determines the heat diffusion in bulk as well as thin film samples.

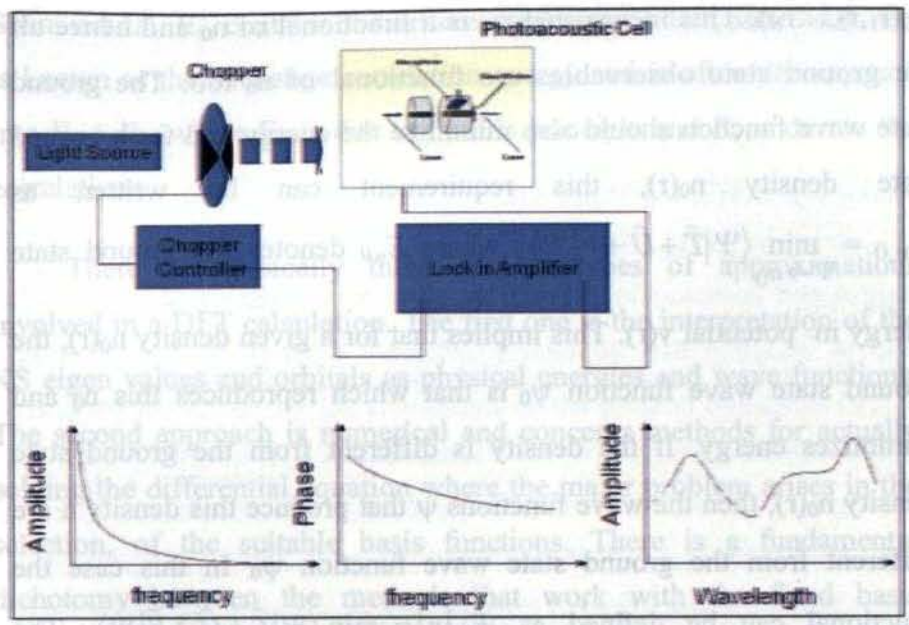

Fig. 2.4 Schematic diagram of the PA experimental arrangement

2.8 Density Functional Theory

The analysis of the PA spectra is based on Density Functional Theory and its approximations for prediction of electronic band structure. Density functional theory is one of the most popular and powerful quantum mechanical approaches to matter and is being successfully applied for the calculation of band structure of solids, binding energy of molecules etc. It is highly versatile owing to the generality in its fundamental concepts and the flexibility in implementing them. The two core elements of DFT are Hohenberg-Kohn (HK) theorem and the Kohn-Sham (KS) equations [31-34]. The HK theorem states that given a ground state density n_0 (r) it is possible to calculate the corresponding ground state wave function

$\psi_0(r_1,r_2,\ldots r_N)$. This means that ψ_0 is a functional of n_0 and hence all the ground state observables are functional of n_0 too. The ground state wave function should also minimize the energy and for a ground state density $n_0(r)$, this requirement can be written as $E_{v,0} = \min_{\Psi \to n_0} \langle \Psi | \hat{T} + \hat{U} + \hat{V} | \Psi \rangle$, where $E_{v,0}$ denotes the ground state energy in potential v(r). This implies that for a given density $n_0(r)$, the ground state wave function ψ_0 is that which reproduces this n_0 and minimizes energy. If the density is different from the ground state density $n_0(r)$, then the wave functions ψ that produce this density n are different from the ground state wave function ψ_0. In this case the functional can be defined as $E_v[n] = \min_{\Psi \to n} \langle \Psi | \hat{T} + \hat{U} + \hat{V} | \Psi \rangle$. The functional $E_v[n]$ is minimized by the ground state density n_0 and its value at minimum is $E_{v,0}$. In the Kohn Sham approach, it does not work exclusively in terms of particle density but with special kind of wave functions (single particle orbital). Though DFT will look like a single particle theory, many body effects will be included via the so-called exchange correlation functional. With the exchange correlation functional, the energy functional can be written as

$$E[n] = T[n] + U[n] + V[n] = T_s[\{\phi_i[n]\}] + U_H[n] + E_{xc}[n] + V[n]$$

The kinetic energy functional $T[n]$ is decomposed into a part representing kinetic energy of non-interacting particles of density n, $T_s[n]$ and the remainder is $T_c[n]$ where c represents correlation and s represents single particle. U_H is the Hartree energy and ϕ_i is the Kohn

Sham orbital. E_{xc} contains the differences between $T-T_s$ and $U-U_H$. E_{xc} is known as the exchange correlation energy and is often decomposed into $E_x + E_c$, where E_x is due to Pauli's principle and E_c is due to the correlations.

There are basically three distinct types of approximations involved in a DFT calculation. The first one is the interpretation of the KS eigen values and orbitals as physical energies and wave functions. The second approach is numerical and concerns methods for actually solving the differential equation where the major problem arises in the selection, of the suitable basis functions. There is a fundamental dichotomy between the methods that work with the fixed basis functions that do not depend on the energy and methods that employ energy dependent basis functions. Fixed basis functions are used in plane wave expansions, linear combination of atomic orbitals (LCAO) approximations, orthogonalized plane wave etc and methods using energy dependent functions are the APW (augmented plane wave) or the Korriga/Kohn/Rostoker [35,36] approaches. However, this distinction becomes less clear-cut with the linear methods in which the energy dependent basis functions are linearized around some fixed reference energy like in Linear Muffin Tin Orbital method (LMTO) [37-40] and Linear Augmented Plane waves approach (LAPW)[40-43]. The third type of approximation involves constructing an expression for the exchange correlation energy functional $E_{xc}[n]$ which contains the many body aspects of the problem. There exists different functional for the local functional, Thomas-Fermi approximation (TF) [44] Local

Density Approximation [LDA][32], Local Spin Density Approximation [45] etc, semi local or gradient functional [Generalized Gradient Approximation (GGA)[46] and Gradient Expansion Approximation (GEA)[47], non local functional (hybrids, orbital functional such as meta-GGA, EXX and SIC and integral dependent functions such as ADA [34].

2.9 Electrical Properties of Polycrystalline Materials

Electrical conductivity measurements are extensively used for investigating the mechanism of charge transport in materials in addition to probing structural defects and internal purity of crystalline solids. The investigations carried out till date on a variety of materials describe their electrical conductivity in terms of electrons/holes, ions, polarons, impurities, defects, vacancies etc. Most of the battery materials available show special property of storing and dissipating electrical energy when subjected to electric fields. In the case of materials of interest in the present work, $LiMPO_4$ (M=Fe, Mn, Ni, Co) olivine phosphates, it has been recently reported that the electron transport mechanism is by means of small polarons [48]. The concept of small polaron model has been detailed in several articles [49,50]. When charge carriers like electrons or holes are present in a polar crystal, the atoms in their environment will be polarized and displaced and produce a local lattice distortion. The ion displacement becomes more pronounced as the charge carriers become more and more localized. The carrier lowers its energy by localizing into such a lattice deformation and becomes self trapped. This quasi particle formed by

the electron and its self-induced distortion is called a small polaron if the range of lattice distortion is of the order of lattice constant. These charge carriers can be either electrons or holes in $LiMPO_4$. Since the hopping process dominates the electrical transport in this material, the dielectric measurements will provide a useful knowledge on the polaron dynamics because a hopping process of polarons has a high probability of involving a dielectric relaxation that contains several significant parameters in the elucidation of the polaron dynamics [51].

2.10 AC Conductivity

The theory involved for the evaluation of a.c conductivity from dielectric constant values is as follows. Any capacitor when charged under a voltage will have some loss current due to ohmic resistance or impedance by heat diffusion [52]. For a parallel plate capacitor of area of cross-section A and plate separation d the a.c conductivity is given by

$$\sigma_{ac} = \frac{J}{E} \qquad \text{.....(1)}$$

where J is the current density and E is the electric field intensity. But the electric field vector is related to the displacement vector D of dipole charges and the complex permittivity of the material ε as

$$E = \frac{D}{\varepsilon} \qquad \text{.....(2)}$$

For a parallel plate capacitor the electric field vector E is related to the applied a.c voltage $V = V_0 \exp(j\omega t)$ as

$$E = \frac{V}{d} \qquad \text{.....(3)}$$

Since the current density $J = \frac{dq}{dt}$ where $q = \frac{Q}{A} = \frac{V\varepsilon}{d}$ (provided by Maxwell's equation), where Q is the charge in coulombs due to a potential difference V volts between the capacitor plates. Hence,

$$J = \frac{dq}{dt} = \frac{d}{dt}\left(\frac{V\varepsilon}{d}\right) = \frac{\varepsilon}{d}\frac{dV}{dt} = \frac{\varepsilon}{d}Vj\omega \qquad \text{.....(4)}$$

Substituting for E and J from equations (2) and (4) we get

$$\sigma_{ac} = \varepsilon j\omega \qquad \text{.....(5)}$$

Since permittivity is a complex quantity, it can be written as $\varepsilon = \varepsilon^{'} - j\varepsilon^{''}$ then

$$\sigma_{ac} = j\omega\left(\varepsilon^{'} - j\varepsilon^{''}\right) = j\omega\varepsilon^{'} + \omega\varepsilon^{''} \qquad \text{.....(6)}$$

Neglecting the imaginary term in the conductivity equation we can write

$$\sigma_{ac} = \varepsilon^{''}\omega \qquad \text{.....(7)}$$

In a dielectric material there will be some power loss because of work done to overcome the frictional damping forces encountered by the dipoles during their rotation. In an ideal case of a.c field the charging current I_C and loss current I_L will be 90^o out of phase with the voltage. But in most of the capacitors due to the absorption of electrical energy some loss current, I_L will also be produced, which will be in

phase with the voltage [52,53]. Charging current, I_C, and loss current, I_L, will make angles δ and θ respectively with the total current I.

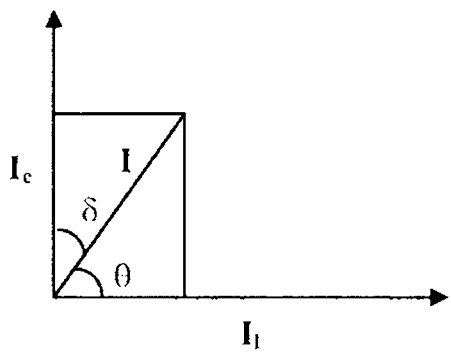

Fig. 2.5 Vector diagram of current component

Generally, sinδ is called the loss factor but when δ is small then sin δ = δ = tanδ. But the two components ε`and ε" of the complex dielectric constant, ε, are frequency dependent and given by

$$\varepsilon` = Do\frac{Cos\delta}{Eo} \qquad \text{.....(8)}$$

$$\varepsilon" = Do\frac{Sin\delta}{Eo} \qquad \text{.....(9)}$$

From equations (8) and (9) we obtain the loss factor as

$$\tan\delta = \frac{\varepsilon"}{\varepsilon`} \qquad \text{.....(10)}$$

From equation (10) and (7) we modify the expression for a.c conductivity as

$$\sigma_{ac} = \omega \tan\delta \varepsilon` \qquad \text{.....(11)}$$

If f is the frequency of the applied field, ε_r the relative permittivity of the material and ε_o the permittivity of free space, then $\omega = 2\pi f$, and $\varepsilon` = \varepsilon_o\varepsilon_r$

Hence from the dielectric loss and dielectric constant, a.c conductivity of the samples can be evaluated using the relation

$$\sigma_{ac} = 2\pi f \tan\delta\varepsilon_o\varepsilon_r \quad \text{.....(12)}$$

Considerable progress has been made by Cole and Cole in utilizing complex plots to explain the dielectric behavior and carrier transport mechanisms in a wide range of solid state materials [52,54,55]. The ac conductivity of a material depends on the dielectric property as well as its capacitance. The variation of ac conductivity with frequency indicates its dispersion, which is attributed to the presence of space charge in material. The behavior of ac conductivity is expressed on the basis of Jonscher's universal power law [56]. $\sigma(\omega) = \sigma_{dc}\left(1+\left(\frac{\omega}{\omega_H}\right)^n\right)$ where σ_{dc} is frequency independent part appearing at high frequency and ω_H corresponds to the crossover frequency separating dc regime from the dispersive conduction (hopping frequency) and the frequency exponent n lies between 0 and 1. The ac activation energy can be obtained by plotting the hopping frequency ω_H and temperature using the relation, $\omega_H = \omega_0 \exp\left(-\frac{E_H}{kT}\right)$.

2.11 DC Conductivity

By Ohms law, $V = IR$ where V is the voltage, I the current and R the resistance. $V = EL$ where E is the electric field and L the length and $I = JA$ where J is the current density and A the area of cross section. Hence, $E = \frac{JAR}{L} = J\rho$, where ρ is the resistivity. In other words, $J = \frac{E}{\rho} = \sigma E$, where σ is the dc electrical conductivity. The dc conductivity measured as a function of the temperature can lead to the information regarding the activation energy from the Arrhenius relation $\sigma(T) = \frac{\sigma_0}{T} \exp\left(-\frac{Ea}{kT}\right)$ where E_a is the activation energy and T the temperature.

2.12 X-Ray Diffraction Analysis

According to Bragg, X-rays behave as if they are reflected by planes of atoms in a crystal and when a beam of X- rays is allowed to fall on a crystal surface at some angle θ, each atom there in acts as a source of scattered radiation of the same wave length. Thus when X-ray beam strikes a crystal surface at an angle θ, a portion is scattered by the layer of atoms at the surface and the unscattered portion of the beam penetrates to the second layer of the atoms, where again a fraction is scattered and the remainder passes on to the third layer. The cumulative effect of this scattering from the regularly spaced centers of the crystal is nothing but diffraction of the beam, which is almost similar to diffraction of visible radiation by a reflection grating.

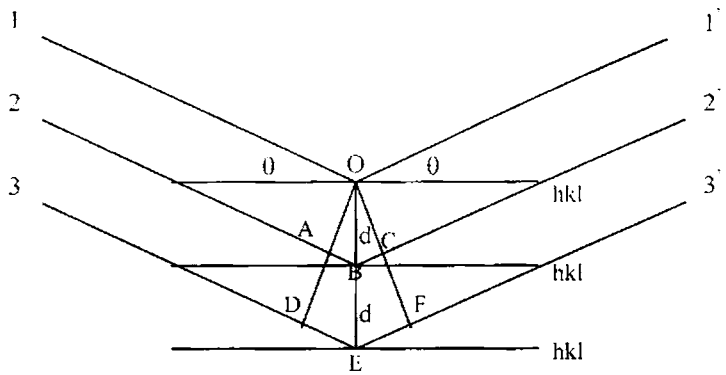

Fig. 2.6 Crystal diffraction

William Henry Bragg and his son William Lawrence Bragg developed a useful relationship between the wavelength of X-rays and the spacing between the lattice planes. As the atoms in a crystal are orderly arranged, a beam of X-rays can be reflected from a plane of atoms similar to the reflection of light from a plane mirror [57,58].

The most important requirements of diffraction are

a. The spacing between the layers of atoms must be roughly the same as the wavelength of radiation

b. The scattering centers must be distributed in a highly regular manner.

By considering a beam of monochromatic X-rays which strikes a set of parallel and equidistant planes called lattice planes or Bragg's planes in the crystal structure at an angle θ (glancing angle) scattering occurs as a result of interaction of radiation with atoms located at different points at various planes. Bragg obtained a formula given by,

$2d_{hkl}\sin\theta = n\lambda$

where n is the order of reflection d_{hkl} the inter-planar distance of the crystal and λ the wave length of X-ray used.

The X-ray diffraction technique can be conveniently employed for the identification and characterization of solids. For elements and compounds, crystallizing in the simple crystal systems such as cubic, tetragonal, hexagonal etc., the Bragg's law enables determination of unit cell parameters with relative ease.

In the X-ray diffractometer, the X-ray source, the specimen and the detector are so arranged to obey Bragg's law. In our set-up (model 1710 Rigaku), filtered copper k_α radiation is used for diffraction. The wavelength of radiation is 1.5414 A°. The accelerating potential applied to the X-ray tube is 30kV and the tube current is 20mA. The sample can be scanned from 0° to 90° and the X-ray diffraction pattern (intensity of diffracted beam versus 2θ) of the sample can be recorded.

2.13 Scherrer Formula

The powder method is a widely used experimental technique for the determination of grain size. Here we make use of the Scherrer formula given by,

$t = 0.9\lambda/\beta \cos\theta$

where β is the full width at half maximum (FWHM) of the most intense diffraction peak and θ, the corresponding angle.

The basic principle underlying the powder technique is that, since millions of tiny crystals in the powder have completely random orientations, all possible diffractions will be available for Bragg reflection to take place [57,58]. Such reflections will take place from many sets of parallel planes lying at different angles to the incident X-ray beam. Moreover; each set will give not only first order reflections but higher order reflections as well. Since all orientations are equally possible, the reflected rays will form a cone whose axis lies along the direction of the incident beam and whose semi vertical angle is twice the glancing angle for that particular set of planes. For each set of planes, and for each order, there will be such a cone of reflected X-rays. Their intersections with a photographic film set with its plane normal to the incident beam form a series of concentric circular rings. Radii of these circular rings are recorded and the film can be used to find the glancing angle and hence the inter-planar spacing of the crystalline substance.

In the powder method the intensity of the reflected beam can also be recorded in a diffractometer, which uses a counter in place of the film to measure intensities. The counter moves along the periphery of the cylinder and records the reflected intensities against 2θ. Peaks in the diffractometer reading correspond to positions where the Bragg condition is satisfied. From the XRD pattern of the powder sample we can calculate the lattice parameter using the formula

$$d_{hkl} = \frac{\lambda}{2\sin\theta}$$

and cubic lattice constant

$$a = d_{hkl}\sqrt{h^2 + k^2 + l^2}$$

The porosity of the samples can be calculated as

$$\text{Porosity} = \frac{X - Raydensity - apparentdensity}{X - Raydensity}$$

Where X- ray density =n (Molecular Mass/ N) (1/Volume of unit cell) n = number of molecules per unit cell.

N = Avogadro number.

2.14 Scanning Electron Microscopy (SEM)

The scanning electron microscope (SEM) provides a means to investigate the surface morphology of the sample. The SEM is a microscope that uses electrons instead of light to form an image. It provides a high resolution and depth of the field images of the sample surface (so closely spaced specimens can be magnified at much higher levels). The SEM has allowed researchers to examine a much bigger variety of specimens.

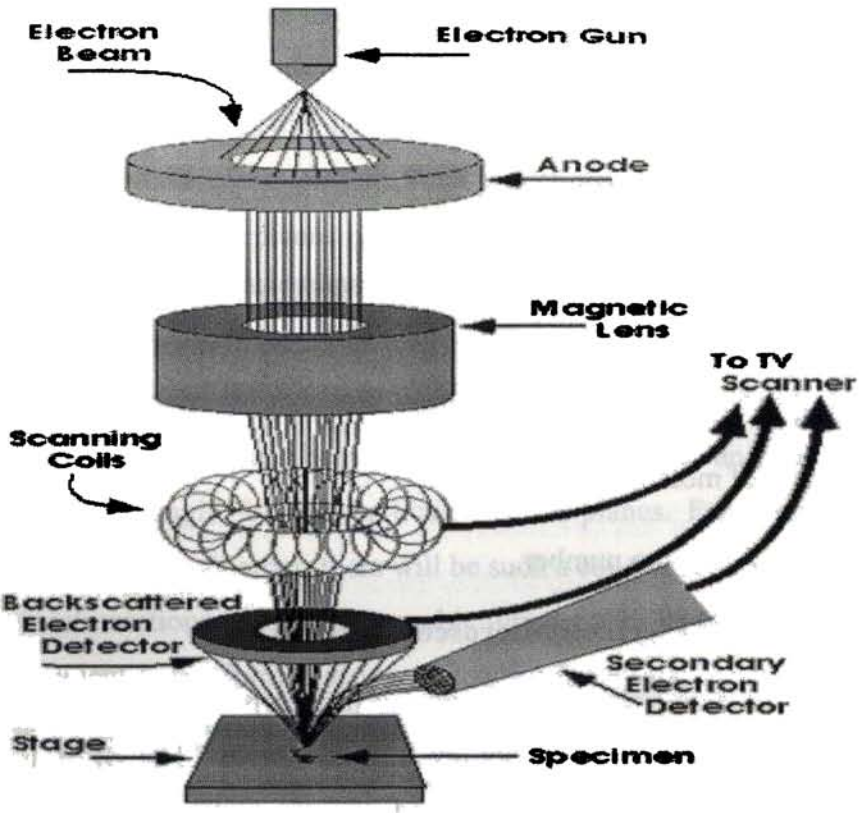

Fig. 2.7 Schematic diagram of SEM

The scanning electron microscope has many advantages over traditional microscopes. The two main improvements over conventional optical microscopes are (i) it can magnify a sample up to $x10^5$ and (ii) it improves the depth of field resolution by a factor around 300. Because the SEM uses electromagnets rather than lenses, the researcher has much more control in the degree of magnification [59]. All of these advantages, as well as the actual strikingly clear images, make the scanning electron microscope one of the most useful instruments in research today.

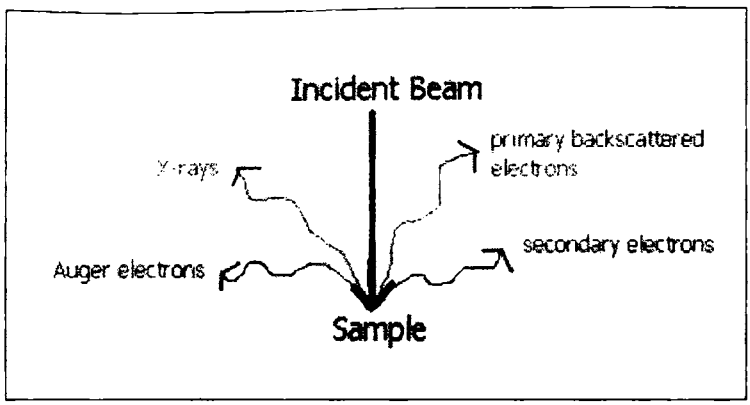

Figure 2.8 Production of secondary electron

The sample is placed inside the microscope's vacuum column through an air- tight door using a load lock facility. Air is pumped out of the column using a combination of different pumps like rotary, turbo molecular or diffusion pumps. A beam of electrons is produced at the top of the microscope by an electron gun. The electron beam follows a vertical path through the microscope, which is held within the vacuum. The beam travels through electromagnetic fields and lenses, which focus the beam down toward the sample. Once the beam hits the sample, electrons and X-rays are ejected from the sample. Detectors collect these X-rays, backscattered electrons, and secondary electrons and convert them into a signal that is sent to a screen similar to a television. This produces the final image. A schematic diagram of SEM is shown in figure 2.7.

2.14.1 Sample Preparation for SEM

Because the SEM utilizes vacuum conditions and uses electrons to form an image, special preparations must be done to the sample. All water must be removed from the samples because the water would

vaporize in the vacuum. All metals are conductive and require no preparation before being used. All non-metals and insulator samples should be coated with gold in order to improve the surface conductivity. This prevents the accumulation of negative surface charges, which might interact with the secondary electron. This process is carried out using a device called a "sputter coater". The sputter coater uses an electric field and argon gas. The sample is placed in a small chamber that is at a vacuum. Argon gas and an electric field cause an electron to be removed from the argon, making the atoms positively charged. The argon ions then become attracted to a negatively charged gold foil. The argon ions knock gold atoms from the surface of the gold foil. These gold atoms fall and settle onto the surface of the sample producing a thin gold coating.

2.15 Transmission Electron Microscopy (TEM)

Transmission electron microscopy was originally used for highly magnified sample images. Later, analytical capabilities such as electron energy loss detectors and light and X-ray detectors were added to the instrument and the technique is now known as analytical transmission electron microscopy (AEM). Transmission electron microscopes are, in principle, similar to optical microscopes; both contain a series of lenses to magnify the sample. The main strength of TEM lies in its extremely high resolution [59,60].

Transmission electron microscopy is a microscopy technique whereby a beam of electrons is transmitted through thin specimen , which interacts with the specimen as it passes through it. An image is

formed from the electrons transmitted through the specimen, magnified and focused by an objective lens and appears on an imaging screen, a fluorescent screen in most TEMs, plus a monitor, or on a layer of photographic film, or to be detected by a sensor such as CCD camera.

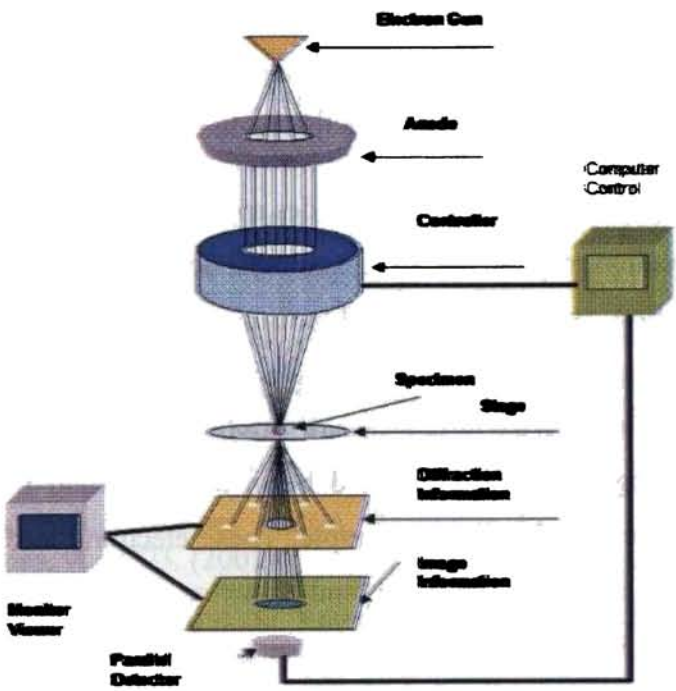

Fig. 2.9 Schematic diagram of transmission electron microscope.

Electrons are usually generated in an electron microscope by thermionic emission from a filament, usually tungsten, or by field emission [59,60]. The electrons are then accelerated by an electric potential (usually 100-400kV) and focused by electrostatic and electromagnetic lenses onto the sample. The beam interacts variously with the sample due to differences in density or chemistry. The

transmitted and forward scattered electrons form a diffraction pattern in the back focal plane and a magnified image in the image plane. The beam that is transmitted through the sample contains information about these differences, and this information in the beam of electrons is used to form an image of the sample. The electrons that remain in the beam can be detected using a photographic film, or fluorescent screen .So areas where electrons have been scattered in the sample can appear dark on the screen, or on a positive image due to this scattering.

The three primary imaging modes are bright-field, dark-field, and high-resolution microscopy. Image contrast does not depend very much on absorption, as it does in optical transmission microscopy, but rather on scattering and diffraction of electrons in the sample. Images formed by transmitted electrons are bright-field images and images formed using a specific diffracted beam are dark-field images. Few electrons are absorbed in the sample. These electrons lead to sample heating. A stationary, parallel and coherent electron beam passes through the sample in TEM forming a magnified image in the image plane, which is then simply projected on to the fluorescent screen.

References

[1] Bauman.R.P.Absorption spectroscopy, (John Wiley & Sons, New York) (1962).

[2] Olsen. E.D. Modern optical methods of analysis, (Mc Graw Hill, New York) (1975).

[3] Jaffe. H.H and Orchin. M., Theory and applications of ultraviolet spectroscopy, (John Wiley & Sons, New York) (1962).

[4] West.W (Edit) Chemical applications of spectroscopy, Vol.IX; Part I (John Wiley & Sons, New York) (1968).

[5] Kliger.D.S (Edit) Ultra sensitive laser spectroscopy, (Academic press, New York) (1983).

[6] Wineforder J.D (Edit) Chemical analysis: A monograph on analytical chemistry and its applications (John Wiley & Sons.Inc) (1996).

[7] Hess. P and Pelzl.J (Eds.), Photoacoustic and photothermal phenomena,(Sspringer-Verlag,Berlin) (1989).

[8] A.Rosencwaig, Phys. Today, September, 23,(1975).

[9] A.Rosencwaig and A.Gersho, Science, 190, 556,(1975).

[10] A.Rosencwaig and A.Gersho,J. Appl. Phys, 64, 64, (1976)

[11] C. Glorieux, J. Fivez and J. Thoen, J. Appl. Phys, 73, 684 . (1993).

[12] A. Calderón, J. J. Alvarado-Gil, Yu. G. Gurevich, A. Cruz-Orea I. Delgadillo H. Vargas L. C. M. Miranda Phys. Rev. Lett. 79, 5022 (1997).

[13] J. A. Balderas-López and A. Mandelis Journal of Applied Physics, 90, 2273. (2001).

[14] Nibu A George, C P G Vallabhan, V P N Nampoori, A K George and P Radhakrishnan J. Phys.: Condens. Matter 13 365.(2001).

[15] Sajan D George, P Radhakrishnan, V P N Nampoori and C P G Vallabhan J. Phys. D: Appl. Phys. 36 990. (2003).

[16] J. Ravi, M. K. Jayaraj, K. A. Vanaja, K. P. R. Nair and T. M. A. Rasheed Semiconductor Sci. Tech. 18, 693 .(2003).

[17] A. Pinto Neto , H. Vargas, N. F. Leite and L. C. M. Miranda, Phys.Rev.B, 40, 3924 (1989).

[18] M. D. Dramićanin , P. M. Nikolić, Z. D. Ristovski, D. G. Vasiljević and D. M. Todorović, Phys. Rev B, 51, 14226 .(1995).

[19] A M. Mansanares, M. L. Baesso, E. C. da Silva, F. C. G. Gandra, and H. Vargas L. C. M. Miranda, Phys. Rev. B, 40, 7912 .(1989).

[20] A M. Mansanares, A. C. Bento, and H. Vargas N. F. Leite and L. C. M. Miranda Phys. Rev. B, 42, 4477. (1990).

[21] Sheenu Thomas, Johney Isaac, and J. Philip Rev. Sci. Instr. 66, 3907 (1995).

[22] Bell.A.G, A.M.J.Sci.20, 305.(1880).

[23] Bell.A.G, Philos.Mag.11, 510.(1881).

[24] Mukherjee K.K.R Fundamentals of photochemistry. (New age International New Delhi).(1978)

[25] Jacob Philip and K. N. Madhusoodanan Phys. Rev. B, 38, 4127 .(1988).

[26] CharlesKittel.Introduction to solid state Physics 7thEdn.John Wiely&Sons.INC-(2000).

[27] J. Ravi, Y. Lu, S. Longuemart, S. Paoloni, H. Pfeiffer, J. Thoen and C. Glorieux, J. Appl. Phys. 97, 14701-1 .(2005).

[28] Caslaw H S, Jaeger J C. Conduction of heat in solids, London: Oxford University Press, (1959).

[29] Jeffrey A Sell, Photothermal investigations of solids and fluids, Boston: Academic Press, (1989)0.

[30] A. Pinto Neto, H. Vargas, N. F. Leite and L. C. M. Miranda, Phys. Rev. B, 41, 9971 (1990)

[31] P. Hohenberg and W. Kohn, Phys. Rev. B, 136, 864 .(1964).

[32] W. Kohn and L. J. Sham, Phys. Rev. 140, A1133 .(1965).

[33] Parr RG, Yang W. Density-Functional Theory of Atoms and Molecules, Oxford, Oxford University Press; (1989).

[34] Capelle K. A bird's-eye view of density-functional theory. ArXiv: cond-mat/0211443.

[35] J. C. Slater, Phys. Rev. 92, 603 (1953)

[36] H. Ebert, Electronic Structure and Physical Properties of Solids,edited by H. Dreysse', Lecture Notes in Physics Vol. 535, Springer, Berlin, p. 191. (2000)

[37] M. Methfessel, M. van Schilfgaarde, and R. A. Casali, Electronic Structure and Physical Properties of Solids: The Uses of the LMTO Method, edited by H. Dreysse, Lecture Notes in Physics Vol. 535 (Springer-Verlag, Berlin) (2000).

[38] J. M. Wills, O. Eriksson, M. Alouani, D. L. Price, Electronic Structure and Physical Properties of Solids: The Uses of the LMTO Method, edited by H. Dreysse, Lecture Notes in Physics Vol. 535 (Springer-Verlag, Berlin) (2000).

[39] M. Methfessel, Phys. Rev. B 38, 1537 (1988).

[40] O. K.Anderson, Phys. Rev. B 12, 3060 (1975)

[41] E. Wimmer, H. Krakauer, M. Weinert, and A. J. Freeman, Phys. Rev. B 24, 864 (1981).

[42] M. Weinert, E. Wimmer, and A. J. Freeman, Phys. Rev. B 26, 4571 (1982).

[43] D. Singh, Planewaves, Pseudopotentials and the LAPW Method, (Kluwer Academic Publishers, Boston/Dordrecht/London, 1994).

[44] S. Vlaev and L. M. Gaggero-Sager Phys. Rev. B, 58, 1142 (1998)

[45] J. P. Perdew and Y. Wang, Phys. Rev B 45 13 244 (1992)

[46] J.P.Perdew, K.Burke snd M. Ernzenhof, Phys. Rev. Lett 77, 3865 (1996)

[47] Abdel-Raouf E. and Mohammed V. Sahni Phys. Rev. B 29, 3687 - 3690 (1984)

[48] Thomas Maxisch, Fei Zhou and Gerbrand Ceder Physical review B 73, 104301 (2006)

[49] David Emin, C. H. Seager, and Rod K. Quinn Phys. Rev. Lett. 28, 813 (1972)

[50] A. S. Alexandrov and P. E. Kornilovitch Phys. Rev. Lett. 82, 807 (1999)

[51] E. Iguchi, N. Nakamura and A. Aoki, Philosophical Magazine B, 78, 65 (1998)

[52] Goswami A.Thin film fundamentals (New Delhi: New Age International (P) Ltd .(1996).

[53] Macdonald J R (ed.) Impedance spectroscopy emphasizing solid state materials and systems (New York: Wiley) (1987)

[54] B.Tareev. Physics of Dielectric materials. MIR publishers Moscow (1979)

[55] Cole K.S and Cole R.H, J.Chem.Phys.9 (194) 131

[56] Jonscher, A.K., Dielectric Relaxation in Solids (London: Chelsea Press) (1983).

[57] B.D Cullity.Elements of X–Ray Diffraction.2ndEdn.Addison-Wesley.INC.(1978)

[58] Vitalij K.Pechrsky Peter Y.Zavalij Fundamentals of Powder Diffraction and Structural Characterization of Materials. Springer. (2005).

[59] Dieter K. Schroder. Semiconductor material and device characterization. John Wiley 3rd Ed.(2005).

[60] R. N. P. Choudhary,Soma Dutta, Awalendra Kumar Thakur and P. K. Sinha Ferroelectrics, 306, 55 (2004)

Chapter 3

Structural Thermal and Spectroscopic Characterization of Spinel Lithium Manganese Oxide ($LiMn_2O_4$)and its de-lithiated form (λ-MnO_2)

This chapter discusses the synthesis of spinel $Li_xMn_2O_4$ and λ-MnO_2 as well as a detailed account of the investigations on these samples including the influence of the lithium content on the thermal and optical properties of $LiMn_2O_4$. Structural characterization is done using X-ray diffraction (XRD), SEM (Scanning Electron Microscopy) and TEM (Transmission Electron Microscopy). The thermal properties of the samples are evaluated from photoacoustic signal amplitude and phase as a function of modulation frequency in reflection configuration while information of their electronic band structure is obtained from the wavelength dependence of its photoacoustic signal. The presence of Jahn Teller (J-T) active Mn^{3+} in $LiMn_2O_4$ makes it viable for Jahn-Teller distortion and hence, the effect of lithium concentration as well as temperature for its occurrence are studied.

3.1 An Introduction to $Li_xMn_2O_4$

For many years, nickel-cadmium had been the only suitable battery for portable equipments, from wireless communications to mobile computing. Nickel-metal-hydride and lithium-ion batteries emerged in the early 1990s, fighting nose-to-nose to gain customer's acceptance. Today, lithium-ion battery is the fastest growing and most promising battery technology. Rechargeable Li-ion cell is the key component in portable, entertainment, computing telecommunication equipments offering high energy density, flexibility and lightweight design [1-3]. The motivation for using this technology is the fact that Li is the most electropositive as well as the lightest metal that facilitate the design of storage systems with high energy density, good energy-to-weight ratio, no memory effect, long-term cycling stability and high charge/discharge rate capabilities. The most advanced batteries available in the market today are Li-ion and Li-ion polymer batteries. Another important factor affecting the demand for new battery systems is the shift towards the exploitation of alternating energy sources to replace the fossil fuel, which is progressively getting exhausted from the earth. To meet with the constantly increasing energy needs of the developed countries of the world, the utilization of discontinuous energy sources such as solar power, wind power etc require batteries as a storage facility. For this application, batteries require the ability to undergo large number of deep charge /discharge cycles with high efficiency.

The advantage of using Li metal was demonstrated in the year 1970 with the assembly of primary lithium cells. Originally, lithium metal foil was used as anode and an inorganic intercalation compound as cathode in secondary Li-batteries, thus exploiting the low weight and high reactivity of lithium. Safety concerns have led, however, to the replacement of metallic lithium by a Li-insertion compound. The discovery of such materials was crucial in the development of rechargeable Li systems. Thus the concept of Li-ion transfer cells was proposed to solve the problem of corrosion and thermal run away and possible explosion. The key to the successful development of a new generation of lithium batteries depends critically on the creation of new electrodes and electrolyte materials with composition and configuration, that offer high power density, long shelf and cycle life, low cost, and minimal capacity fade and disposal problems.

A lithium ion rechargeable battery is known as a rocking chair battery due to the two-way motion of lithium ions, i. e. between the anode and the cathode through the electrolyte (Figure 3.1). During charging the lithium ions undergo deintercalation from the cathode into the electrolyte and intercalation (process of insertion) of lithium ions from the electrolyte into the anode and vice versa during discharging. Electrochemical reactions consisting of electron and lithium ion insertion into/extraction from a solid matrix with out much destruction of the core structure are called topotactic reactions and the materials for which such reversible reactions proceed are called insertion compounds. These insertion materials comprise the electrodes of Li ion

batteries for better safety and cycle life of the cells. Usually, the cathode materials are air stable lithium metal oxides (LMO) and anode electrodes are carbon materials. The cells are fabricated in discharged state, so that the freshly prepared cells cannot deliver electricity. On charging, Li ions move from positive (cathode) to negative electrode (anode) storing electricity in the solid matrix and on discharging the cells can deliver electricity by the return of lithium ions to the cathode. In other words, the cells are operated with lithium-ion shuttling between positive and negative electrodes. Hence these insertion materials (electrodes) are extremely important in developing the Li-ion batteries.

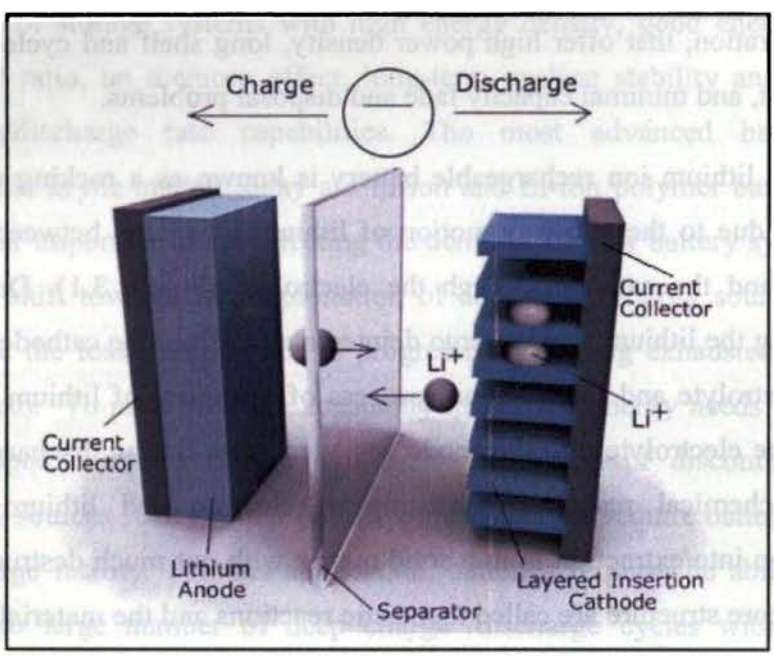

Fig. 3.1 Shows the Li-ion rocking chair battery

The conventionally used LMO cathode is $LiCoO_2$, which acts as the source of Li ions that carries the electric charge through the electrolyte [1,4]. However, $LiMn_2O_4$ is widely recognized as a potential substitute for $LiCoO_2$ and is used in high energy density batteries for high power cell applications [1, 3]. It is exploited very much as a battery cathode in lithium ion cells due to its availability, non-toxicity, and least environmental hazards (eco-friendly 'green' nature)[1,3,5-10] besides cheapness compared to its counterpart materials like $LiCoO_2$ and $LiNiO_2$. The possibility of cycling 0.8 Li per Mn_2O_4 unit electrochemically from its core spinel structure corresponding to a complete utilization capacity has prompted its usefulness in terms of charge-discharge control when employed as cathode in Li-ion batteries. Moreover and more importantly, the high rate capability of the Mn-O system could be advantageous not only for discharge, but also for rapid recharge of the cell. The above features have recently occupied a place of pride among the battery manufactures to utilize the spinel $LiMn_2O_4$ as a Li^+ source electrode for practical high voltage Li-ion technology.

Interest in the spinel $LiMn_2O_4$ as electrode in rechargeable lithium-ion batteries stems from the fact that the lithium ions can be removed (de-intercalated) and reinserted (intercalated) into this compound topotactically [11-13]. This spinel can de-intercalate Li^+ ions at 4.2 volts becoming λ-MnO_2 (spinel structure) and intercalate Li^+ ions at approximately 2.9 V to yield $LiMn_2O_4$. The good voltage regulation during cycling, the excellent electro-chemical reversibility,

and the theoretical specific capacity (148 mAh/g) make the spinel $LiMn_2O_4$ an attractive cathode material.

Moreover, unlike layered structured cobalt oxide materials, all atoms in spinel shaped manganese oxides are connected via genuine chemical bonds with large channels in the lattice for Li insertion and hence they have low discharge capacity and structural stability at moderately high temperature [1]. However, batteries made of $LiMn_2O_4$ electrodes show drastic capacity fading after each charge-discharge cycle which may be due to the instability of the organic based electrolyte in the high voltage region, dissolution of $Li_xMn_2O_4$ electrode in the electrolyte as Mn^{2+} ions and onset of Jahn-Teller effect in deeply discharged $LiMn_2O_4$ electrodes [11].

3.2 Structure of $LiMn_2O_4$

The compound $LiMn_2O_4$ belongs to the normal spinel structure with a general formula AB_2O_4. There are eight occupied tetrahedral (or A) sites and 16 occupied octahedral (or B) sites in a unit cube (Figure 3.2). In the $LiMn_2O_4$ spinel, the Li ions occupy tetrahedral sites [13] each surrounded by 4oxygen ions; the Mn ions occupy octahedral sites, each surrounded by six oxygen ions.

Here the oxygen anions form the face centered cubic packing. For every 4 oxygen anions there are four octahedral sites and eight tetrahedral sites. Out of these twelve, only three are needed to fill the cat ions of the above formula. In the normal spinel structure, A cat ions are in the tetrahedral voids and B are in the octahedral voids.

The spinel phase of $LiMn_2O_4$ belongs to the Li-Mn-O system that has been studied in detail as an insertion electrode for secondary lithium cells. In the system the lithium ions occupy the 8a tetrahedral interstitials and manganese cations occupy 16d octahedral interstitials of a cubic close packed array constructed by the oxygen anions located at the 32e positions of the Fd 3m space group [13,14] [In a crystal, point group symmetry operations can be combined with translational symmetry elements provided they are compatible. Such combinations are called space groups]

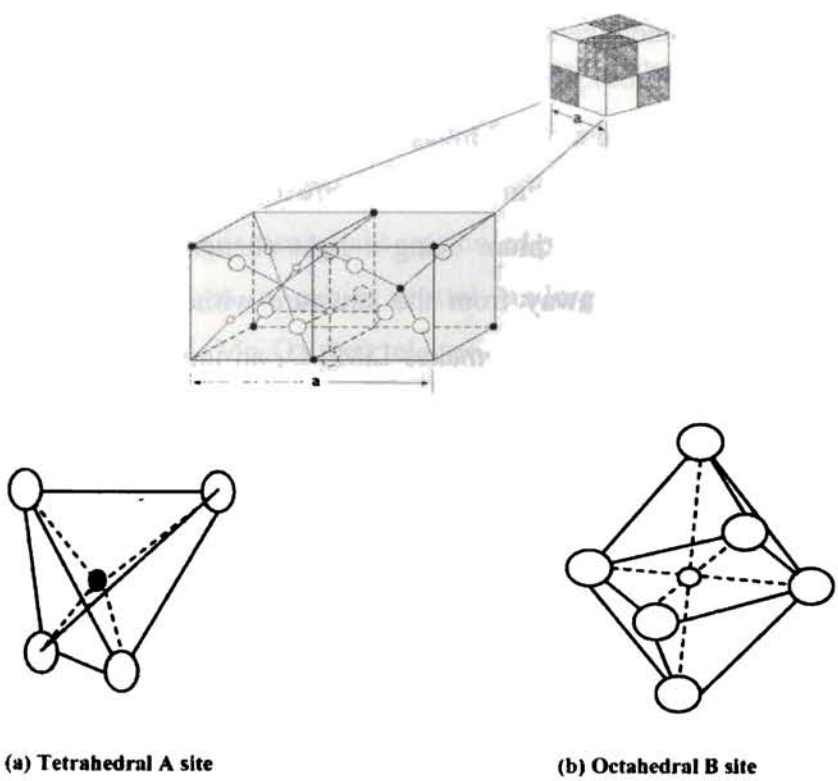

Fig. 3.2 Cubic spinel structure of $LiMn_2O_4$

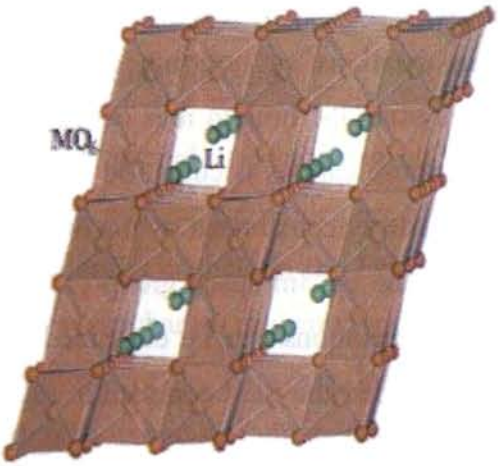

Fig. 3.2a The spinel-like structure with MO_6 octahedral and Li atoms taking tetrahedral positions

The spinel structure of $LiMn_2O_4$ is composed of MnO_6 octahedral framework (Figure3.2a) within which there are tetrahedral channel sites for Li to occupy [15]. Lithium being a light element can be easily inserted into or taken away from the structure without causing any structural changes. This aspect makes $LiMn_2O_4$ an important material from the point of application as electrode material in rechargeable lithium batteries.

The electronic structure of any material is arguably its most important signature, which is responsible for most of its properties and dependent on several factors including its crystal structure and bond formation. Since the Mn-ion is in octahedral symmetry, the electronic structure of $Li_xMn_2O_4$ compound is governed by a strong hybridization between the Mn d and O p atomic orbitals where its d_{z^2} and $d_{x^2-y^2}$ atomic orbitals directly overlap with the p_x, p_y and p_z.

orbitals of oxygen along the octahedral directions. This σ overlap creates the e_g bands, of which the bonding band, e^b_g, has a predominant oxygen p-character and the antibonding band, e^*_g, has a predominant metallic d-character. The remaining d_{xy}, d_{yz} and d_{xz} orbitals point away from oxygen and have only a minor π overlap- giving rise to the nonbonding t_{2g} bands. In $Li_xMn_2O_4$ spinels, the Fermi level E_F lies within the nonbonding t_{2g} bands. Similarly, the overlap of oxygen-p with Mn-p and oxygen-p with Mn-s gives rise to t_{1u} and a_{1g} bands, respectively. There is considerable amount of intermixing between e^b_g, t_{1u} and a_{1g} bands and are collectively known as O 2p bands because of their predominant oxygen-p character [16,17,32]. The band gap of $Li_xMn_2O_4$ is reported to be around 1 eV [17]. However, there are also other absorption peaks apart from the fundamental absorption edge [18,19] Berg et al have derived that when a cubic crystal undergoes a tetragonal JT distortion as in $LiMn_2O_4$ their electronic structure gets modified in the form of splitting up of each Mn t_{2g} and Mn e^*_g band into two [20]. Another challenge in the study of Li transfer in LMOs is its effect on the band structure of LMO [21]. In the rigid band picture, Li intercalation into LMO raises the host Fermi level due to band filling of the host material. On the contrary, in the non-rigid band picture, Li intercalation does not affect the host Fermi level, but its density of states translates to lower energies due to electron transfer from lithium to oxygen [17].

3.2.1 Layered Lithium Metal Oxide Li_xMO_2

The layered $LiMO_2$ are traditional cathode materials that have been thoroughly studied experimentally and theoretically. The layered structure can be envisioned as two interpenetrating fcc lattices, one consisting of oxygen, and the other consisting of alternating (111) planes of Li and Transition Metal (TM) ions (Figure.3.3) [22]. In the $R\bar{3}m$ space group the Li and the metal ions remain fixed in the ideal rock salt positions, but the whole (111) oxygen planes may relax in the (111) direction giving rise to different slab spaces that affect lithium mobility.

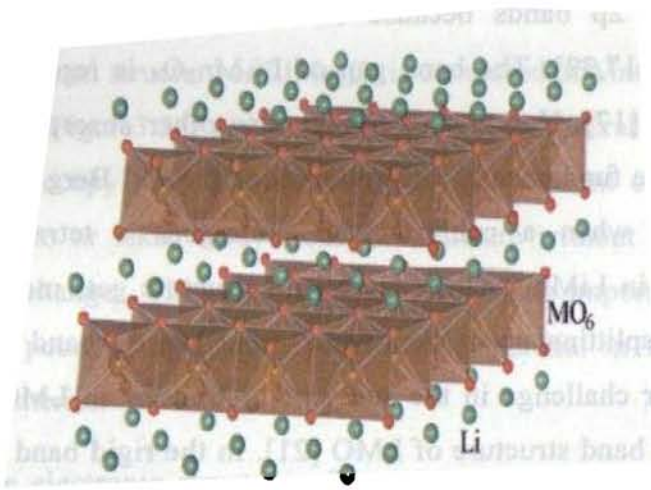

Fig. 3.3 The layered structure with MO_6 octahedral and lithium atoms.

3.3 Lithium Extraction / Insertion Mechanism in the Spinel $LiMn_2O_4$

The compound $LiMn_2O_4$ is a stable phase in the middle of the discharge curve of λ-MnO_2. On further reduction, the material converts into $Li_2Mn_2O_4$ [23]. The phases and phase transitions during reduction

from λ-MnO_2 to $LiMn_2O_4$ have been the focus of debate in many publications [24]. From $LiMn_2O_4$ to $Li_2Mn_2O_4$, there is a distinct first order phase transition. When Li ions are inserted into the spinel host structure, they occupy the octahedral 16csites. Since this site is face sharing with the 8a tetrahedra, the Li ions in the tetrahedral site are instantly displaced into the vacant 16c site, causing a first-order phase transition. When the Mn^{3+} (d^4) concentration increases, Jahn-Teller (JT) distortion also occurs with a gain in energy equal to ε (Figure.3.4) The crystal symmetry decreases from cubic(c/a = 1.0) to tetragonal (c/a ~ 1.16); this imposes a large strain on the individual spinel particles, that ultimately results in electromechanical grinding; the reversibility of this phase transition is poor [24,40]. However, it has been shown in recent studies that significant strain effects and nano-sized regions are introduced into the $LiMn_2O_4$ material by ball milling and possibly partial oxidation, resulting in a good utilization of the material on Li insertion to $Li_2Mn_2O_4$ [24,41]. Figure 3.4 shows a schematic representation of the splitting of the Mn 3d orbital in Mn^{3+} (d^4). The situation is quite different during the removal of Li from the $LiMn_2O_4$ structure; the unit cell volume decreases gradually and isotropically as the Li-ion concentration decreases. The removal of Li from $LiMn_2O_4$ occurs through a two - step reaction around 4V;two potential plateaus can be discerned in the curve, separated by 100-150mV. Rigorous studies have also shown that the material goes through at least one two–phase region during charge /discharge [23,24]. The structure of these intermediate phases are not yet determined, but single-crystal studies have shown that super structures may occur in the upper part of potential curve (23, 24,44).

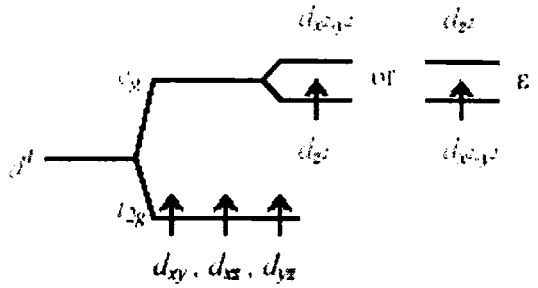

Fig. 3.4 --Schematic representation of the splitting of the Mn 3d orbital in Mn^{3+} (d^4).

3.4 Synthesis

3.4.1 $Li_xMn_2O_4$

A large number of methods are available for the preparation of $LiMn_2O_4$ spinel. In this work stoichiometric $LiMn_2O_4$ is prepared by direct solid-state reaction of Li_2CO_3 (99.99%pure) and $MnCO_3$ (99.99% pure) in the molar ratio 10:40 [25]. The reactants are pre-dried at 200°C in separate crucibles for 5 hours. The de-hydrated reactants are weighed out using an electronic balance. Then the reactants are mixed thoroughly and finely ground under acetone in an agate mortar. The organic solvent acetone in this mixture gets evaporated off. The mixture is then calcined at 600°C for 12 hours to get rid of CO_2. After cooling to room temperature the mixture is again ground under acetone in the agate mortar. The sample so obtained is pelletised with a load of 5 T. The compound is then sintered at 800°C for 24 hours in air and cooled to room temperature at about 0.33°C/min [26]. Similarly $Li_{0.8}Mn_2O_4$, $Li_{0.9}Mn_2O_4$, $Li_{1.1}Mn_2O_4$, $Li_{1.2}Mn_2O_4$, samples are prepared by changing the molar ratio of Li_2CO_3 and $MnCO_3$, to 8:40, 9:40 .11:40

and 12:40 respectively. The chemical reaction, taking place can be written as

$$2Li_2CO_3 + 8\,MnCO_3 + 3O_2 \longrightarrow 4LiMn_2O_4 + 10CO_2$$

The grinding and sintering are repeated until the product obtained is a fine-grained material of micrometer size. The compound obtained is characterized immediately after synthesis by X-ray diffraction analysis [model: 1710 Rigaku]. The phase purity of the material was confirmed by the XRD analysis.

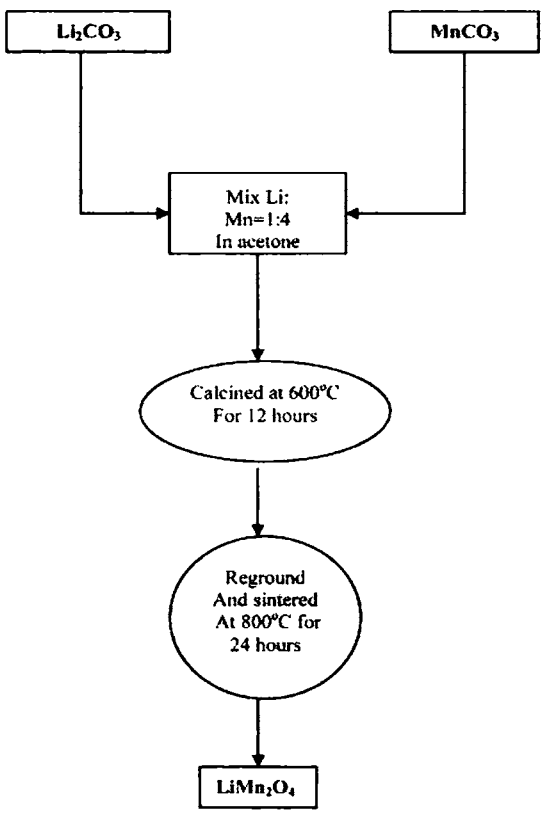

Fig.3. 5 Route map of the synthesis of $LiMn_2O_4$

3.4.2 λ-MnO_2 Spinel

λ-MnO_2 spinel is prepared by chemical delithiation from $LiMn_2O_4$ [25]. For this, $LiMn_2O_4$ is treated with a solution of HCl-H_2O (1:33V/V) and stirred for 5hours at room temperature using a magnetic stirrer arrangement.

The lithium composition and lattice constant of λ-MnO_2 depend not only on the kind and concentration of the acid solution used, but also on the synthesis conditions of the original $LiMn_2O_4$, such as sintering temperature and cooling rate.

The precipitate is filtered and washed several times with distilled water and dried. The structural analyses of both the samples are done by X-ray diffraction. The samples are pelletised by applying different pressures.

A temperature above 800°C may affect the structural stability of the spinel. Moreover, the final product may contain impurity phases, irregular morphology and larger particle size. High calcination temperature may affect the cycling properties and reduce its electro-chemical features. In general, for the battery applications, it is believed that single phase products with good crystallinity, homogeneity, uniform particle morphology with submicron size distribution and high surface area are considered as the most desired ones in order to achieve higher electrode activity. The synthesis of single-phase products demands lower synthesis temperatures in order to accomplish the above features.

A chemically synthesized sample has several advantages over an electrochemically prepared sample since (a) it has no additives, such as a binder or carbon, which must be treated as impurities in the analysis (b) the experiment can be performed rapidly because there is no need for cell construction and the subsequent charge-discharge processes. However, a very long time is required to get a sample to the equilibrium state.

3.5 Characterization of $LiMn_2O_4$ & λ-MnO_2

3.5.1 X-Ray Diffraction Analysis

The XRD spectra are initially recorded for fine powdered samples of both $LiMn_2O_4$ and λ-MnO_2 to identify them. The intensified planes are marked on the pattern. Figure3.6 shows the XRD diffraction pattern of $LiMn_2O_4$ spinel sintered at 800^0C. The analysis confirms the formation of the spinel structure without any impurity phase. Considering the intensities and positions of the peaks we observe a good agreement between the results and those reported by other workers [14,16,40].

The XRD spectrum of this sample contains at least 8 peaks, well in agreement with the spinel structure of $LiMn_2O_4$. From the XRD pattern of the powder sample the lattice parameter is calculated. The lattice parameters vary slightly corresponding to the variation in the d values of $LiMn_2O_4$ and λ-MnO_2 as expected.

Table 3.1 Lattice constants of $LiMn_2O_4$ and λ-MnO_2

Sample	d (111)plane (A°)	a(A°)
$LiMn_2O_4$	4.782	8.282
λ-MnO_2	4.694	8.149

The porosity of the samples can be calculated as

Porosity = [X ray density-Apparent density]/ X ray density

Where X- ray density = n (Molecular Mass/ N)(1/Volume of unit cell)

n = number of molecules per unit cell. N = Avogadro number.

In the present case n = 8. The apparent density of the sample is obtained by dividing the mass of the pellet by its volume.

A single phase of cubic spinel with the space group Fd3m has been confirmed by XRD analysis. The cubic lattice constant of $LiMn_2O_4$ based on the (111) peak is calculated as a = 8.282 A° corresponding to d = 4.782 A°.The λ-MnO_2 obtained is also well indexed by the single phase of the cubic Fd3m with lattice constant 8.129 A^0. The particle size is almost the same as the pristine $LiMn_2O_4$ spinel [14]. The grain size is calculated as 0.251μm. Results indicate that the product obtained immediately after preparation has gained the single- phase spinel structure with out any residual impurities observable from XRD measurements. The sharp peaks indicate the increase in crystallinity and ordering of local structure and release of lattice strain

The XRD pattern of λ-MnO_2 shows a remarkable reduction in intensity and slight broadening of the spinel peaks .The cubic lattice constant obtained was a = 8.1294A° corresponding to d = 4.694A° based on the (111) peak. These results show that there is a reduction in the crystallinity of the material. The mass loss due to lithium extraction is reflected in the smaller value of lattice parameter obtained. The XRD

studies have shown that each material is composed of a single phase with out the presence of detectable Li_2MnO_3, which often contaminates the spinels with high Li/Mn ratios [12].

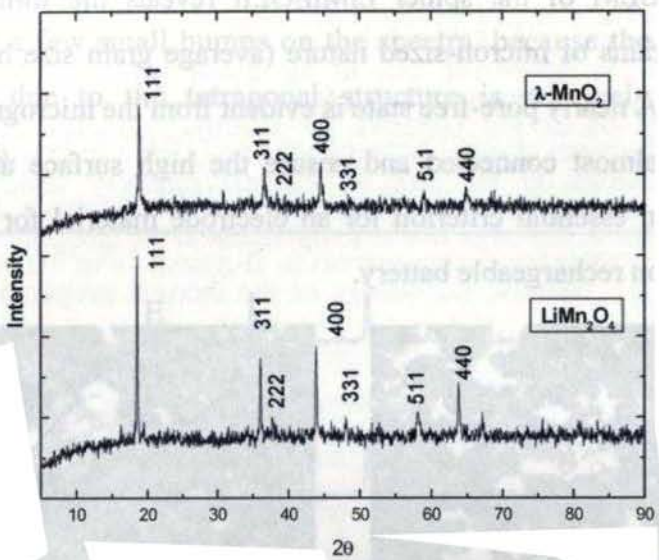

Fig. 3.6 XRD patterns of λ–MnO_2 & $LiMn_2O_4$

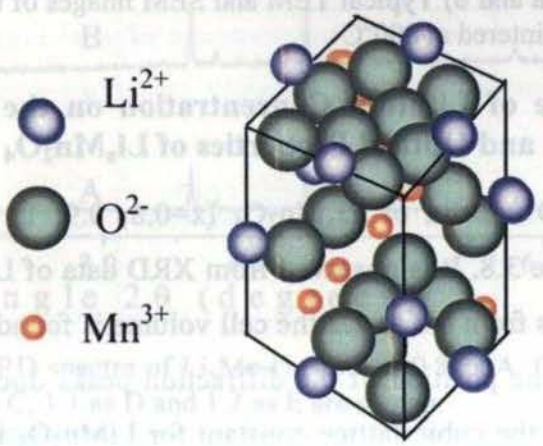

Fig. 3.7 Crystal structure of $LiMn_2O_4$

3.5.2 Electron Microscopy

To measure the physical grain size of the spinel product, the SEM and TEM analysis are carried out. Figure 3.7.1 (a) and (b), show the TEM and SEM of the spinel $LiMn_2O_4$.It reveals the formation of spherical grains of micron-sized nature (average grain size being less than 1μm). A nearly pore-free state is evident from the micrograph. The grains are almost connected and ensure the high surface area. This feature is an essential criterion for an electrode material for the high energy Li-ion rechargeable battery.

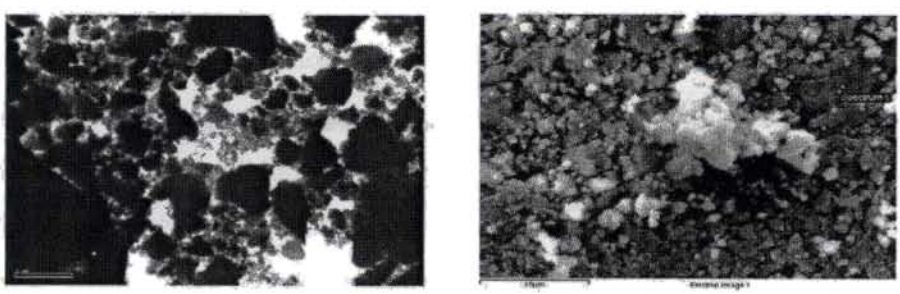

(a) TEM image of $LiMn_2O_4$ **(b) SEM image of $LiMn_2O_4$**

Fig 3.7.1 (a and b) Typical TEM and SEM images of the spinel sintered at 800°C

3.6 Influence of Lithium Concentration on the Structural, Thermal and Optical Properties of $Li_xMn_2O_4$

The XRD spectra of $Li_xMn_2O_4$ (x=0.8, 0.9, 1, 1.1, 1.2) are shown in Figure 3.8. It is observed from XRD data of $Li_xMn_2O_4$ that when x changes from 0.8 to 1.2 the cell volume is found to be almost a constant, as the position of the diffraction peaks does not change with x. In fact, the cubic lattice constant for $LiMn_2O_4$ is determined as 8.242 A^0 and its cell volume is 5.599×10^{-28} m^3. The additional

peaks appearing for $Li_{1.1}Mn_2O_4$ and $Li_{1.2}Mn_2O_4$ can be ascribed to the appearance of tetragonal structure, as a structural distortion, in the cubic structure. Moreover, in the case of $Li_{1.1}Mn_2O_4$ unlike that of $Li_{1.2}Mn_2O_4$, these additional peaks are not easily observable except for a few small humps on the spectra, because the structural distortion due to the tetragonal structure is relatively small in $Li_{1.1}Mn_2O_4$.

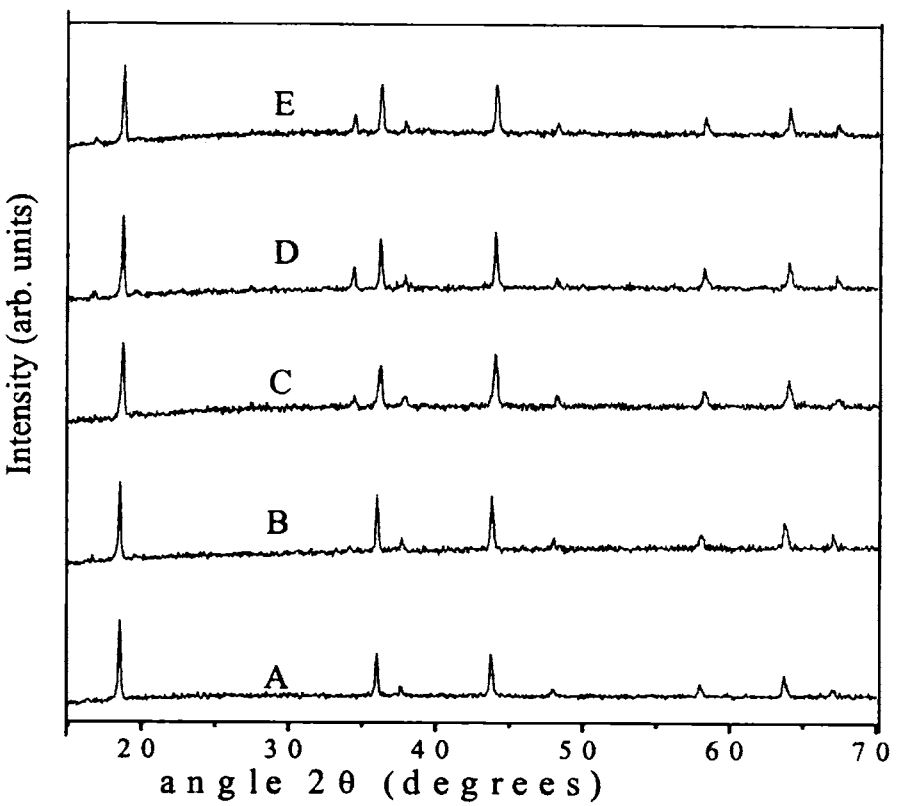

Fig. 3.8 XRD spectra of $Li_xMn_2O_4$ with x=0.8 as A, 0.9 as B, 1.0 as C, 1.1 as D and 1.2 as E are shown.

3.7 Thermal Properties of $Li_xMn_2O_4$

Information about the thermal properties of $LiMn_2O_4$ is of paramount importance since its limited Li cycling and storage performances at elevated temperatures is a key issue in its commercial use [26, 27,28]. Moreover, one of the major issues confronting the development of Li ion batteries for Electric Vehicles and Hybrid Electric Vehicles is the risk of thermal runaway under abusive conditions due to the large rise in temperature at the electrodes or in the electrolyte [1]. Besides, knowledge of the thermal properties such as thermal diffusivity, specific heat and thermal conductivity can throw light on the structural properties of $Li_xMn_2O_4$ materials. The fundamental quantity that enters into heat transfer situations, not at steady state, is thermal diffusivity, which is a measure of how quickly a body can change its temperature, which increases with the ability of the body to conduct heat (thermal conductivity) and decreases with the amount of heat required to change the temperature of the body (specific heat). Therefore, these three parameters are of vital importance in the context of devices under actual operating conditions when subjected to a thermal load.

3.7.1 Determination of Thermal Diffusivity of $Li_xMn_2O_4$ using PA Technique

The thermal diffusivity values are obtained using Photoacoustic (PA) technique with a homemade PA cell employed in reflection configuration as mentioned in chapter 2. Light beam from a 20 mW He-Ne laser (632. 8 nm) is modulated using a mechanical chopper (SR

540), which is allowed to fall on a sample that is fixed to the PA cell. The modulation frequency is varied from 5 Hz to 400 Hz and the corresponding modulated pressure signal generated is detected by a commercial condenser microphone. The output signal from the microphone is fed to a lock-in-amplifier (SR 830) through a pre-amplifier (SR 550). All the instruments are computer controlled using the RS-232 port of a PC. The experimental setup is standardized using commercially available Si wafer whose thermal diffusivity is calculated to be 0.81×10^{-4} m^2s^{-1} which is in perfect agreement with the standard values.

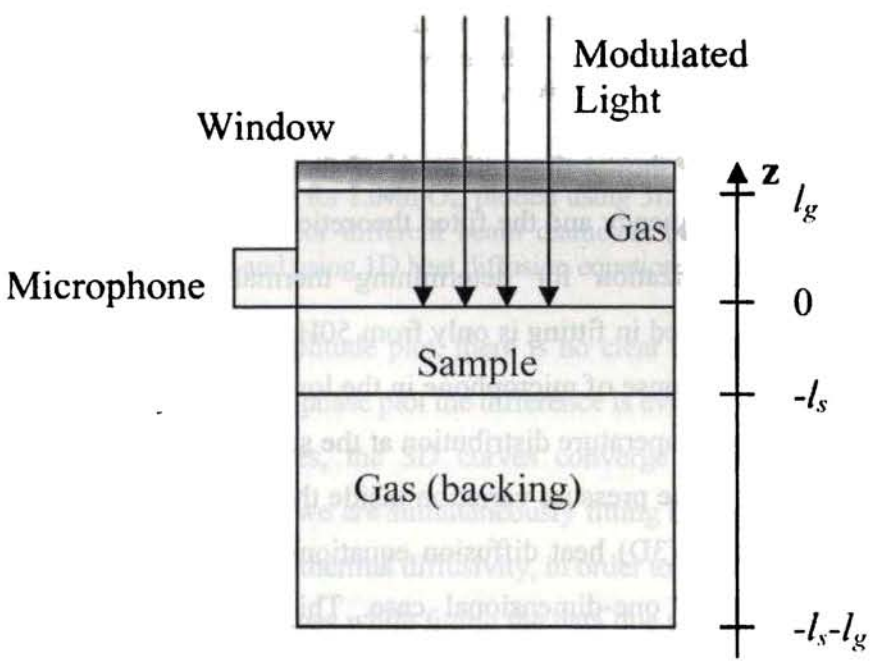

Fig .3.9 Schematic diagram of the PA cell arrangement

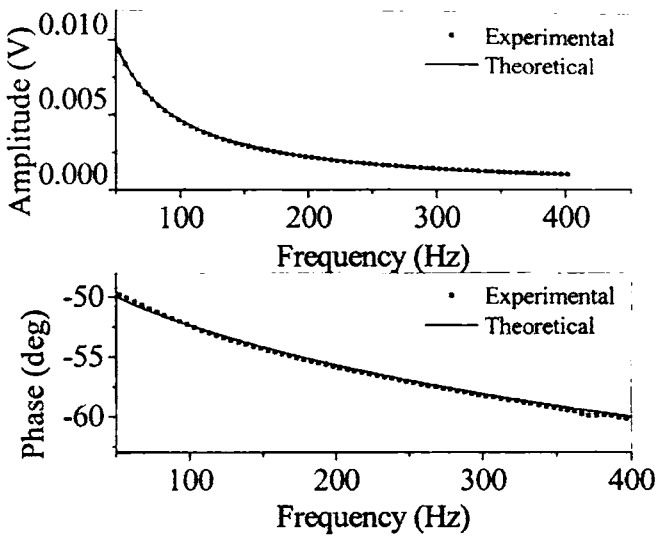

Fig. 3.10 The experimentally obtained and theoretically fitted amplitude and phase variations of $LiMn_2O_4$ with Frequency are given

Figure 3.10 shows the variation of amplitude and phase for $LiMn_2O_4$ with frequency and the fitted theoretical curve obtained using chi-square minimization for determining thermal diffusivity. The frequency range used in fitting is only from 50Hz to 400 Hz, in order to avoid any bad response of microphone in the low frequency region. For determining the temperature distribution at the sample surface, which is used to calculate the pressure variation inside the PA cell, the complex three dimensional (3D) heat diffusion equations are solved instead of the much simpler one-dimensional case. This is done taking into account of the spot size (~4mm) used in the experiment and thereby avoiding any error that can arise from the 3D effects while fitting the amplitude and phase for determination of thermal diffusivity [29]. The

3D effect on the PA signal for various spot sizes is shown in Figure 3.11 for the case of $LiMn_2O_4$.

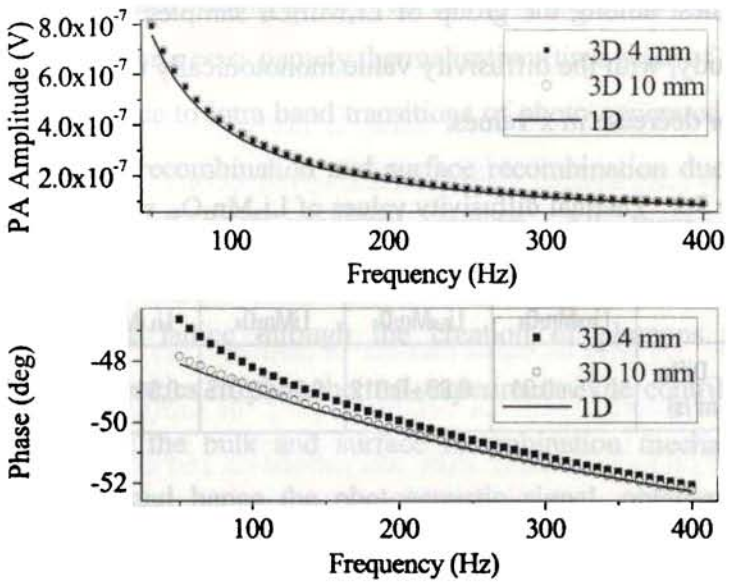

Fig. 3.11 The variation of PA amplitude and phase with respect to frequency for $LiMn_2O_4$, plotted using 3D heat diffusion equation for different beam diameters (4 mm and 10 mm) and using 1D heat diffusion equation.

Though in the amplitude plot, there is no clear difference between 1D and 3D theory, in the phase plot the difference is evident. It is observed that for larger spot sizes, the 3D curves converge towards the one-dimensional case. Since we are simultaneously fitting both amplitude and phase plots for obtaining thermal diffusivity, in order to minimize the error in thermal diffusivity values while fitting the data due to limited spot size, we have used the 3D thermal diffusion equations. The thermal diffusivity values of $Li_xMn_2O_4$ (x=0.8,0.9,1,1.1,1.2) for various values of x are tabulated in Table 3.2 (as per the Figures3.13a, 3.13b, 3.13c, 3.13d,and

3.13e) and their variation is shown graphically in Figure 3.12 for better understanding. It can be seen that thermal diffusivity of $LiMn_2O_4$, i.e. x=1, is the highest among the group of $Li_xMn_2O_4$ samples considered in the present study, with the diffusivity value monotonically decreasing with an increase or decrease in x values.

Table 3.2 Thermal diffusivity values of $Li_xMn_2O_4$, with x=0.8, 0.9, 1.0, 1.1 and 1.2 are given

	$Li_{0.8}Mn_2O_4$	$Li_{0.9}Mn_2O_4$	$LiMn_2O_4$	$Li_{1.1}Mn_2O_4$	$Li_{1.2}Mn_2O_4$
Thermal Diffusivity (10^{-4} m^2/s)	0.75±0.01	0.86±0.012	0.94±0.015	0.81±0.012	0.61±0.01

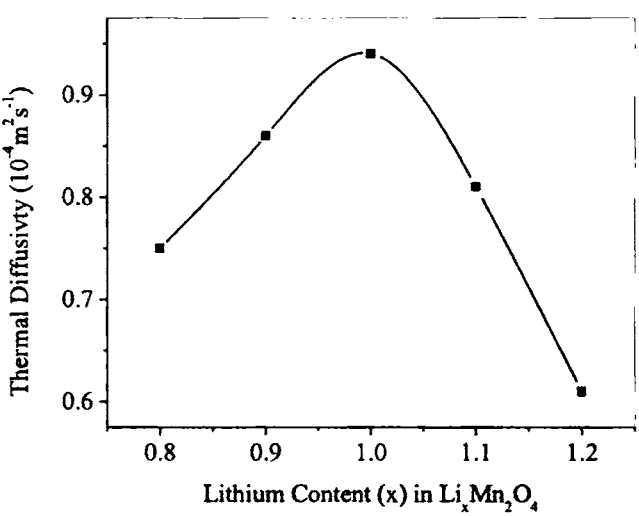

Fig. 3.12 Variation of thermal diffusivity with respect to Li content in $Li_xMn_2O_4$

The heat generation and transport mechanisms in $Li_xMn_2O_4$ can be explained on the basis of those in semiconductors due to the fact that $LiMn_2O_4$ is a small-polaron semiconductor since the e_g electrons on Mn^{3+}

ions are trapped in local lattice relaxations and, as a result, their mobility carries an activation energy [30]. The heat generation due to absorption in semiconductors when irradiated with an intensity modulated light beam arises due to three processes namely thermalisation (time scale of the order of pico seconds) due to intra band transitions of photo-generated carriers, nonradiative bulk recombination and surface recombination due to inter band transitions of photo-generated carriers. All these different mechanisms finally result in the creation of heat energy, which is then transferred to the lattice through the creation of phonons. At low modulation frequencies of photothermal experiments, the contribution to the heat flow by the bulk and surface recombination mechanisms is negligibly small and hence the photoacoustic signal, obtained in this experiment, which employs low modulation frequencies, is solely due to the thermal wave component of the phonon-assisted heat conduction process [39]. This phonon assisted heat conduction is adversely affected by phonon-phonon interactions, phonon scattering by imperfections and at boundaries. Moreover, recent studies on $LiMn_2O_4$ have shown that the phonons due to the vibrational modes of $LiMn_2O_4$ are due to the complex movements involving all the atoms of the crystal structure rather than due to individual LiO_4 tetrahedron vibrational modes and MnO_6 octahedron vibrational modes [32].

From the fact that thermal diffusivity value of $LiMn_2O_4$ is the maximum among $Li_xMn_2O_4$ samples, it can be inferred that the crystal structure is less distorted at x=1 for $Li_xMn_2O_4$, because thermal diffusivity value can be treated as a direct measure of phonon group velocity and

phonon scattering. That is, the higher the phonon scattering, the lower will be the phonon group velocity and hence the lesser will be the thermal conductivity and diffusivity values [26]. The delithiated form of $Li_xMn_2O_4$, λ-MnO_2, is considered to be an ionic crystal having Mn^{4+} in tetravalent state. On the other hand, it has been observed that Li^+ in $LiMn_2O_4$ is fully ionized which demands a reduction in the valency of Mn from 4 to 3.5 which is believed to be achieved by reducing 50% of Mn^{4+} ions in λ-MnO_2 to Mn^{3+} ions. In fact, $LiMn_2O_4$ can be considered as $LiMn^{3+}Mn^{4+}O_4$ with an equal number of isotropic $Mn^{4+}O_4$ octahedra and Jahn-Teller-distorted $Mn^{3+}O_4$ octahedra [17]. In $Li_xMn_2O_4$, for $x \leq 1$, Li cations are on 8a tetrahedral sites, Mn cations on 16d octahedral sites and O anions on 32e positions which give rise to a cubic spinel structure. In fact, $Li_xMn_2O_4$ can be represented by a supercell as $[(Li_8)^{8a}\ (Mn_{16})^{16d}\ (O_{32})^{32e}]$ with clear representation of the number and position of each type of atom in it[31]. An important feature of the spinel structure is that each 8a tetrahedron shares all four faces with 16c octahedra. The maximum tetrahedral-site occupancy is 50% as in $LiMn_2O_4$ which corresponds to x=1 and brings more structural symmetry to this structure compared to $Li_xMn_2O_4$, with $x<1$. However, when $x>1$, in addition to the 8a tetrahedral sites, the vacant 16c octahedral sites also get occupied with Li ions [27] which can be represented in the supercell model as $[(Li_8)^{8a}\ (Li_y)^{16c}\ (Mn_{16})^{16d}\ (O_{32})^{32e}]$ with y taking values from 1 to 8. This is consistent with our observation that the deviation in the XRD pattern from the cubic spinel structure starts around x=1 as shown in Figure 3.8 It is quite evident in the XRD pattern that for x=1.1 and 1.2 in $Li_xMn_2O_4$, additional peaks at 16.8^0 and 34.5^0, other than that of cubic spinel structure, appear. It is supposed

that these extra peaks correspond to the Li occupancy of the octahedral, interstitial 16c sites in addition to the 8a octahedral sites, suggesting that the crystal structure is in slightly mixed phase. The filling up of vacant 16c sites by Li ions along with the complete transfer of Li ions from 8a sites to 16c sites results in the tetragonal structure of $Li_2Mn_2O_4$. Therefore, when $x<1$ in $Li_xMn_2O_4$, less than 50% of the available 8a sites are filled by Li ions and when $x>1$, in addition to the 8a sites, 16 c interstitial sites are also occupied with Li ions, both effects causing a reduction in symmetry and are sources of defects. The phonon scattering and a subsequent decrease of phonon group velocity decreases with crystal symmetry and increases with defects. Thus, it can be argued that the crystal structure of $Li_xMn_2O_4$ with maximum symmetry and minimum defects is that with $x=1$ which corresponds to $LiMn_2O_4$. Therefore, it is quite evident why the thermal diffusivity of $LiMn_2O_4$ is greater than other samples in the range of Li content studied in this work.

The cause of reduction of thermal diffusivity upon Li deintercalation of $LiMn_2O_4$ is attributed to the increase in phonon scattering due to reduction in crystal symmetry [26]. From the results, it can be deduced that the thermal diffusivity of $LiMn_2O_4$ is the maximum among $Li_xMn_2O_4$ ($0<x<1.2$) and decreases steadily as the Li concentration decreases and reaches a minimum for λ-MnO_2 [42]. The variation in thermal diffusivity values with Li content is significant due to the fact that during the actual operation of a Li ion battery, thermal diffusivity of the $Li_xMn_2O_4$ cathode will be increasing with respect to its Li content. In other words, thermal diffusivity of Li battery cathode (λ-MnO_2) will be increasing during Li

intercalation, which happens during Li ion battery discharging. Similarly, thermal diffusivity of Li ion battery cathode ($LiMn_2O_4$) decreases during Li ion battery charging as Li is deintercalated from it.

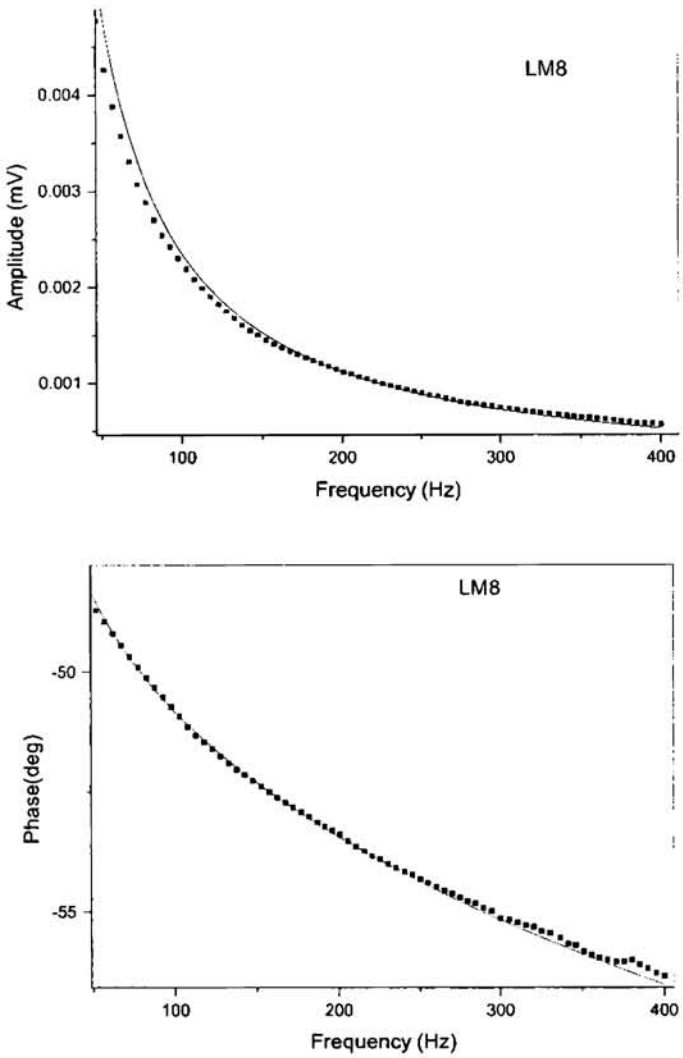

Fig. 3.13a. The experimentally obtained and theoretically fitted amplitude and phase variation of $Li_{0.8}Mn_2O_4$ with frequency

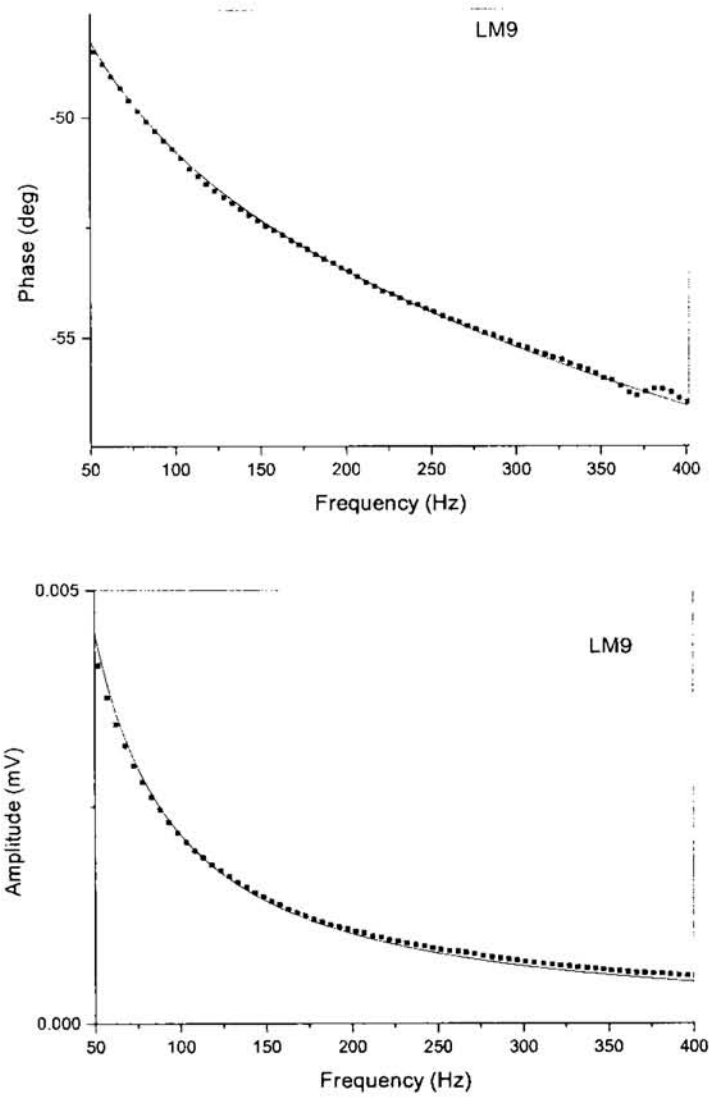

Fig 3.13 b. The experimentally obtained and theoretically fitted amplitude and phase variation of $Li_{0.9}Mn_2O_4$ with frequency

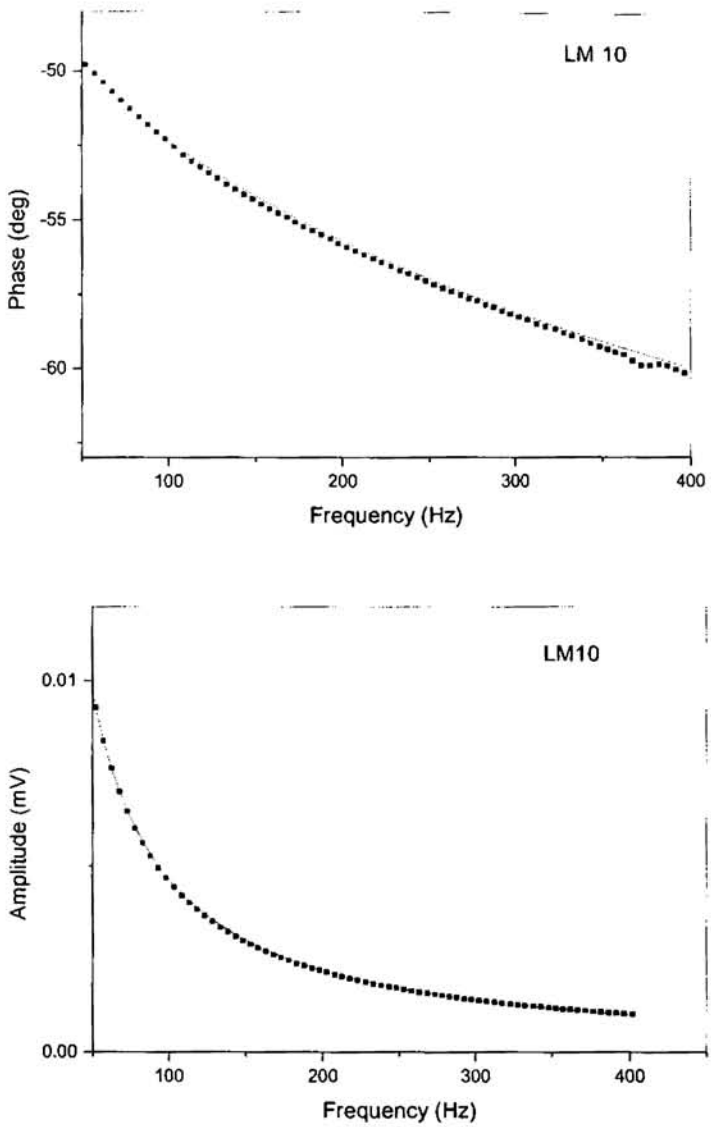

Fig. 3.13c The experimentally obtained and theoretically fitted amplitude and phase variation of $LiMn_2O_4$ with frequency

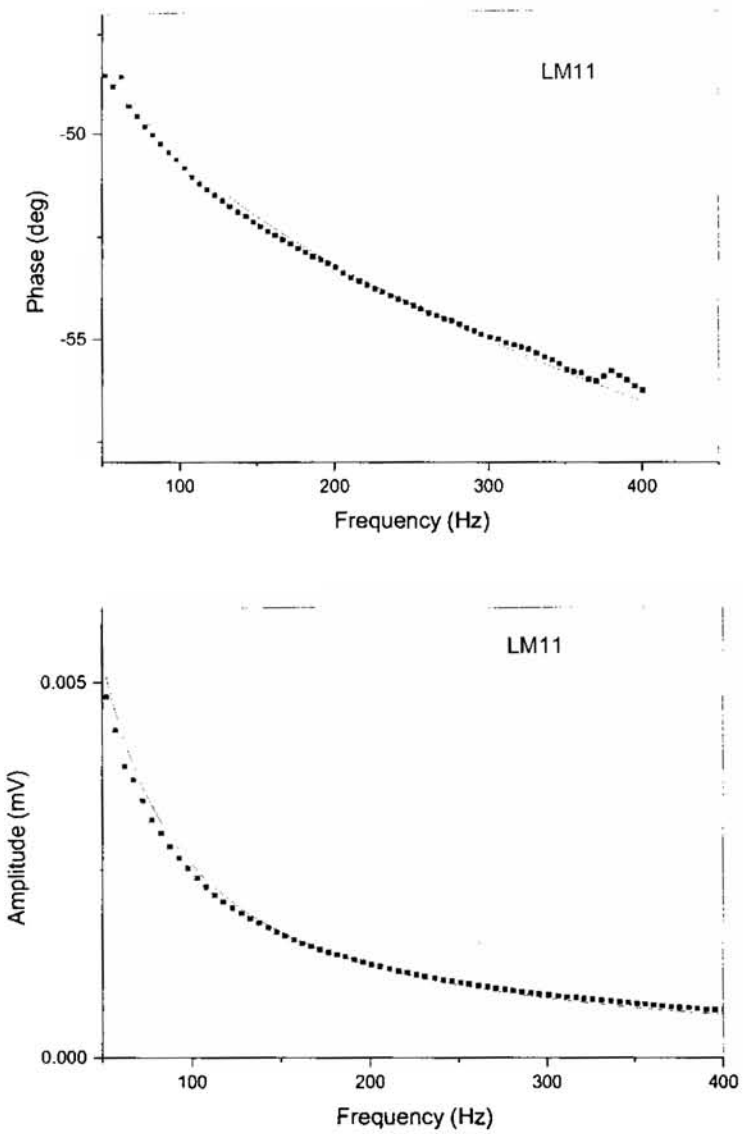

Fig. 3.13d The experimentally obtained and theoretically fitted amplitude and phase variation of $Li_{1.1}Mn_2O_4$ with frequency

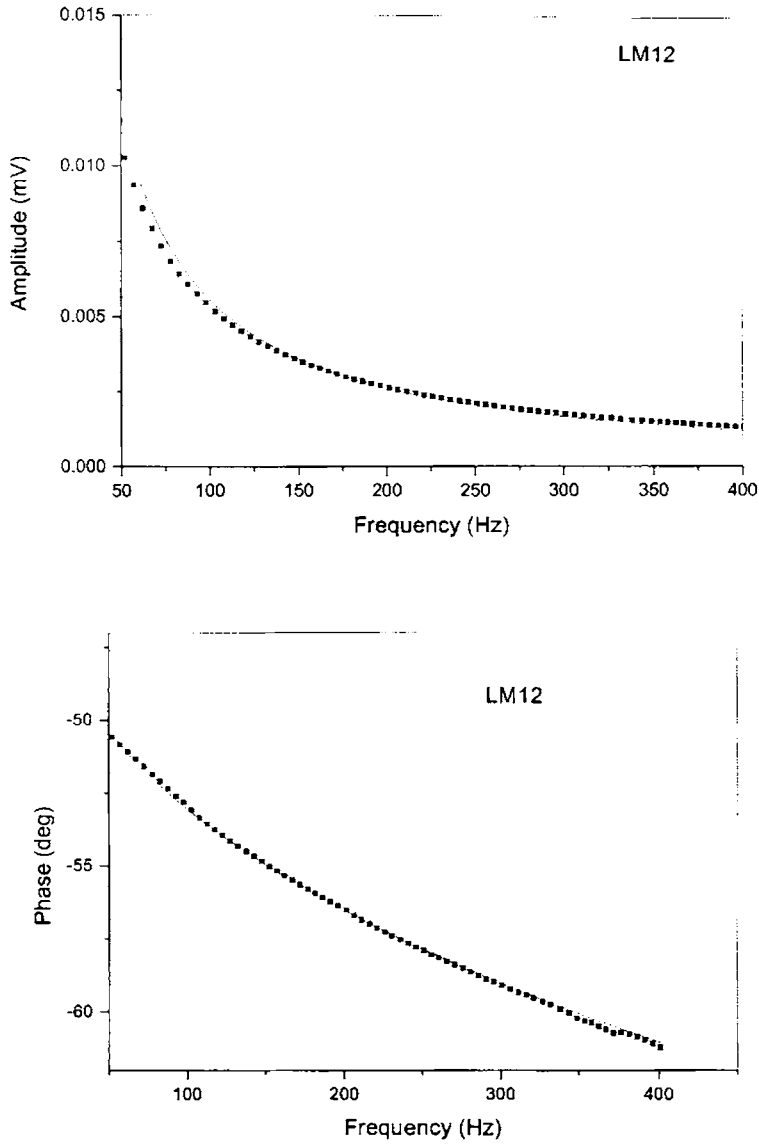

Fig. 3.13e The experimentally obtained and theoretically fitted amplitude and phase variation of $Li_{1.2}Mn_2O_4$ with frequency

3.8 Jahn-Teller Distortion Studies on $Li_xMn_2O_4$

In the late 1930's Jahn and Teller published a group- theoretical (symmetry based) theorem. It states, "For non-linear molecules, a nuclear configuration which begets an orbitally degenerate occupied state is unstable with respect to one without such orbital degeneracy."[33]. Empirically, it is found that formally octahedral or tetrahedral d^9 complexes are highly distorted and, to a slightly lesser extent, the same is true of high spin octahedral d^4 species also.

As mentioned above$LiMn_2O_4$ has cubic spinel structure (space group $Fd\bar{3}m$), with Li ion on 8a tetrahedral sites, Mn on 16d octahedral sites, and O ions on 32e positions, as the stable phase at room temperature [18,19,26,34]. However, the cooperative Jahn-Teller (JT) distortion in $LiMn_2O_4$ occurring below 290K, which disfigures its cubic phase with tetragonal phase, is an order to disorder, first-order type phase transition [34,35]. This lattice instability due to the JT distortion together with a subsequent volume increase upon Li intercalation into $LiMn_2O_4$ occurring at these not so low temperatures leads to its fracture with a probable loss of electrical contact with the current collector on repeated cycling or over discharging and is a major problem with the commercial use of $LiMn_2O_4$ spinel. In fact, $LiMn_2O_4$ can be equivalently represented as $LiMn^{3+}Mn^{4+}O_4$ with an equal number of isotropic $Mn^{4+}O_4$ octahedra and JT-distorted $Mn^{3+}O_4$ octahedra because only the high spin Mn^{3+} favors dynamic JT distortion. It is also observed that addition of metallic dopants (M) such as Co, Ni etc can reduce the amount of JT distortion in $Li_xM_yMn_{2-y}O_4$

due to the reduction in the number of Mn^{3+} ions because of their substitution by M ions [36]. Moreover, $Li_xM_yMn_{2-y}O_4$ has been reported to have a better cycle life compared to $LiMn_2O_4$. At room temperature, JT effect is pronounced only when the concentration of Mn^{3+} ions exceeds that of Mn^{4+} ions by a critical value. i.e. when $x>1.08$ [23]. Therefore, in $LiMn_2O_4$, where the number of Mn^{3+} ions equals that of Mn^{4+} ions, JT distortion is absent at room temperature. However, JT distortion is found to occur in $LiMn_2O_4$ below the transition temperature, around 290 K [34,35]. The appearance of JT distortion in $Li_xMn_2O_4$ with $x>1.08$ is due to the maximum occupancy of about 50% of 8a tetrahedral sites which is the case with $LiMn_2O_4$ and further addition of Li ions as in $Li_{1.1}Mn_2O_4$ results in the filling up of 16c octahedral sites causing a tetragonal distortion to the cubic structure.

Thermal diffusivities of $Li_{0.9}Mn_2O_4$, $LiMn_2O_4$ and $Li_{1.1}Mn_2O_4$, polycrystalline pellets above and below Jahn-Teller transition temperature, i.e., at 298K and at 280K respectively, are determined using photoacoustic techniques in the reflection configuration. The experimental setup is the same as mentioned previously in the chapter2. The low temperature measurements are done by keeping the PA cell in an ice bath inside a thermocole box and the temperature is allowed to stabilize prior to the measurement. During the measurement (20 minutes approximately per scan) the temperature shows a fluctuation of only one degree, which will not affect the measurement as the samples are well below the transition, point 290K.

Figures 3.14 and 3.15 show experimentally obtained and theoretically fitted curves of amplitude and phase variation of $LiMn_2O_4$ with frequency at room temperature (298 K) and at low temperature (280 K) respectively. In order to account for the 3 dimensional (3D) effects due to the limited spot-size of the excitation beam (~4mm), the complex 3D heat diffusion equations are solved for determining the temperature distribution at the sample surface, thereby avoiding errors on thermal diffusivities [29]. Simultaneous fitting of the amplitude and phase data minimizes error on the calculated thermal diffusivities. The thermal diffusivities of $Li_xMn_2O_4$ at room temperature (as per figures3.13b and3.13d) and at low temperature (as per figures 3.16 and 3.17) are shown in Table 3.3 and are graphically shown in figure 3.18

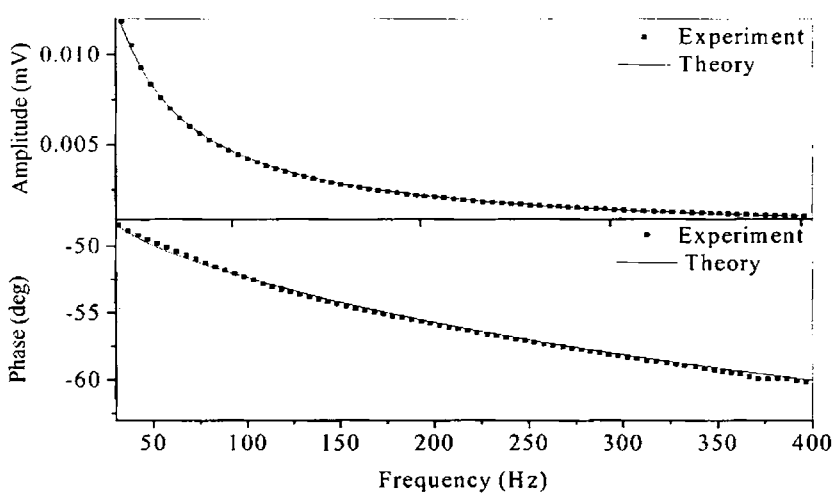

Fig.3.14 The experimentally obtained and theoretically fitted amplitude and phase variation of $Li_xMn_2O_4$ (x=1) with frequency for 298 K.

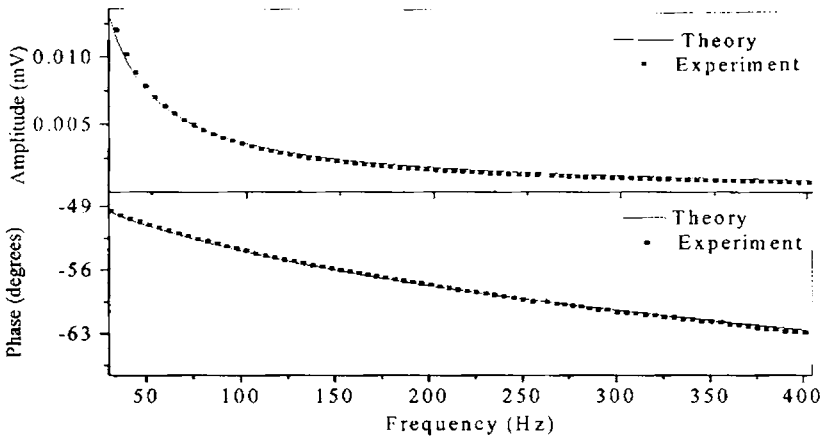

Fig. 3.15 The experimentally obtained and theoretically fitted amplitude and phase variation of $Li_xMn_2O_4$ (x=1) with frequency for 280 K.

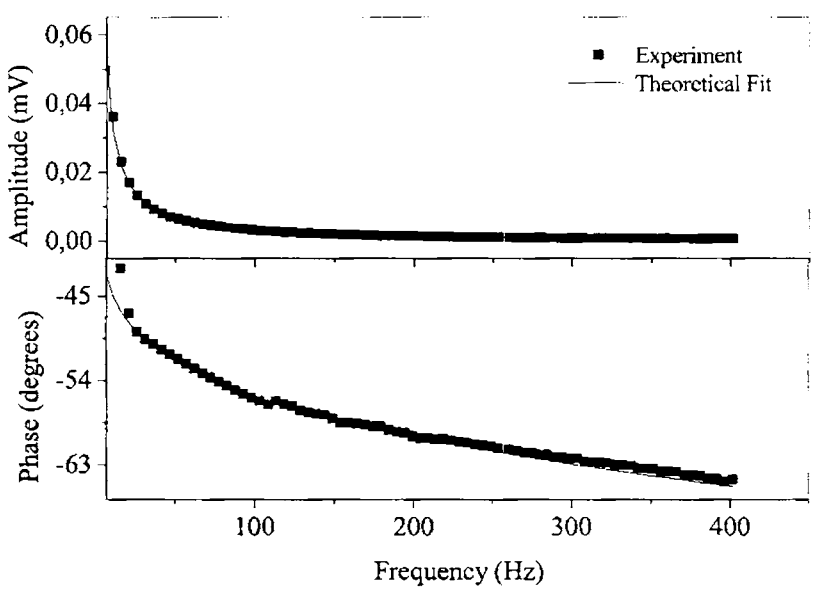

Fig. 3.16 The experimentally obtained and theoretically fitted amplitude and phase variation of $Li_xMn_2O_4$ (x=0.9) with frequency for 280 K.

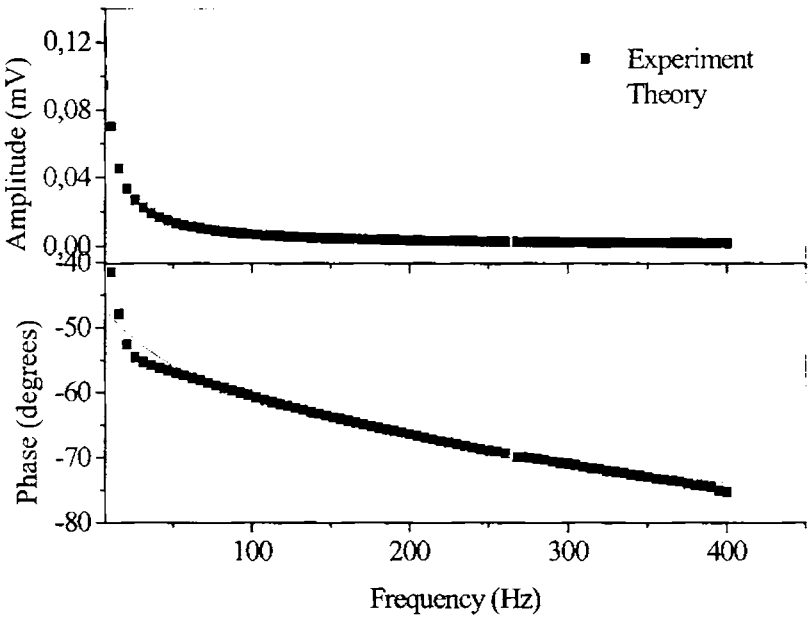

Fig. 3.17 The experimentally obtained and theoretically fitted amplitude and phase variation of $Li_xMn_2O_4$ (x=1.1) with frequency for 280 K.

Table 3.3 Thermal diffusivities of $Li_{0.9}Mn_2O_4$, $LiMn_2O_4$ and $Li_{1.1}Mn_2O_4$ above and below JT transition temperature

	$Li_{0.9}Mn_2O_4$	$LiMn_2O_4$	$Li_{1.1}Mn_2O_4$
Thermal Diffusivity (10^{-4} m^2/s) at 298 K	0.86±0.012	0.94±0.015	0.81±0.012
Thermal Diffusivity (10^{-4} m^2/s) at 280 K	0.71±0.01	0.75±0.017	0.44±0.006

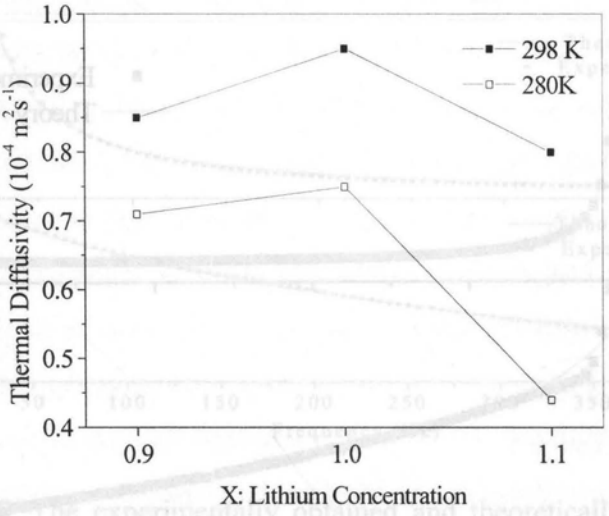

Fig. 3.18 Variation of thermal diffusivity with Li content for 298 K and 280 K

The maximum thermal diffusivity for $LiMn_2O_4$ among $Li_xMn_2O_4$ samples under investigation shows that its crystal structure is less distorted, since thermal diffusivity is a direct measure of phonon group velocity and phonon scattering [28]. In $Li_xMn_2O_4$ with x<1, Li cations are on 8a tetrahedral sites, Mn cations on 16d octahedral sites and O anions on 32e positions, giving rise to a cubic spinel structure. This tetrahedral-site occupancy maximum is 50% corresponding to x=1 ($LiMn_2O_4$) and it can be considered to be more symmetric than $Li_{0.9}Mn_2O_4$. However, when x>1, in addition to the 8a tetrahedral sites, the vacant 16c octahedral sites also get occupied. In fact, the filling up of vacant 16c sites by Li ions along with the complete transfer of Li ions from 8a sites to 16c sites results in the tetragonal structure of $Li_2Mn_2O_4$. Thus the crystal structure of $LiMn_2O_4$ has maximum

symmetry. Phonon scattering and subsequent reduction in phonon group velocity decreases with increase in crystal symmetry and increases with defects. Therefore, the thermal diffusivity value of $LiMn_2O_4$ is greater than other $Li_xMn_2O_4$ samples. These arguments regarding the crystal structure distortion are supported by X-ray diffraction spectra of $Li_{0.9}Mn_2O_4$ $LiMn_2O_4$ and $Li_{1.1}Mn_2O_4$ at room temperature (298K) as shown in figure-3.8. The XRD spectra of $Li_{0.9}Mn_2O_4$ and $LiMn_2O_4$ show that they have pure cubic spinel structure as previously reported [14,26,43]. However, in the XRD spectrum of $Li_{1.1}Mn_2O_4$, there are two additional peaks, one at 16.8^0 and another at 34.5^0, suggesting that $Li_{1.1}Mn_2O_4$ does not have a perfect cubic crystal structure. These extra peaks of $Li_{1.1}Mn_2O_4$ correspond to the Li occupancy of the octahedral, interstitial 16c sites in addition to the 8a tetrahedral sites, suggesting that its cubic crystal structure is distorted by the presence of a tetragonal phase, which reduces its crystal symmetry compared to $LiMn_2O_4$.

The thermal diffusivity values of all the $Li_xMn_2O_4$ samples at 280 K (below the JT transition temperature), are less than those corresponding to room temperature values. This reduction in diffusivities is associated with the JT distortion in $Li_xMn_2O_4$, which deforms its cubic phase, thereby abating the crystal symmetry as well as phonon group velocity. The reduction in the thermal diffusivity is different for $Li_{0.9}Mn_2O_4$, $LiMn_2O_4$ and $Li_{1.1}Mn_2O_4$ being 20%, 30%and 45% respectively. This could be associated with the Mn^{3+} content of $Li_xMn_2O_4$, which is responsible for the JT distortion whose amount increases in the order

$Li_{0.9}Mn_2O_4$, $LiMn_2O_4$ and $Li_{1.1}Mn_2O_4$. In $LiMn_2O_4$, where the number of Mn^{3+} ions equals that of Mn^{4+} ions, JT distortion is absent at room temperature and occurs below the transition temperature, around 290 K [19,35]. At room temperature, JT distortion is pronounced only when the concentration of Mn^{3+} ions exceeds that of Mn^{4+} ions by a critical value (when x>1.08)[23] which is the case with $Li_{1.1}Mn_2O_4$.This JT distortion will strengthen with decrease in temperature and will be completed around 70 K [23]. Therefore, $Li_{1.1}Mn_2O_4$ can have more distortion at 280 K than at 298 K compared to $Li_{0.9}Mn_2O_4$ and $LiMn_2O_4$. In the case of $Li_{0.9}Mn_2O_4$, although the number of Mn^{3+} ions is less than the number of Mn^{4+} ions, there is a small shift in the value of thermal diffusivity when the temperature is lowered. This is not expected as it has been proved that for x=0.5, JT distortion does not exist even below the transition temperature [35]. This could be due to the fact that, compared to x=0.5, the number of Mn^{3+} ions in $Li_{0.9}Mn_2O_4$ is not considerably less than the number of Mn^{4+} ions and hence JT distortion is likely to happen. This explains the different reductions in thermal diffusivities of $Li_{0.9}Mn_2O_4$, $LiMn_2O_4$ and $Li_{1.1}Mn_2O_4$ below the transition temperature.

3.9 Studies on Optical Absorption Spectra of $Li_xMn_2O_4$ using Photoacoustic Spectroscopy

Optical absorption spectra of $Li_xMn_2O_4$ are obtained using Photoacoustic (PA) technique with a homemade PA cell employed in reflection configuration. For the absorption spectra measurements, the experimental setup used is the same as that for the thermal diffusivity

measurements, with the He-Ne laser being replaced by 250 W quartz tungsten halogen lamp. A monochromator attached to the output side of the tungsten halogen lamp selects the wavelength of excitation at a resolution of 5nm. The excitation beam is modulated at a constant frequency of 10 Hz.

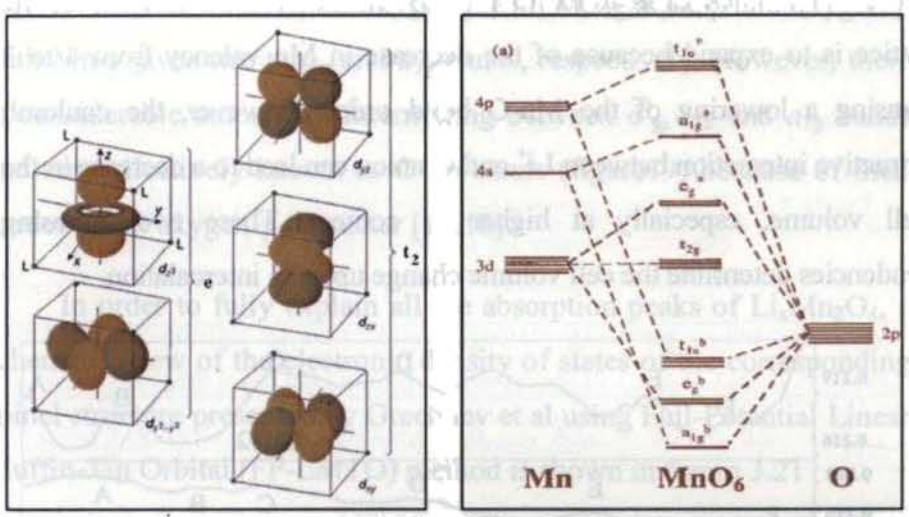

Fig.19 The d-Orbital splitting

The PA spectra of $Li_xMn_2O_4$ samples are shown in Figure 3.20. It may be noted that the PA spectrum is given in terms of wavelength in order to facilitate good visibility of the absorption peaks and also since the signal is recorded in linear steps of wavelength. The resolution of the measurements is restricted to 5 nm (0.02 eV at 575 nm) for having a good signal to noise ratio. The appearance of peaks in the absorption spectrum and their shift, if any, with respect to Li content of $Li_xMn_2O_4$ can be ascribed to the influence of cell volume and cell structure on the electronic structure and band formation. This is due to the fact that the electron density of states of $Li_xMn_2O_4$ is related to the volume of the unit cell of the

crystal. Though in most of the studies, it has been observed that the cell volume of $Li_xMn_2O_4$ is proportional to x, it has been theoretically predicted that the cell volume change of $Li_xMn_2O_4$ on Li intercalation can be either positive or negative depending on the value of x in $Li_xMn_2O_4$ [16,23 37]. When Li is added to $Li_xMn_2O_4$, one of the tendencies of the lattice is to expand because of the decrease in Mn valency from 4 to 3 causing a lowering of the Mn-O bond order. However, the coulomb attractive interaction between Li^+ and O anion can lead to a decrease in the cell volume, especially at higher Li content. These two opposing tendencies determine the cell volume change upon Li intercalation.

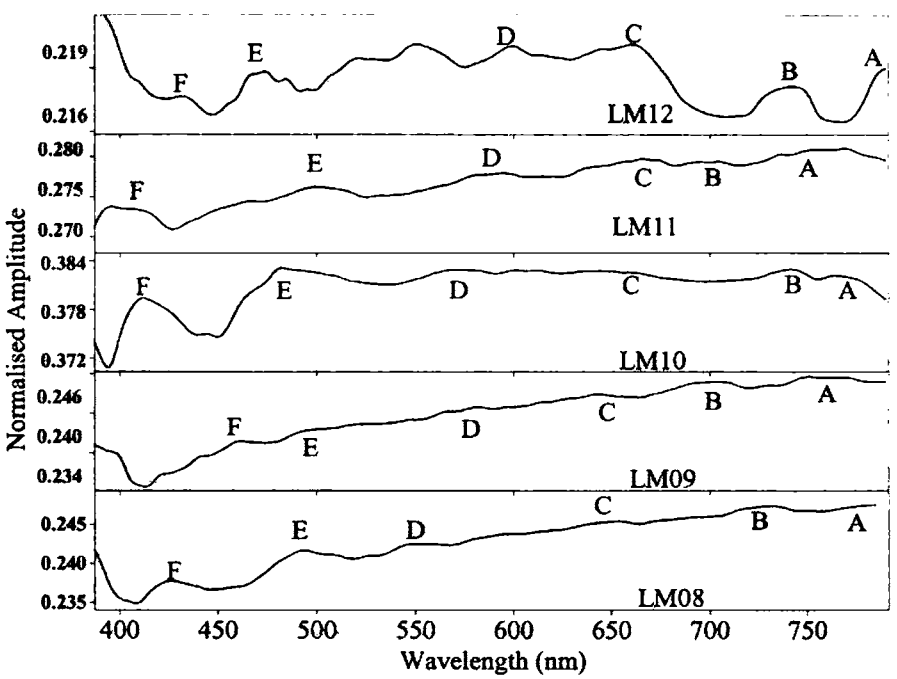

Fig.3.20 Absorption spectra of $Li_xMn_2O_4$ with x=0.8 as LM08, 0.9 as LM09, 1.0 as LM10, 1.1 as LM11 and 1.2 as LM12 are shown. The various absorption peaks are marked as A, B, C, D, E and F whose energy values are given in Table 3.4

Before going into the detailed analysis of the absorption spectra and identification of the peaks, the various bands present in $Li_xMn_2O_4$ are outlined. As mentioned in section 3.2, the Fermi level E_F of $Li_xMn_2O_4$ spinels lies within the partially filled nonbonding t_{2g} bands [6,17,38,39]. The overlap of oxygen-p with Manganese-p and oxygen-p with Mn-s gives rise to t_{1u} and a_{1g} bands, respectively. However, there is considerable amount of intermixing between e^b_g, t_{1u} and a_{1g} bands and are collectively known as O 2p bands (figure19) because of their predominant oxygen-p character [17,18].

In order to fully explain all the absorption peaks of $Li_xMn_2O_4$, a schematic view of the electronic density of states of the corresponding spinel structure presented by Grechnev et al using Full-Potential Linear Muffin-Tin Orbital (FP-LMTO) method is shown in figure 3.21

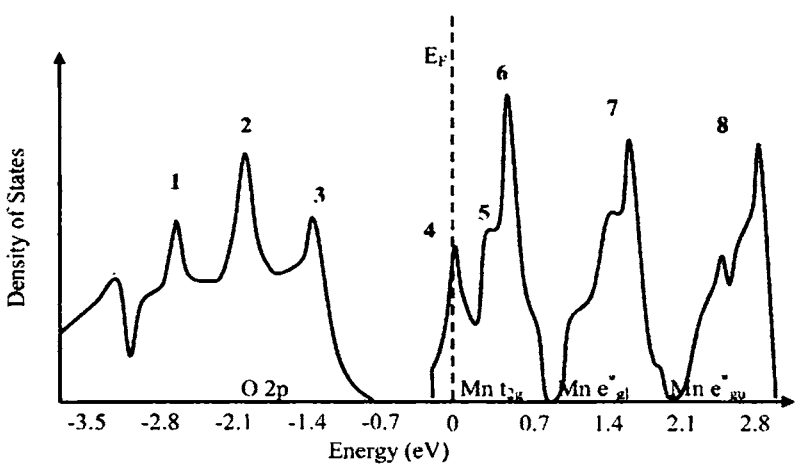

Fig 3.21 Schematic diagram of the electron density of states of $LiMn_2O_4$ as given by Grechnev et al [6] is shown. The relevant band peaks of O 2p, Mn t_{2g}, Mn e^*_{g1} and Mn e^*_{gu} are marked and their corresponding energies are given in Table 3.4a.

The band energy corresponding to zero eV represents the Fermi level, which resides in Mn t_{2g} band. The bands lying above Mn t_{2g} band are the lower Mn e^*_g, Mn e^*_{gl}, and the upper Mn e^*_g, Mn e^*_{gu}, bands. It is noteworthy that the density of states of O 2p and Mn t_{2g} bands have a few sharp peaks and their identification with the corresponding energy values are given in Table 3.4. The Arabic numerals in this table are used to facilitate the identification of their position in the electron density of states.

Table 3.4 Energies corresponding to the various peaks in the electron density of states of $Li_xMn_2O_4$, according to Grechnev [6] et al are given

Band	1	2	3	4	5	6	7	8
Peak	O $2p_l$	O $2p_m$	O $2p_u$	Mn t_{2g}	Mn t_{2gm}	Mn t_{2gu}	Mn e^*_{gl}	Mn e^*_{gu}
Energy (eV)	-2.8	-1.8	-1.4	0	0.45	0.6	1.4-1.6	2.7

Table 3.5 gives the observed peak values of the absorption spectra of $Li_xMn_2O_4$ samples and the association of their origin with the corresponding electronic transitions between the various peaks of electron density of states, given in Table 3.4 indicating their energy differences. It may be noted that, many transitions between the band peaks have coinciding energy, thus reducing the number of observable absorption peaks. Further, it is evident that there is no absorption peaks appearing in the photon energy range 2.2 eV – 2.5 eV in the case of $Li_xMn_2O_4$, with $x \leq 1$, where the crystal structure is assumed to be purely spinel. It is remarkable that all the observed absorption peaks have a one to one correspondence with the theoretically presented electron density of states by the FP-LMTO method by Grechnev et.al [6]. However, it can be seen that there are small differences between the

experimentally observed absorption peaks and the theoretically predicted ones, which may be due to the band structure differences of $Li_xMn_2O_4$ from $LiMn_2O_4$ and also may be due to deviations from the exact compositional stoichiometry of the samples. Moreover, the overall behavior of the absorption spectrum of pelletised $LiMn_2O_4$ powder in the present study is similar to the spectrum calculated by Grechnev et al except the manifestation of a few peaks in our spectrum [6]. However, if closely observed one can see that there are some undulations in that theoretical curve of Ref 6. Moreover, the absorption curve obtained by Kushida et al in Ref: 20 for $LiMn_2O_4$ thin film using transmission spectroscopy is also similar to the present spectrum and the small difference in the two spectra may be due to the difference in the physical nature of the samples, thin film in Ref 20 and pelletised powder in the present case.

Table 3.5 Experimentally determined energies of absorption peaks of $Li_xMn_2O_4$ and the corresponding band transitions with energy values are given

	$Li_{0.8}Mn_2O_4$	$Li_{0.9}Mn_2O_4$	$LiMn_2O_4$	$Li_{1.1}Mn_2O_4$	$Li_{1.2}Mn_2O_4$
A) Mn t_{2g}-Mn e^*_g (1.4-1.6 eV)	790 nm (1.57 eV)	750 nm (1.62 eV)	770 nm (1.61 eV)	775 nm (1.60 eV)	790 nm (1.57 eV)
B) O $2p_m$-Mn t_{2g} (1.8 eV)	720 nm (1.72 eV)	700 nm (1.78 eV)	740 nm (1.68 eV)	740 nm (1.68 eV)	745 nm (1.66 eV)
C) O $2p_u$-Mn t_{2g} (2.0 eV)	645 nm (1.92 eV)	640 nm (1.94 eV)	660 nm (1.88 eV)	670 nm (1.85 eV)	665 nm (1.87 eV)
D) O $2p_t$-Mn t_{2g} (2.2 eV)	545 nm (2.28 eV)	575 nm (2.17 eV)	575 nm (2.17 eV)	585 nm (2.12 eV)	590 nm (2.10 eV)
E) O $2p_l$-Mn t_{2g} (2.6 eV)	495 nm (2.50 eV)	480 nm (2.58 eV)	485 nm (2.55 eV)	495 nm (2.50 eV)	475 nm (2.60 eV)
F) Mn t_{2g}-Mn e^*_g (2.7 eV), O $2p_l$-Mn t_{2g} (2.8 eV) & O $2p_u$- Mn e^*_g (2.8 -3eV)	435 nm (2.85 eV)	454 nm (2.73 eV)	410 nm (3.02 eV)	430 nm (2.88 eV)	440 nm (2.82 eV)

There is only a negligible shift in the positions of the peaks as x varies though there are a few peaks appearing in the energy range 2.2 eV – 2.5 eV for $Li_xMn_2O_4$, with x>1. Some of those additional peaks are the peaks at 520 nm (2.38 eV), at 550 nm (2.25 eV) and the cluster of peaks between 470 nm and 490 nm, occurring in the case of $Li_{1.2}Mn_2O_4$. The following explanation is proposed for not observing any considerable shift in the peak as well as for the additional peaks occurring for x>1. As mentioned before, the shift in peaks is controlled by the cell volume changes as the x value changes. However, in the present study where x changes from 0.8 to 1.2 the cell volume is found to be almost a constant, which is quite obvious from the XRD data of $Li_xMn_2O_4$ as the position of their diffraction peaks does not change with x. In fact, the cubic lattice constant for $LiMn_2O_4$ is determined as 8.242 A^0 and its cell volume is 5.599×10^{-28} m^3. The additional peaks appearing for $Li_{1.1}Mn_2O_4$ and $Li_{1.2}Mn_2O_4$ can be ascribed to the appearance of tetragonal structure, as a structural distortion, in the cubic structure. Moreover, in the case of $Li_{1.1}Mn_2O_4$ unlike that of $Li_{1.2}Mn_2O_4$, these additional peaks are not easily observable except for a few small humps on the spectra, because the structural distortion due to the tetragonal structure is relatively small in $Li_{1.1}Mn_2O_4$. It may also be noted that the electron density of states corresponding to the tetragonal state has more peaks than the corresponding spinel state [34]. Since, the Mn=O bond length remains almost a constant for the various $Li_xMn_2O_4$ samples, the only possibility for deviation in the absorption spectra for higher Li content is the change in the shape of the crystal structure from pure cubic spinel shape for low Li content samples to a mixture of cubic spinel and tetragonal phases in the case of higher Li content $Li_xMn_2O_4$ samples which fully validates our

observation from the XRD data that the crystal phase is not pure spinel, but a mixture of cubic and tetragonal structures.

3.10 Studies on Optical Absorption Spectra of $LiMn_2O_4$ and λ-MnO_2 using Photoacoustic Spectroscopy

Optical absorption spectrum of $LiMn_2O_4$ is compared with that of λ-MnO_2 and are shown in figure 3.22. The absorption peaks in the figure is marked as I, II, etc. for $LiMn_2O_4$ and I', II', etc. for λ-MnO_2, which can be related to the band structures of $LiMn_2O_4$ and λ-MnO_2.

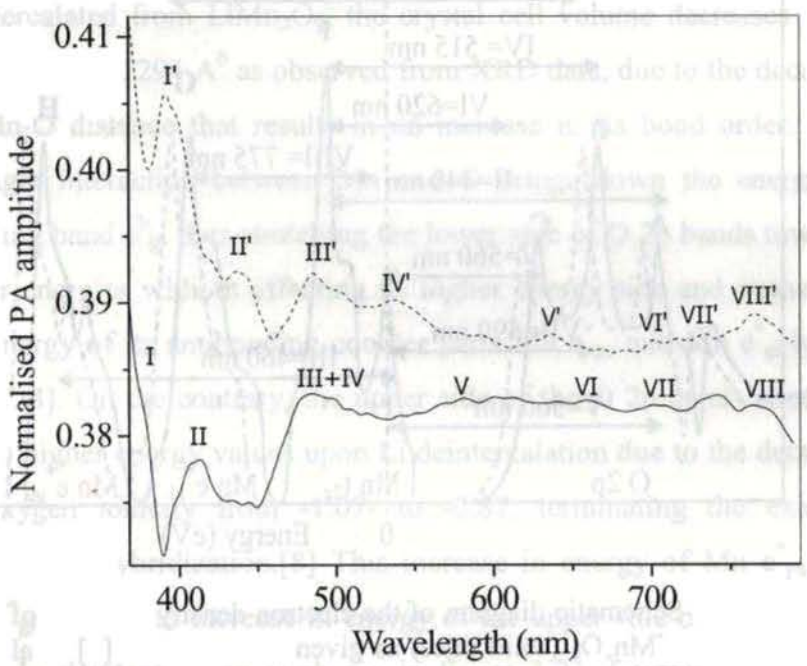

Fig. 3.22 The normalized PA spectra of $LiMn_2O_4$ (solid lines) and λ-MnO_2 (dashed lines) are shown. The transitions are represented in roman numerals for $LiMn_2O_4$ and primed roman numerals for λ-MnO_2.

In order to explain the absorption spectra of $LiMn_2O_4$ and λ-MnO_2 ,the electronic structure of cubic spinel $LiMn_2O_4$ determined by Grechnev et al using full-potential linear muffin-tin orbital(FP-LMTO) approach[34] and its possible modification due to Li deintercalation, taking into account of change in cell volume and chemical effect of Li are shown in figure 3.23

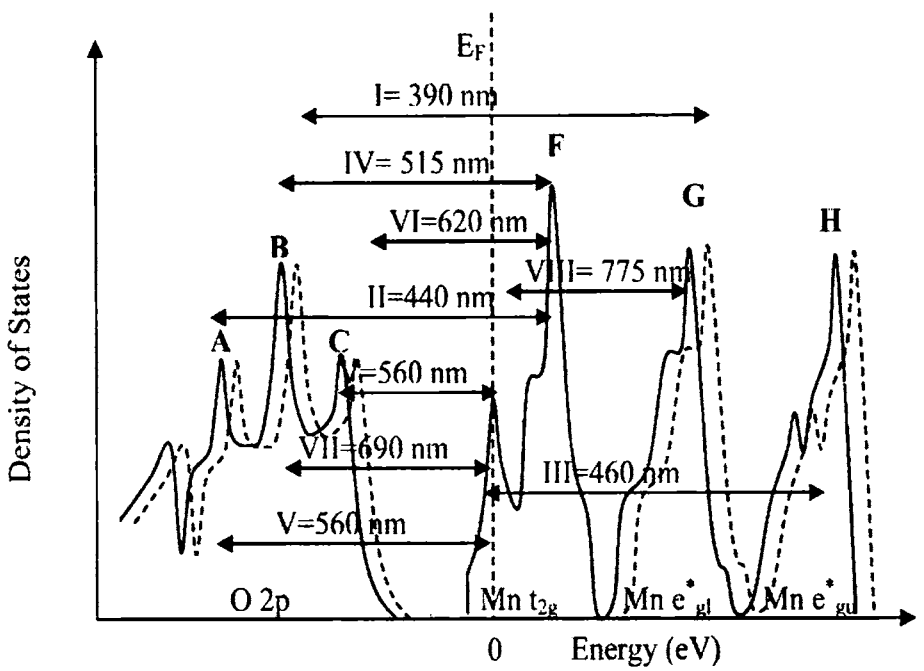

Fig. 3.23 Schematic diagram of the electron density of states of $LiMn_2O_4$ (solid lines) as given by Grechnev [6] et al and that of λ-MnO_2 (dashed lines) are shown. The relevant band peaks of O 2p, Mn t_{2g}, Mn e^*_{gl} and Mn e^*_{gu} are marked as A, B, C, D, E and F, and possible transitions along with their transition energies in wavelength are shown.

The electronic structure of $LiMn_2O_4$ is governed by a strong hybridization between the O p and Mn d states, giving rise to the O 2p bands with a considerable amount of intermixing between e^b_g, t_{1u} and a_{1g} bands and having predominantly oxygen-p character, and Mn d bands consisting of the nonbonding t_{2g} bands and the antibonding e^*_g bands with a predominant metallic d-character. The e^*_g bands comprise the higher energy Mn e^*_{gu} band and the lower energy Mn e^*_{gl} band. Along with the strongly hybridized Mn-3d/ O-2p levels, there exists a relatively weak hybridization between Li-2p/O-2p levels. When Li is deintercalated from $LiMn_2O_4$, the crystal cell volume decreases from 8.284 A^0 to 8.1294 A^0 as observed from XRD data, due to the decrease in Mn-O distance that results in an increase in its bond order. This stronger interaction between Mn and O brings down the energy of bonding band e^b_g, thus stretching the lower side of O 2p bands towards lower energies without affecting its higher energy side and pushes up the energy of its antibonding counter parts Mn e^*_{gu} and Mn e^*_{gl} bands [8,17,34]. On the contrary, the upper side of the O 2p bands stretches out to higher energy values upon Li deintercalation due to the decrease in oxygen ionicity from -1.07- to -0.87, terminating the existing Li-2p/O-2p hybridization.[8] This increase in energy of Mn e^*_{gu} and Mn e^*_{gl} bands and increase in energy of the upper side of O 2p bands upon Li deintercalation is shown in figure 3.23. Energy of the non-bonding t_{2g} band which houses Fermi level E_F is unaffected due to Li deintercalation.

The group of transitions, II, IV, V, VI and VII originating from transition betweens O 2p and Mn t_{2g} bands is labeled as Group 1 and the set of transitions III and VIII, which arises due to transitions between Mn t_{2g} - Mn e^*_{gu} bands and Mn t_{2g} - Mn e^*_{gl} bands is labeled as Group 2. The third set, Group 3, containing only transition I originates from O 2p - Mn e^*_{gl} band transition. These peaks are identified in the spectrum of $LiMn_2O_4$, given in figure 3.22. It can be seen that Group 1 peaks of $LiMn_2O_4$ are red-shifted (move towards higher wavelength side of the spectrum) by about 0.2 eV (30nm at 425 nm) upon Li deintercalation, which is due to the increase in bond order upon Li deintercalation. On the contrary, the second set of peaks of $LiMn_2O_4$, Group 2, is blue shifted (move towards lower wavelength side of the spectrum) by a small amount, upon Li deintercalation which is due to the change in ionicity of oxygen. The absorption peak due to transition I also shifts towards lower energy side alike Group 1, but by a lower amount, 0.17 eV (20 nm at 380 nm). This transition, I, has 2 opposing effects acting on it arising from the effects affecting Groups 1 and 2. Group 1 tends to move towards the low energy side and Group 2 towards the higher energy side, upon Li deintercalation in $LiMn_2O_4$. However, the effect on Group 1 is much stronger than that on Group 2, resulting in a shift in peak I that follow the behavior of Group 1.

3.11 Effect of Jahn Teller Distortion on the Spectra of $Li_xMn_2O_4$

The low temperature measurements are done by keeping the PA cell in an ice bath inside a thermocole box and the temperature is allowed to stabilize prior to the measurement. During the period

of measurement (45 minutes approximately) the temperature showed a fluctuation of only 1.5 °C. Figure3.24 shows the phase plot of $LiMn_2O_4$ at 298 K showing the constancy of phase in the measurements

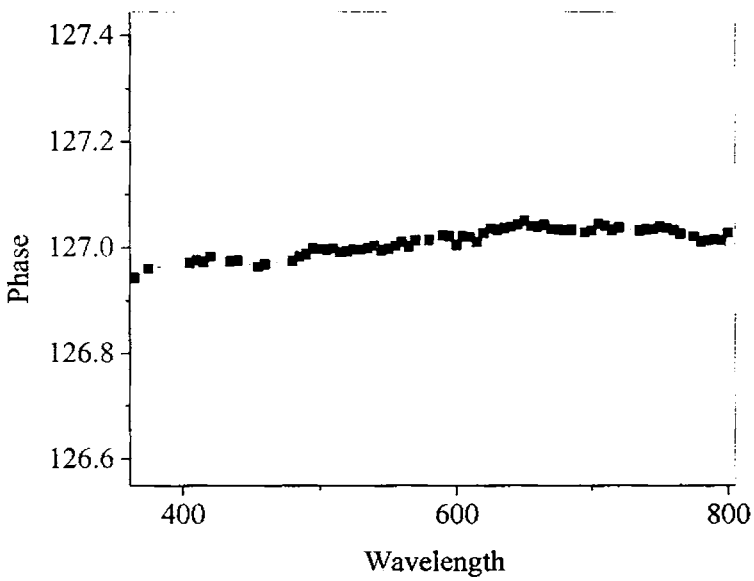

Fig. 3.24 Phase plot of $LiMn_2O_4$ at 298 K

Figures 3.25, 3.26 and 3.27 show the PA spectra of $Li_{0.9}Mn_2O_4$, $LiMn_2O_4$ and $Li_{1.1}Mn_2O_4$ at two temperatures, 298 K and 280 K which are respectively above and below the JT phase transition temperature. The x and y scales of these three figures are purposefully adjusted to be the same to facilitate a good comparison between the graphs.

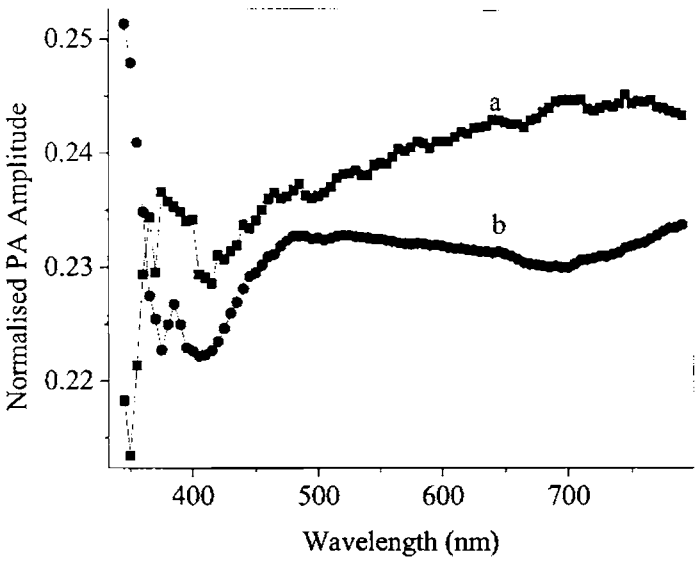

Fig. 3.25 Normalised PA Spectrum of $Li_{0.9}Mn_2O_4$ at 298 K (a) and 280 K (b)

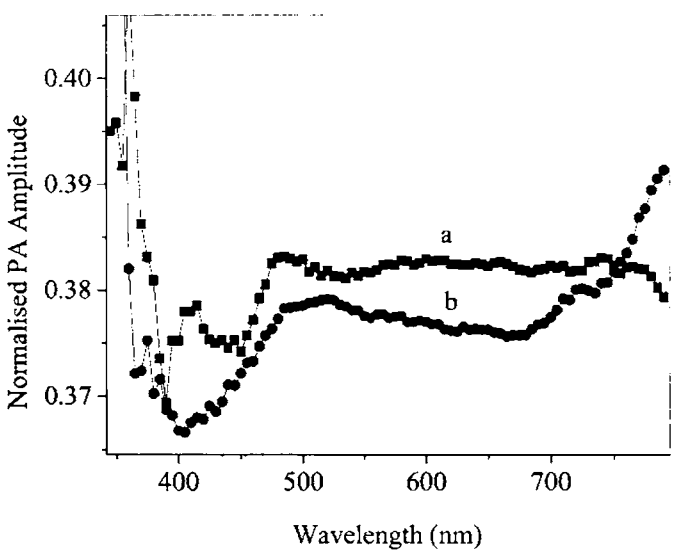

Fig. 3.26 Normalised PA Spectrum of $LiMn_2O_4$ at 298 K (a) and 280 K (b)

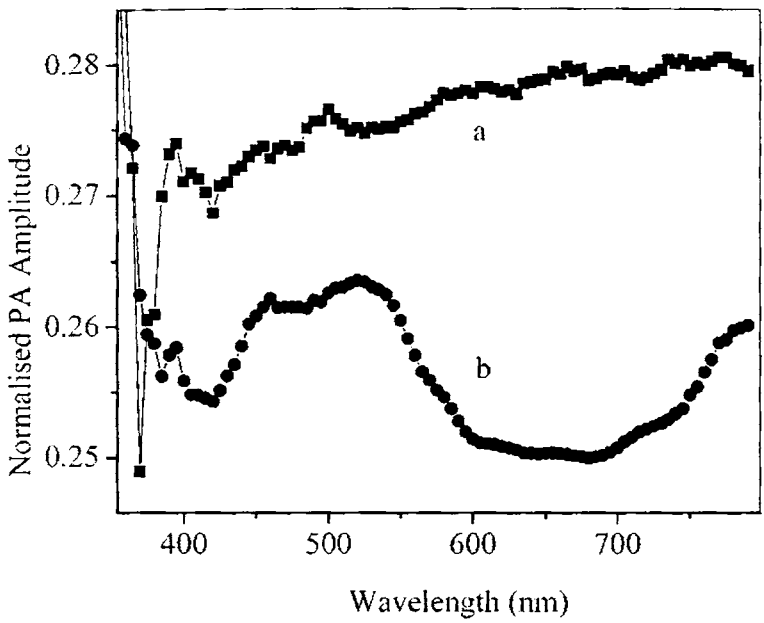

Fig. 3.27 Normalised PA Spectrum of $Li_{1.1}Mn_2O_4$ at 298 K (a) and 280 K (b)

The spectra of $LiMn_2O_4$ and $Li_{1.1}Mn_2O_4$ at 280 K appear to be significantly different from their corresponding spectra at 298 K. This is evident from the appearance of two broad absorption peaks for $LiMn_2O_4$ and $Li_{1.1}Mn_2O_4$ at 280 K, one near 500 nm and another near 800 nm, which are absent in their spectra at 298 K. The PA spectra of $Li_{0.9}Mn_2O_4$ at 298 K and 280 K show only a minor difference with each other with a modification of the general shape of the absorption curve in the wavelength range 500 nm – 800 nm. However, there is no appearance of any new absorption peaks, one near 500 nm and another near 800 nm, when the temperature of $Li_{0.9}Mn_2O_4$ is lowered to 280 K, as in the case of $LiMn_2O_4$ and $Li_{1.1}Mn_2O_4$ These effects are explained on the basis of the predominant JT tetragonal distortion in cubic

$Li_xMn_2O_4$ which brings forth a modification in their electronic structure.

Berg et al have derived that when a cubic crystal undergoes a tetragonal JT distortion, as in $LiMn_2O_4$ and $Li_{1.1}Mn_2O_4$, their electronic structure gets modified in the form of splitting up of each Mn t_{2g} and Mn e^*_g band into two [16,17]. This splitting causes the small absorption peaks of $LiMn_2O_4$ and $Li_{1.1}Mn_2O_4$ at 298 K, between 550 and 700 nm, whose origin is already attributed to O 2p - Mn t_{2g} electronic transitions, to shift to both higher (blue shift) and lower (red shift) energies at 280 K and results in the appearance of two new absorption peaks, one around 500 nm and another around 800nm as shown in figures3.26and 3.27. This shifting of peaks is not a constant for all the absorption peaks because of the difference in their origin. The shift will be more for a transition involving Mn t_{2g} and Mn e^*_g bands compared to that between O 2p and Mn t_{2g} bands, because in the first case both the bands are shifted due to JT distortion and in the second case only Mn t_{2g} band is shifted. If we assume that the centre of the peaks between 550 and 700 nm is at 625 nm, then the JT distortion causes it to get blue shifted by 125 nm to the peak around 500 nm and red shifted by 175 nm to the peak around 800 nm. Hence the absorption peaks are both blue and red shifted as can be observed in Figures 3.26 and 3.27which are respectively for $LiMn_2O_4$ and $Li_{1.1}Mn_2O_4$. Moreover, the modification of the absorption spectrum is most dramatic in the case of $Li_{1.1}Mn_2O_4$ which conforms to the previous discussion about its plentitude of Mn^{3+} ions.

3.12 Conclusions

$Li_xMn_2O_4$ (with x=0.8,0.9,1,1.1, and1.2) bulk samples are prepared by solid-state reaction technique and λ-MnO_2 is obtained by chemical de- lithiation of $LiMn_2O_4$.Structural characterization of these samples is carried out using XRD, SEM and TEM techniques. From the XRD investigations it is seen that in $Li_xMn_2O_4$ samples the cell volume remains almost a constant when x changes from 0.8 to 1.2.This is because the position of the diffraction pattern does not change with x. The additional peaks appearing for x=1.1 and x=1.2 can be ascribed to the presence of tetragonal structure as a structural distortion in the cubic phase. SEM and TEM investigations reveal the formation of micrometer sized (nearly 2.5μm) spherical grains, which are almost connected ensuring high surface area. This feature is a highly desired characteristic for the materials to be used as a cathode in high-energy lithium ion rechargeable batteries.

The thermal properties of the samples are analyzed from photoacoustic signal amplitude and phase as a function of modulation frequency in reflection configuration. The thermal diffusivity of $LiMn_2O_4$ is significantly higher than the rest of the group and the value decreases monotonically as the lithium content changes from x=1 in $Li_xMn_2O_4$.The present work points to the fact that the thermal diffusivity value of $LiMn_2O_4$ cathode and hence its heat dissipation capability is not a constant in time during the operation of $LiMn_2O_4$ based Li-ion battery. This observation of the variation of thermal diffusivity with lithium content in $Li_xMn_2O_4$ can shed light on the heat

propagation mechanism in $LiMn_2O_4$ cathodes and may lead to addressing the thermal stability issues related to $LiMn_2O_4$ based Li- ion batteries.

From the wavelength dependence of the photo acoustic signals, information about the electronic band structure of the samples has been obtained. The peaks obtained in the absorption spectra of the samples can be associated with the electron density of states determined by FP-LMTO method by Grechnev et al, which provides a strong experimental verification of these calculations for the first time. The modification of the electronic band structure of $LiMn_2O_4$ upon de-intercalation of lithium to form λ-MnO_2 has been investigated using photo acoustic spectroscopy. These investigations reveal that upon lithium de-intercalation of $LiMn_2O_4$ the effect of change in oxygen ionicity is stronger than the effect of cell volume change for modifying the electronic band structure of $LiMn_2O_4$ around its Fermi level.

Other significant observations of the present study include the evidence of Jahn-Teller (JT) distortion in $Li_xMn_2O_4$ samples, probed by photo acoustic technique. In $Li_xMn_2O_4$ samples the effect of lithium concentrations as well as temperature for promoting the occurrence of Jahn-Teller distortion is studied for the first time using the photo acoustic technique. These investigations establish the fact that the substantial Jahn-Teller distortion observed in $LiMn_2O_4$ and $Li_{1.1}Mn_2O_4$ is due to the higher Mn^{3+} ions content in these materials.

References

[1] H. Yang, S. Amiruddin, H. J. Bang, Y. K. Sun, J. Prakash, J. Indust. Eng. Chem. 12, 12 (2006)

[2] J. Vetter, P. Nov´ak, M. R. Wagner, C. Veitb, K. -C. M¨oller, J. O. Besenhard, M. Winter, M. Wohlfahrt-Mehrens, C. Vogler, 1, A. Hammouched, J. Power Sources, 147, 269 (2005)

[3] H. T. Huang and P. G. Bruce, J. Power Sources 54, 52 (1995)

[4] J. –M. Tarascon and M. Armand, Nature, 414, 359 (2001)

[5] W. I. F. David, M. M. Thackeray, L. A. De Picciotto and J. B. Goodenough, J. Solid State Chem., 67, 316 (1987)

[6] G. E. Grechnev, R. Ahuja, B. Johansson and O. Eriksson, Phys. Rev. B, 65, 174408 (2002)

[7] J. Molenda, S. Swierczek, M. Molenda and J. Marzec, Solid State Ionics, 135, 53 (2000)

[8] Y. Liu, T. Fujiwara, H. Yukawa and M. Morinaga, Solid State Ionics, 126, 209 (1999)

[9] L. Ning, J. Wu, C. Zhou, S. Yao, Z. Pi and H. Cheng, Int. J. Quantum Chem., 107, 225 (2007)

[10] A.K.Padhi, K.S., Nanjundaswamy and J.B. Goodenough, J. Electrochemical Society 144., 1188 (1997)

[11] Y. J. Park, J. G. Kim, M. K. Kim, H. G. Kim, H. T. Chung and Y. Park, J. Power Sources, 87, 69 (2000)

[12] Brett Ammundsen.etal.Solid state Ionics 97,269-276(1997)

[13] Charles Kittel. "Introduction to Solid state Physics" 7th Edn.John Wiely& Sons. INC- (2000)

[14] S. Chitra, P. Kalyani et al. Physical Properties of $LiMn_2O_4$ Spinel Prepared at moderate temperature. Ionics 4 (1998)

[15] C. Ouyang, H. Deng, Z. Ye, M. Lei and L. Chen, Thin Solid Films 503, 268 (2006)

[16] H. Berg, K. Goransson, B. Nolang and J. O. Thomas, J. Mat. Chem. 9 2813 (1999)

[17] M. K. Aydinol, A. F. Kohan, G. Ceder, K. Cho and J. Joannopoulos, Phys. Rev. B, 56, 1354 (1997)

[18] *S. Thomas Lee, K. Raveendranath, M. Rajive Tomy, M.Paulraj, S. Jayalekshmi and Jyotsna Ravi, Appl. Phys. Lett. 90, 161912 (2007)*

[19] S. Thomas Lee, K. Raveendranath, M. Rajive Tomy, Nibu A. George, S. Jayalekshmi and J. Ravi, J. Phys. D: Appl. Phys. 40, 3807-3810 (2007)

[20] K. Kushida and K. Kuriyama, App. Phys. Lett., 77, 4154 (2000)

[21] M Wakihara, H. Ikuta and Y Uchimoto, Ionics 8, 329 (2002)

[22] W. S. Yoon, K. Y. Chung, K. H. Oh and K. B. Kim, J. Power Sources, 119-121, 706 (2003)

[23] Thackeray M. M., David W.I.F., Bruce P.G., Goodenough J.B., Material Research Bulletin 18, 461-472, (1983)

[24] M.MThackeray,P.J.Johnson,dePiccioto,P.G.Bruce,andJ.B.Goodenough.Mat.Res.Bull.19,179(1984)

[25] Guohua Li, Astuo Yamada, Yuzuru Fukushima, Kiyoshi Yamaura, Takamitsu Saito, Takuya Endo, Hideto Azuma, koji Sekai, Yoshio Nishi, *Solid State Ionics* 130, 221 (2000)

[26] K. Raveendranath, Jyotsna Ravi, S. Jayalekshmi, T. M. A. Rasheed and K. P. R. Nair, Mater. Sci. Eng. B, 131, 210 (2006)

[27] M. M. Thackeray, M. F. Mansuetto, D. W. Dees, D. R. Vissers, Mat. Research Bull., 31, 133 (1996)

[28] L. Pascual, M. L. Perez-Revenga , R. M. Rojas, J. M. Rojo, J. M. Amarilla, Electrochemical Acta, 51, 3193 (2006)

[29] J. Ravi, Y. Lu, S. Longuemart, S. Paoloni, H. Pfeiffer, J. Thoen and C. Glorieux, J. App. Phys. 97 014701-1 (2005)

[30] E. Iguchi, N. Nakamura, A. Aoki, Phil. Mag. B, 78, 65 (1998)

[31] T. Minami, M. Tatsumisago, M. Wakihara, C. Iwakura, S. Kohjiya and I. Tanaka, Solid State Ionics for Batteries, Springer Tokyo, 258-269 (2005)

[32] A. Paolone, C. Castellano, R. Cantelli, G. Rousse and C. Masquelier, Phys. Rev. B, 68, 14108 (2003)

[33] Malcom Gerloch,Edwin C.Constable "Transition Metal Chemistry"VCH Pulishers,Newyork,NY,(USA)(1994)

[34] S. K. Mishra and G. Ceder, Phys. Rev. B, 59, 6120 (1999)

[35] V. W. J. Verhoeven, I. M. de Schepper, G. Nachtegaal, A. P. M. Kentgens, E. M. Kelder, J. Schoonman and F. M. Mulder, Phys. Rev. Lett. 86, 4314 (2001)

[36] B. Banov, Y. Todorov, A. Trifonova, A. Momchilov, V. Manev, J. Power Sources 68, 578 (1997)

[37] C. Glorieux, J. Fivez and J. Thoen, J. Appl. Phys, 73, 684 (1993)

[38] H. Yamaguchi, A. Yamada and H. Uwe, Phys. Rev. B, 58, 8 (1999)

[39] N. A. George, C. P. G. Vallabhan, V. P. N. Nampoori and P. Radhakrishnan, Opt. Eng., 41, 251 (2002)

[40] S.R.S Prabhakaran, Nasiman B, S.S.Michael, M.Massot, C. Julien, Solid State Ionics 112 ,25 (1998)

[41] S.H Kang, J.B.Goodenough and L.K.Rabenberg, Chem.Mater.13, 1758(2001)

[42] K.Raveendranath. M.Phil Project Report. Department of Physics CUSAT (2003).

[43] Joint Committee on Powder Diffraction Standards, Files 38-789 (λ-MnO_2), 35-782 ($LiMn_2O_4$), 38-299 ($Li_2Mn_2O_4$), 84-1634 (Li_2MnO_3)

[44] H.Bjork, T.Gustafson, J.O.Thomas, Eelectrochem.Commun, 3,187 (2001)

Chapter 4

Structural Thermal Spectroscopic and Electrical Characterization of Phospho - Olivine $LiFePO_4$ and Effect of Carbon Nano Tubes as Additives

This chapter deals with the synthesis of olivine $LiFePO_4$ and a detailed account of its structural, thermal, electrical and optical properties. Structural characterization is done using X-ray diffraction (XRD), SEM (Scanning Electron Microscopy) and TEM (Transmission Electron Microscopy). The electrical transport properties are determined using impedance spectroscopy. The thermal properties of the samples are evaluated from photoacoustic signal amplitude and phase as a function of modulation frequency in reflection configuration while information of their electronic band structure is obtained from the wavelength dependence of its photoacoustic signal. Diffuse reflection spectroscopic technique has been used to evaluate the band gap of this material.

$LiFePO_4$ has many advantages when selected as cathode material in rechargeable lithium ion batteries as detailed in the first chapter.Inspite of these advantageous aspects the poor electrical conductivity of the material is the main hindrance for its commercial applications. In the present work attempts have been made to improve the electrical conductivity of $LiFePO_4$ by adding small amounts of Multi Walled Carbon Nano Tubes (MWNT).Subsequently, the influence of this addition on the structural, thermal, optical and electrical properties of $LiFePO_4$ has also been studied in detail.

4.1 Introduction

Olivine lithium metal phosphates, $LiMPO_4$ (M=Fe, Mn, Co, Ni) have attracted particular attention due to their high energy density, low cost and good environmental compatibility of their basic constituents. Moreover, these compounds display high redox potentials, fast Li^+ ion transport, excellent thermal stability, high lithium intercalation potential (not too high to decompose the electrolyte) and energy density comparable to that of conventional lithium metal oxides [1-6].

Lithium metal phosphates (LMPs) adopt an olivine-related structure, which consists of a hexagonal closed-packing (hcp) of oxygen atoms with Li^+ and M^{2+} cations located in half of the octahedral sites and P^{5+} cations in 1/8 of the tetrahedral sites as shown in Figure 4.1[7-10]. This structure may be described as chains (along the c direction) of edge-sharing MO_6 octahedra, which are cross-linked by the PO_4 groups forming a three-dimensional (3-D) network. Tunnels perpendicular to the [001] and [100] directions contain octahedrally coordinated Li^+ cations (along the b axis) which are mobile in these cavities. These compounds generally crystallize in the orthorhombic (Pnma space group) system [11, 12]. In phospho-olivines, all of the oxygen ions form strong covalent bonds with P^{5+} to form the PO_4^{3-} tetrahedral polyanions and stabilize the entire three-dimensional framework. This guarantees stable operation at higher temperatures and extreme safety under abusive conditions, which adds greatly to the attractiveness of the olivine-type cathode [13-15].

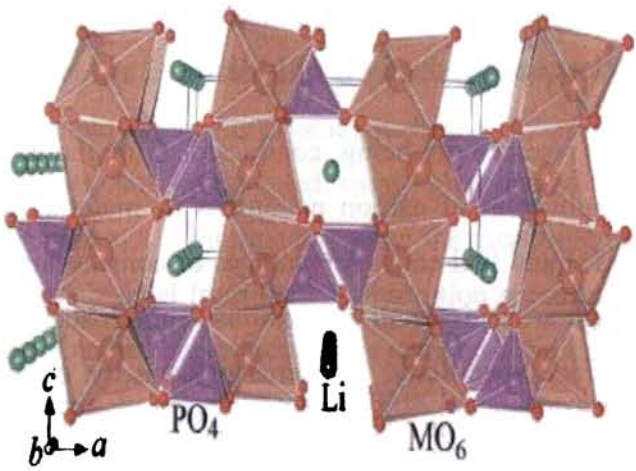

Fig. 4.1 Polyhedra representation of the structure of $LiMPO_4$, with arrays of Li-ions (green) along b axis, nearly co-planar MO_6 (brown) octahedra and PO_4 (purple) tetrahedra.

The major problem facing the commercial use of these Lithium Metal Phosphates (LMPs) is their poor rate capability, which is attributed to their low electronic conductivity and slow kinetics of Li diffusion through the interfaces. Two approaches have been attempted to overcome this problem. One is to enhance electrical conductivity by coating an electron-conducting layer around the particles, such as carbon [16-17], copper [18] and silver [19], or by doping with guest cations [20]. The other is to minimize particle size by modifying the synthesis conditions, such as using solution method [21] or lowering the sintering temperature [2]. In the proposed work we suggest another way to improve the electrical conductivity of LMPs (typically $10^{-7} - 10^{-3}$ Sm^{-1}) by doping them with carbon nanotubes (CNTs), which have high electrical conductivity (as high as 10^{5} Sm^{-1}). We expect these CNTs to serve as

micro conductors within and between the grains of LMPs, thereby increasing the electrical conductivity of LMPs.

Currently, research is being conducted throughout the world targeting the application of carbon nanotubes as materials for use in transistors [22-31] and fuel cells. Advantages of considering nanotubes for energy storage are their small dimensions, smooth surface topology and perfect surface specificity. The energy capacity of any battery including Li-ion battery is determined by the lithium saturation concentration of the electrode materials. For Li, this is the highest in nanotubes if all the interstitial sites (inter-shell van der Waals spaces, inter-tube channels, and inner cores) are accessible for Li intercalation. Zhao et al have investigated the possibility of achieving the lithium capacity of the nanotubes corresponding to the stoichiometry of LiC_2, which is considerably improved compared to the graphite anode (LiC_6) [32]. Experimentally, lithium capacity of the nanotube can be significantly increased up to the stoichiometry of LiC_3 by ball milling nanotubes into the fractured structure or chemically etching them to the short segments. Lithium can easily diffuse not only to the exterior but also to the interior of such nanotubes through the created defects with at least nine-sided rings or their open ends [33,34]. Nishidate et al [35] have applied the density-functional theory to study energetics of Li ion adsorption on single-walled carbon nanotubes (SWNTs) using both the local-density approximation (LDA) and the generalized-gradient approximation (GGA) for the exchange-correlation energy function [36].

$LiFePO_4$ is prepared by solid-state reaction technique and its optical, thermal, and electrical characteristics are studied. X ray Diffraction, SEM and TEM are employed for the crystal structure analysis. The optical and thermal properties are investigated using photoacoustic technique as described in Chapter 3. Information about the electronic band structure and band gap is obtained from the PA absorption spectra. The electronic band structure obtained experimentally is compared with already existing theoretical models based on Density Functional theory (DFT) with relevant approximations and suitable choice of basis functions [40]. The electrical properties are investigated using complex plane impedance analysis and dc conductivity measurements. These measurements will give information regarding the different relaxation phenomena in the material due to the contribution from the bulk, grain boundaries and material-electrode interfaces.

In order to improve electrical conductivity of $LiFePO_4$ varying percentage by weight of MWNTs are added to $LiFePO_4$.Consequently the influence of this addition on the structural and electronic band structure of this material is verified. Photoacoustic measurements (both frequency scan and wavelength scan) are performed for determination of the thermal properties and the absorption spectra, which can be correlated with the structural and electronic band structure modifications.

4.2 Synthesis of $LiFePO_4$

The $LiFePO_4$ phospho-olivine samples are prepared as microcrystalline powder by solid state chemical reaction between Li_2CO_3, $(NH_4)_2HPO_4$ and $FeC_2O_42H_2O$ (99.9%pure) [1]. The

intimately ground stoichiometric amounts of reactants are calcined at 300 °C - 350 °C to drive away the gases. The mixture is then reground and pelletised at a load of 5T. The pellets thus obtained are sintered in argon atmosphere at 750°C for 24hours.The compound obtained is characterized immediately after synthesis by X- ray diffraction analysis (Model: 1710 Rigaku) for phase purity and crystal structure. The X ray diffraction (XRD) pattern obtained for $LiFePO_4$ is shown in the figure 4.2. The peaks obtained conform well to those already reported [2]. Different weight percentages of Multi walled carbon nanotubes (MWNT) of 10 to 20nm diameter are added to $LiFePO_4$ and are mixed well in an agate mortar for 2 hours. The powders are pressed into pellets of 13mm diameter and 1.5mm thickness using a hydraulic press. The pellets are then heat treated at 350°C for 5hours in flowing Argon. The samples are then cooled to room temperature. Figure 4.4 shows the TEM images of the pure and doped (1% MWNT) $LiFePO_4$. TEM image clearly shows the presence of carbon nano tubes.

4.3 Structural Characterization

The XRD spectra of pure and doped $LiFePO_4$ are shown in Figure 4.3, where all the spectra seem to be exactly the same. However, on a closer look, it may be observed that XRD spectrum of 2% MWNT added $LiFePO_4$ has broader peaks than the corresponding peaks of pure $LiFePO_4$, which is ascribed to the structural distortion of its olivine structure. Though unobserved due to the fundamental limit of detection of XRD, it is believed that adding MWNT to $LiFePO_4$ distorts its crystal structure for all concentrations of MWNT. The

TEM image of pure $LiFePO_4$ given in figure 4.4 reveal an average particle size of 150 nm and that of one percent MWNT doped $LiFePO_4$ (Figure 4.4b) manifests an average MWNT length of 200 nm. Correspondingly, SEM images, shown in figures 4.5a and b demonstrate an increase in packing density of $LiFePO_4$ in accordance with MWNT concentration. This may be due to the attachment of $LiFePO_4$ particles to nanotubes as observed in TEM images shown in Figure 4.4b. It can be seen that MWNT is present outside the $LiFePO_4$ grains too. These MWNT having very high electrical conductivity can function as bridges between various $LiFePO_4$ particles thus enhancing the bulk conductivity of the material. Furthermore, it is possible to identify the doped samples from their physical appearance alone, because the pink color of pure $LiFePO_4$ darkens with the addition of MWNT.

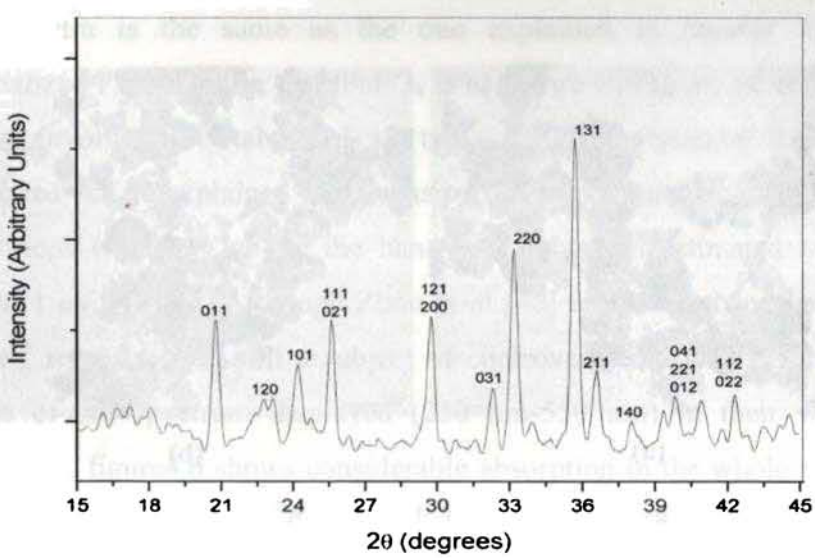

Fig.4.2 X-ray diffraction spectrum of $LiFePO_4$

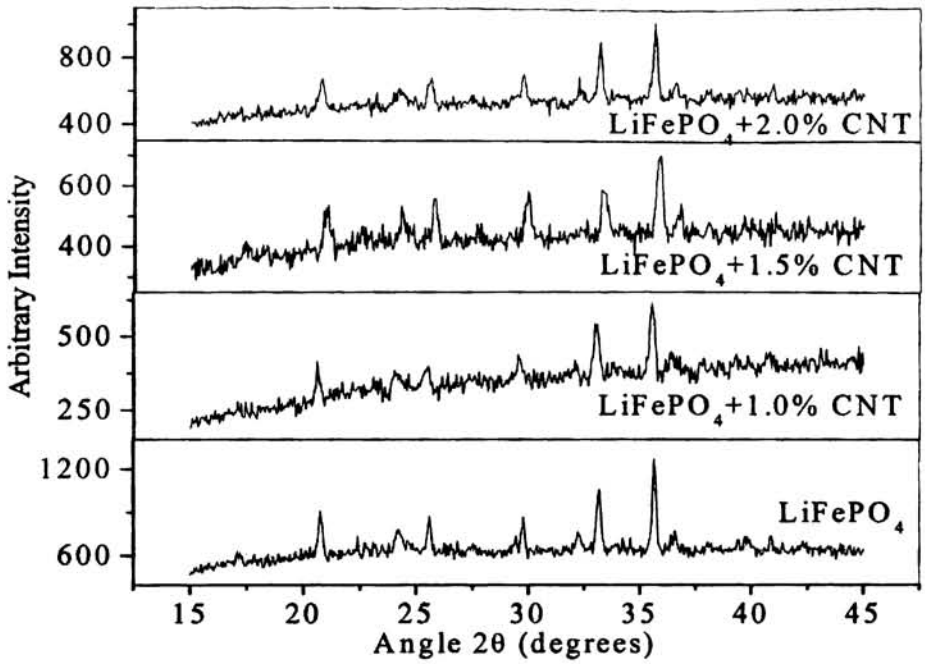

Fig. 4.3 XRD spectra of pure and MWNT doped $LiFePO_4$

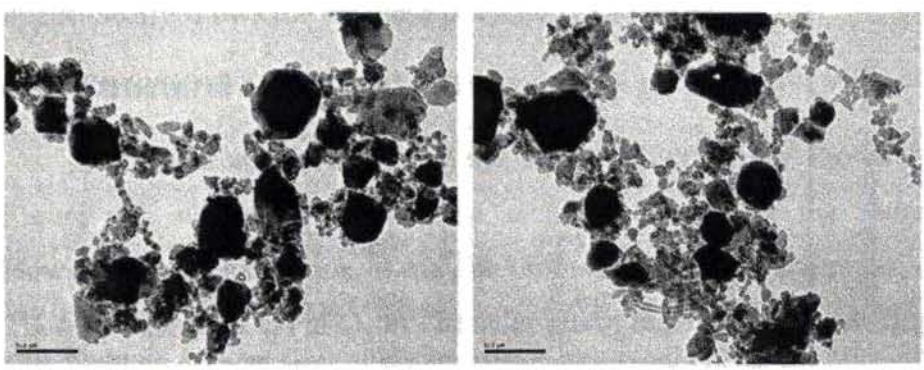

(a) **(b)**

Fig.4.4 TEM images of (a) pure $LiFePO_4$ and (b) 1% CNT doped $LiFePO_4$

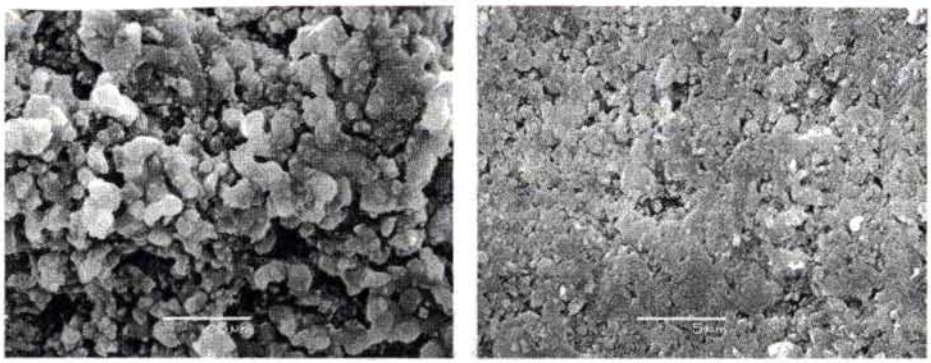

Fig. 4.5 SEM images of (a) pure $LiFePO_4$ and (b) 1% CNT doped $LiFePO_4$

4.4 Experimental Verification of Electronic Band Structure of $LiFePO_4$ and its Modification upon Carbon Nanotube Doping by Photoacoustic Spectroscopy

Optical absorption spectra of $LiFePO_4$ are recorded using PA spectroscopy. The influence of MWNT on absorption spectra of $LiFePO_4$ is also studied. The experimental setup used for recording the PA spectra is the same as the one explained in chapter 3.The normalized PA spectrum of $LiFePO_4$ is as shown in Figure 4.6 and the peaks involved are tabulated in table 4.1. The spectral features exhibited can be explained on the basis of the electronic band structure transitions occurring above the band gap, which is estimated to be below 1 eV [40-46]. Although Zhou et al [46] reported a band gap of 3.7 eV recently; it is still a subject of controversy due to the limited range of the spectrum displayed (250 nm-550 nm) in their work. Moreover, figure4.6 shows considerable absorption in the whole range of the present measurement, 1.5 eV – 3.5 eV and hence this measurement also contradicts the 3.7 eV band gap demonstrated by

Zhou et al. However, it may be noted that, due to the limited wavelength range of measurement (1.5 eV – 3.5 eV), the exact value of band gap cannot be determined from the recorded PA spectrum.

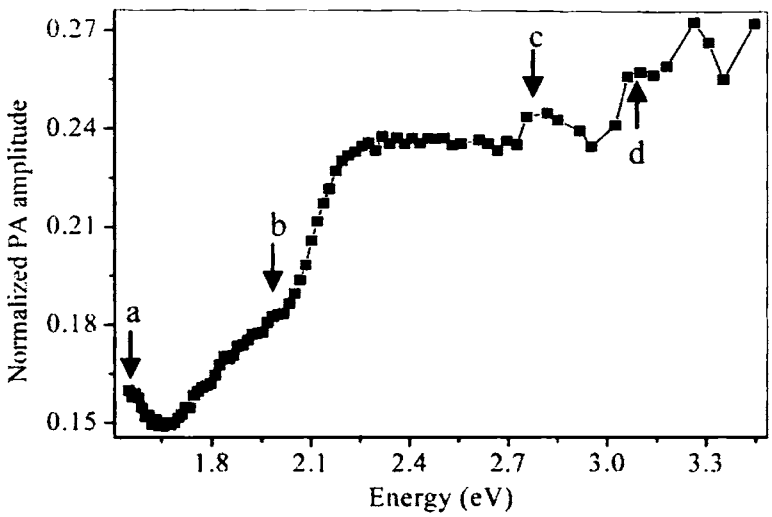

Fig.4.6 The PA spectrum of $LiFePO_4$

Table 4.1 Energy values of peaks identified in the PA spectrum

Peaks	a	b	c	d
Energy	1.55 eV (800 nm)	2.03 eV (611 nm)	2.79 eV (444 nm)	3.0 eV (413 nm)

In $LiFePO_4$, Fe ions being in the octahedral environment of the O^{2-} ions, 3d bands of the Fe are split into states of t_{2g} (three fold) and e_g (two fold) symmetries. According to Xu et al, the Fermi level lies in the t_{2g} spin down band and in the gap of the spin up bands with $t_{2g}^{3\uparrow}e_{2g}^{2\uparrow}$, $t_{2g}^{1\downarrow}e_{2g}^{0\downarrow}$ being the possible electronic configuration [40]. There exists an energy gap between the 3d up spin and 3d down spin bands as well as between the down spin levels $t_{2g}^{\downarrow}$ and $e_{2g}^{\downarrow}$. The spectral features

observed in the figure 4.6 complies well with the density of states calculated on the basis the above electronic band structure. The recent work by Hunt et al [40,65] utilizing Resonant Inelastic X ray Scattering (RIXS) also agrees well with the DOS prediction by Xu et al [40,41].

Table 4.2 Comparison between absorption peaks experimentally obtained and theoretically predicted with the corresponding electronic transitions

Transitions	Experimental (eV)	Literature
$e_{2gu}^{\uparrow} - t_{2gm}^{\downarrow}$	1.55	1.5 [40,41]
$e_{2gu}^{\uparrow} - t_{2gu}^{\downarrow}$, $e_{2gl}^{\uparrow} - t_{2gm}^{\downarrow}$	2.03	2.0 [40,41,65]
$e_{2gu}^{\uparrow} - e_{2gl}^{\downarrow}$	2.79	2.6-2.7 [40,41,65]
$t_{2gl}^{\uparrow} - t_{2gm}^{\downarrow}$, $t_{2gu}^{\uparrow} - t_{2gu}^{\downarrow}$, $e_{2gl}^{\uparrow} - t_{2gu}^{\downarrow}$, $e_{2gu}^{\uparrow} - e_{2gu}^{\downarrow}$	3.0	3.0 [40,41,65]

Four major spectral features denoted by arrows i.e. the half peak around 1.5 eV, a jump in absorption around 2.03 eV, a small peak around 2.79 eV and the absorption features in and around the range 3 eV are discussed. All these peaks correspond to the transitions between the 3d spin up states $t_{2g}^{\uparrow}e_{2g}^{\uparrow}$ and the 3d spin down states $t_{2g}^{\downarrow}$ and $e_{2g}^{\downarrow}$ above the Fermi level. The peak around 1.5 eV corresponds to the transition from $e_{2gu}^{\uparrow}$ spin up state below the Fermi level to upper level of $t_{2gm}^{\downarrow}$ (m denotes the middle level and u represents the upper level). The surge in absorption around 2.03 eV could possibly be due to different transitions like $e_{2gu}^{\uparrow}$ to the two levels of $t_{2g}^{\downarrow}$ (i.e. $t_{2gm}^{\downarrow}$ and $t_{2gu}^{\downarrow}$) lying above the Fermi level having slightly different energies. The small peak at 2.79 eV can be attributed to the transition from $e_{2gu}^{\uparrow}$ (upper level of spin up band $e_{2g}^{\uparrow}$) to lower level of spin down band

$e_{2gl}^{\downarrow}$. The absorption peak around 3 eV can be due to various transitions, from lower level of the spin up t_{2g} band, $t_{2gl}^{\uparrow}$ to the middle level of the spin down t_{2g} band, $t_{2gm}^{\downarrow}$, from the upper level of spin up t_{2g} band, $t_{2gu}^{\uparrow}$, to the upper level of the spin down t_{2g} band, $t_{2gu}^{\downarrow}$ and from upper level of the spin up band $e_{2gu}^{\uparrow}$ to the upper level of the spin down band $e_{2gu}^{\downarrow}$. For the sake of clarity, these transitions are tabulated in the table 4.2. Please note that u, m and l subscripts denote upper, middle and lower levels.

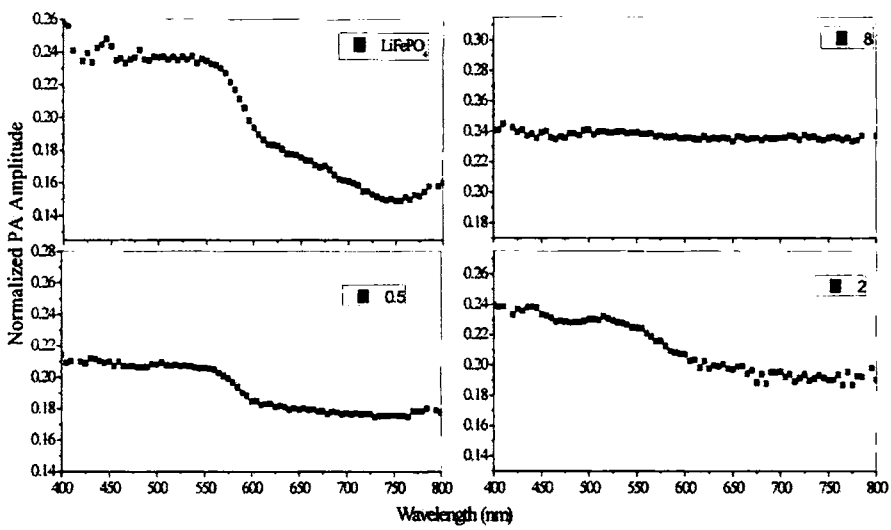

Fig. 4.7 Shows a comparison between the PA spectrum of pure $LiFePO_4$ and spectra of $LiFePO_4$ having 0.5%, 2% and 8% of MWNT as additives.

Figure 4.7 depicts the modification of the absorption spectrum of $LiFePO_4$ upon addition of MWNT. The major difference between the pure and MWNT added samples are in the region of 550 nm - 800 nm (1.5 eV – 2.25 eV). As the concentration of MWNT increases this

region becomes relatively flat with almost equal absorption through out, suggesting a broad absorption in these regions. Besides, the major jump in the absorption around 2 eV, seems to be decreasing with increase in MWNT concentration or rather this could be due to the fact that as the absorption in the region 600nm-800 nm increases, the amplitude of the jump is reduced. Moreover, the peak around 1.5 eV (i.e 800 nm) is suppressed as the doping concentration increases. We propose that these observations could possibly be due to a combination of two phenomena while MWNT is introduced in $LiFePO_4$ namely the coulomb interaction between the MWNT and the transition metal ion Fe in $LiFePO_4$, which broadens the already existing energy levels and introduction of defect states in the energy gap between spin up and spin down 3d bands. These two phenomena create room for almost continuous absorption as the concentration of carbon nanotube reaches 8%, throughout the entire excitation wavelength.

4.5 Electrical Properties of Pure and MWNT Doped $LiFePO_4$

Electrical conductivity measurement is an extensively used tool for investigating the mechanism of charge transport in materials in addition to its potential use for probing structural defects and internal purity of crystalline solids. The investigations carried out till date on a variety of materials describing their electrical conductivity in terms of electrons/holes, polarons, impurities etc give the electrical conduction a firm footing. Most of the battery materials available show dielectric

property and show the special property of storing and dissipating electrical energy when subjected to electric fields.

In the case of $LiFePO_4$, it has been recently reported that the electron transport mechanism is by means of small polarons [47]. The concept of small polaron model has been detailed in several articles [48,49]. When excess charge carriers like electrons or holes are present in a polar crystal, the atoms in its environment will be polarized and displaced and produce a local lattice distortion. The ion displacement becomes more pronounced as the charge carriers become more and more localized. The carrier lowers its energy by localizing into such a lattice deformation and becomes self trapped. This quasi particle formed by the electron and its self-induced distortion is called a small polaron if the range of lattice distortion is of the order of lattice constant. These charge carriers can be either electrons or holes in $LiFePO_4$. Since the hopping process dominates the electrical transport in this material, the dielectric measurements will provide useful information on the polaron dynamics, because a hopping process of polarons has a high probability of involving a dielectric relaxation that contains several significant parameters in the elucidation of the polaron dynamics [50-53].

It is observed that the electrical conductivities, both ac and dc conductivity, of MWNT added $LiFePO_4$ is directly related to the MWNT concentration. The observed improvement of electrical conductivities (dc conductivity) upon adding MWNT shown in Figure 4.8 is substantiated on the basis of complex impedance analysis.

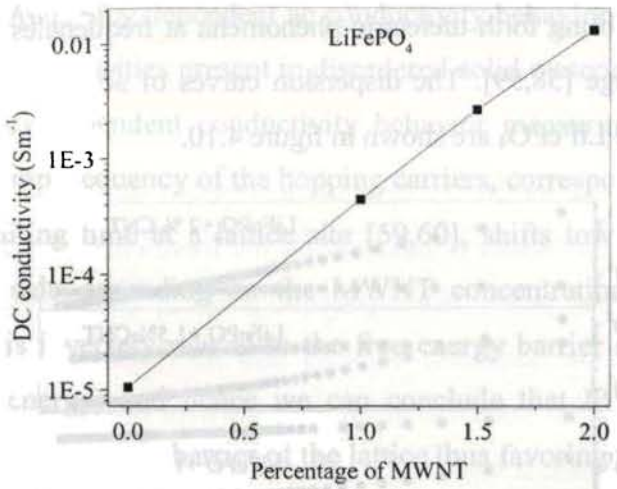

Fig. 4.8 DC conductivity is shown as a function of MWNT concentration

As mentioned earlier $LiFePO_4$ is regarded as a small polaron semiconductor similar to other Li-ion battery cathode materials such as $LiMn_2O_4$, where its electronic conductivity is associated with charge carrier hopping [54-57]. The loss tangent plots also do not show any peak, thus associating their dielectric behavior to hopping of charge carriers [56]. The dispersion curves of the real and imaginary parts of the complex dielectric constant for the doped and undoped $LiFePO_4$ are shown in figure 4.9. The shape of the curves of all the samples calls for 'charge carrier' behavior to be cited, instead of 'dipolar' behavior, as the dominant cause of their dielectric response [58]. These charge carriers, typically ions or hopping electrons, dominate the conducting and dielectric response by moving freely in extended trajectories, thus producing 'giant polarizabilities'. From the observation of Low Frequency Dispersion (LFD), a term used to identify dielectric behavior due to electron hopping, in $LiFePO_4$, it can be deduced that the electrons here are not free due to

their ability to bring forth dielectric phenomena at frequencies below the microwave range [58,59]. The dispersion curves of ac conductivities of doped and pure $LiFePO_4$ are shown in figure 4.10.

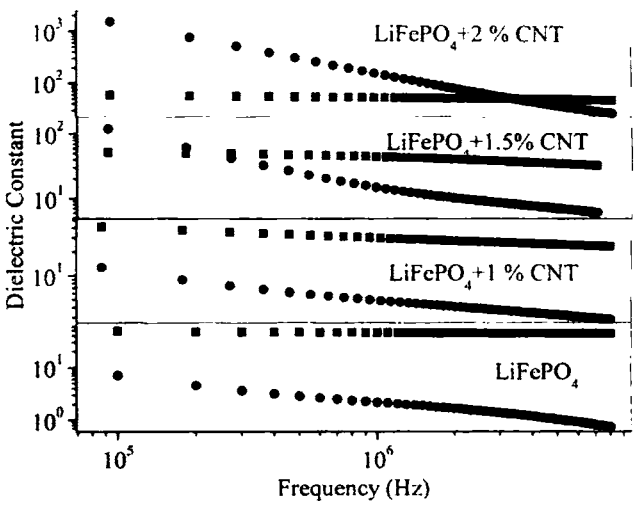

Fig. 4.9 Dispersion curves of Real Part [■] and Imaginary Part [•] of Dielectric Constant

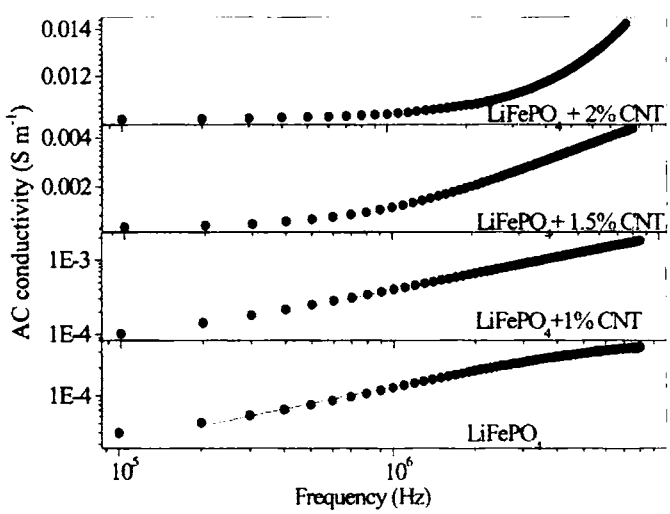

Fig. 4.10 Dispersion curves of ac conductivities of MWNTdoped and pure $LiFePO_4$

This frequency dependent ac conductivity behavior is a signature of the in homogeneities present in disordered solid materials. The onset of frequency dependent conductivity behavior measuring the lowest effective jump frequency of the hopping carriers, corresponding to their longest waiting time at a lattice site [59,60], shifts towards the high frequency side depending on the MWNT concentration. This jump frequency is inversely related to the free energy barrier (related to ac activation energy) and hence we can conclude that MWNT doping reduces the free energy barrier of the lattice thus favoring the electronic conduction process in MWNT doped $LiFePO_4$. Applying Jonscher's universal power law [60] to the frequency dependent ac behavior, the hopping frequencies are calculated and are given in Table 4.3 .It is evident that there is a sudden surge of hopping frequency value upon one percent doping with MWNT and this increase continues for higher doping concentrations. The diffusion coefficient of carriers is the product of hopping length squared and hopping frequency [61]. Therefore, it is possible to assign a direct correlation between electrical conductivities, both ac and dc parts and the electron diffusion coefficient and hence the hopping frequency.

Table 4.3 Hopping frequencies are given as a function of MWNT doping concentration

MWNT doping concentration	0 percent	1 percent	1.5 percent	2 percent
Hopping Frequency	18.9 KHz	1.21 MHz	3.6 MHz	8.12 MHz

Dielectric response due to carrier hopping can also be described on the basis of quasi-DC conduction (q-DC) model of Dissado and Hill, where the transport of charged particles is assumed to be along defined paths such that the longer the displacement of the charge, the lower the number of paths available or equivalently the more difficult the transport becomes [62]. The power law exponents, given in Table 4.4, calculated independently from dielectric constant and ac conductivity dispersion curves are found to coincide in accordance with the theory [63]. The power law exponent, n reflects the extent of binding between the charge transported (electron in the present case) and its counter charge (ion here). MWNT doping decreases the power law exponent except in the case for 1% MWNT doping. Therefore, it may be argued that MWNT doping, by and large reduces binding interaction between the electrons and the ions of the lattice thereby increasing the electronic conductivity of the material. The characteristic frequency defined as the frequency below which the charged particles become free of their locality ensuring movement to longer distances, obtained from dielectric constant dispersion curves, increases in accordance with the MWNT concentration as is the case for hopping frequency and conductivities. Hence, it may be envisaged that the addition of MWNT frees the electrons from their locality, contributing positively to the ac and dc conductivities of $LiFePO_4$.

Table 4.4 Power Law Exponent, n is given as a function of MWNT doping concentration

MWNT doping concentration	0 percent	1 percent	1.5 percent	2 percent
Power Law Exponent, n	0.61	0.71	0.60	0.30

The Nyquist plot obtained for $LiFePO_4$, shown in figure 4.11 is similar to that reported by Delacourt et.al [64]. It may be noted that the dielectric properties of the samples under study are measured only in the frequency range 10^5 – 10^7 Hz because the sample's resistance is too law to give a measurable dielectric behavior in other frequency ranges. This limitation in the frequency range restricts the manifestation of the expected complete semicircle for the Nyquist curve. Following the arguments of Delacourt et al, at room temperature, the only contribution to the curve for $LiFePO_4$ is expected from the bulk conduction in $LiFePO_4$ [64]. When the MWNT concentration is 1%, the crest of the semicircular Nyquist curve shifts towards high frequencies and with a higher concentration of 1.5% of MWNT, this trend continues and the crest of the semicircle is seen. When the MWNT concentration becomes 2% the Nyquist curve reaches still higher frequencies and hence the other side of the semicircle is seen here. It is obvious that as the MWNT doping concentration increases the material tries to have more contribution from the grain boundaries to electrical conduction. This may be due to the increase in the presence of high conducting phase (MWNT) outside the grains to reduce the cross-grain resistance, which is confirmed by TEM analysis.

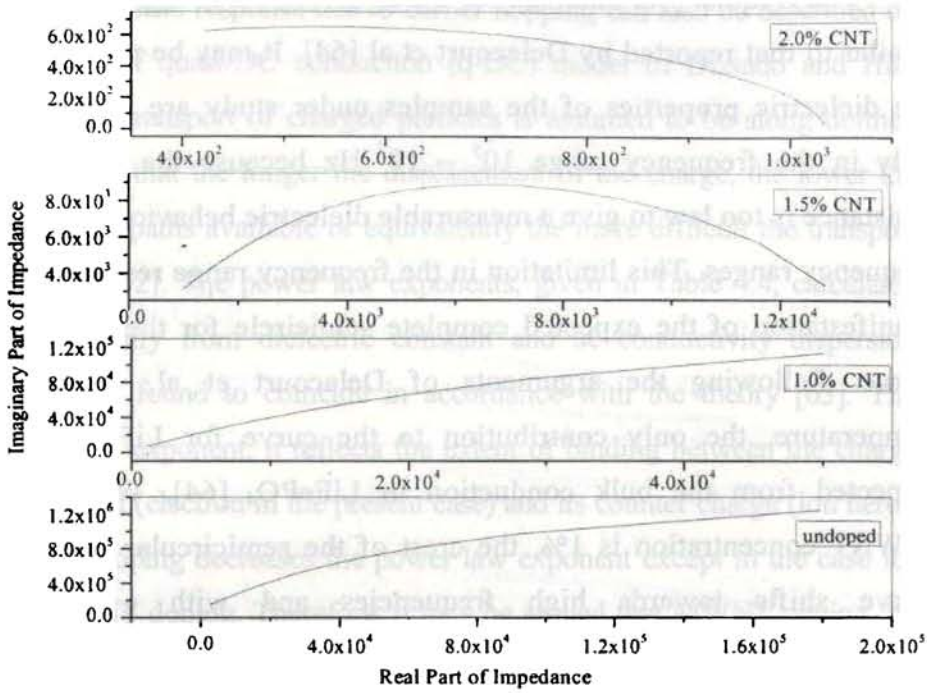

Fig. 4.11 Nyquists plots for pure and MWNT doped $LiFePO_4$

Hence, from the foregoing discussion it is clear beyond doubt that MWNT doping to $LiFePO_4$ improves its ac and dc electrical conductivity.

4.6 Band Gap Confirmation of Phospho Olivine $LiFePO_4$ and Effect of Carbon Nano Tube on its Electronic Band Structure

The attempts of several workers by different approaches based on Density Functional Theory (DFT) for a complete understanding of electronic structure of $LiFePO_4$, have led to a notable controversy regarding the band gap as mentioned earlier [11,40-46,65,66] and the electronic structure of the material. Although, most of researchers have agreed to a band gap between 0 and 1 eV [11,40-45,65] a recent work

by Zhou et al has reported a value of 3.7 eV calculating it using Generalized Gradient Approximation (GGA) +U computation and proved it using a Diffuse Reflectance Spectrum (DRS) in a limited wavelength range 250 nm-550 nm [46,66]. An attempt to resolve this dispute can shed light on the density of states and hence on the electronic band structure.

In this study, we have estimated the band gap of $LiFePO_4$ from a reflectance spectrum recorded in the range 300-2000 nm to clear the air of ambiguity surrounding the band gap. We have also assigned the peaks, which agree well with the density of states calculation of Xu et al [40,41] and electronic structure prediction using Resonant Inelastic X-ray Scattering (RIXS) by Hunt et al [65]. We have also doped $LiFePO_4$ with 0.5%, 1% and 2% MWNT with a view to improving its electrical conductivity. MWNTs are well known for its high electrical and thermal conductivities along with many other highly desirable properties [22-32]. The influence of doping MWNT on the electronic band structure of $LiFePO_4$ is also studied.

The reflectance spectra are recorded using a portable radiometer, Field spec^{TM} in the range 300-2000 nm with a spectral resolution of 1nm. A tungsten halogen lamp (150W) is used as the excitation source. The reflected light was collected using a fibre optic bundle having an acceptance angle of 25 degrees provided along with the instrument [67]. This implies that the distance between the sample and the fibre bundle determines the collection area. The stray light is avoided using a black background. The spectrum of the excitation lamp used is first

recorded using a teflon piece and is then normalized from the sample spectra to obtain the reflectance.

The diffuse reflectance spectrum of $LiFePO_4$ is as shown in figure 4.12. The onset of the linear increase of reflectance can be correlated with the tail of the absorption spectrum [68,69] and using this definition the band gap is estimated to be 0.83 eV where the reflectance reduces roughly by 45%. This is well in agreement with the calculated band gap range of Xu et al [40,41]. However, Zhou et al [66] has recently reported a band gap of 3.7 eV for $LiFePO_4$ from diffuse reflectance spectra in the range 200 nm-550nm with a mention that no significant change has been detected till 2000nm which is contradictory to spectrum shown in figure 4.12. Moreover, in the spectrum reported by Zhou et al, the maximum reflectance is only about 25% which itself, is low. Figure 4.13 shows the range 2.75eV-4eV (450 nm-300 nm) of our spectrum and it can be clearly seen that the reflectance is considerably small in this range compared to the rest of the spectral range suggesting high absorption at these wavelengths. In addition, the dip at 1.55 eV should correspond to an absorption peak, which is highly unlikely for being an excited state absorption at these power levels of excitation light beam.

The dips at 0.91eV, 1.25 eV, 1.55 eV, 2.eV, 2.5 eV and 3.6 eV in the reflectance spectrum are likely to correspond to various allowed transitions which can be explained by Density of States (DOS) calculated by Xu et al [40,41] and also agrees well with the DOS calculated using Resonant Inelastic X ray Scattering (RIXS) by Hunt et al [65-69]. The energy values corresponding to the dips in the

reflectance spectrum are correlated with DOS prediction by these calculations and are tabulated in table 4.5. (note that the subscript *l* , *m* and *u* together with g denotes lower, middle and upper respectively).

Figure 4.14 shows the spectra recorded by doping $LiFePO_4$ with 0.5%, 1% and 2 % of MWNT. The doping has affected considerably the spectral range1200 nm-2000 nm (~1eV-0.62eV), where the overall reflectance reduces progressively as the doping concentration increases. Moreover, the dip observed at 0.91 eV vanishes completely. We propose that these observations could be possibly due to a combination of two phenomena while MWNT is introduced in $LiFePO_4$ namely (i) the coulomb interaction between the MWNT and the transition metal ion Fe in $LiFePO_4$, which broadens the already existing energy levels and (ii) introduction of defect states in the energy gap between spin up and spin down 3d bands and in between the $t_{2g}^{\downarrow}$ and $e_{2g}^{\downarrow}$ 3d spin down bands. Hence the disappearance of the spectral feature at 0.91 eV and the overall reduction in the reflectance could be attributed to the additional levels formed in between the $t_{2g}^{\downarrow}$ and $e_{2g}^{\downarrow}$ 3d spin down bands forming almost a continuum when the doping reaches 2%.

Figure 4.15 shows the expanded graph in the visible region in order to have a clear understanding of changes in this region due to doping. The reflectance peak at around 680 nm (~1.8eV) in $LiFePO_4$ is suppressed and when the doping concentration is 2%, the region is almost flat. In other words, the prominent dip around 790 nm (~1.55 eV) is disappearing as the doping concentration reaches 2% and the overall reflectance is

considerably reduced. This implies that on doping with MWNT, additional energy levels are not only formed between the $t_{2g}^{\downarrow}$ and $e_{2g}^{\downarrow}$ 3d spin down bands but also in the gap between 3d spin up and spin down bands.

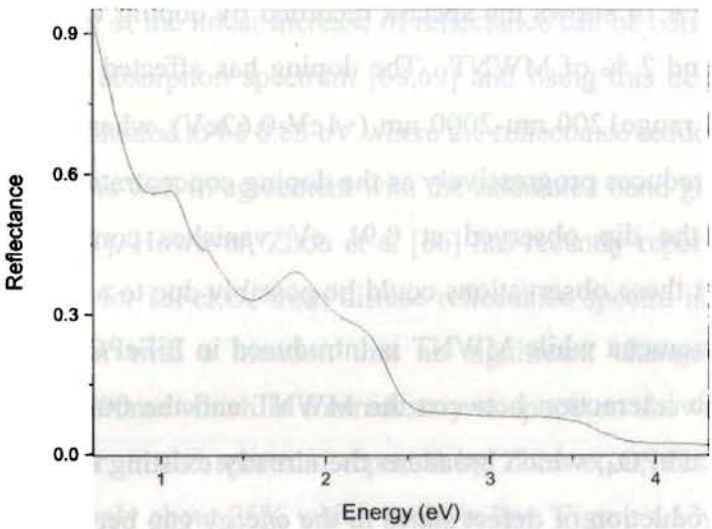

Fig. 4.12 The diffuse reflectance spectrum of $LiFePO_4$

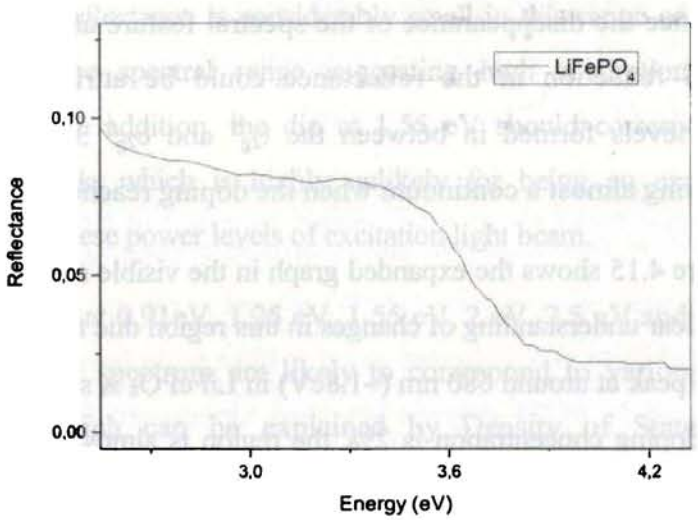

Fig. 4.13 Variation of reflectance with energy in the range 2.75eV-4eV (450 nm-300 nm)

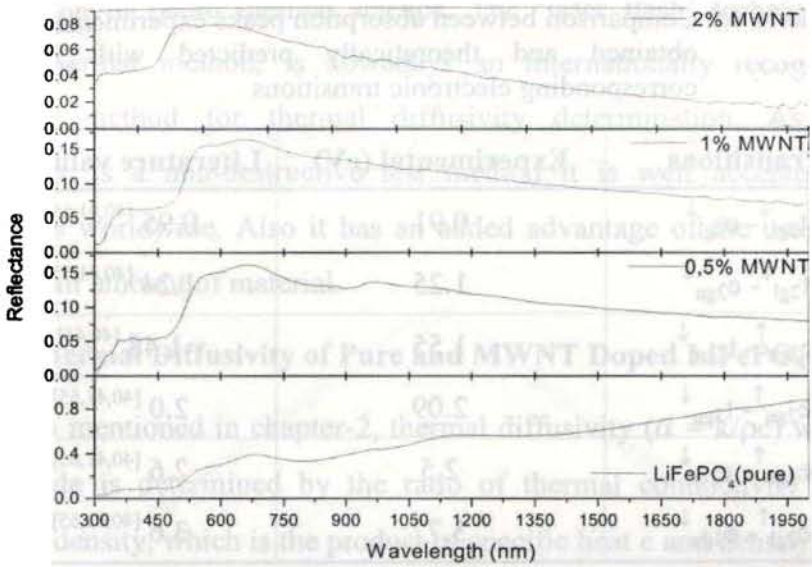

Fig.4.14 Diffuse reflectance spectra recorded by doping $LiFePO_4$ with 0.5%, 1% and 2 % of MWNT.

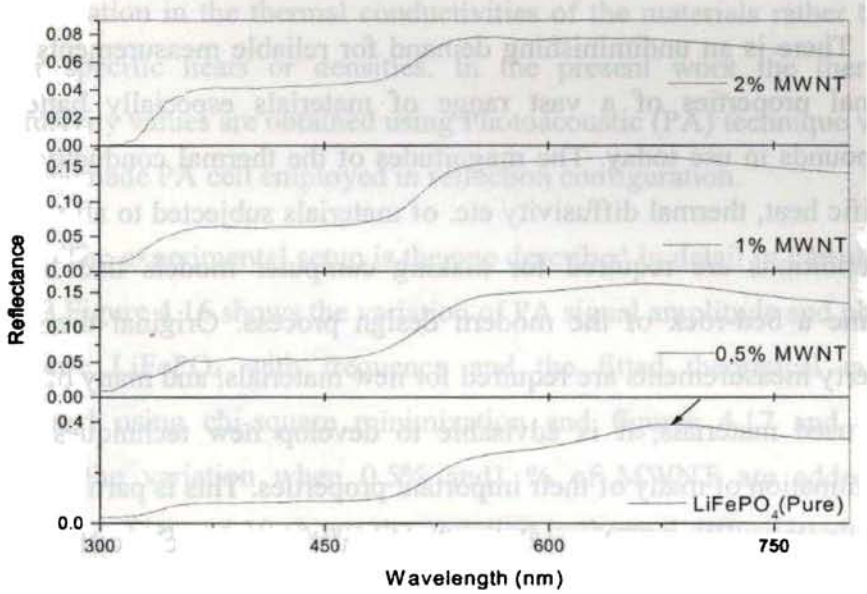

Fig.4.15 Shows the expanded graph in the visible region

Table 4.5 Comparison between absorption peaks experimentally obtained and theoretically predicted with the corresponding electronic transitions

Transitions	Experimental (eV)	Literature value(eV)
$t_{2gl}^{\downarrow} - e_{2gl}^{\downarrow}$	0.91	0.95 [40,41,65]
$t_{2gl}^{\downarrow} - e_{2gu}^{\downarrow}$	1.25	1.24 [40,41,65]
$e_{2gu}^{\uparrow} - t_{2gm}^{\downarrow}$	1.55	1.48 [40,41]
$e_{2gu}^{\uparrow} - t_{2gu}^{\downarrow}$	2.09	2.0 [40,41,65]
$e_{2gu}^{\uparrow} - e_{2gl}^{\downarrow}$	2.5	2.6 [40,41,65]
$e_{2gl}^{\uparrow} - e_{2gu}^{\downarrow}$	3.77	3.6 [40,41,65]

4.7 Thermal Characterization of $LiFePO_4$ using Photoacoustic Technique

There is an undiminishing demand for reliable measurements of thermal properties of a vast range of materials especially battery compounds in use today. The magnitudes of the thermal conductivity, specific heat, thermal diffusivity etc. of materials subjected to all types of conditions are required for making computer models that have become a bed-rock of the modern design process. Original thermal property measurements are required for new materials, and many of the long used materials, it is advisable to develop new techniques for determination of many of their important properties. This is particularly true of thermal diffusivity/thermal conductivity which can vary considerably with composition and microstructure produced in a material during specific production process. The determination of the thermal properties has become an important well-established

application of photo thermal science. The 'laser flash' technique, a photo thermal method, is nowadays an internationally recognized standard method for thermal diffusivity determination. As this technique is a non-destructive test method it is well accepted by scientists worldwide. Also it has an added advantage of the usage of very small amount of material.

4.7.1 Thermal Diffusivity of Pure and MWNT Doped $LiFePO_4$

As mentioned in chapter-2, thermal diffusivity ($\alpha = k/\rho c$) whose magnitude is determined by the ratio of thermal conductivity k to thermal density, which is the product of specific heat c and density ρ, is a thermal parameter, which determines the rate of heat diffusion in a medium. The "bulk" (solid samples) of this variation is a reflection of the variation in the thermal conductivities of the materials rather than their specific heats or densities. In the present work the thermal diffusivity values are obtained using Photoacoustic (PA) technique with a homemade PA cell employed in reflection configuration.

The experimental setup is the one described in detail in Chapter 2 and 3.Figure 4.16 shows the variation of PA signal amplitude and phase of pure $LiFePO_4$ with frequency and the fitted theoretical curve obtained using chi-square minimization and figures 4.17 and 4.18 shows the variation when 0.5% and1 % of MWNT are added to $LiFePO_4$. Figure 4.19 shows the variation in thermal diffusivity due to the addition of MWNT in different concentrations. The dots represent the experimental data and the line represents the theoretical fit to the experimental data according R - G theory [37-39,70]

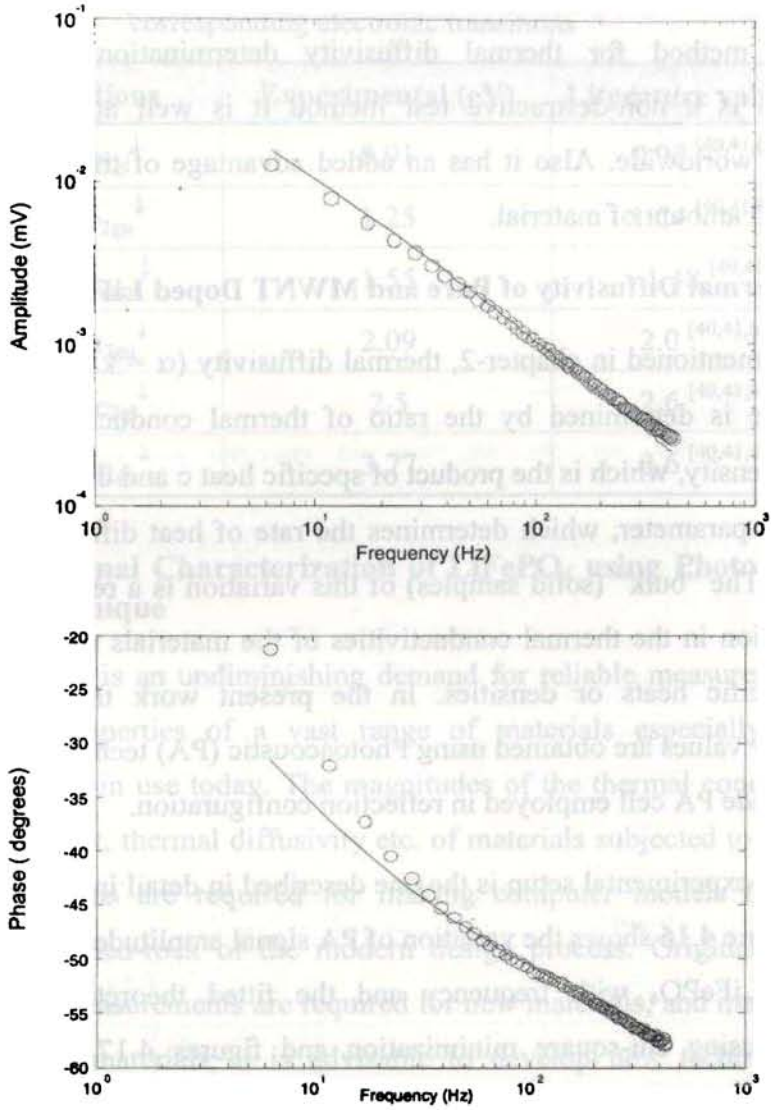

Fig.4.16 The experimentally obtained and theoretically fitted amplitude and phase variation of $LiFePO_4$with Frequency

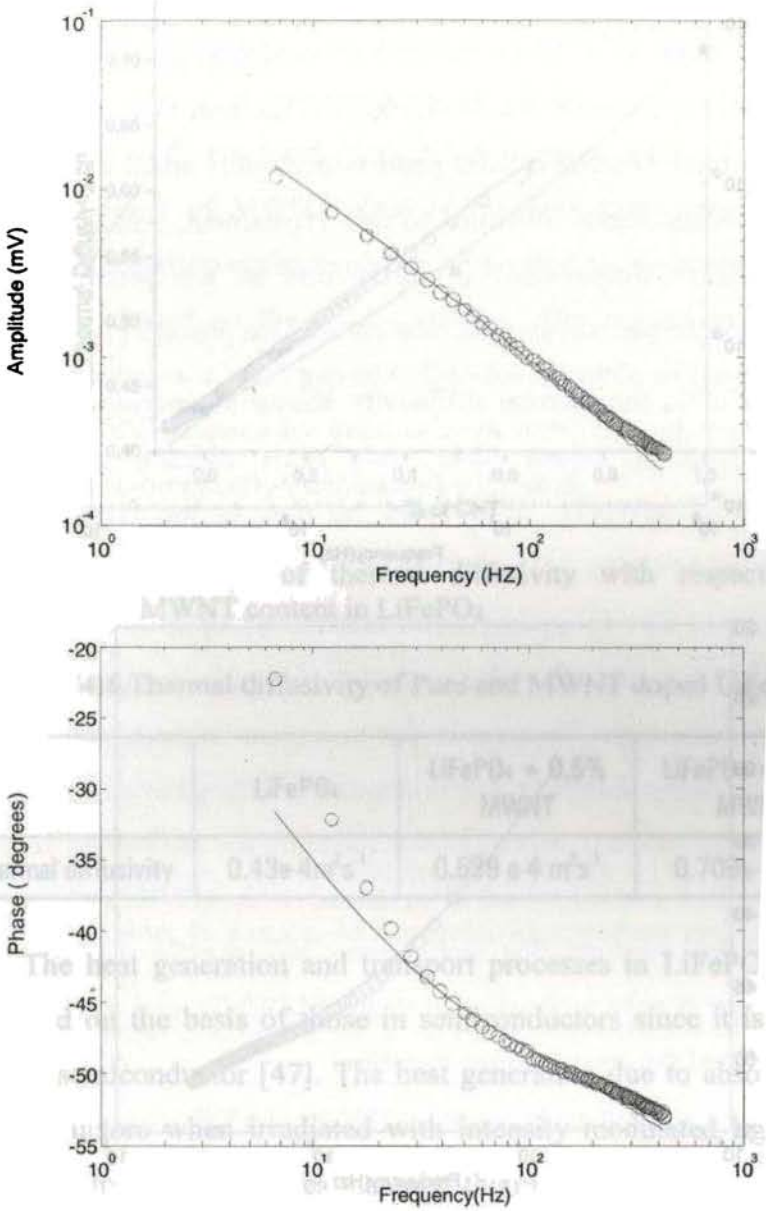

Fig. 4.17 The experimentally obtained and theoretically fitted amplitude and phase variation of $LiFePO_4$ + 0.5% MWNT with Frequency

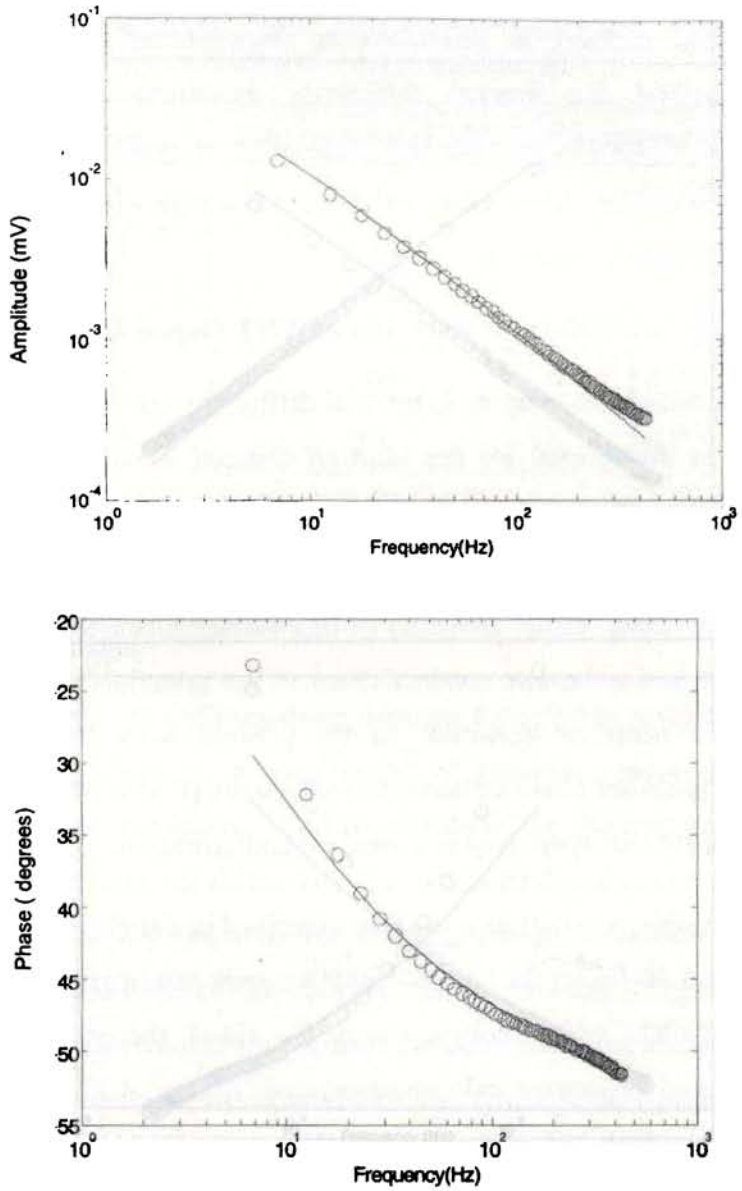

Fig 4.18 The experimentally obtained and theoretically fitted amplitude and phase variation of LiFePO4 + 1%MWNTwith Frequency

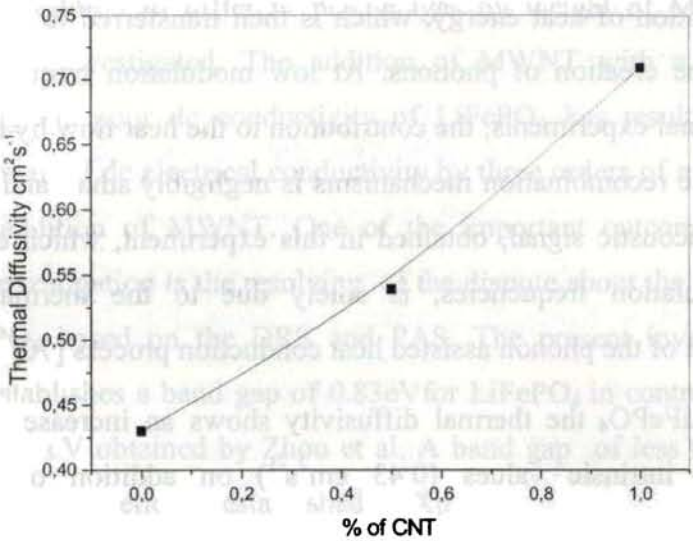

Fig. 4.19: Variation of thermal diffusivity with respect to MWNT content in $LiFePO_4$

Table 4.6. Thermal diffusivity of Pure and MWNT doped $LiFePO_4$

	$LiFePO_4$	$LiFePO_4$ + 0.5% MWNT	$LiFePO_4$ + 1.0 % MWNT
Thermal diffusivity	0.43e-4m^2s^{-1}	0.539 e-4 m^2s^{-1}	0.709e-4 m^2s^{-1}

The heat generation and transport processes in $LiFePO_4$ can be explained on the basis of those in semiconductors since it is a small polaron semiconductor [47]. The heat generation due to absorption in semiconductors when irradiated with intensity modulated light beam arises due to three processes, namely, thermalisation due to intraband transitions of photogenerated carriers, and nonradiative bulk recombination and surface recombination due to interband transitions of photogenerated carriers. All these different mechanisms finally result

in the creation of heat energy, which is then transferred to the lattice through the creation of phonons. At low modulation frequencies of photothermal experiments, the contribution to the heat flow by the bulk and surface recombination mechanisms is negligibly small and, hence, the photoacoustic signal, obtained in this experiment, which employs low modulation frequencies, is solely due to the thermal wave component of the phonon assisted heat conduction process [70].

In $LiFePO_4$ the thermal diffusivity shows an increase from its respective intrinsic values (0.43 cm^2s^{-1}) on addition of various percentages of MWNTs. This could be due to the high thermal diffusivity of MWNTs (~1cm^2s^{-1}) [71]. The increase in the thermal diffusivity may also be an indication that the addition of MWNTs to $LiFePO_4$ does not cause any change in the original lattice structure and the crystal symmetry. We support this argument using a well-known fact that any lattice distortion due to dopants or change in size of atoms will scatter the lattice phonons thereby reducing the thermal diffusivity [72]. The TEM picture of $LiFePO_4$ doped with MWNTs shown in figure 4.4 also supports this fact. Hence, we propose that in these samples there is only a physical mixing of MWNTs and the addition has not affected the crystal lattice structure.

4.8 Conclusions

$LiFePO_4$ phospho olivine micro crystalline sample has been successfully prepared by employing solid state reaction technique and detailed investigations have been carried out on its structural, thermal, optical and electrical propreties. The modifications of these properties

upon the addition of different percentages by weight of MWNT to $LiFePO_4$ are ivestigated. The addition of MWNT with a view to improving the poor dc conductivity of $LiFePO_4$ has resulted in an enhancement of dc electrical conductivity by three orders of magnitude for 2% addition of MWNT. One of the important outcome of the present investigation is the resolving of the dispute about the band gap of $LiFePO_4$ based on the DRS and PAS. The present investigation clearly establishes a band gap of 0.83eVfor $LiFePO_4$ in contrast to the value of 3.7eV obtained by Zhou et al. A band gap of less than 1eV has also been thoretically established by Xu et al.

References

[1] Padhi, A. K.; Nanjundaswamy, K. S.; Goodenough, J. B. J. Electrochem. Soc., 144, 1188 (1997)

[2] Yamada, A.; Chung, S. C.; Hinokuma, K. J. Electrochem. Soc.,148, A224 (2001)

[3] Masquelier, C.; Padhi, A. K.; Nanjundaswamy, K. S.; Goodenough, J. B. J. Solid State Chem. 135, 22 (1998)

[4] K.Amine, H.Yasuda, M.Yamachi, Electrochem and solid state Lett. 3, 178 (2000)

[5] A.Yamada, Y.Kudo., K Y Liu, J.Electrochem.Soc.148 A 1153 (2001)

[6] A.Yamada, Y.Kudo., K Y Liu, J.Electrochem.Soc.148 A 747 (2001)

[7] S. Geller., J.L.Durand., Acta Crystallogr., 13, 325 (1960)

[8] F.Zhou, C A Marianetti, M.Cococcioni, D.Morgan and G.Ceder Phy.Rev B. 69, 201101(R) (2004).

[9] C. V. Ramana, A. Ait-Salah, S. Utsunomiya,U Becker, A. Mauger, F. Gendron,C. M. Julien Chem. Mater. 18, 3788 (2006)

[10] J.M.Tarascon and M Armand, Nature , 414, 359 (2006)

[11] A. Yamada, M. Hosoya, S.-C. Chung, K. Hinokuma, Y. Kudo, K.-Y. Liu, in: A. Manthiram, P.N. Kumta, S.K. Sundaram and G. Ceder (Eds.), Materials for Electrochemical Energy Conversion and Storage, American Ceramic Society, Westerville,189 (2002)

[12] A. Yamada, M. Hosoya, S.C. Chung, Y. Kudo, K.Y. Liu, in: G. Nadri, R. Koetz, B. Scrosati, P.A. Moro, E.S. Takeuchi (Eds.), Advanced Batteries and Super capacitors, The Electrochemical Society, Pennington, NJ, PV2001 (2001)

[13] S-Y Chung, J.T. Bloking., Y.-M. Chiang, Nature Materials, 1, 123-128 (2002)

[14] P. Subramanya Herle, B. Ellis, N. Coombs and l. F. Nazar, Nature materials 3, 147 (2004)

[15] H.Huang, S.-C.Yin, L. F. Nazar, Electrochem. Solid-State Lett., 4, A170 (2001)

[16] Y.Inaba et al.Extended abstracts of the 22nd symposium on Solid state Ionics in Japan p.53(1993)

[17] S. S. Zhang , J. L. Allen, K. Xu and T. R. Jow, J. Power Sources, 147, 234 (2005)

[18] F. Croce, A. D'Epifanio, J. Hassoun, A. Deptula, T. Olczac and B. Scrosati, Electrochem. Solid State Lett. 5 A47 (2002)

[19] K.S. Park, J.T. Son, H.T. Chung, S.J. Kim, C.H. Lee, K.T. Kang, H.G. Kim, Solid State Commun. 129, 311 (2004)

[20] S. Shi, L. Liu, C. Ouyang, D.S. Wang, Z. Wang, L. Chen, X. Huang, Phys. Rev. B 68, 195108 (2003)

[21] A. Singhal, G. Skandan, G. Amatucci, F. Badway, N. Ye, A. Manthiram, H. Ye, J.J. Xu, J. Power Sources 129,38 (2004)

[22] S. Iijima, Nature 354, 56 (1991)

[23] M. Endo, S. Iijima, and M.S. Dresselhaus, Carbon Nanotubes, Carbon 33 (1996)

[24] T. W. Ehhesen and P. M. Ajayan, Nature 358, 220 (1992)

[25] M. Endo and H. W. Kroto, J. Phys. Chem. 96, 6941 (1992).

[26] J. W. G. Wildoer, L. C. Venema, A. G. Rinzler†, R. E. Smalley. & C. Dekker, Nature, 391, 59 (1998)

[27] C. Dekker, Physics Today 52, 22 (1999)

[28] http://online.kitp.ucsb.edu/online/qhall_c98/dekker/

[29] P. M. Ajayan, Chem. Rev. 99, 1787 (1999)

[30] T Bordjiba, M Mohamedi1 and L e H Dao, Nanotechnology 18, 035202 (2007)

[31] H. W. Ch. Postma, T. Teepen, Z. Yao, M. Grifoni, and C.Dekker 293, 76 (2001)

[32] J. Zhao, A. Buldum, J. Han, and J. Lu, Phys. Rev. Lett. 85, 1706 (2000)

[33] B. Gao, C. Bower, J. Lorentzen, L. Fleming, A. Kleinhammes, X. Tang, L. McNeil, Y. Wu, and O. Zhou, Chem. Phys. Lett. 327, 69 (2000)

[34] H. Shimoda, B. Gao, X. P. Tang, A. Kleinhammes, L. Fleming, Y.Wu, and O. Zhou, Phys. Rev. Lett. 88, 015502 (2001)

[35] K. Nishidate and M. Hasegawa, Phys. Rev. B 71, 245418 (2005)

[36] V. Meunier, J. Kephart, C. Roland, and J. Bernholc, Phys. Rev. Lett. 88, 075506-1 (2002)

[37] A.Rosencwaig, Phys. Today, September, 23,(1975)

[38] A.Rosencwaig and A.Gersho, Science, 190, 556,(1975)

[39] A.Rosencwaig and A.Gersho,J. Appl. Phys, 64, 64, (1976)

[40] Xu Y -N, Chung S -Y, Bloking J T Chiang Y-M and Ching W Y Electrochem. Solid State Lett. 7 A131 (2004)

[41] Xu Y -N, Ching W Y and Chiang Y -M J. *Appl. Phys* 95 6583(2004)

[42] Tang P and Holzwarth N A W *Phys. Rev. B* 68 165107(2003)

[43] Yamada A, Hosoya H, Chung S –C, Kudo Y, Hinokuma K, Liu K –Y and Nishi Y, *J. Power Sources* 119-121, 232 (2003)

[44] Shi S, Ouyang C, Xiong, Z, Liu L, Wang Z, Li H, Wang D-s, Chen L and Huang X Phys. Rev. B 71, 144404 (2005)

[45] Shi, S. Liu, L. Ouyang, C. Wang, D. S. Wang, Z. Chen, L. & Huang, X. *Phys. Rev. B* 68, 195108 (2003)

[46] Zhou F, Cococcioni M, Marianetti C A, Morgan D and Ceder G Phys. Rev. B 70 235121(2004)

[47] Thomas Maxisch, Fei Zhou and Gerbrand Ceder Physical review B 73, 104301 (2006)

[48] David Emin, C. H. Seager, and Rod K. Quinn Phys. Rev. Lett. 28, 813 (1972)

[49] A. S. Alexandrov and P. E. Kornilovitch Phys. Rev. Lett. 82, 807 (1999)

[50] E. Iguchi, N. Nakamura and A. Aoki, Philosophical Magazine B, 78, 65 (1998)

[51] R. N. P. Choudhary,Soma Dutta, Awalendra Kumar Thakurand P. K. Sinha Ferroelectrics, 306, 55 (2004)

[52] Yan-Zhen Wei, S. Sridhar, J. Chem. Phys 99, 3119 (1993)

[53] S. K. S. Parashar, R. N. P. Choudhary, and B. S. Murty, J. Appl. Physics 94, 6091 (2003).

[54] S. Thomas Lee, K. Raveendranath, M. Rajive Tomy, M.Paulraj, S. Jayalekshmi, K. P. R. Nair and Jyotsna Ravi, Phys. Rev. B 76 115112-1 (2007)

[55] S. Thomas Lee, K. Raveendranath, M. Rajive Tomy, M.Paulraj, S. Jayalekshmi and Jyotsna Ravi, Appl. Phys. Lett 90 161912/1-3 (2007)

[56] S. Thomas Lee, K. Raveendranath, M. Rajive Tomy, Nibu A. George, S. Jayalekshmi and Jyotsna RaviJ.Phys. D: Appl. Phys. 40 3807-3810 (2007)

[57] K. Raveendranath, Rajive M. Tomy, S. Jayalekshmi, Jyotsna Ravi and S. Thomas Lee, Appl. Phys A DOI: 10.1007/s00339-007-4294(2007)

[58] B. Ellis, L. K. Perry, D. H. Ryan and L. F. Nazar, Small Polaron Hopping in Li_xFePO_4 Solid Solutions: Coupled Lithium-Ion and Electron Mobility, J. Am. Chem. Soc. 128 11416-11422 (2006)

[59] A. K. Jonscher, Dielectric Relaxation in Solids, J. Phys. D 32 R57 – R70 (1999)

[60] G. W. Bak and A. K. Jonscher, Low-frequency dispersion in hopping electronic systems, J. Mat. Sci. 34, 5505-5508 (1999)

[61] E. Barsoukov and J. R. Macdonald, Impedance Spectroscopy: Theory, Experiment, andApplications, Second Edition, John Wiley and Sons, 47 (2005)

[62] T. Ramdeen, L. A. Dissado and R. M. Hill, Influence of adsorbed water on the dielectric response of a ceramic material, J. Chem. Soc. Faraday Trans. 1 80, 325 (1984)

[63] S. Kasap, P. Capper, Dielectric Response, Springer Handbook of Electronic and Photonic Materials (2006)

[64] C. Delacort, L. Laffont, R. Bouchet, C. Wurm, J.-B. Leriche, M. Maorcrette, J.-M. Tarascon and C. Masquelier, Toward Understanding of Electrical Limitations (Electronic, Ionic) in $LiMPO_4$ (M=Fe, Mn) Electrode Materials, J. Electrochem. Soc. 152, A913-A921 (2005)

[65] Hunt A, Ching W –Y, Chiang Y –M and Moewes A *Phys. Rev. B* 73 205120(2006)

[66] F. Zhou, K. Kang, T.Maxisch, G. Ceder & D. Morgan Solid.State Communications, 132,181 (2004)

[67] Jyotsna Ravi, S. Thomas Lee, M. Paulraj & R. Hernandez, Appl. Spectroscopy 61 444 (2007)

[68] P. D. Fochs, Proc. Phys. Soc. 69, 70 (1955)

[69] D.M Liu and W.H.Taun,Mat.chem..and Phy,48,258(1997)

[70] N. A. George, C. P. G. Vallabhan, V. P. N. Nampoori, and P. Radhakrishnan, Opt. Eng. -Bellingham- 41, 251 (2002)

[71] Da Jiang Yang, Qing Zhang, George Chen, S. F. Yoon, J. Ahn, S. G. Wang, Q. Zhou, Q. Wang, and J. Q. Li Physical review B 66, 165440 (2002)

[72] K.Raveendranath, J.Ravi, S.Jayalekshmi, T M A Rasheed, K P R Nair, Mater.Sci.Eng.B. 131, 210-215, (2006)

Chapter 5

Structural Thermal Spectroscopic and Electrical Characterization of Phospho - Olivine $LiNiPO_4$ and Effect of Carbon Nano Tubes as Additives

A detailed account of the synthesis and various characterisation of lithium nickel phosphate ($LiNiPO_4$) form the essence of this chapter. The material is prepared by solid-state chemical reaction. Structural characterisations of $LiNiPO_4$ both in pristine and MWNT doped forms are done using X-ray diffraction (XRD), SEM (Scanning Electron Microscopy) and TEM (Transmission Electron Microscopy). The thermal properties of olivine $LiNiPO_4$ are determined by photoacoustic technique in reflection configuration. The photoacoustic signal amplitude and phase are simultaneously fitted using Rosencwaig-Gersho theory by solving three dimensional heat diffusion equations for obtaining the thermal diffusivity. The influence of adding various percentages by weights of MWNT to $LiNiPO_4$ is also investigated. Information of their electronic band structure of $LiNiPO_4$ is obtained from the wavelength dependence of its photoacoustic signal. Reflectance spectrum of $LiNiPO_4$ is recorded in the energy range 0.5 eV-3.5 eV. The dips in the reflectance spectra, which correspond to absorption peaks, are identified with various electronic transitions in accordance with existing theoretical predictions of its electronic band structure. The modification of the reflectance spectra on addition of various percentages by weights of multiwalled carbon nanotubes is explained on the basis of the formation of defect states. The dc electrical conductivity studies are also carried out in $LiNiPO_4$ and the effect of the addition of MWNT on the dc conductivity is also investigated.

5.1 Introduction

The pioneering work of Goodenough and co-workers in 1997 recognized phospho-olivines ($ABPO_4$) as promising positive electrode material for use in lithium ion rechargeable batteries. The potential of $LiMPO_4$ (M=Fe, Ni, Mn, Co) compounds for battery applications is the driving force for selecting $LiNiPO_4$ for the present investigation.

Lithium phosphates possess good chemical and thermal stability for technological applications they are now in the forefront among all other solid-state electrodes. Environmentally green and economically viable electrodes are the need of the hour. In these context $LiNiPO_4$ posses all these qualities, except the required range of electronic conductivity. Inspite of good cyclability and low cost it has inherently low electronic conductivity. In the present study attempts have been made to improve the electronic conductivity of $LiNiPO_4$ by adding MWNTs in different weight percentages.

The large family of compounds of the $ABPO_4$ type (A and B being mono- and divalent cations, respectively) exhibits different frameworks depending on the relative size of the A and B ions, for example, arcanite-, trydimite-, or olivine-type structures. For the A ions of small size, as in the case of Li^+, the resulting compounds, lithium transition metal phosphates ($LiMPO_4$ with M= Fe, Ni, Co, Mn) adopt the olivine-like (Mg_2SiO_4) structure containing high-spin M^{2+}ions. These phosphates exhibit a variety of structural features, the most prominent of which is the existence of tunnels in which small ions can move freely, a property that makes them potential hosts for the

insertion and extraction of ions. As a result of their high capacity, good thermal stability, and environmental benignity, these compounds have been proposed as alternative electrode materials for rechargeable lithium-ion batteries.

The crystal structure of $LiNiPO_4$ is made up of two types of polyhedra, distorted NiO_6 octahedral units that are corner shared and cross-linked with the PO_4 tetrahedral oxo-anions forming a three-dimensional network with tunnels that are occupied by Li ions along the (010) and (001) directions. In this network, nearly close-packed oxygen ions can be found in hexagons with Li and Ni ions located at the centre of octahedral sites. [1]. $LiNiPO_4$ has high redox potential [1-5,7], good thermal stability and high specific capacity but suffers from a serious setback, low electronic conductivity in the range from 10^{-10} S/cm to 10^{-5} S/cm, limiting its rate capability and, hence, their device applicability [8-11]. Though the source of the low electronic conductivity is controversial, many reports claim a correlation between the electronic conductivity and band gap. Various models have been proposed to calculate its electronic band structure where the electronic band structure and the band gap predict $LiNiPO_4$ to be an insulator or a semi metal [3, 6, 12-14].

A schematic representation of the olivine structure is shown in Figure5.1. As a result of this typical structural configuration, it is believed that the strong covalent PO_4 unit tends to reduce the covalency of the M-O bond, modifying the redox potential for the $M^{2+/3+}$ couple and thus producing a useful potential for lithium extraction and re

insertion. Various research groups using both experimental and theoretical methods have studied different aspects, such as synthesis, structural and vibrational properties, electrochemistry, and magnetism, of $LiMPO_4$ [12-14].

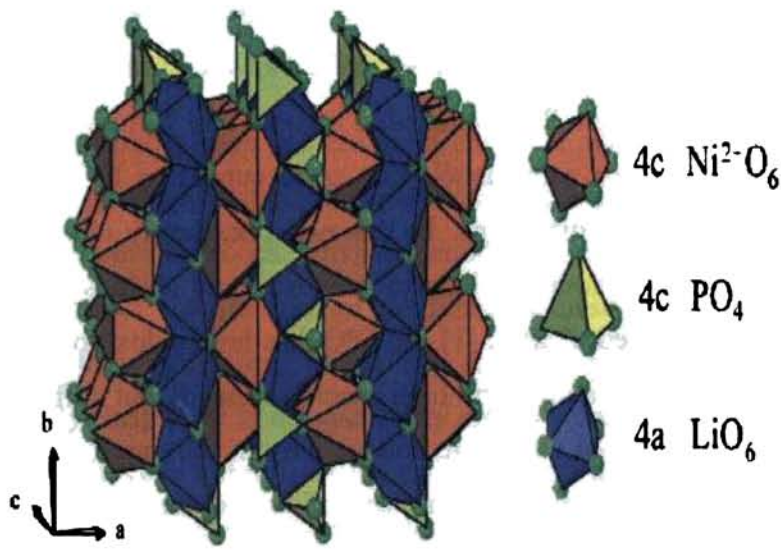

Fig. 5.1 Schematic representation of the olivine-like structure showing the three-dimensional network formed by cross-linked NiO_6 and PO_4 polyhedra.

5.2 Synthesis of $LiNiPO_4$

The $LiNiPO_4$ phospho-olivine is prepared as a microcrystalline powder by solid-state chemical reaction. The precursors used are Li_2CO_3, $(NH_4)_2HPO_4$ and NiO (99.9%pure). Stoichiometric amounts of reactants are mixed and ground in an agate mortar. The well ground mixture is pre-sintered at 120°C for 12hours and reground adding acetone for homogeneity in the mixture. The mixture is then heated at 500 °C for 4hours to drive away the gases. The

decomposed mixture is cooled and ground. The powder sample so obtained is pelletised at a load of 5T and is sintered in air at 800°C for 24hours.These pellets are then cooled to room temperature. MWNTs by different percentage of weights are added to $LiNiPO_4$ powder and mixed well. The mixtures are pelletised and are heated at 350 degrees for 5 hours in flowing Argon atmosphere. The compound obtained was characterized immediately after synthesis by X- ray diffraction analysis (Model: 1710 Regaku). The phase purity of the material was also confirmed by XRD analysis. The chemical reaction can be written as follows.

$$2NiO + 2(NH_4)_2HPO_4 + Li_2CO_3 \xrightarrow{800^0C} 2LiNiPO_4 + 4NH_3 + CO_2 + 3H_2O$$

5.3 Structural Characterisation

Figure 5.2 shows the X- ray Diffraction (XRD) spectrum of $LiNiPO_4$. It agrees well with the already reported XRD spectrum of $LiNiPO_4$ confirming the single-phase olivine like structure [8, 23]. The lattice parameters of $LiNiPO_4$ calculated from XRD pattern are $a\sim=9.96A^0$, $b\sim=5.82A^0$ and $c\sim= 4.64A^0$ which are well in agreement with the existing reports [24, 25]. Figure 5.3 shows the X-ray diffraction patterns of olivine $LiNiPO_4$, MWNT, and the nano composites of $LiNiPO_4$, with different weight percentages of MWNT. From the XRD spectrum it is seen that the olivine structure of $LiNiPO_4$ is slightly distorted (indicated by peak broadening) upon the addition of MWNTs for all concentrations.

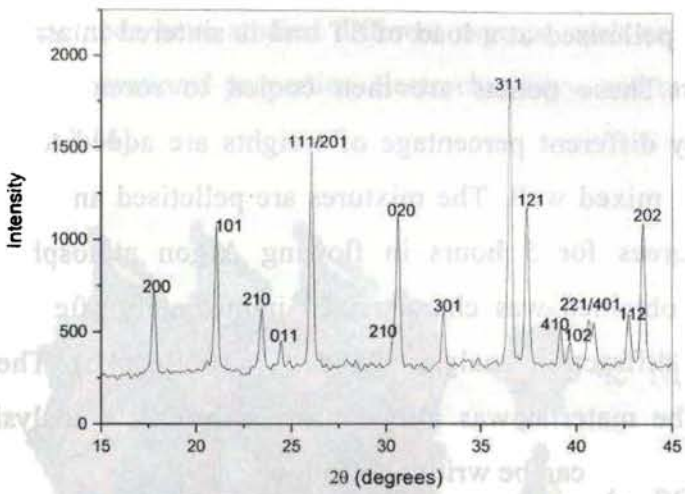

Fig. 5.2 X-Ray Diffraction Patterns of Olivine $LiNiPO_4$

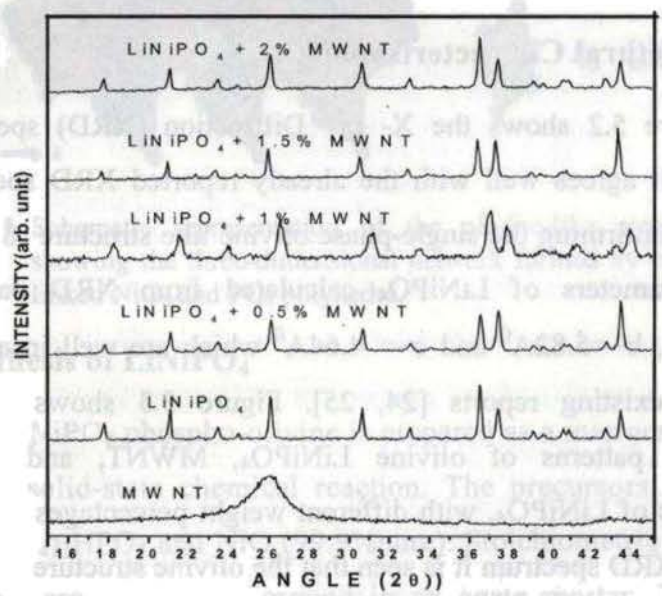

Fig. 5.3 X-Ray Diffraction Patterns of Olivine $LiNiPO_4$, Multi Walled Carbon Nanotubes, and the nano composites of $LiNiPO_4$, with different weight percentages of MWNT.

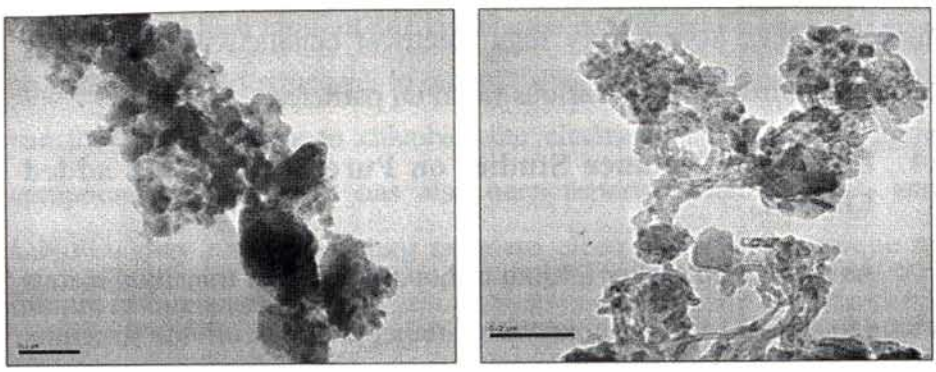

(a) **(b)**

Fig.5.4 TEM images of (a) pure $LiNiPO_4$ (b) 1% MWNT doped $LiNiPO_4$

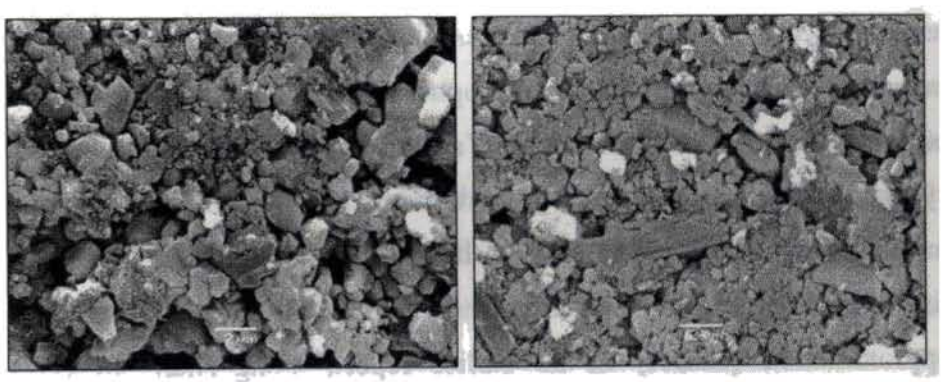

Fig. 5.5 SEM images of (a) pure $LiNiPO_4$ (b) 1% MWNT doped $LiNiPO_4$

The TEM result of $LiNiPO_4$ (figure5.4) indicates the presence of well-defined microcrystalline particles. The corresponding SEM image (figure5.5) exhibit crystallites of the order of a few hundred nanometres. It is consistent with the observations of XRD spectrum where the patterns indicate the formation of well-crystallised particles with average size of 0.2μm from Scherrer`s formula. The TEM result of MWNT doped $LiNiPO_4$ show the presence of carbon nanotubes of average length 200nm and is seen outside the $LiNIPO_4$ grains also.

These MWNTs having very high electrical conductivity can act as connecting wires between various $LiNiPO_4$ particles.

5.4 Diffuse Reflectance Studies on Pure and MWNT added $LiNiPO_4$

As mentioned earlier lithium orthophosphates of transition metals belong to a class of polyanions with a rather complex olivine structure. Recently, $LiNiPO_4$ has attracted a great deal of attention because of its potential as a low-cost cathode electrode material for Li-ion batteries. Unlike the layered compounds $LiCoO_2$ or $LiNiO_2$, which have been used as electrodes in Li-ion batteries, the electronic structure and the magnetic properties of lithium orthophosphates have not been studied in detail and remain controversial. Yamada and co-workers have made systematic studies on various properties of $LiMPO_4$ compounds. They have also reported a calculation of their electronic structures using the linear augmented plane wave method within the local spin-density approximation (LSDA) In an earlier report, Yong_Nian Xu et.al suggested that $LiFePO_4$ may be a half metal with 100% spin polarization. However, experimental conductivity measurement on pure polycrystalline samples showed extremely low conductivity that is typical of an insulator. This is tentatively explained as due to the extremely large electron effective mass in the Fe-3*d* bands. Earlier Santoro and Newnham have suggested that the magnetic structure for the lithium orthophosphates is antiferromagnetic and the interaction between the magnetic ions is that of super exchange type. It is possible that $LiMPO_4$ poly anion compounds fall into the category of Mott

insulators in which intra-atomic correlation is sufficiently strong to give an insulating band structure. In other words, it may not be sufficient to use the LSDA theory to calculate the electronic structures of these compounds. Recently, it has also been reported that $LiCoPO_4$ and $LiNiPO_4$ may have interesting magneto electric properties unique to lithium orthophosphates.

Spectroscopic measurements above the band gap energy of a material can help in understanding possible allowed electronic transitions in the material [21,28-31]. In the present work we have recorded the reflectance spectrum of $LiNiPO_4$ in the wavelength range 0.5 eV- 3.5eV, which exhibits dips (corresponding to peaks in absorption) from 0.7eV. Based on the reflectance (absorption) characteristics, we can have correlation with existing electronic band structure predictions of Xu et al [15,27]. Moreover, we have added few percentages by weight of MWNT to LiNiPO4 with a view to improving the electronic conductivity. The influence of this addition on the reflectance spectra is also investigated.

Diffuse reflectance spectrum is recorded using a portable spectro radiometer (Field SpecTM), the details of which are published elsewhere [22]. Tungsten Halogen lamp (250W) is used as the light source. The radiance of the sample is recorded in a black background and is normalized with the radiance of a Teflon piece for removing the spectral features of light source, for obtaining the reflectance spectrum. Figure 5.6 shows the reflectance spectrum of $LiNiPO_4$.

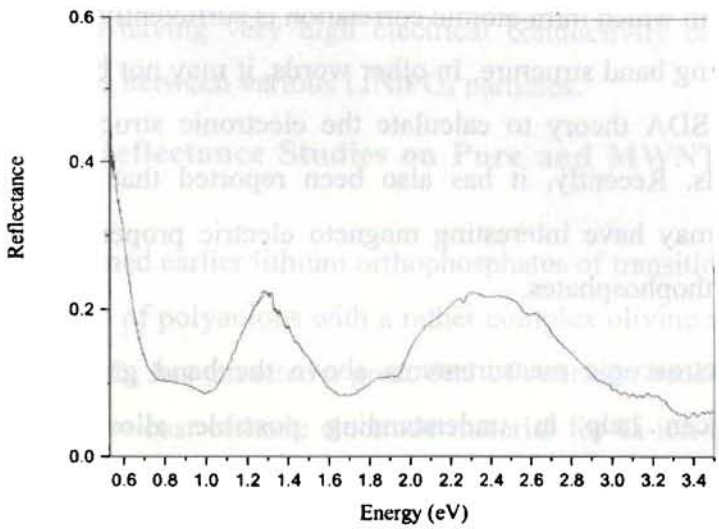

Fig.5.6 The reflectance spectrum of $LiNiPO_4$.

The dips in the reflectance spectrum should correspond to peaks in the absorption spectrum. The onset of the linear increase of reflectance can be correlated with the tail of the absorption spectrum [26] and using this definition the band gap is estimated to be roughly 0.7 eV. The different peaks can be correlated with transitions between different 3d levels of Ni ion. Ni ions being in an octahedral environment of O^{2-} ions, the 3d bands of Ni are split into states of t_{2g} (three fold) and e_g (two fold) symmetries. The band gap obtained supports the fact that the Fermi level lies in the t_{2g} spin down band and e_{2g} spin down band [17, 26]. Hence the possible electronic configuration could be $t_{2g}^{3\uparrow}e_{2g}^{2\uparrow}$, $t_{2g}^{3\downarrow}e_{2g}^{0\downarrow}$ since the number of 3d electrons in $LiNiPO_4$ is 8. The reflectance spectrum exhibits three broad peaks in the ranges, 0.7eV-1.27eV, 1.3 eV-2.29 eV and 2.4eV-3.4 eV. These peaks are correlated with various allowed transitions

(Table 5.1) in accordance with the density of states prediction by Xu et al [15,27] though one to one correspondence of different transitions could not be drawn due to broadness of the peaks.

Table 5.1 Correlation with various allowed transitions in accordance with the density of states prediction by Xu et al [15,27]

ENERGY RANGE (eV)	TRANSITIONS
0.7-1.27	$t_{2gu}^{\downarrow} \rightarrow e_{2gl}^{\downarrow}$ (0.7 eV) $e_{2gu}^{\uparrow} \rightarrow e_{2gl}^{\downarrow}$ (0.85eV) $t_{2gm}^{\downarrow} \rightarrow e_{2gl}^{\downarrow}$(1eV) $t_{2gl}^{\downarrow} \rightarrow e_{2gu}^{\downarrow}$(1.1eV) $t_{2gu}^{\downarrow} \rightarrow e_{2gu}^{\downarrow}$(1.2eV)
1.3-2.29	$t_{2gm}^{\uparrow} \rightarrow e_{2gl}^{\downarrow}$ (2.25eV) $t_{2gu}^{\uparrow} \rightarrow e_{2gl}^{\downarrow}$ (2eV) $e_{2gl}^{\uparrow} \rightarrow e_{2gu}^{\downarrow}$ (2 eV) $t_{2gl}^{\downarrow} \rightarrow e_{2gu}^{\downarrow}$ (1.6eV) $e_{2gl}^{\uparrow} \rightarrow e_{2gl}^{\downarrow}$ (1.5eV) $t_{2gm}^{\downarrow} \rightarrow e_{2gu}^{\downarrow}$ (1.35 eV)
2.4-3.4	$t_{2gl}^{\uparrow} \rightarrow e_{2gl}^{\downarrow}$(2.45 eV) $t_{2gu}^{\uparrow} \rightarrow e_{2gu}^{\downarrow}$(2.5 eV) $t_{2gm}^{\uparrow} \rightarrow e_{2gu}^{\downarrow}$ (2.75 eV) $t_{2gl}^{\uparrow} \rightarrow e_{2gu}^{\downarrow}$ (2.95 eV)

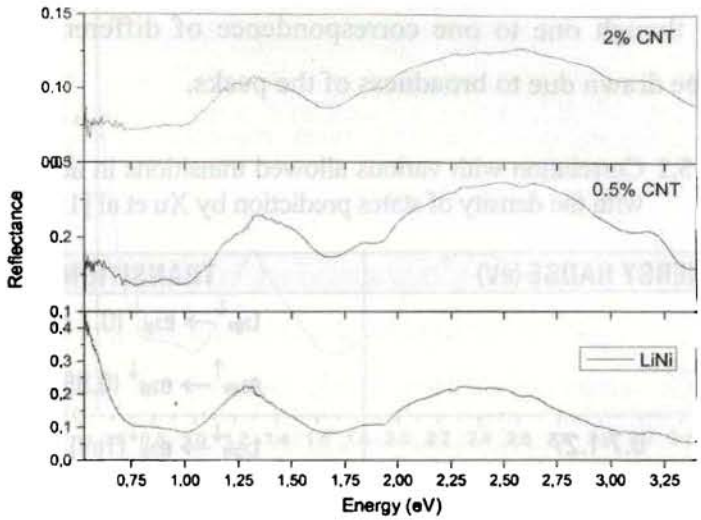

Fig. 5.7 The reflectance spectra of MWNT added $LiNiPO_4$

Figure 5.7 shows the changes in the reflectance spectra of $LiNiPO_4$ when 0.5% MWNT and 2% MWNT are added and are compared with that of the pure $LiNiPO_4$. The major changes on addition of various percentages by weights of MWNT occur in the region of 0.5eV to 0.75 eV, where there is considerable absorption in the case of MWNT mixed samples compared to pure $LiNiPO_4$. This could be due to formation of defect states in the gap between the t_{2g} spin down bands and the e_{2g} spin down bands.

5.5 Studies on Electronic Band Structure of $LiNiPO_4$ and its Modification upon MWNT addition by Photoacoustic Spectroscopy

In chapter 2 we have discussed the Rosencwaig-Gersho theory (R-G theory), which gives a satisfactory explanation to the generation of photo acoustic effect in condensed media. Here we have recorded the

optical absorption spectrum of $LiNiPO_4$ are using PA spectroscopy. The experimental arrangement is the same as the one that mentioned in the previous chapter. The influence of addition of MWNT on absorption spectrum of $LiNiPO_4$ is also studied. The normalized PA spectrum of $LiNiPO_4$ is shown in Figure 5.8 and the peaks involved are tabulated in Table 5.2. The spectral features exhibited can be explained on the basis of the electronic band structure transitions occurring above the band gap, which is estimated to be below 1 eV [27] Moreover, figure 5.8 shows considerable absorption in the whole range of the present measurement, 1.5 eV – 3.5 eV. However, it may be noted that, due to the limited wavelength range of measurement (1.5 eV – 3.5 eV), the exact value of band gap cannot be determined from the recorded PA spectrum.

The Ni ions in the $LiNiPO_4$ olivine are in the octahedral environment of the O^{2-} ions. The 3d bands of Ni are split into states of t_{2g} (three fold) and e_g (two fold) symmetries as explained earlier in the DRS studies. According to Xu et al, the Fermi level lies in the t_{2g} spin down band and in the gap of the spin up bands [27] with $t_{2g}^{3\uparrow}e_{2g}^{2\uparrow}$, $t_{2g}^{3\downarrow}e_{2g}^{0\downarrow}$ being the possible electronic configuration. There exists an energy gap between the 3d up spin and 3d down spin bands as well as between the down spin levels $t_{2g}^{\downarrow}$ and $e_{2g}^{\downarrow}$. The spectral features observed in the figure 5.8 agree well with the density of states calculated on the basis of the electronic band structure by Hunt et al [32] and DOS prediction by Xu et al [27].

Here five spectral features denoted on the spectrum are discussed. All these peaks correspond to the transitions between the 3d spin up states $t_{2g}^{\uparrow}e_{2g}^{\uparrow}$ to the 3d spin down states $t_{2g}^{\downarrow}$ and $e_{2g}^{\downarrow}$ above the Fermi level. The peaks around 1.6 eV –1.62 eV may be due to the transition from $t_{2gl}\downarrow$-$e_{2gu}\downarrow$, $t_{2gm}\downarrow$- $e_{2gu}\downarrow$ while the small absorption around the 1.75 eV can be possibly due to the transition $e_{2gl}\uparrow$- $e_{2gu}\downarrow$. The cluster of small peaks in the range 2.57eV-2.64eV can be attributed to $t_{2gl}\uparrow$- $e_{2gl}\downarrow$, $t_{2gm}\uparrow$- $e_{2gl}\downarrow$, $t_{2gu}\uparrow$- $e_{2gu}\downarrow$. The transitions $t_{2gm}\uparrow$- $e_{2gu}\downarrow$, $t_{2gl}\uparrow$- $e_{2gu}\downarrow$ contributes to the peak in the range 2.9eV-3eV. (Here u, m and l subscripts denote upper, middle and lower levels). These transitions are tabulated in Table 5.2.

The modification of the absorption spectrum of $LiNiPO_4$ upon addition of MWNT is given in figure 5.9. We have chosen three different concentrations to show the variation. As we introduce MWNT, there is an increase in total absorption as the PA amplitude shows an increase with increase in concentration of MWNT. As the concentration increases from zero to 2% MWNT, it starts exhibiting a continuous absorption in the range 1.5 to 2 eV. The range 2eV to 2.5 remains the same in 0.5 %MWNT, with just increase in PA amplitude in the1.5eV to 2 eV range and hence there appears a dip in the region 2eV to 2.5 eV. This dip starts decreasing as the concentration of MWNT increases. The PA amplitude increase in 1.5eV-2eV range can be due to the introduction of defect states between the Fermi level and the lower $e_{2gl}\downarrow$. There can also be introduction of defect states between the $e_{2gl}\downarrow$ and $e_{2gu}\downarrow$ and transitions take place to these states. Hence, it can be concluded that as the concentration of MWNT increases,

number of defect states between the Fermi level and the lower $e_{2gl}\downarrow$ increases.

Table 5.2 Transitions of $LiNiPO_4$ [Comparison between absorption peaks experimentally obtained and theoretically predicted with the corresponding electronic transitions]

Transitions	Experimental (eV)	Literature (eV)
$t_{2gl}\downarrow$-$e_{2gu}\downarrow$, $t_{2gm}\downarrow$- $e_{2gu}\downarrow$	1.6-1.62	1.6
$e_{2gl}\uparrow$- $e_{2gu}\downarrow$	1.75	1.7
$t_{2gu}\uparrow$- $e_{2gl}\downarrow$	2	2.07
$t_{2gl}\uparrow$- $e_{2gl}\downarrow$, $t_{2gm}\uparrow$- $e_{2gl}\downarrow$, $t_{2gu}\uparrow$- $e_{2gu}\downarrow$,	2.57-2.64	2.6
$t_{2gm}\uparrow$- $e_{2gu}\downarrow$, $t_{2gl}\uparrow$- $e_{2gu}\downarrow$	2.9-3	2.9-3

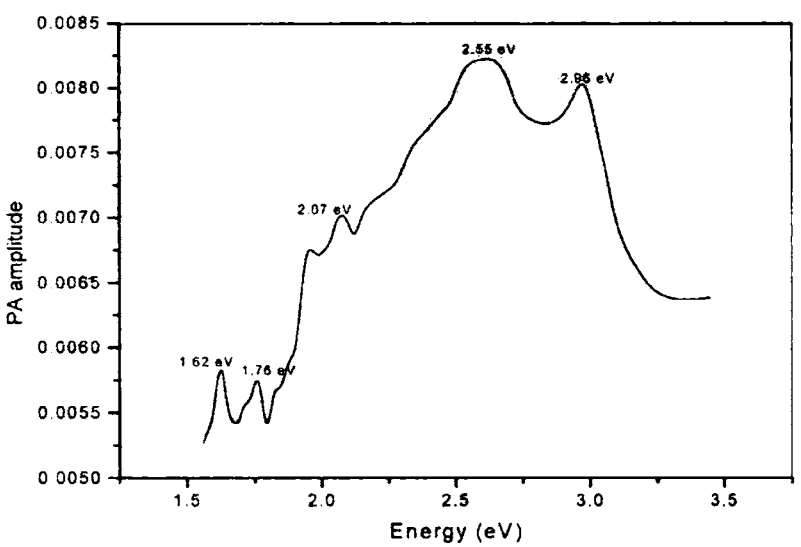

Fig. 5.8 The PA spectrum of $LiNiPO_4$

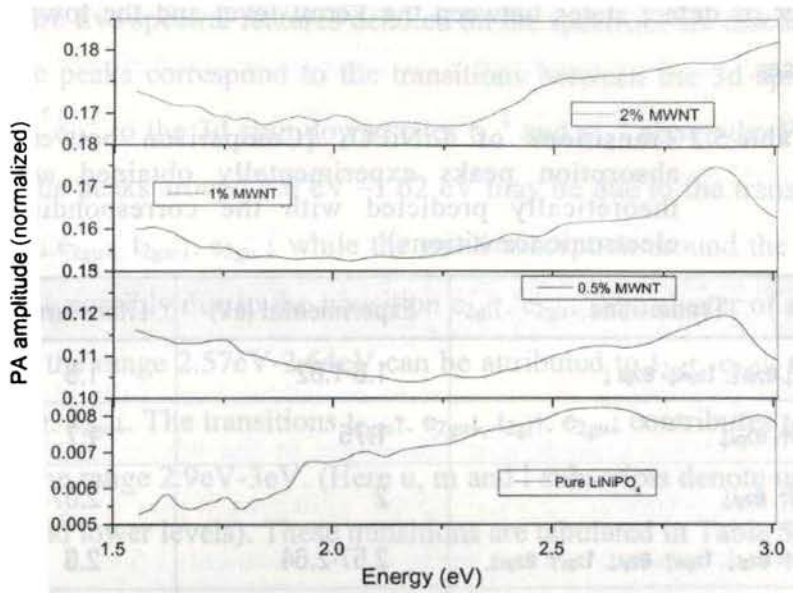

Fig 5.9 Comparison between the PA spectrum of pure $LiNiPO_4$ and the spectra of $LiNiPO_4$ doped with 0.5%, 1% and 2% of MWNT

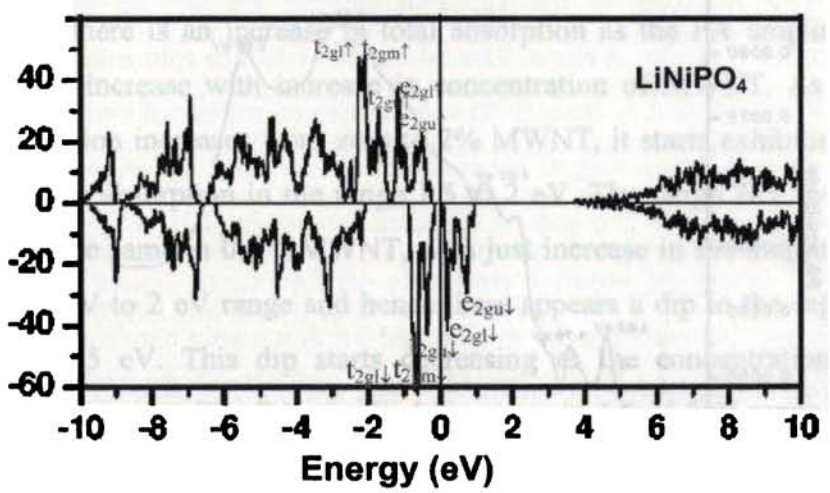

Fig.5.10 Theoretically estimated electronic transitions in $LiNiPO_4$ by Xu Y –N et.al& Hunt et.al

5.6 Thermal Properties of Pure and MWNT added $LiNiPO_4$

The thermal studies of pure and MWNT added lithium nickel phosphate at room temperature are presented here. The low electronic conductivity of the phospho olivine $LiNiPO_4$ has prompted us to add additives such as MWNT to enhance the transport of electrons through the boundaries of the grains. So it is customary to study the variation of thermal properties of such composites. The thermal properties of these materials are basically determined by their composition and structure. It is the rate of heat diffusion that essentially determines the thermal resistance and performance of a battery, thereby the efficiency. In the case of a battery thermal accumulation causes thermal induced stresses in the material, which in turn causes, catastrophic failure and deterioration of the cycle life.

The thermal diffusivity values of $LiNiPO_4$ are obtained using PA technique with a homemade PA cell employed in reflection configuration [30,32]. Light beam from a 20 mW He-Ne laser (632.8nm) modulated using a mechanical chopper (SR 540) is used as the excitation beam and is allowed to fall on the sample that is fixed to the PA cell. The modulation frequency is varied from 10 to 400Hz, and the corresponding modulated pressure signal generated is detected by a microphone (Bruel and Kjaer). The output signal from the microphone is fed to a lock-in amplifier (SR 830) through a preamplifier (SR 550). All the instruments are computer controlled using the RS-232 port of a personal computer. The experimental set up is standardized using a commercially available Si wafer whose thermal diffusivity is calculated to be 0.81×10^{-4} m^2 s^{-1}, which is in perfect agreement with the standard values.

Figure 5.11 shows the variation of PA signal amplitude and phase of pure $LiNiPO_4$ with frequency and the fitted theoretical curve obtained using chi-square minimization and figures 5.12 to 5.14 show the variation when 0.5%, 1 % and 1.5%of MWNTs are added to $LiNiPO_4$. The dots represent the experimental data and the line represents the theoretical fit.

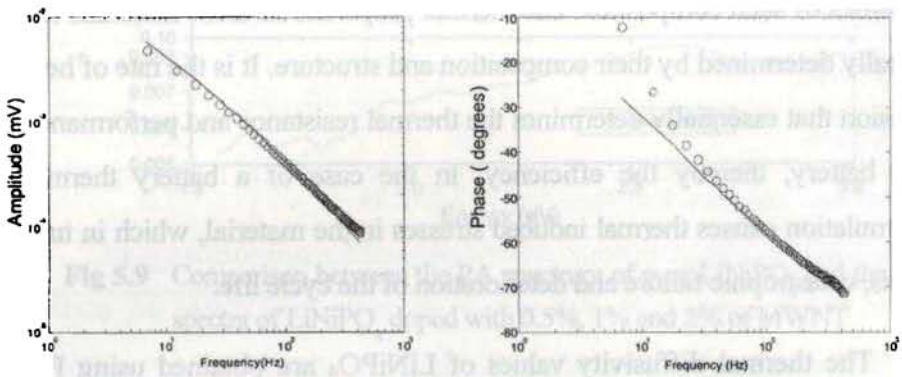

Fig. 5.11 The experimentally obtained and theoretically fitted amplitude and phase variation of $LiNiPO_4$with Frequency

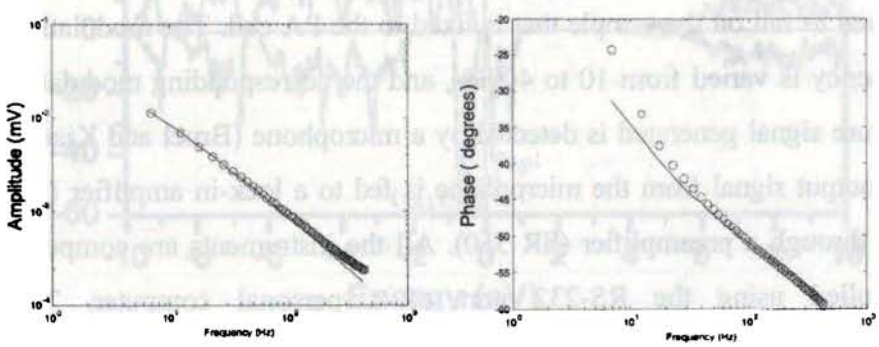

Fig.5.12 The experimentally obtained and theoretically fitted amplitude and phase variation of [$LiNiPO_4$ +0.5% MWNT] with Frequency

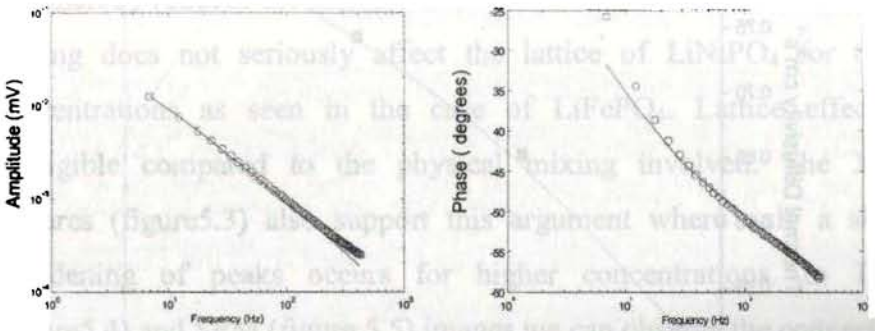

Fig. 5.13 The experimentally obtained and theoretically fitted amplitude and phase variation of [$LiNiPO_4$+1%M WNT] with Frequency

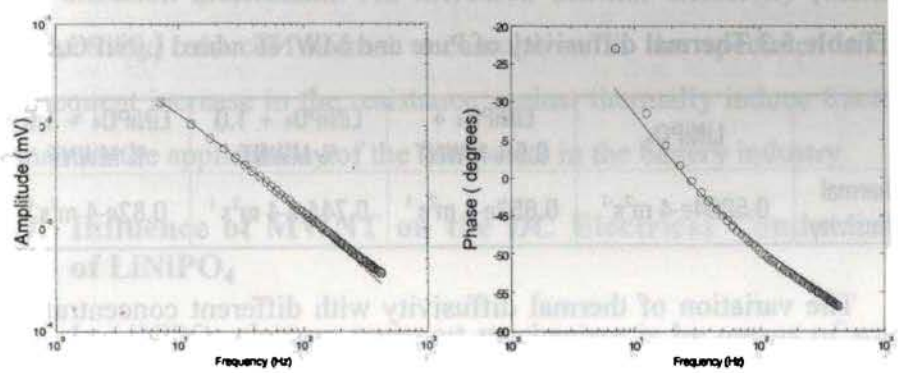

Fig. 5.14 **The experimentally obtained and theoretically fitted amplitude and phase variation of [$LiNiPO_4$+1.5% MWNT] with Frequency**

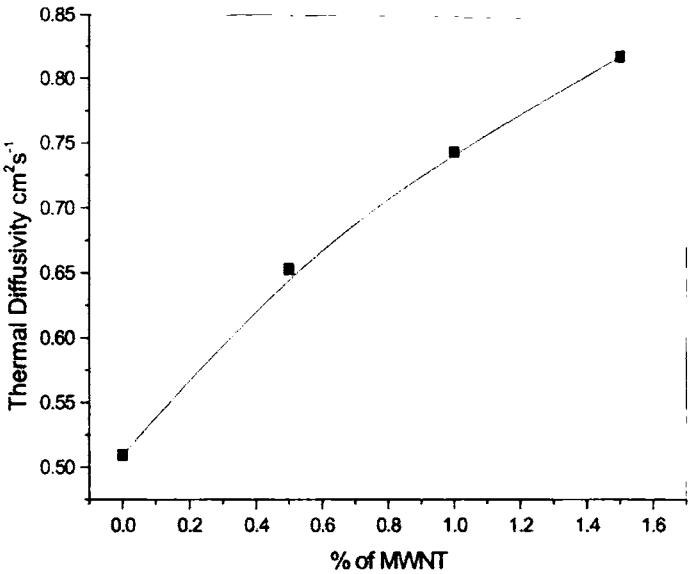

Fig.5.15 Variation of thermal diffusivity with respect to MWNT content in $LiNiPO_4$

Table 5.3 Thermal diffusivity of Pure and MWNT added $LiNiPO_4$

	$LiNiPO_4$	$LiNiPO_4$ + 0.5% MWNT	$LiNiPO_4$ + 1.0 % MWNT	$LiNiPO_4$ + 1.5 % MWNT
Thermal Diffusivity	0.5094e-4 m^2s^{-1}	0.653e-4 m^2s^{-1}	0.744 e-4 m^2s^{-1}	0.82e-4 m^2s^{-1}

The variation of thermal diffusivity with different concentration of MWNT is tabulated in table 5.3. It is seen from table 5.3 that the thermal diffusivity of $LiNiPO_4$ is increasing from its intrinsic value($0.51 cm^2s^{-1}$) with increase in concentration of MWNT. The variation of thermal diffusivity due to this addition is shown graphically in figure 5.12. This increase could be due to the high thermal diffusivity of MWNTs ($\sim 1 cm^2s^{-1}$)

The thermal diffusivity normally decreases when a material is doped because it affects the crystal lattice, enhances phonon scattering and thereby reduces the thermal diffusivity. However, here the MWNT mixing does not seriously affect the lattice of $LiNiPO_4$ for these concentrations as seen in the case of $LiFePO_4$. Lattice effect is negligible compared to the physical mixing involved. The XRD pictures (figure5.3) also support this argument where only a slight broadening of peaks occurs for higher concentrations. In TEM (figure5.4) and SEM (figure 5.5) images we can observe the connecting wire nature of MWNT. Thermal conductivity of MWNT is extremely high. The interconnected net provides an efficient way to heat transport processes across the composite by electrons and therefore enhances the heat diffusion mechanism. An increased thermal diffusivity (thermal conductivity) reduces thermal accumulation in the specimen and a consequent increase in the resistance against thermally induce fracture enhances the applicability of the composite in the battery industry.

5.7 Influence of MWNT on the DC Electrical Conductivity of $LiNiPO_4$

In $LiNiPO_4$ electron transport mechanism is by means of small polarons [11,30-32]. As mentioned in chapter 4, when excess charge carriers like electrons or holes are present in a polar crystal, the atoms in their environment will be polarized and displaced and producing a local lattice distortion. The localized carrier lowers its energy by getting trapped into such a lattice deformation. These charge carriers can be either electrons or holes. Since the electrical transport in this

material is dominated by hopping process, MWNT addition reduces the free energy barrier of the lattice thus favoring the electronic conduction process in MWNT added $LiNiPO_4$ as in $LiFePO_4$.

It is observed that the dc electrical conductivity, of MWNT added $LiNiPO_4$ is directly related to the MWNT concentration. The MWNT having very high electrical conductivity can function as connecting wires between $LiNiPO_4$ particles. This is evident from the TEM images also. The MWNT is present out side the grain boundaries as well. These two factors enhance the bulk conductivity of $LiNiPO_4$ and bring about a nine order of increase in the conductivity when 2% of MWNT is added to the pristine $LiNiPO_4$.

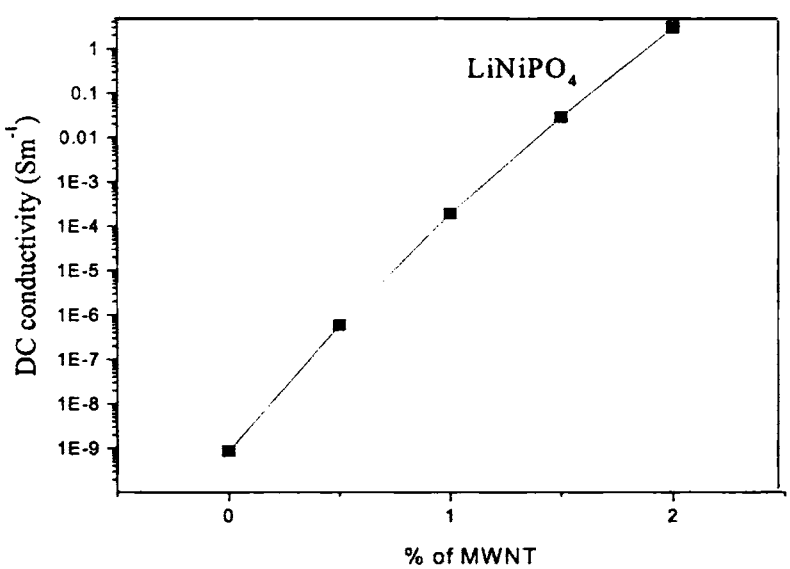

Fig 5.16 Variation of DC conductivity with percentage weight of MWNT measured at room temperature

5.8 Conclusions

The salient features of the electronic band structure of $LiNiPO_4$ are experimentally established based on the DRS and PA investigations. The modification of the reflectance spectra and photo acoustic spectra on adding various percentages by weight of MWNTs points to formation of defect states between the Fermi level and the lower $e_{2g}\downarrow$. The addition of MWNT considerably enhances the room temperature dc electrical conductivity of $LiNiPO_4$.The highlights of the present investigations include the strong correlation between the experimentally observed electronic band structure characterization and the already existing theoretically predicted ones and the considerably large enhancement of dc electrical conductivity of $LiNiPO_4$ (about nine order with the addition of 2% MWNT). We haven't observed any evidence for lattice modifications of $LiNiPO_4$ due to the addition of MWNT and further investigations are required for the confirmation of any lattice modifications.

References

[1] K. Phadhi, K.S. Nanjundaswamy, J.B. Goodenough, J. Electrochem. Soc. 144 1188 (1997)

[2] A. Yamada, S.C. Chung, K. Hinokuma, J. Electrochem. Soc. 148 A224 (2001).

[3] A. Yamada, S. C. Chung, J. Electrochem. Soc. 148 A960 (2001).

[4] A. Yamada, Y. Kudo, K.-Y. Liu, J. Electrochem. Soc. 148 A747 (2001).

[5] A. Yamada, Y. Kudo, K.-Y. Liu, J. Electrochem. Soc. 148 A1153 (2001).

[6] F. Zhou M. Cococcioni, C. A. Marianetti, D. Morgan, and G. Ceder, Phy. Rew. B 70, 235121 (2004)

[7] P. Deniard, A.M. Dulac, X. Rocquefelte, V. Grigorova, O. Lebacq, A. Pasturel, S. Jobic, J. Phys. Chem. Solids 65, 229 (2004).

[8] Solid state ionics-Advanced Materials for Emerging Technologies, by BVR Chowdari,page 337

[9] S. Y. Chung, J. T. Bloking, and Y. M. Chiang, Nat. Mater. 1, 123, (2002)

[10] C. Delacourt, L. Laffont, R. Bouchet, C. Wurm, J. B. Leriche, M.Morcrette, J. M. Tarascon, and C. Masquelier, J. Electrochem.Soc. 152, A913 (2005)

[11] Thomas Maxisch, Fei Zhou and Gerbrand Ceder, PHYSICAL REVIEW B 73, 104301-1-6 (2006)

[12] P. S. Herle, B. Ellis, N. Coombs and L. F. Nazar, Nat.Mat. 3, 147-152 (2004)

[13] X Li, F Kang, X Bai, W Shen, Electro.Chem.Commu. 9, 663-666 (2007)

[14] S.Shi,C Ouyang,Z.Xiang,L,Liu,Z Wang, H Li, D-S Wang,L Chen, X Huang, Phys Rev B, 71, 144404 1-6 (2005)

[15] Y N Xu, W Y Ching Y M Chiang J.Appl.Phys., 95(11),6583-6586, (2004)

[16] Aintzane Goñi*a* , Luis Lezama*a* , María Isabel Arriortua*b* , Gaston E. Barberis*a,c* and Teófilo Rojo, . Mater. Chem., 10, 2779 - 2785 (2000)

[17] Devaraj Shanmukaraj and Ramaswamy Murugan, Ionics 10 ,88-92 (2004)

[18] D. Vaknin,1 J. L. Zarestky,1 J.-P. Rivera,2 and H. Schmid2, Physical Review letters 92(20), 207201-1-4(2004)

[19] J. Wolfenstine and J. Allen Journal of Power Sources 142 389–390(2005)

[20] J. Wolfenstine, J. Allen Journal of Power Sources 136, 150–153(2004)

[21] C.M. Julien, P. Jozwiak, J. Garbarczyk Proceedings of the International Workshop "Advanced Techniques for Energy Sources Investigation and Testing" 4 – 9, Sofia, Bulgaria ,Sept. (2004)

[22] J.Ravi, S.Thomas Lee, M.Paulraj, R.Hernandez, , Applied Spectroscopy, 61(4),444-446,(2007)

[23] C. V. Ramana,,A. Ait-Salah,. Utsunomiya, U. Becker, A. Mauger, F. Gendron, and C. M. Julien, Chem. Mater, 18, 3788-3794 (2006)

[24] I Kornev, M Bichurin, JP Rivera, S Gentil, H Schmid, A GM Jansen, P WYder, Phys.Rev.B, 62(18), 12247-12252 (2000)

[25] M Piana, M Arrabito, S Bodoardo, A D Epifanio, D Satolli, F Croce, B Scrosati, Ionics, 8, 17-26(2002)

[26] P. D. Fochs, Proc. Phys. Soc. 69, 70 (1955).

[27] Xu, Y. N.; Chung, S. Y; Bloking, J. T.; Chiang, Y. M.; Ching, W. Y. Electrochem Solid-State Lett., 7, A131(2004)

[28] Tokumoto H , Tokumoto M. and Ishiguro T. Journal of the Physical society ofJapan, 50, 602 (1981)

[29] Kinney J.B,Staley R.H,Annual Reviews 12.295(1982)

[30] S.Thomas Lee, K.Raveendranath, M.Rajive Tomy, M.Paul Raj, S .Jayalekshmi,J.Ravi Appl. Phys. Lett. 90, 161912(2007)

[31] S Thomas Lee, K.Raveendranath, Rajive M Tomy, M. Paul Raj, S. Jayaleskmi,K.P.R Nair, J.Ravi, Phys. Rev. B 76, 115112(2007)

[32] Hunt A, Ching et al A Phys. Rev. B 7,205120(2006)

Chapter 6

Conclusion and Future Challenges

The conclusions drawn from the present investigations are summarized in this chapter. The significant outcomes of the present study are highlighted. The prospects for further investigations in this direction are also discussed.

Conclusions

In recent years, the search for high energy density cathode materials for applications in rechargeable lithium ion batteries has captured special attention and momentum among the research community across the world. Li-ion batteries are the market fore runners due to their compact size, higher energy densities and power source stability to above 500cycles. Due to the high reactivity of metallic lithium, attempts have been made to use lithium based poly crystalline oxides or phosphates as electrodes for use in Li-ion rechargeable batteries.

Thermal wave physics has been an active area of research as it has created basis for several new and revolutionary measurement technologies. All the photothermal techniques are based on the detection of the thermal waves generated in the specimen after illumination with pulsed or chopped optical radiation. Photoacoustic technique, which is based on the generation and propagation of thermal waves and subsequent effects in the specimen as well as in the coupling medium, allows the evaluation of many of the material parameters, which are hard to measure using conventional techniques.

Over the past two decades, many researchers all around the world have paid much attention to the thermal characterization of cathode materials both in pure and doped forms with a special emphasis on the influence of doping on the fundamental properties of these materials. These investigations are extremely important as a thorough understanding of the fundamental properties such as thermal diffusivity and its variation with doping are essential for getting a better insight into the physical processes tacking place in these materials. Even though, a large amount of research material has been published on the structural, electronic, electrochemical and magnetic properties of lithium based battery materials (oxides and phosphates) reports on their optical and thermal properties are quite scarce. The reason for the scarcity of studies on the optical properties may be due to the fact that these materials are optically opaque and most of the optical absorption spectroscopy studies rely on the transmission technique. In the present work we have employed Photoacoustic Spectroscopy (PAS) for

determining the optical absorption spectra of $Li_xMn_2O_4$ and $LiMPO_4$ (M=Fe, Ni) due to its unique advantage of directly measuring the amount of light absorbed by a material. It possesses zero-base line advantage, which means that signals are generated only if there is an optical absorption event. Moreover, scattered light, which presents such a serious problem in conventional spectroscopic techniques, presents no difficulties in PAS.In this context; PAS is a good tool for the evaluation of thermal diffusivity of compound semiconductors such as battery materials, which show semiconducting properties in its pristine form.

In spite of the existence of several photothermal techniques, photoacoustic technique has gained wide popularity due to the simplicity of experimental setup and the possibility of simultaneous measurement of thermal and transport properties with good accuracy. Photoacoustic phase measurement is an excellent approach to investigate the heat transport mechanism as well as electronic transport propreties. In the present work, measurements carried out on $LiMn_2O_4$, $LiFePO_4$ and, $LiNiPO_4$ reveal the effectiveness of open cell photoacoustic technique determine various optical and thermal parameters of poly crystalline semiconducting samples.

The currently used cathode material for commercialized lithium ion battery is $LiCoO_2$, which is expensive, toxic, possesses limited practical capacity (<140 mAh g−1) and rates, and suffers from stability problems at elevated temperatures in the common electrolyte solutions. Consequently, intense research on identifying new cathode materials for Li-ion batteries is being carried out today by hundreds of research

groups throughout the world. Other alternatives for LiCoO2 are the spinel system $LiMn_2O_4$ and the phospho olivines $LiMPO_4$ (M= Fe, Mn, Co, Ni etc). Lithium metal phosphates, $LiMPO_4$ (M=Fe, Mn, Co, Ni) have attracted particular attention due to their high energy density, low cost and good environmental compatibility of its basic constituents. Moreover, these compounds display high redox potentials, fast Li^+ ion transport, excellent thermal stability, high Lithium intercalation potential, and energy density comparable to that of conventional lithium metal oxides.

In the present work the spinel system $Li_xMn_2O_4$ (x=0.8 to 1.2) and phospho olivines $LiMPO_4$ (M=Fe,Ni) have been investigated with special emphasis on elucidating their optical and thermal behaviour using PAS. For the $Li_xMn_2O_4$ spinel system the theoretical prediction of the electronic structure by Full-Potential Linear Muffin-Tin Orbital (FP-LMTO method) has been experimentally verified for the first time employing photo acoustic technique. The variation of thermal diffusivity with changing x values in $Li_xMn_2O_4$ is extensively studied to explain the influence of lithium concentration on the thermal properties which, has been correlated with the structural asymmetry and defects in $Li_xMn_2O_4$. In the optical absorption spectrum recorded in the visible range, six prominent absorption peaks associated with the O 2p - Mn t_{2g}, O 2p - Mn e_g and Mn t_{2g} - Mn e_g band transitions for $Li_xMn_2O_4$ with $x \leq 1$, are observed experimentally for the first time substantiating the electronic structure predicted by FP-LMTO method.

Photo acoustic technique has also been used to understand the Jahn-Teller distortion in Li_xMn2O_4. PA spectra of $Li_{0.9}Mn_2O_4$, $LiMn_2O_4$ and $Li_{1.1}Mn_2O_4$ at two temperatures, 298 K and 280 K, which are respectively above and below Jahn-Teller phase transition temperature, 290 K, are determined. The spectra of $LiMn_2O_4$ and $Li_{1.1}Mn_2O_4$ below the transition temperature are found to be significantly different from their respective spectra above the transition temperature. However, the PA spectra of $Li_{0.9}Mn_2O_4$ at both these temperatures show only a minor difference between each other compared to the changes occurring in $LiMn_2O_4$ and $Li_{1.1}Mn_2O_4$. These effects are explained on the basis of the predominant JT tetragonal distortion in cubic $Li_xMn_2O_4$ with a high Li content, which brings forth a modification in their electronic structure. JT distortion is substantial in $LiMn_2O_4$ and $Li_{1.1}Mn_2O_4$ due to their higher Mn^{3+} ions content than in $Li_{0.9}Mn_2O_4$.

The thermal diffusivity values of $Li_xMn_2O_4$ determined using PA technique at two temperatures, 298 K and 280 K, above and below their Jahn-Teller phase transition temperature (290 K) show a drastic reduction from their corresponding room temperature values. The percentage of reduction in the thermal diffusivity of $Li_xMn_2O_4$ increases with their Li content. These effects are associated with the reduction in crystal symmetry due to structural deformation by Jahn-Teller distortion observed in $Li_xMn_2O_4$ below the transition temperature.

A comparison of the optical absorption spectra of cubic spinel $LiMn_2O_4$ and its delithiated form λ-MnO_2 determined using photoacoustic spectroscopy show shifts in the absorption peaks upon de-intercalation. The observed shifts are explained on the basis of non-rigid band model suggesting a change in oxygen ionicity during lithium de-intercalation. These results show that, upon lithium deintercalation of $LiMn_2O_4$, the effect of change in oxygen ionicity is stronger than the effect of cell volume change for modifying the electronic structure of $LiMn_2O_4$ around its Fermi level.

The experimental investigations on $LiFePO_4$ for understanding the electronic band structure based on the optical absorption by photoacoustic spectroscopy points to a much reduced band gap than put forward by Zhou et al. This conclusion is based on the fact that the excitation wavelengths are well below 3.7 eV and there is considerable absorption in the whole wavelength range of excitation (1.5 eV -3.5 eV). Any possibility of excited state absorption can be ruled out taking into account the power levels used for excitation and hence the resulting peaks in the absorption spectra should be due to transitions taking place above the band gap which agrees well with the electronic band structure predictions by Xu et al. These observations also suggest that the band gap should be lower than 1.5 eV. The modification of the optical absorption spectra upon introducing various weight percentages of MWNT into $LiFePO_4$, with a view to improving the electronic conductivity of the latter, is also studied. Two mechanisms, namely the coulomb interaction between the transition metal ion of $LiFePO_4$

and MWNT and the formation of defect states while MWNT is introduced into $LiFePO_4$ are proposed for explaining this modification.

An improvement in the electronic transport properties and thereby in the dc and ac electrical conductivities is observed on doping $LiFePO_4$ with MWNT. This enhancement of electrical conductivity is substantiated using SEM, TEM and impedance spectroscopy techniques. TEM images exhibit the adhesion of $LiFePO_4$ particles to MWNT and SEM images reveal the dependence of packing density on MWNT concentration. Impedance spectroscopic analysis is primarily carried out using Bode plots, Nyquist plots and AC conductivity plots. The Bode plots manifest the characteristics of low frequency dispersion, for pure and doped $LiFePO_4$, pointing to electron hopping. The increase in critical frequency involved in low frequency dispersion with an increase in MWNT content implies a reduction in the electron locality upon MWNT doping. The dispersion curve of ac conductivity reveals the increase in electron hopping frequency with MWNT content. Based on these extensive analysis we suggest that the conduction mechanism in pure $LiFePO_4$ solely due to bulk conduction while in MWNT doped $LiFePO_4$, in addition to bulk conduction there could be contribution from conduction across grain boundaries whose strength is directly related to the MWNT content.

The diffuse reflectance spectra of $LiMPO_4$ (M=Fe, Ni) recorded in the energy range 0.5 eV-3.5 eV give primary evidence of the electronic band structure. The dips observed in the diffuse reflectance spectra of $LiMPO_4$ (M=Fe, Ni) can be correlated to absorption peaks.

These peaks are identified with various electronic transitions in accordance with existing theoretical predictions of their electronic band structure. The modification of the reflectance spectra on addition of various percentages by weight of MWNTs is explained on the basis of the formation of defect states.

The thermal parameters of $LiMPO_4$ (M=Fe, Ni) are determined for the first time using the well-known photoacoustic technique. The increase in thermal diffusivity of $LiFePO_4$ and $LiNiPO_4$ on addition of MWNTs can be attributed to the high thermal diffusivity of the MWNT. The addition of MWNT brings about appreciable enhancement of the electrical conductivity of $LiFePO_4$ and $LiNiPO_4$ without disturbing the lattice symmetry of these materials. Hence MWNT doped $LiFePO_4$ and $LiNiPO_4$ offer excellent prospects of applications as cathode materials in rechargeable lithium ion batteries.

6.1 Highlights of the Present Study in a Nutshell.

a. The electronic structure of $Li_xMn_2O_4$ predicted by Full-Potential Linear Muffin-Tin Orbital (FP-LMTO) method is experimentally verified for the first time.

b. The present work could solve the dispute about the band gap of Li $FePO_4$ from the photo acoustic and diffuse reflectance studies.

c. The electronic conductivity of the phospho olivines $LiFePO_4$ and $LiNiPO_4$ could be enhanced considerably by adding small amounts of MWNT without causing any

structural distortion. This aspect is quite significant as far as the battery applications of these materials are concerned and points towards the high prospects of applications of MWNT doped $LiFePO_4$ and $LiNiPO_4$ as cathode materials in rechargeable lithium ion batteries.

6.2 Future prospects

a. In the present investigations the non-destructive technique of photo acoustic spectroscopy has been efficiently employed to investigate the thermal and the optical properties of three important cathode materials $Li_xMn_2O_4$ (x=0.8, 0.9, 1, 1.1, 1.2) and $LiFePO_4$ and $LiNiPO_4$. It would be interesting to carry out photo acoustic measurements on $Li_xMn_2O_4$ system during the charge – discharge cycle which might provide valuable insight into the Lithium dynamics within the system.

b. With the Lithium phosphates the studies could be extended to nano crystalline samples with particle size around 10nm. Solgel synthesis techniques of $LiFePO_4$ and $LiNiPO_4$ in the presence of the complexing agent citric acid can be employed to get nano crystalline samples of these phosphates with very good electronic conductivity in the range of a few Siemens/cm. The reduced particle size and improved electronic conductivity can enhance the energy density and rate capability and also guarantee long term cyclability for these cathode materials.